

Aus der Klinik für Allgemeine, Unfall- und Wiederherstellungschirurgie
Klinik der Ludwig-Maximilians-Universität München

&

Aus der Fakultät für Angewandte Naturwissenschaften und Mechatronik
Hochschule für Angewandte Wissenschaften München



HM 

*Structural and biomechanical analysis of articular cartilage of mouse
genetic models via atomic force microscopy*

Dissertation

zum Erwerb des Doktorgrades der Naturwissenschaften
an der Medizinischen Fakultät der
Ludwig-Maximilians-Universität zu München

vorgelegt von

Lutz Fleischhauer

aus

Bad Soden am Taunus

Jahr

2021

Mit Genehmigung der Medizinischen Fakultät
der Universität München

Erstgutachter: PD Dr. Attila Aszodi
LMU München

Zweitgutachter: Prof. Dr. rer. nat. Hauke Clausen-Schaumann
HAW München

Dekan: Prof. Dr. Thomas Gudermann

Tag der mündlichen Prüfung: 11.04.2022

Affidavit



Eidesstattliche Versicherung

Fleischhauer, Lutz

Name, Vorname

Ich erkläre hiermit an Eides statt, dass ich die vorliegende Dissertation mit dem Titel:

„Structural and biomechanical analysis of articular cartilage of mouse genetic models via atomic force microscopy”

selbständig verfasst, mich außer der angegebenen keiner weiteren Hilfsmittel bedient und alle Erkenntnisse, die aus dem Schrifttum ganz oder annähernd übernommen sind, als solche kenntlich gemacht und nach ihrer Herkunft unter Bezeichnung der Fundstelle einzeln nachgewiesen habe.

Ich erkläre des Weiteren, dass die hier vorgelegte Dissertation nicht in gleicher oder in ähnlicher Form bei einer anderen Stelle zur Erlangung eines akademischen Grades eingereicht wurde.

Muenchen, 16.07.2021

Ort, Datum

Lutz Fleischhauer

Unterschrift Doktorandin bzw. Doktorand

Table of contents

AFFIDAVIT.....	3
TABLE OF CONTENTS.....	4
ABBREVIATIONS.....	5
LIST OF PUBLICATIONS	7
1. MY CONTRIBUTION TO THE PUBLICATIONS.....	9
2. INTRODUCTION	11
2.1 OSTEOARTHRITIS.....	11
2.2 ARTICULAR CARTILAGE	12
2.2.1 <i>Impact of the nervous system on articular cartilage</i>	16
2.2.2 <i>The matrilin family</i>	17
2.3 BIOMECHANICAL ANALYSIS OF ARTICULAR CARTILAGE VIA THE ATOMIC FORCE MICROSCOPE ...	18
2.4 THE DESTABILIZING MEDIAL MENISCUS MODEL	21
2.5 AIMS OF THIS THESIS	23
3. SUMMARY	25
4. ZUSAMMENFASSUNG.....	29
5. PAPER I	33
6. PAPER II	49
7. PAPER III	75
8. REFERENCES	86
SUPPLEMENT A: PAPER IV	97
SUPPLEMENT B: PAPER V	110
ACKNOWLEDGEMENT	127
CURRICULUM VITAE.....	128

Abbreviations

ADAMTS	A disintegrin and metalloproteinase with thrombospondin motifs
ACL	Anterior cruciate ligament
ACLT	Anterior cruciate ligament transection
AC	Articular cartilage
AFM	Atomic force microscopy
BMP-2	Bone morphogenetic protein-2
CGRP	Calcitonin gene-related peptides
CT	Computer tomography
DMM	Destabilizing medial meniscus
EGF	Epidermal growth factor
ECM	Extracellular matrix
EZM	Extrazelluläre Matrix
F	Femur
IT-AFM	Indentation-type atomic force microscopy
ITM	Interterritorial matrix
KO	Knockout
LMTL	Lateral meniscotibial ligament
MMP-13	Matrix metalloproteinase 13
MMTL	Medial meniscotibial ligament
MM	Medial meniscus
MED	Multiple epiphyseal dysplasia
OA	Osteoarthritis
PCM	Pericellular matrix
PRELP	Proline And Arginine Rich End Leucine Rich Repeat Protein
SLRP	Small leucine-rich repeat proteoglycan
Substance P	Substance pain/powder

TAC-1	Tachykinin Precursor 1
T	Tibia or Threonin
TGF- β	Transforming growth factor beta
TRPV4	Transient receptor potential cation channel subfamily V member 4
vWA	von Willebrand factor A-like

List of publications

This thesis is based on the following publications:

I. *Sensory neuropeptides are required for bone and cartilage homeostasis in a murine destabilization-induced osteoarthritis model*

Dominique Muschter¹, **Lutz Fleischhauer¹**, Shahed Taheri¹, Arndt F Schilling, Hauke Clausen-Schaumann, Susanne Grässel

Bone. 2020, 133:115181

¹contributed equally

II. *Mice Lacking the Matrilin Family of Extracellular Matrix Proteins Develop Mild Skeletal Abnormalities and Are Susceptible to Age-Associated Osteoarthritis*

Ping Li, **Lutz Fleischhauer**, Claudia Nicolae, Carina Prein, Zsuzsanna Farkas, Maximilian Michael Saller, Wolf Christian Prall, Raimund Wagener, Juliane Heilig, Anja Niehoff, Hauke Clausen-Schaumann, Paolo Alberton, Attila Aszodi

International Journal of Molecular Science. 2020, 21(2): p. 666

III. *The Matrilin-3 T298M mutation predisposes for post-traumatic osteoarthritis in a knock-in mouse model*

Patrick Seifer, Eric Hay, **Lutz Fleischhauer**, Juliane Heilig, Wilhelm Bloch, Stephan Sonntag, Doron Shmerling, Hauke Clausen-Schaumann, Attila Aszodi, Anja Niehoff, Martine Cohen-Solal, Mats Paulsson, Raimund Wagener, Frank Zaucke

Osteoarthritis and Cartilage. 2021, (1): p. 78-88

IV. *Imbalanced cellular metabolism compromises cartilage homeostasis and joint function in a mouse model of mucopolidosis type III gamma*

Lena Marie Westermann, **Lutz Fleischhauer**, Jonas Vogel, Zsuzsa Jenei-Lanzl, Nataniel Floriano Ludwig, Lynn Schau, Fabio Morelini, Anke Baranowsky, Timur A Yorgan, Giorgia Di Lorenzo, Michaela Schweizer, Bruna de Souza Pinheiro, Nicole Ruas Guarany, Fernanda Sperb-Ludwig, Fernanda Visioli, Thiago Oliveira Silva, Jamie Soul, Gretl Hendrickx, J Simon Wiegert, Ida VD Schwartz, Hauke Clausen-Schaumann, Frank Zaucke, Thorsten Schinke, Sandra Pohl, Tatyana Danyukova

Disease Models & Mechanisms. 2020, 13(11):dmm046425

V. ***Basement membrane stiffness determines metastases formation***

Raphael Reuten, Sina Zendehtoud, Monica Nicolau, **Lutz Fleischhauer**, Anu Laitala, Stefanie Kiderlen, Denise Nikodemus, Lena Wullkopf, Sebastian Rune Nielsen, Sarah McNeilly, Carina Prein, Maria Rafeeva, Erwin M Schoof, Benjamin Furtwängler, Bo T. Porse, Hyobin Kim, Kyoung Jae Won, Stefanie Sudhop, Kammilla Westarp Zornhagen, Frank Suhr, Eleni Maniati, Oliver M.T. Pearce, Manuel Koch, Lene Broeng Oddershede, Tom Van Agtmael, Chris D. Madsen, Alejandro E. Mayorca-Guiliani, Wilhelm Bloch, Roland R. Netz, Hauke Clausen-Schaumann, Janine T. Erler

Nature Materials. 2021, 20(6):892-903

The following work is not published yet, but mentioned in the text:

VI. ***Biomechanical analysis with IT-AFM of the articular cartilage zones in the murine DMM model***

Lutz Fleischhauer, Dominique Muschter, Paolo Alberton, Susanne Grässel, Attila Aszodi, Hauke Clausen-Schaumann

Manuscript

1. My contribution to the publications

Paper I: This paper was published with shared first authorship. The work was divided into three equally important main parts: AFM indentation measurements, which were carried out by LF, CT scans, carried out by ST and histology, carried out by DM. The work done by all three first authors was of equal value, so that the first authorship was shared. In detail: I prepared all the tissue sections for AFM analysis. I carried out all AFM measurements. I also analyzed all AFM indentation measurements, processed them and prepared the related figures for this publication. I wrote the “Materials and Methods” part and helped with the correction of the manuscript.

Paper II: I performed tissue sectioning of the 4 months and 1 year old mice for AFM indentation measurements. I did AFM imaging and indentation measurements as well as data analysis for the articular cartilage samples. I wrote the “Materials and Methods” part and prepared the figure related to my AFM measurements.

Paper III: I did tissue sectioning, AFM indentation measurements, data analysis, wrote the “Materials and Methods” part and prepared the figure related to my work for publication.

Paper IV: I supervised Jonas Vogel when he performed the AFM measurements. I did the data analysis and created the figures for the publication. I wrote the “Materials and Methods” part and helped correcting the manuscript.

Paper V: I did tissue sectioning and subsequently conducted the AFM indentation measurements on the basement membrane. I analyzed the AFM data and developed a unique method to identify the basement membrane in

the AFM data. I prepared the figure and wrote the “Materials and Methods” related to my work in the publication.

Paper VI: I did tissue sectioning, AFM indentation measurements, histological staining and histological scoring. I prepared all figures and did the data analysis. I wrote the manuscript.

2. Introduction

2.1 Osteoarthritis

The musculoskeletal system is responsible for the stability, movement and flexibility of the mammalian organism. It consists of muscles, tendons, cartilage, bones, joints and other connective tissues. If any of these given components do not work properly due to an injury, genetic predisposition or age-associated factors, the movement and stability are restricted. The most frequent musculoskeletal disease worldwide is osteoarthritis (OA) and its prevalence is rising [1, 2]. Affected patients are complaining about swollen joints, pain and a decreased agility and mobility. The currently available treatments address only the symptoms or are invasive strategies for advanced OA, such as complete knee replacement or autologous cartilage transplantation. However, this does not lead to a full regeneration and the artificial joint has often to be replaced after a usage of up to 25 years [3]. The joint most commonly affected by OA is the knee [4]. Up to now, several factors are known that can induce OA. These include increasing age, high prevalence of obesity, injuries and the menopause [5 – 8]. OA is conservatively defined by cell stress and the slow degradation of articular cartilage (AC) where anabolic and catabolic pathways are activated but catabolic pathways predominate. Today, OA is seen as a multifactorial and whole joint disease that has genetic, biological and/or biomechanical reasons [9]. AC is responsible for the lubrication of the joints and needs to withstand high shear stress and compressive forces to protect the underlying bone. Physiological loading is a constant stimulus which AC or chondrocytes are exposed to. The biomechanics of the extracellular AC matrix is therefore a crucial parameter [10]. Thus, healthy articular cartilage is highly adapted to this complex mechanical environment [11]. Today, new therapies are on the way, which are addressing anabolic, catabolic or inflammatory pathways, the subchondral

bone or the nervous system [12]. Nevertheless, the homeostasis of articular cartilage is still not fully understood and more research is needed to provide satisfactory treatments, including treatments for early OA.

2.2 Articular Cartilage

Cartilage is a resilient tissue and serves as a structural component which protects the end of long bones. Interestingly, it does not contain any blood vessels or nerve fibers. Three types of cartilage are known in the human body: the elastic, the fibrous and the hyaline cartilage. Elastic cartilage contains mainly collagen II and elastin and is found in the outer ear, the epiglottis and some parts in the larynx. Fibrous cartilage is found for instance in the menisci and the annulus fibrosus of the intervertebral disc containing mainly collagen I. Hyaline cartilage is composed of collagens and proteoglycans and found transiently in embryonic bone templates and in permanent tissues such as the ribs, the nose or joint surfaces. Hyaline cartilage located on joint surfaces is also called articular cartilage (AC). AC is composed out of the extracellular matrix (ECM) and to a small extent (5-10%) out of chondrocytes. It can be divided into four zones, the superficial, the middle, the deep and the calcified zone [13]. Each zone has unique characteristics in terms of cell shape, matrix composition and fiber alignment [14] (Fig. 1). The non-calcified and calcified AC is separated by a narrow line called the tidemark and the calcified cartilage is firmly attached to the underlying subchondral bone (Fig. 1).

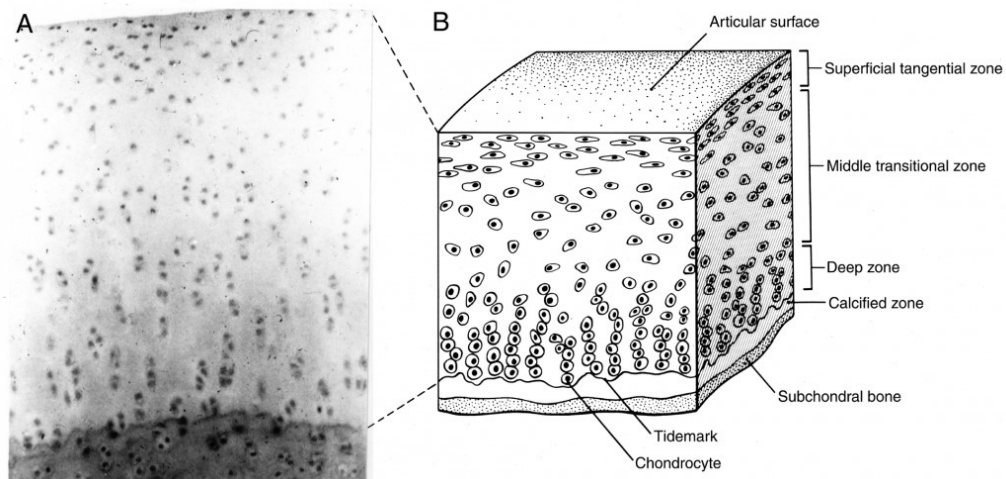


Figure 1 A) Histologic section of normal adult articular cartilage B) Articular cartilage scheme originating from: Mow VC, Proctor CS, Kelly MA: Biomechanics of articular cartilage, in Nordin M, Frankel VH (eds): Basic Biomechanics of the Musculoskeletal System, ed 2. Philadelphia, PA, Lea & Febiger, 1989, pp 31–57.)

In general, the ECM is mainly comprised of collagen II, a triple-helical fiber-forming structural protein. Three identical alpha-chains (*COL2A1*) form molecules that wrap around each other forming a genuine collagen fiber. These fibers are showing a characteristic periodic 67 nm spacing, termed D-band structure, due to their amino acid sequence and the subsequent folding. The collagen family consists of 28 members. They can be subdivided into fibril-forming and fibril-associated collagens with interrupted triple helices (FACIT), network-forming and miscellaneous collagens [15]. Collagen II is the main structural component of the developing endochondral bones and the AC. Mice deficient in collagen II (*Col2a1*^{-/-}) die at birth due to improper formation of the cartilaginous elements, unable to support breathing, while heterogenous *Col2a1*^{+/-} mice are viable and show major structural impairments and a lower stiffness of the AC [16, 17]. Besides collagen II, there are also collagens III, VI, IX, X, XI, XII and XIV that are playing important roles in AC [18]. Collagen III is copolymerized and cross-linked to collagen II fibrils like collagen IX and XI. It is mostly located in the pericellular matrix, the matrix compartment closest to the chondrocytes, and in the superficial zone

[19]. Interestingly, it is also upregulated in AC affected by OA [20]. Recently, a biomechanical study on collagen III deficient mouse has shown that AC stiffness decreases even though matrix crosslinks increase [21]. Collagen VI is a network-forming collagen and is found in the pericellular matrix. It has several binding sites for other collagens and also for soluble factors [22]. Additionally, the group of Farshid Guilak could show that it contributes largely to the stiffness of the pericellular matrix [23]. Therefore, collagen VI plays a major role in connecting the chondrocytes to the extracellular matrix and maintaining its biomechanical properties. Type IX collagen, a heterotypic ($\alpha 1$, $\alpha 2$, $\alpha 3$ chains) minor FACIT collagen, covalently binds to the surface of collagen II. Its distribution pattern is changed in OA cartilage and mice lacking collagen IX develop severe OA [24]. The heterotrimeric ($\alpha 1$, $\alpha 2$, $\alpha 3$ chains) collagen XI is classified as fibrillar collagen and is formed with the support of collagen II and IX. The absence of collagen XI in mice results in severe chondrodysplasia and perinatal lethality, whereas heterozygous deletion of *Coll11a1* encoding the $\alpha 1$ polypeptide chain lead to OA, which highlights its important function in AC homeostasis [25]. Research is ongoing and additional collagens are found in AC or linked to OA pathogenesis [26].

The other important components of the ECM are the proteoglycans, with aggrecan being the most abundant one. Aggrecan has a typical bottlebrush structure that contains a core protein made of one globular and two interglobular domains with around 100 chondroitin and about 30 keratan sulfate chains attached to it [27]. Chondroitin sulfate chains possess a high negative charge that leads to water attraction and therefore a high osmotic pressure, giving cartilage the capacity of resisting high compressive forces. These aggrecan monomers are non-covalently linked to hyaluronic acid stabilized by linker proteins. Hyaluronic acid is also a widely used therapeutic against OA

[28]. Nevertheless, the clinical outcome is not satisfying and better interventions need to be developed. Recently, a study could show that in a hypomorphic aggrecan mouse model the stiffness of the AC is increased and spontaneous OA is more likely [29]. The other proteoglycans are present in a smaller amount, such as versican and small leucine-rich repeat proteoglycans (SLRPs) that are divided into class I (decorin, biglycan, asporin), class II (fibromodulin, lumican, keratocan, osteoadherin, PRELP), class III (epiphycan, mimecan, opticin) and class IV (chondroadherin, chondroadherin-like). Additionally, there is the group of glycoproteins containing the matrilin family or the thrombospondin family that are fulfilling diverse functions. Proteoglycans do not only possess structural or adaptor functions, but may also mediate the immune response or bind to different growth factors [30]. Therefore, proteoglycans, glycoproteins, as well as collagens, are contributing to biomechanics and to signaling pathways of articular cartilage.

In OA, it is known that before protein alteration is detectable via histochemical staining, biomechanical alterations are measurable [31, 32]. Biomechanics are drastically altered due to the overexpression of catabolic enzymes such as matrix metalloproteinase 13 (MMP-13) and 'A disintegrin and metalloproteinase with thrombospondin motifs 4 and 5' (ADAMTS-4/-5) resulting in degradation of collagens and aggrecan, respectively [33, 34]. The complex interplay between the components of this protein network is highly important to maintain the biomechanical properties of AC, to withstand the forces up to three times the body weight during walking [35]. This biomechanical alterations are sensed in different ways by chondrocytes. They possess, on one hand, the mechanosensitive channels Piezo1, Piezo2 and TRPV4 [36, 37]. On the other hand, integrins, a genuine class of cell adhesion receptors, are also playing a major role in mechanosensing [38]. If this balanced biomechanical environment is altered via matrix cross-linking or disrupting the collagen/proteoglycan network, chondrocyte metabolism is

dysregulated [39, 40]. Thus, the early diagnosis of OA is of high importance to intervene with this protein degradation process, which leads to further disease progression of biomechanical alterations.

2.2.1 Impact of the nervous system on articular cartilage

OA is a multifactorial disease and different factors, such as the nervous system, are believed to influence disease progression. Although cartilage does not contain nerve fibers and blood vessels, chondrocytes do possess receptors for neurotransmitters and can even express substance P, a neurotransmitter mainly expressed by neurons [41, 42]. This makes them susceptible to neuronal signaling. Neurotransmitters are divided into sensory and sympathetic transmitters. The most prominent one of the sympathetic neurotransmitters is noradrenaline. Typical sensory neurotransmitters are tachykinins, including substance P, which is responsible for nociception and inflammation, as well as calcitonin gene-related peptides (CGRPs). CGRPs occur in two forms: α CGRP and β CGRP. The β -form is less well studied and most of the current research focuses on the α -form. CGRP is mainly known for its vasorelaxation effect and CGRP-inhibitors are widely used to treat migraine. In the progression of OA, cartilage is severely modified, including innervation and vascularization even beyond the tidemark [43]. Additionally, neurons of the dorsal root ganglia and the periosteum increase their α CGRP expression and chondrocytes extracted from OA cartilage express more substance P upon mechanical stimulation [44, 45]. In a study by Heffner et al. they reduced the peripheral sensory nerve function by capsaicin injection. Capsaicin is known to lead to the loss of both small myelinated and unmyelinated fibers [46]. After mechanical loading in this mouse model α CGRP expression was increased underlining the biomechanical adaption role of neurotransmitters. Furthermore, bone mineral content and the mineral apposition rate were increased [47]. The only study investigating β CGRPs

showed no osteogenic stimulatory effect of β CGRPs in vitro [48]. Two different knockout (KO) studies in mice with *Tac1*, coding for substance P, and an α CGRP showed that the complete absence of these neurotransmitters affected bone healing or load-induced bone formation, respectively [49, 50]. Thus, sensory neurosignaling has a structural role in the musculoskeletal system and, in particular, in degenerating cartilage.

2.2.2 The matrilin family

The matrilin family consists of four members all of which are proteoglycan-associated adaptor proteins. Apart from matrilin-3, they all possess two von Willebrand factor A-like (vWA) domains. They also contain several epidermal growth factor (EGF) like domains and a coiled-coil (CC) α -helical oligomerization module. Due to their vWA domain, they are able to interact with several other ECM proteins like collagen II, IX, and XI, decorin, biglycan or aggrecan [30, 51]. Signaling molecules like bone morphogenetic protein-2 (BMP-2) or transforming growth factor β (TGF- β) may bind to the EGF-like domains [52], underlining the multifunctional role of the matrilin family. Matrilin-3 and -1 are found almost exclusively in cartilage, whereas 2 and 4 are more widely distributed. Matrilin-1 is associated with idiopathic scoliosis, but the link to OA seems to be weak [53, 54]. One matrilin-1 KO study did not show any obvious skeletal phenotype [55], whereas another KO study reported an altered fibril organization of the collagen-2 network [56]. Mutations in the vWA domain or the first EGF-like domain of matrilin-3, respectively, are associated with multiple epiphyseal dysplasia (MED) and hand OA [57, 58]. MED patients suffer in childhood from joint pain/stiffness and develop OA early in adulthood. There are two additional studies for matrilin-3 KO mice. One did not show any sign of dysfunction [59], whereas the other study proposed a premature hypertrophy during development, an increased bone mineral density in adulthood and the mice were predisposed

for severe spontaneous OA [60]. Interestingly, matrilin-3 is highly upregulated in the middle and deep zone during OA and is able to induce several catabolic pathways [61, 62]. Thus, the full function of matrilin-3 is not clear yet and further investigation is needed. Therefore, a double knockout (Matrilin-1 and -3) was generated. In this mouse model, thicker collagen fibrils and an upregulation of matrilin-4 was observed [63]. From this observation, a compensation mechanism has been proposed among the matrilin members. Matrilin-2 and -4 knockout studies did not reveal any severe skeletal phenotype [64]. Matrilin-2 was found to be upregulated in OA tissue, but its role could not be elucidated [65]. Therefore, up to now, there is no link between matrilin-2 or matrilin-4 genes to chondrodysplasias or OA. The detailed function and the interplay of the matrilin family members in musculoskeletal tissues still require further research.

2.3 Biomechanical analysis of articular cartilage via the atomic force microscope

In 1986, Binnig, Quate and Gerber developed the atomic force microscope (AFM) (Fig. 2) [66].

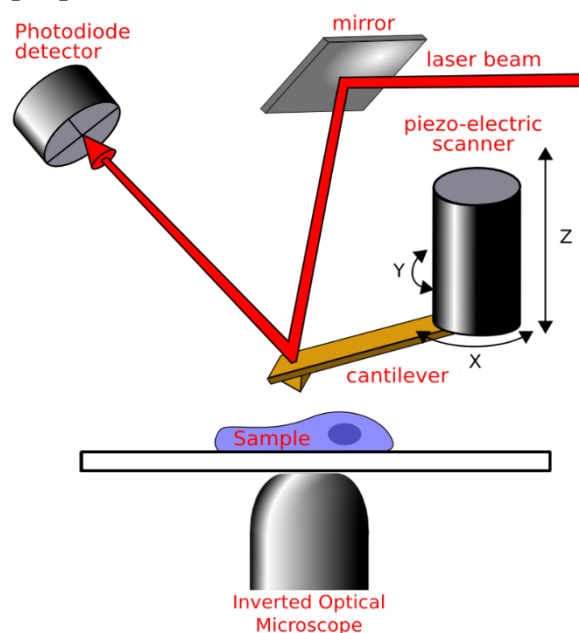


Figure 2 Schematics of an AFM setup. Modified from: <https://www.pngwing.com/de/free-png-itsog> (assessed: 15.06.2021 13:41)

The AFM relies on the principle that a microscopic cantilever spring, assembled together with a micro- or nanometer-sized tip, is bent due to atomic interaction forces between the tip and the surface. This procedure revolutionized the field of nanotechnology. One application of the AFM is the possibility to indent different materials with the AFM tip while determining the applied force. This so-called indentation-type atomic force microscopy (IT-AFM) gave a paramount insight into the biomechanics of, for example, whole tissues or single cells [67, 68]. One application of interest is the analysis of the biomechanics of AC. The indentation generates a force-distance curve from which the Young's Modulus can be extracted with an elastic model, usually a modified Hertz model [69, 70] (Formula 1). The classical Hertz model assumes an indentation with a spherical indenter into a linear elastic half-space. The Hertz model modified by Sneddon also considers different indenter geometries. The modified Hertz model for a four-sided pyramidal indenter, which is used in this thesis, is [71]:

$$F(\delta) = \frac{\tan \alpha * E}{\sqrt{2} * [1 - \nu^2]} * \delta^2 \quad (1)$$

Here, F is the applied force at the indentation depth δ . α is the half-opening angle of the pyramidal tip. E is the Young's modulus of the indented material. Young's modulus is a key parameter to describe the elastic properties of a material and is referred to as stiffness in the following.

Even though cartilage is not a linear elastic material, the Hertz model is a reasonable first order approximation for cartilage, providing the effective Young's Modulus of cartilage at a given indentation rate and allowing a quantitative comparison between different cartilage samples [72]. This technique enabled the analysis of cartilage biomechanics with a lateral resolution in the nanometer range. Throughout the last years, numerous studies have

been done on different cartilage sites and with different indenter geometries [73 – 78]. Thus, in order to compare the different studies, one has to pay attention to how the experiments were carried out. In the following, some biomechanical studies on articular knee cartilage are summarized. On one hand, for example, it could be shown that the AC possesses a stiffness gradient with increasing stiffness from the superficial to the deep zone [29, 73 – 76]. On the other hand, one study showed a decrease in AC stiffness from the superficial to the deep zone [83]. These contradictory results were also observed in knockout mice or comparing OA cartilage versus normal cartilage. One study of decorin knockout mice showed an increase in stiffness [84], whereas another study reported a decrease when decorin was knocked out [85]. Of interest, a protective role against spontaneous OA was proposed in the study where an increase in stiffness was observed [84]. When comparing OA cartilage versus normal cartilage biomechanics, conflicting results show either an increase or a decrease in stiffness when measured on native, cryo-preserved sections of the AC [32, 73, 80, 81]. This effect can be explained by the different indenter sizes and geometries used. When a decreasing stiffness is observed, always micrometer-sized spheres (radius of several μm 's) were used. In contrast, the increasing stiffness was detected when nanometer-scaled, pyramidal shaped tips were used. In 2009, Stolz et al. proposed that the measurement with a nanometer-scaled tip is more sensitive than a micrometer sized tip and is therefore able to detect biomechanical changes in the progression of OA much better [78]. Additionally, the same group demonstrated that a nanometer-sized tip is even able to discriminate between the proteoglycan and the collagen stiffness [88]. The bimodal stiffness observed in this study was also seen in further studies on cartilaginous tissue [29, 68]. Recently, we also demonstrated that the stiffness of the basement membrane, which is only about 400 nm thick, can be measured using a nanometer-sized tip [84 – 86]. This would not be possible with a spherical

tip with a radius of several micrometers. Therefore, one has to carefully distinguish between nano- and micro-scale indentation. Another advantage of the nanometer-sized tip is the possibility of visualizing the collagen structure by AFM topography imaging in contact-mode [92].

Several studies showed a decrease in AC stiffness during OA progression when measured on top of the intact condyle [6, 82, 88]. However, when measuring on cross sections the stiffness increased in each AC zone [73, 80]. Of interest is also the observed decreasing cartilage microstiffness measured on top of the condyle during ageing [6]. This allows us to conclude, that the biomechanical AC environment is highly dynamic. It depends on the protein composition that is changing during development and ageing. Nevertheless, an altered biomechanical environment can lead to OA or even protect from it as shown in the decorin KO mice. In the near future, AC biomechanics should be analyzed with a precise age-association and higher spatial resolution to get a better understanding of the underlying mechanisms. AC stiffness measurement is still a developing field: To which degree each protein is contributing to maintain AC biomechanical properties needs to be further illuminated.

2.4 The destabilizing medial meniscus model

OA is a disease that has different causes for occurrence as already mentioned in chapter 2.1. One of the reasons are injuries in the knee joint that can lead to post-traumatic osteoarthritis. In 2007, Glasson and colleagues developed the destabilizing medial meniscus model (DMM model) in mice to mimic this condition [94]. In this operation, the medial meniscotibial ligament of the mouse knee joint is surgically severed (Fig. 3).

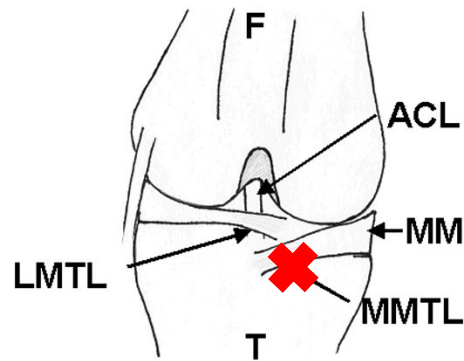


Figure 3 Diagram of the right knee joint of the mouse. F = femur; T = tibia; MM = medial meniscus; ACL = anterior (cranial) cruciate ligament; MMTL = medial meniscotibial ligament; LMTL = lateral meniscotibial ligament. red cross = The MMTL is transected to generate destabilization of the medial meniscus (DMM). The ACL is transected in the ACLT model. Modified from Glasson et al. (2007) [94]

Glasson et al. could show that the DMM model is easier to perform and less invasive than the anterior cruciate ligament transection (ACLT) method, which is widely used to induce OA in various animal species. In addition, DMM provoked a less severe OA resembling the OA progression observed in humans more closely. Since then, the DMM model has been widely used and analyzed. A lot of studies showed different aspects of OA pathology like arthrosis grading, alteration in the subchondral bone, site-specific cartilage degeneration, osteophyte formation, gait disparity or alterations in bone mineral density in the DMM model [31, 32, 45, 79, 89, 90]. Less attention was paid to cartilage stiffness alterations, although loads are changing dramatically due to the induced joint instability [91, 92]. Two papers are addressing AC stiffness in the DMM model in detail. Doyran et al. showed a decrease in medial condyle stiffness during OA progression, which becomes significant one week after the operation. Also on the lateral condyle, a decreased stiffness was measurable two weeks after the operation. Measurements were conducted on top of the condyle with a spherical indenter ($R = 5 \mu\text{m}$) [31]. Chery et al. used $6 \mu\text{m}$ tissue sections and measured the stiffness of the pericellular matrix (PCM) and the interterritorial matrix (ITM) in the middle/deep zone [32]. They showed a decrease in stiffness in the PCM after one

week and in the ITM after two weeks when measuring with a sphere ($R = 2.25 \mu\text{m}$). None of the studies discriminated between the three articular cartilage zones and between the medial and lateral side. Therefore, we addressed this question and observed a stiffness gradient throughout the AC zones and an increased stiffness after surgery in the DMM model, that was always greater on the lateral than on the medial side [87].

2.5 Aims of this thesis

Articular cartilage needs to withstand high shear and compressive forces every day. Thus, AC is confronted with a highly dynamic biomechanical environment and it is crucial to maintain its biomechanical and structural integrity. For this reason it is of pivotal importance to obtain a better, quantitative understanding of AC biomechanics in normal and diseased tissue at various morphological and pathological stages.

At the onset and during the progression of OA, AC stiffness is altered and protein degradation takes place. Various factors are influencing OA pathogenesis including the nervous system and the composition and assembly of the ECM. However, their contribution to the proper biomechanical properties of the AC is not fully understood.

Aim 1: Chondrocytes possess neurotransmitter receptors and innervation along with vascularization is a distinguished feature of OA. It has previously been shown that *Tac1*-KO and α CGRP-KO mice display decreased bone healing as well as load-induced bone formation. Therefore, we assumed that during the initiation of OA the nervous system plays a crucial role in maintaining the biomechanical and structural integrity of the AC. Thus, our goal was to measure via IT-AFM with a nanometer-sized tip the depth-dependent AC stiffness at two different time points after OA induction to illuminate the role of these neurotransmitters during the course of OA. Therefore, 12-weeks-old male Wildtype, *Tac1*-KO and α CGRP-KO mice were used and

post-traumatic osteoarthritis was induced via the DMM model. After two and eight weeks, AC stiffness was assessed in both groups, DMM and Sham, respectively. Each group contained three mice and cryosections of the medial tibia plateau were used.

Aim 2: The role of the matrilin-family in AC biomechanics was of additional interest. Matrilins serve as connector proteins between collagens and proteoglycans. In addition, several matrilin mutations are linked to diseases of the musculoskeletal system. Single and double knockouts of members of the matrilin family showed contradictory results with collagen fibril thickening and compensatory regulation in between the protein family. The loss of the whole matrilin-family could potentially alter biomechanics, as connecting proteins are missing in this network. Thus, our goal was to measure the AC stiffness of *Matn1-4^{-/-}* mice in two different age groups and to measure the collagen fiber diameter to shed light on the function of the matrilin family. Medial tibia cartilage from 4-month and one-year-old *Matn1-4^{-/-}* mice was used to assess stiffness in all three non-calcified AC zones. In addition, the collagen fiber diameter was measured using AFM topography images of the middle and deep zones of 4-month-old mice.

Aim 3: Furthermore, mutations in matrilin-3 lead to multiple epiphyseal dysplasia (MED) and hand OA. Matrilin-3 is able to form heterooligomers with matrilin-1. It connects proteoglycans and collagens, and a *MATN3* mutation can possibly alter AC protein composition and network stability [99]. Thus, we assumed that introducing the matrilin-3 T298M mutation (in human T303M) linked to hand OA leads to an altered AC stiffness via insufficient connecting capability. Our aim was then to assess the AC stiffness T298M-Mat3 knock-in and wildtype mice at 4-weeks-old of age via IT-AFM to find a link between matrilin-3 and cartilage homeostasis.

3. Summary

AC is a highly specialized tissue that withstands high shear and compressive forces to provide frictionless movement of the musculoskeletal system. It permanently covers the ends of long bones in the diarthrodial joint. AC is predominantly composed of a bulky ECM and chondrocytes are making up just a small percentage of the whole tissue (5-10%). The ECM is a highly interconnected network of collagens and proteoglycans. Collagen fibrils provide tensile strength, whereas the proteoglycan aggrecan due to its high negative charge density leads to water attraction and therefore contributes to the compressive stiffness of AC. Pathological mechanisms can occur if this network is disturbed due to genetic mutations or an altered biomechanical load due to an injury or obesity. OA is the main musculoskeletal disease worldwide and primarily diagnosed by the structural and biochemical degeneration of the AC. Today, it is known that OA is a multifactorial disease and it is seen as a whole joint disease.

One important factor in OA pathogenesis is the sensory nervous system influencing bone and cartilage structure and function. Two main sensory neurotransmitters are substance P, encoded by the *Tac1* gene, and α CGRP. We hypothesized that the absence of these neurotransmitters in the joint will also alter the progression of OA and may change biomechanical properties of the articular cartilage. In order to assess our assumption, we utilized the *Tac1* and the *α CGRP* knockout mouse lines and induced post-traumatic OA via the DMM model. In Paper I, we have demonstrated for the first time that α CGRP-KO mice exhibit an early onset OA at 4 weeks post-operation compared with Sham mice. In contrast, the wildtype mice and *Tac1*-KO mice developed significant OA degradation at 8 weeks and 12 weeks, respectively. Thus, we could show that in wildtype, cartilage stiffness of the medial tibia plateau increased significantly two weeks after the DMM operation compared to Sham, but the increase became less pronounced after eight weeks.

In the superficial zone, a decrease in stiffness was observed in Tac1-KO mice, whereas α CGRP-KO showed an increase in stiffness after two and eight weeks, compared to Sham. In the middle and deep zones, an increased stiffness was observed in both genotypes. Important in the comparison is that Tac1 KO showed a higher stiffness in the Sham-operated group. Interestingly, biomechanical alterations were the first ones to appear two weeks after DMM surgery at the medial tibia plateau. Other alterations such as bone mineral density, medial tibia plateau length, osteophyte formation, calcified cartilage thickness and bone volume of meniscal ossicles have appeared only later. We could show for all analyzed parameters significant alterations for each neurotransmitter. Therefore, our results demonstrate that the nervous system has a significant influence on AC biomechanics and a modulating role for α CGRP and substance P in bone and cartilage homeostasis during OA can be assumed. Taken together, we demonstrated that the biomechanical properties of the AC ECM are changing dramatically after induction of post-traumatic OA via the DMM model and the sensory nervous system contributes to it.

The cartilage ECM is a highly connected network of a variety of collagens and proteoglycans. The non-collagenous matrilin family serves as connector proteins between collagens and proteoglycans. The family consists of four members whereby mutations in matrilin-1 and -3 genes are associated with chondrodysplasias, OA or other forms of musculoskeletal disorders. Single or double knockout studies did show mild skeletal phenotypes and compensation in between family members. Thus, the exact function of the whole family is still unknown. We were then the first ones generating a quadruple knockout (matrilin-1-4 null, *Matn1-4^{-/-}*) mouse line lacking all matrilins and then analyzed the skeleton (Paper II). By high resolution AFM imaging, we have observed thickening of the collagen fibers in the growth plate and in the middle and deep zones of AC of mutant mice. Even though fibrils were

thicker, no stiffness change was observed in the middle and deep zones, but the superficial zone was stiffer in 4-months-old *Matn1-4^{-/-}* mice compared to wildtype. At one year of age, superficial and middle zone stiffness was significantly decreased, while the deep zone was stiffer in the quadruple knock-out mice. The altered biomechanics of the AC was accompanied by a more severe, age-associated OA phenotype in 18-months-old *Matn1-4^{-/-}* mice compared with control mice. We observed a similar, severe spontaneous AC degradation in *Matn4^{-/-}* mice leading to the assumption that matrilin-4 is of high importance in maintaining articular cartilage homeostasis while aging. Interestingly, the matrilin 1-4 KO mice developed up to normal size and no obvious phenotype was observed in the growth plate. Nevertheless, an altered vertebral pattern was seen in the *Matn1-4^{-/-}* mice characterized by the transition of the last lumbar vertebra into a sacral identity. In conclusion, the matrilin family is dispensable for a normal skeletal development except for the lumbosacral pattern, but matrilin-4 seems to play an important role in healthy cartilage homeostasis in aged AC. Biomechanical alterations occurred even before spontaneous OA developed in matrilin 1-4 KO mice.

Another important member of the matrilin family is matrilin-3 as human *MATN3* mutations are associated with various forms of chondrodysplasia and hand OA. Matrilin 3 is mainly found in cartilaginous tissues and only possesses one vWA domain. The human T303M mutation has been suggested to be associated with hand OA. To address this hypothesis and to identify possible pathological mechanisms we were the first ones generating the mouse equivalent T298M *Matn3* knock-in line (Paper III). We could show that the AC stiffness of the mutant was higher in the middle and deep zone and it was more prone to OA after the medial meniscotibial section. Additionally, collagen fibril diameter was thicker and the endochondral ossification in the proximal tibia was disturbed. Thus, we concluded that the matrilin-3 T298M mutation indeed leads to a phenotype more susceptible for

post-traumatic osteoarthritis. Further analysis with this knock-in mouse line will reveal the underlying cause of how matrilin-3 is leading to this alteration.

In this thesis, we revealed the structural and biomechanical role of the sensory nervous system after post-traumatic OA induction, the association of the matrilin-3 T298M mutation with OA and the role of the entire matrilin family, particularly matrilin-4, in the maintenance of healthy AC biomechanics.

4. Zusammenfassung

Artikulärer Knorpel ist ein hochspezialisiertes Gewebe, das hohen Scher- und Druckkräften standhält, um eine reibungslose Bewegung des muskuloskelettalen Systems zu ermöglichen. Die Epiphysen der Knochen sind damit ausgekleidet und bilden so einen Hauptbestandteil der Gelenke. Artikulärer Knorpel besteht hauptsächlich aus extrazellulärer Matrix (EZM). Einen kleinen Anteil des gesamten Knorpels machen Chondrozyten aus (5-10%). Die Knorpel EZM ist ein stark verzweigtes Netzwerk aus Kollagenen und Proteoglykanen. Kollagene dienen in erster Linie als strukturelle Komponenten die dem Knorpel Zugfestigkeit verleihen, während die hohe negative Ladung der Proteoglykane zu einer Wasserspeicherung führt und somit zur Druckresistenz beiträgt. Pathologien können auftreten, wenn dieses Netzwerk durch genetische Mutationen der beteiligten Proteine oder durch biomechanische Fehlbelastungen, beispielsweise Verletzungen oder Adipositas, gestört ist. Die weltweit am häufigsten vorkommende muskuloskelettale Erkrankung ist Arthrose welche sich hauptsächlich durch die Degeneration des artikulären Knorpels definiert. Heute weiß man jedoch, dass Arthrose eine multifaktorielle Erkrankung ist und als eine Erkrankung des gesamten Gelenks gesehen werden muss. Ein Faktor ist der Einfluss des sensorischen Nervensystems auf die Knochen- und Knorpelstruktur. Zwei wichtige sensorische Neurotransmitter sind die Substanz P, kodiert durch das *Tac-1* Gen, und α CGRP. Wir stellten daraufhin die Hypothese auf, dass die Abwesenheit beider sensorischer Neurotransmitter sowohl das Fortschreiten der Arthrose als auch die biomechanischen Eigenschaften des Knorpels verändert. Um diese Hypothese zu überprüfen, verwendeten wir ein *Tac-1*-knockout und ein α CGRP-knockout Mausmodell und induzierten in diesen Mäusen zum ersten Mal posttraumatische Arthrose durch Sektion des medialen meniskotibialen Bandes (DMM-Modell). Die α CGRP-knockout Mäuse zeigten im Vergleich

zum Wildtypen ein früheres Einsetzen der Arthrose, welches durch einen erhöhten OARSI-Score festgestellt wurde. Als letztes waren erste Arthroseanzeichen beim Tac-1-knockout sichtbar. Im Vergleich zum nicht-operierten Knie (Sham) nahm die Knorpelsteifigkeit beim Wildtyp nach zwei Wochen auf dem medialen Tibiaplateau nach der DMM Operation signifikant zu. Dieser Anstieg wurde jedoch nach acht Wochen geringer. Beim Tac1-knockout konnte eine Abnahme der Steifigkeit in der Superficialzone beobachtet werden, während der α CGRP-knockout eine Zunahme nach zwei und acht Wochen im Vergleich von DMM zu Sham zeigte. In beiden Genotypen wurde ein Anstieg der Steifigkeit in den beiden weiteren Zonen beobachtet. Zu beachten gilt, dass der Tac-1 knockout verglichen mit dem α CGRP-knockout eine höhere Steifigkeit in der scheinoperierten Gruppe zeigte. Interessanterweise waren die ersten Veränderungen die Biomechanischen, welche zwei Wochen nach der DMM-Operation am medialen Tibiaplateau auftraten. Weitere Veränderungen, wie die Knochenmineraldichte, die Länge des medialen Tibiaplateaus, die Osteophytenbildung, die Dicke des kalzifizierten Knorpels und das Knochenvolumen der Meniskusknöchelchen, traten erst später auf. Für alle analysierten Parameter konnten wir signifikante Veränderungen feststellen. Wir konnten also zeigen, dass α CGRP und die Substanz P eine modulierende Rolle in der Knochen- und Knorpelhomöostase/-mechanik während posttraumatischer Arthrose spielen. Von besonderer Bedeutung ist die zunehmende Steifigkeit in allen Knorpelzonen des Wildtyps nach der Induktion von Arthrose durch den DMM Eingriff. Die biomechanische Veränderung muss also als grundlegender pathologischer Mechanismus von Arthrose verstanden werden. Zusammenfassend verändern sich die biomechanischen Eigenschaften der extrazellulären Knorpelmatrix nach Induktion einer posttraumatischen Arthrose über das DMM-Modell dramatisch, insbesondere unter Einfluss des sensorischen Nervensystems.

Die extrazelluläre Knorpelmatrix ist ein stark verzweigtes Netzwerk aus einer Vielzahl von Kollagenen und Proteoglykanen. Die Mitglieder der proteoglykan-assoziierten Matrilin-Familie dienen als Verbindungsproteine zwischen Kollagenen und Proteoglykanen. Mutationen in den Genen von zwei der vier Mitglieder Matrilin-1 und -3, sind mit Chondrodysplasien, Arthrose oder anderen Formen von muskuloskelettalen Erkrankungen assoziiert. Einzel- oder Doppel-knockout-Studien zeigten milde skelettale Phänotypen und eine Kompensation zwischen den Familienmitgliedern. Daher ist die genaue Funktion der gesamten Familie noch nicht bekannt. Aufgrund dessen generierten wir zum ersten Mal einen knockout der gesamten Matrilinfamilie (Matrilin-1-4). Wir konnten eine Verdickung der Kollagenfasern in der Wachstumsplatte und in der Tangential- und Radiärzone des artikulären Knorpels beobachten. Obwohl die Fibrillen dicker waren, wurde keine Steifigkeitsänderung beobachtet. Nichtsdestotrotz zeigte die Superficialzone eine erhöhte Steifigkeit bei vier Monate alten Mäusen. Im Alter von einem Jahr war die Steifigkeit der Superficial- und Tangentialzone signifikant verringert, jedoch war die Radiärzone bei den Knockout-Mäusen steifer. Diese veränderte Biomechanik kann möglicherweise das altersassoziierte, spontane Auftreten der Kniegelenksarthrose in den Matrilin 1-4 Knockout-Mäusen erklären. Wir verglichen daraufhin diese Ergebnisse mit einem Matrilin-4 knockout-Modell. Diese Mäuse entwickelten einen ähnlichen Arthrosentyp, was wiederum zu der Annahme führt, dass Matrilin-4 bei der Aufrechterhaltung der Homöostase des artikulären Knorpels während des Alterns wahrscheinlich die tragendste Rolle spielt. Spannenderweise entwickelten sich die Matrilin-1-4-knockout Mäuse bis zu einer normalen Größe und es wurde kein offensichtlicher Phänotyp in der Wachstumsplatte beobachtet. Jedoch konnte eine veränderte Anzahl der Lendenwirbel beobachtet werden. Zusammenfassend lässt sich also feststellen, dass die Matrilin-Familie für eine normale Skelettentwicklung entbehrlich ist, allerdings eine tragende

Rolle bei der Entwicklung der Lendenwirbelsäule spielt. Des Weiteren waren die biomechanischen Eigenschaften verändert und im Alter trat ein erhöhtes Risiko für spontane Arthrose auf. Dies konnten wir hauptsächlich auf Matrilin-4 zurückführen.

Ein wichtiges Mitglied der Matrilin-Familie ist Matrilin-3, da Mutationen in diesem Gen mit Chondrodysplasien und Arthrose der Hand assoziiert sind. Es kommt hauptsächlich in knorpeligem Gewebe vor und besitzt nur eine vWA-Domäne. Die menschliche Mutation T303M, die der T298M Mutation in der Maus entspricht, wird mit Handarthrose in Verbindung gebracht. Um diesen Sachverhalt zu begründen, generierten wir zum ersten Mal T298M-Matrilin-3-knock-in Mäuse um mögliche pathologische Mechanismen zu entschlüsseln. Wir konnten zeigen, dass die Steifigkeit des artikulären Knorpels in der Tangential- und Radiärzone erhöht war im Vergleich zum Wildtyp. Des Weiteren war die Mutante nach medialer Meniskotibialektion anfälliger für Arthrose. Zusätzlich war der Durchmesser der Kollagenfibrillen dicker und die enchondrale Ossifikation in der proximalen Tibia war gestört. Daraus schlossen wir, dass die Matrilin-3 T298M-Mutation tatsächlich zu einem murinen Phänotyp führt, der anfälliger für posttraumatische Arthrose ist. In der Zukunft müssen weitere Analysen mit diesem Mausmodell durchgeführt werden, um die zugrundeliegenden Ursachen aufzudecken.

In dieser Dissertation konnte gezeigt werden, dass das sensorische Nervensystem nach der Induktion von posttraumatischer Arthrose eine große Rolle in der Aufrechterhaltung von der Struktur und der Biomechanik des artikulären Knorpels spielt, dass die Matrilin-3 T298M-Mutation mit muriner Arthrose assoziiert ist und dass die gesamte Matrilin-Familie bei der Aufrechterhaltung einer gesunden Biomechanik des Knorpels eine tragende Rolle spielt, insbesondere Matrilin-4.

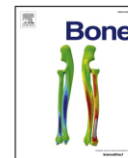
5. Paper I

Bone 133 (2020) 115181



Contents lists available at ScienceDirect

Bone

journal homepage: www.elsevier.com/locate/bone

Full Length Article

Sensory neuropeptides are required for bone and cartilage homeostasis in a murine destabilization-induced osteoarthritis model

Dominique Muschter^{a,1}, Lutz Fleischhauer^{b,c,d,1}, Shahed Taheri^{e,1}, Arndt F. Schilling^c, Hauke Clausen-Schaumann^b, Susanne Grässel^{a,*}^a Dept. of Orthopaedic Surgery, Experimental Orthopaedics, Centre for Medical Biotechnology (ZMB), Bio Park 1, University of Regensburg, Germany^b Department of Applied Sciences and Mechatronics, University of Applied Sciences Munich, Germany^c Laboratory of Experimental Surgery and Regenerative Medicine, Clinic for General, Trauma and Reconstructive Surgery, Ludwig-Maximilians-University, Munich, Germany^d Center for NanoScience, Ludwig-Maximilians-University, Munich, Germany^e Department of Trauma Surgery, Orthopedics and Plastic Surgery, University Medicine Göttingen

ARTICLE INFO

Keywords:

Osteoarthritis
Destabilization of the medial meniscus
Substance P
alpha-Calcitonin gene-related peptide
Bone
Cartilage

ABSTRACT

Numerous studies identified a role for the sensory neuropeptides substance P (SP) and alpha calcitonin gene-related peptide (α CGRP) in osteoarthritis (OA) pain behavior. Surprisingly, little attention has been paid on how their trophic effects on cartilage and bone cells might affect structural changes of bone and cartilage in OA pathology. Here, we sought to elucidate sensory neuropeptides influence on structural alterations of bone and cartilage during murine OA pathophysiology. OA was induced by destabilization of the medial meniscus (DMM) in the right knee joint of 12 weeks old male C57Bl/6J wildtype (WT) mice and mice either deficient for SP (tachykinin 1 (Tac1) $-/-$) or α CGRP. By OARSI histopathological grading we observed significant cartilage matrix degradation after DMM surgery in α CGRP-deficient mice after 4 weeks whereas Tac1 $-/-$ scores were not different to sham mice before 12 weeks after surgery. Indentation-type atomic force microscopy (IT-AFM) identified a strong superficial zone (SZ) cartilage phenotype in Tac1 $-/-$ Sham mice. Opposed to WT and α CGRP $-/-$ mice, SZ cartilage of Tac1 $-/-$ mice softened 2 weeks after OA induction. In Tac1 $-/-$ DMM mice, bone volume to total volume ratio (BV/TV) increased significantly compared to the Tac1 $-/-$ Sham group, 2 weeks after surgery. WT mice had reduced BV/TV compared to α CGRP $-/-$ and Tac1 $-/-$ mice after 12 weeks. Increased calcified cartilage thickness and medial condyle diameter were detected in the medial tibia of all groups 8 weeks after OA induction by nanoCT analysis. Meniscal ossification occurred in all OA groups, but was significantly stronger in the absence of neuropeptides. Increased serum concentration of the respective non-deleted neuropeptide was observed in both neuropeptide-deficient mice strains.

Both neuropeptides protect from age-related bone structural changes under physiological conditions and SP additionally demonstrates an anabolic effect on bone structure preservation in a pathophysiological situation. Both neuropeptide deficient mice display an intrinsic structural cartilage matrix phenotype that might alter progression of cartilage degeneration in OA.

1. Introduction

Osteoarthritis (OA) is one of the most common musculoskeletal

disorders worldwide and was ranked the 11th highest contributor to global disability in the Global Burden of Disease 2010 study [1]. OA constitutes a tremendous social and economic burden for the affected

Abbreviations: OA, osteoarthritis; DMM, destabilized medial meniscus; SP, substance P; α CGRP, alpha-calcitonin gene-related peptide; IT-AFM, indentation-type atomic force microscopy; μ CT, micro-computed tomography; nanoCT, ultrahigh-resolution nano-computed tomography; WT, wildtype; Tac1, tachykinin 1; BV, bone volume; TV, total volume; CTX-I, carboxy-terminal telopeptide of type I collagen; CTX-II, carboxy-terminal telopeptide of type II collagen; SZ, superficial zone; MZ, middle zone; DZ, deep zone; TRAcP5b, tartrate-resistant acid phosphatase form 5b

* Corresponding author at: Department of Orthopedic Surgery, Experimental Orthopedics, University of Regensburg, ZMB/BioPark 1, Am Biopark 9, 93053 Regensburg, Germany.

E-mail addresses: dominique.muschter@ukr.de (D. Muschter), lutz.fleischhauer@hm.edu (L. Fleischhauer), shahed.taheri@med.uni-goettingen.de (S. Taheri), arndt.schilling@med.uni-goettingen.de (A.F. Schilling), clausen-schaumann@hm.edu (H. Clausen-Schaumann), susanne.graessel@ukr.de (S. Grässel).

¹ These authors contributed equally.

<https://doi.org/10.1016/j.bone.2019.115181>

Received 29 April 2019; Received in revised form 13 November 2019; Accepted 28 November 2019

Available online 08 January 2020

8756-3282/ © 2019 Published by Elsevier Inc.

individual and the worldwide healthcare systems [2]. The outdated view of OA as a result of wear and tear processes has been replaced and these days OA is considered to be a disease of the whole joint affecting tissues like articular cartilage, subchondral bone, the synovium, adjacent ligaments, the meniscus and even muscles, nerves and local fat pads [3].

Soft tissues as well as bone are innervated by sensory and sympathetic nerve fibers, which are important for proper bone and joint development. In bone, sensory nerve fibers containing the neuropeptides substance P (SP) and alpha-calcitonin gene-related peptide (α CGRP) were found to be located near blood vessels targeting the periosteum, bone marrow as well as compact and trabecular bone structures [4]. Distribution of α CGRP-positive nerve fibers showed higher immunoreactivity in the epiphysis compared to the metaphysis, where the nerves were located along trabecular structures. In rat knee joints, nerves containing α CGRP originating from the periosteum, tendon and muscle insertions are able to protrude into the surface of the articular and meniscal cartilage thereby coming in close contact with chondrocytes [5]. Additionally, free nerve endings are observed, that are located in the immediate vicinity of bone cells like osteoclasts, osteoblasts and osteocytes. Bone cells as well as chondrocytes (only SP) express receptors for SP and α CGRP and might be modulated in their differentiation and function [6]. Furthermore, bone cells as well as chondrocytes show expression of the neuropeptides (own unpublished data for α CGRP), creating a local neuropeptide microenvironment independent from the central nervous system (CNS). Especially chondrocytes, tenocytes and osteocytes express SP and its receptor, the neurokinin receptor 1 (NK1R), acting as mechanosensors implicated in structure preservation mechanisms of their respective tissues [7–10]. Studies using predominantly mice with altered local neuropeptide availability demonstrate a clear effect on bone matrix structure. In our group, we observed that fracture healing was affected in mice with a deletion of the SP-encoding gene tachykinin 1, but also the biomechanical quality of the non-fractured leg differed from wildtype mice [11]. In mice lacking the expression of α CGRP, Schinke et al. demonstrated the development of an osteopenic phenotype in the vertebrae at the age of six months, associated with decreased bone formation [12]. Mechanical loading of the right ulna of these mice lead to reduced mineral apposition responses and new periosteal bone formation [13]. Capsaicin treatment of neonatal mice leading to diminished SP and α CGRP availability altered the adaptive response of bone to tibial compressive forces [14]. Altogether, these studies indicate a clear role for the sensory neuropeptides in physiological maintenance of bone structure. In OA, an increase of SP immunohistochemical staining was observed in areas of bone erosion and osteophyte remodeling areas, as well as in cells located in bone cysts and the subchondral bone plate [15,16]. The appearance of SP and α CGRP has been linked to pain generated in various joint tissues including the subchondral bone [17]. Furthermore, SP coupled to self-assembled peptide nanofibers profoundly accelerated cartilage matrix regeneration by recruitment of mesenchymal stem cells in a rat OA model [18]. Nevertheless, studies on the influence of SP and α CGRP on OA-related structural changes in cartilage and bone are rare. Here, we therefore studied the progression of degenerative changes in cartilage and bone in mice lacking either the expression of SP ($Tac1^{-/-}$) or α CGRP (α CGRP $^{-/-}$) after surgical destabilization of the medial meniscus (DMM). Our results indicate that sensory neuropeptides deserve more attention as modulators of OA and non-OA related structural changes in cartilage and bone.

2. Material and methods

2.1. Animals

The DMM model was described as a testosterone-driven pathology hence male mice were used in this study [19]. For induction of OA, 8–10 weeks old, male C57BL/6J (WT) were purchased from Charles

River Laboratories (Sulzfeld, Germany) and were adapted to standard housing conditions under a 12 h dark/light cycle until the age of 12 weeks. Age- and sex-matched $Tac1^{-/-}$ (SP-deficient, kindly gifted from A. Zimmer, University Bonn [20]) and α CGRP $^{-/-}$ mice (generated by R.B. Emeson [21], kind gift from T. Schinke/M. Amling, Eppendorf University Hospital Hamburg) with WT background were used for comparative analysis. The mice had access to food and water ad libitum. All animal experiments were approved by the ethical committee of the local authorities (Regierung von Unterfranken, Bavaria, AZ 55.2-2531-2-289, date of approval July 27th 2016).

2.2. Destabilization of the medial meniscus (DMM)

Osteoarthritis was induced following a method described by Glasson [22]. Briefly, after intraperitoneal anaesthesia with fentanyl, medetomidin and midazolam, a 3 mm skin incision was made between the distal patella and the proximal tibia plateau of the right leg, exposing the knee joint. The joint capsule was opened with a 1–2 mm incision medial to the patellar tendon. For induction of OA, the medial meniscotibial ligament was dissected carefully after visualization using micro scissors. Sham surgery was performed in the right knee of the control group with visualization of the ligament only. Joint capsule and skin were closed and animals received analgesia (buprenorphine in 0.9% NaCl solution, 0.1 mg/g bodyweight). Immediately after surgery, animals were allowed to move freely and recover from surgery. After 2, 4, 8 and 12 weeks animals were anaesthetized, blood was collected via retro-orbital puncture and animals were killed by cervical dislocation. Knee joints were prepared and stored at -80°C until μ CT analysis followed by histological analysis. For Atomic Force Microscopy (AFM) and nanoCT, 6 animals per genotype and time-point (3 DMM/3 Sham) were euthanized for analysis 2 and 8 weeks after surgery for each method and prepared as described in the respective section.

2.3. MicroCT analysis

MicroCT (μ CT) analysis was performed in cooperation with the microCT facility of the RCBE (Regensburg Center of Biomedical Engineering) of the University of Applied Sciences Regensburg. Native samples were thawed and scanned in air using a Phoenix v tome XS computer tomograph (GE Sensing & Inspection, Boston, MA, USA; DFG number: INST 102/11-1 FUGG). Samples were scanned using an x-ray voltage of 35 kV and x-ray current of 270 μA at $20\times$ magnification and 10 μm voxel size. FastScan was used for knee joints isolated 4 and 12 weeks after surgery, taking 1 picture per position (1 picture/ 0.3° angle). For 2 and 8 weeks after surgery, samples were scanned taking 3 pictures per position. Comparison of both methods showed only little differences in precision. The software used with the system was the VGStudio MAX 2.4.0 software (Volume Graphics, Heidelberg, Germany). Analysis of the medial compartment of the subchondral bone was performed using the myVGL 3.0 software (Volume Graphics, Heidelberg, Germany). Bone volume (BV) to total volume (TV) ratio as well as bone surface (BS) to BV was analyzed in the medial subchondral bone. The volume of interest (VOI) was adjusted in the medial subchondral bone compartment of the tibia to avoid inclusion of the subchondral bone plate, cortical bone, as well as the growth plate.

2.4. Ultra-high resolution nanoCT analysis

2 and 8 weeks after surgery, knee joints of WT, $Tac1^{-/-}$ and α CGRP $^{-/-}$ mice were prepared and fixed for 16 h in 4% paraformaldehyde and stored in 70% ethanol afterwards. Knee joints were scanned in 70% EtOH using a Scanco μ CT 50 (Scanco Medical, Brüttisellen, Switzerland; DFG number: 3230/30009760) device. Two scans were performed. First, imaging acquisition was conducted at 90 kVp, 88 μA , 6.8 μm voxel size, 800 ms integration time, and with a 0.50-mm-thick aluminum filter for beam hardening reduction. The

images were then used to create a 3D reconstruction and topographical changes of the calcified cartilage, meniscal ossicles, and potential osteophyte formations were qualitatively assessed using the 3D reconstructions. A higher resolution measurement (2.0 μm voxel size, 1500 ms, 90 kVp, 88 μA) was also performed for each sample. The optimal threshold was applied according to Scanco's preset settings (lower threshold: 685.3 mg HA/cm³, upper threshold: 3000 mg HA/cm³, Sigma: 0.8, Support 1). After re-orientation with ImageJ version 1.51J8 (NIH, USA), the length of the medial condyle (as an indicator for osteophyte formation) and the lateral condyle was measured at 300 μm distally to the growth plate from the surface of the subchondral bone. The length was defined as the distance from the center of the condyle in proximity of the trochlear groove to the medial prominence. Bone volume to total volume (BV/TV) was measured in the medial epiphysis in a 200 μm region, starting 270 μm distal to the surface of the subchondral bone and avoiding encompassing of the subchondral bone plate, cortical bone, as well as the epiphyseal line. Anterior meniscal ossicles were contoured manually and segmented using the built-in Scanco software. The region of interest (ROI) in sham mice was \sim 600 μm , and in DMM mice \sim 1600 μm owing to the irregular surface expansion of the ossicles along the long axis of the tibia. Parameters were calculated using Scanco's bone trabecular morphometry evaluation script (plate model). Calcified cartilage (CC) of the tibial subchondral bone was extracted from the subchondral bone plate semi-automatically based on differences in greyscale values implementing a different threshold setting. The lower threshold was set at 396.0 mg HA/cm³, while the Gauss sigma and support were respectively set at 2 and 4, in order to blur out small cavities on the surface of the subchondral bone. The thickness of the CC was then measured with the aid of Scanco's OpenVMS software. Color maps of the thickness were obtained from the bins of values and subsequent histograms. To enhance the visualization, the maximum value of the color legends was scaled to 80 μm for all samples. Furthermore, bone mineral density (BMD) of the medial tibial epiphysis as well as of meniscal ossicles was extracted from data.

2.5. Indentation-type atomic force microscopy

Atomic force microscopy was solely used in the indentation mode. For indentation-type atomic force microscopy (IT-AFM), native, non-fixed knee tissues 2 and 8 weeks after surgery were snap frozen and cut in frontal direction into 20 μm slides using a cryotome (Leica CM 1950). The frontal cut revealed the different cartilage zones. To maintain tissue integrity throughout AFM measurements, transparent adhesive tape (tesafilm Nr.: 57330-00000) was used to obtain the tissue sections which were then attached to a glass slide via a double adhesive tape (tesafilm Nr.: 56661-00002). IT-AFM was carried out using a NanoWizard I AFM (JPK Instruments, Berlin, Germany) in combination with an inverted optical microscope (Axiovert 200, Carl Zeiss Micro Imaging GmbH, Göttingen, Germany) for precise lateral positioning of the AFM-tip. The influence of external noise was reduced by placing the whole set-up on an active vibration isolation table (Micro 60, Halcyonics, Göttingen, Germany) inside a 1 m³ soundproof box.

Indentation experiments were performed with silicone-nitride cantilevers (MLCT, Cantilever E, Bruker) with a nominal spring constant of 0.1 N/m, a nominal tip radius of 20 nm and a pyramidal tip shape. For each cantilever the spring constant was determined individually using the thermal noise method [23]. During measurements, the tissue sections were immersed in PBS (Biochrom Dulbeccos PBS w/o Mg²⁺/Ca²⁺, pH 7.4, Berlin, Germany). Each force map contained 25 \times 25 force-indentation curves equally distributed over an area of 3 \times 3 μm^2 . The vertical tip velocity was 10 $\mu\text{m/s}$ throughout all IT-AFM measurements. The frontal cut allowed the indentation of the individual cartilage zones (superficial, middle and deep zone, respectively). All three zones were investigated by IT-AFM using the frontally cut tissue sections. In total, 6 \times 625 force-curves for each cartilage zone, each genotype and each time-point were assessed on two different sections per animal. The Young's Modulus was extracted by fitting the Hertz-Sneddon model for a pyramidal indenter to the approach part of the force-indentation curves up to an indentation depth of 500 nm, using the JPK Data Processing Software (Version 5.0.96, JPK Instruments) [24]. Subsequently, stiffness distributions were generated with the Igor Pro software (Version 6.3.7.2, WaveMetrics, Portland, OR, USA) and the two maxima of the bimodal distributions were determined by fitting a linear combination of two Gaussian distributions to the data [25]. Loparic et al. observed a similar bimodal nano-stiffness in mature articular cartilage. This group demonstrated that the first peak can be attributed to the proteoglycan phase and the second peak to the collagen fibrils [26].

2.6. Histology and OA-score

After μCT scanning, samples were fixed in 4% paraformaldehyde/PBS for 16 h and decalcified in 20% EDTA/PBS, pH 7.4 for 5 weeks. Samples were embedded in paraffin and 6 μm frontal sections were taken using a microtome. For evaluation of cartilage degradation, 5–6 sections in 60–90 μm intervals were deparaffinized, rehydrated and stained with Safranin O, Weigert's iron hematoxylin and Fast Green and scored by two blinded, independent observers according to the OARSI guidelines [27] with little modifications (Table 1). Sections were scanned with 10 \times magnification using the TissueFAXS system (DFG code: INST 89/341-1 FUGG) from TissueGnostics (Vienna, Austria). Maximum OARSI scores of the medial femur condyle and the medial tibia plateau were averaged and are displayed in the graphs.

Furthermore, medial tibial osteophyte size (0 = none, 1 = small, approx. same thickness as the adjacent cartilage, 2 = medium, 1–3 \times the thickness of the adjacent cartilage, 3 = large, > 3 \times the thickness of the adjacent cartilage) and maturity (0 = none, 1 = predominantly cartilaginous, 2 = mix of cartilage and bone, 3 = predominantly bone) were evaluated in the same sections used for the OARSI score according to the grading system developed by C. Little [28]. Size and maturity scores were each averaged over the number of sections analyzed per animal and recorded. In addition, the sum of both scores is presented.

Table 1
OARSI guidelines for assessment of murine cartilage degradation (modified after [27]).

Grade	Osteoarthritic damage
0	Normal
0.5	Loss of Safranin O staining without structural changes
1	Small fibrillations without loss of cartilage/uneven surface
2	Vertical clefts and erosions down to the layer immediately below the superficial layer and some loss of surface lamina
3	Vertical clefts/erosions to the calcified cartilage < 25% of the articular surface
4	Vertical clefts/erosions to the calcified cartilage 25–50% of the articular surface
5	Vertical clefts/erosions to the calcified cartilage 50–75% of the articular surface
6	Vertical clefts/erosions to the calcified cartilage > 75% of the articular surface

2.7. Immunohistochemistry for neuropeptide receptor expression

Sections were deparaffinized and rehydrated. Antigen retrieval for the calcitonin receptor-like receptor (CRLR) and receptor activity modifying protein 1 (Ramp1) was performed in 0.1 M citric acid buffer (pH 6) in a water bath at 60 °C for 24 h. For the neurokinin receptor 1 staining, sections were digested enzymatically by a sequential treatment with 0.05% proteinase XXIV (#P8038, Sigma Aldrich, St. Louis, MO, USA) for 10 min followed by 0.1% hyaluronidase (#H3506, Sigma Aldrich, St. Louis, MO, USA) treatment for 90 min at room temperature (RT). Endogenous peroxidase was blocked with 3% peroxide for 10 min at RT followed by blocking of nonspecific binding using 5% goat serum (#ab7481, Abcam, Cambridge, UK) in TBS + 0.1% Tween-20 for 1 h at RT. CRLR was detected using a polyclonal rabbit (rbt) anti-mouse antibody from Bioss (dilution 1:1000, #1860R, Boston, MA, USA) diluted in Signal Stain Antibody Diluent from Cell Signaling (#8112, Cambridge, UK). Polyclonal rbt IgG was used as isotype control (#NB81056910, Novus Biologicals, Centennial, CO, USA). NK1R was stained using monoclonal rbt anti-mouse NK1R antibody from Abcam (dilution 1:1000, #ab183713) and Ramp1 was detected using monoclonal rbt anti-mouse Ramp1 antibody from Abcam (dilution 1:1000, #ab156575), both diluted in Signal Stain Antibody Diluent. Monoclonal rbt IgG isotype control was purchased from Abcam (#ab172730). Sections were incubated with primary antibodies overnight at 4 °C. Primary antibodies were detected with the ready-to-use Signal Stain Boost IHC Detection Reagent from Cell Signaling (#8114) for 30 min at RT and signal detection was performed using the 3,3'-Diaminobenzidine (DAB) Liquid Substrate System tetrahydrochloride from Sigma Aldrich (#D7304). Nuclei were counterstained with hematoxylin (#1.05174.0500, Merck, Darmstadt, Germany) and sections were mounted with Roti Mount Aqua (#2848, Roth, Karlsruhe, Germany). Sections were scanned with 20× magnification using the TissueFAXS system from TissueGnostics. Nuclei located in the meniscus were counted for absolute cell numbers and cells with a brown staining representing receptor-positive cells were counted manually by a blinded observer to prevent bias. Counting was performed using the counting tool from Adobe Photoshop CS4 (San Jose, CA, USA) that prevents double-counts and omissions. Staining was assessed as positive when the cell was significantly darker compared to the isotype control but there was no discrimination between a weaker and a stronger staining. Positive cells were presented as percentage of absolute cell numbers thus eliminating confounding effects of varying meniscus size (assuming proportional variation in absolute cell numbers) in the different sections. This method of quantification allows a reliable comparison of receptor staining in the different groups [29].

2.8. Osteoclast staining and evaluation

Sections were deparaffinized, rehydrated and stained for tartrate-resistant acid phosphatase (TRAP) using the "Acid phosphatase, leukocyte (TRAP) Kit" from Sigma (St. Louis, MO, USA). Use of the tartrate solution included into the kit assured specific staining for TRAP apart from other acid phosphatases. Sections were scanned at 20× magnification using the TissueFAXS system (DFG code: INST 89/341-1 FUGG) from TissueGnostics (Vienna, Austria). Adobe Photoshop CS4 (San Jose, CA, USA) was used to manually count osteoclasts in the four compartments of the subchondral bone (medial femur condyle/tibia plateau, lateral femur condyle/tibia plateau) and to determine the length of the respective bone surface. Three sections through the weight bearing region and one section in the non-bearing region (proximal to the patellar region) were analyzed. Only cells with a red-brown staining directly attached to the bone surface were counted as osteoclasts.

2.9. Serum analysis

Blood was collected by retroorbital puncture from anesthetized

mice and serum was collected after centrifugation. Enzyme-linked immunosorbent assays were used to measure expression of the neuropeptides SP (#ADI-900-018, Enzo Life Sciences, Farmingdale, NJ, USA) and α CGRP (#EK-015-09, CGRP rat/mouse Enzyme Immunoassay (EIA) Kit, Phoenix Pharmaceutical Inc., Burlingame, CA, USA). Murine tartrate-resistant acid phosphatase form 5b (TRAcP5b, MouseTRAP™, SB-TR103, IDS Immunodiagnostic Systems, Frankfurt/Main, Germany) and carboxy-terminal telopeptide of type I collagen (CTX-I, CEA665Mu, Cloud-Clone Corp., Houston, TX, USA) were analyzed as markers for osteoclast activity and bone degradation respectively, according to the manufacturer instructions. Serum interleukin-1 β (IL-1 β) concentrations were analyzed using the Mouse IL-1 beta/IL-1F2 DuoSet ELISA (DY401-05) in conjunction with the DuoSet Ancillary Reagent Kit 2 (DY008, both R&D systems by Bio-technie, Minneapolis, MN, USA). Carboxy-terminal telopeptide of type II collagen (CTX-II) was analyzed in urine samples using the urine preclinical CartiLaps (CTX-II) EIA from IDS (#AC-09F1). CTX-II values were related to urinary creatinine measured with the creatinine (urinary) colorimetric assay kit from Cayman Chemicals (#500701, Ann Arbor, MI, USA).

2.10. Statistical analysis

A power analysis was performed to determine the number of animals for this study using the G*Power software (Heinrich-Heine University Düsseldorf, [30]) assuming a standard deviation of 20% and a power of 80%. For the key variable, the histopathological OARSI score of paraffin sections, 6 animals per group were calculated using the Wilcoxon-Mann-Whitney Test (two groups, two tailed, normal parent distribution) to assure that means differ with a probability of error of $\alpha \leq 0.05$. Higher standard deviation of α CGRP $^{-/-}$ mice for the key variable BV/TV in the μ CT analysis required 8 animals per group.

GraphPad prism 6 (San Diego, CA, USA) was used to prepare all graphs and to perform statistical analysis. One-way analysis of variance (ANOVA) was applied to analyze if means of the various groups (for one time point) differed significantly from each other. Following statistically significant group comparison using ANOVA, Bonferroni post-hoc test was applied to test which means of selected groups differ significantly. Group comparisons for tibial condyle diameter, BMD of tibial epiphysis and meniscal ossicles as well as calcified cartilage thickness were analyzed using two-way ANOVA followed by Tukey post-hoc test that is more robust for larger number of comparisons. p values < 0.05 were considered statistically significant. The ratio of serum SP concentrations of α CGRP $^{-/-}$ mice and serum α CGRP $^{-/-}$ concentrations of Tac1 $^{-/-}$ mice to serum concentrations of respective WT groups (set to 1) were analyzed using the Wilcoxon signed rank test that allows comparisons of values to hypothetical values. A 2-sided t -test of independent samples was used to compare surgery-related or genotypic differences of the 1st (proteoglycan) or the 2nd (collagen) peak obtained by IT-AFM. All results are depicted as box plots showing the mean and the upper and lower interquartile range with whiskers encompassing the minimum and the maximum value of each group. Results of the nanoCT analysis are presented as bars showing the mean and the standard error of the mean (SEM). Results of atomic force microscopy are presented in histograms and bars representing mean \pm SEM.

3. Results

3.1. Neuropeptides as serum markers for osteoarthritis

To evaluate the eligibility of SP and α CGRP as serum biomarkers for OA pathology, we determined the concentration of both neuropeptides in the serum of WT DMM and Sham mice, 2 and 12 weeks after OA induction. We did not detect significant OA-related differences in SP and α CGRP serum concentrations in WT mice. By trend, SP concentration was reduced 2 weeks after DMM surgery in WT mice

2.7. Immunohistochemistry for neuropeptide receptor expression

Sections were deparaffinized and rehydrated. Antigen retrieval for the calcitonin receptor-like receptor (CRLR) and receptor activity modifying protein 1 (Ramp1) was performed in 0.1 M citric acid buffer (pH 6) in a water bath at 60 °C for 24 h. For the neurokinin receptor 1 staining sections were digested enzymatically by a sequential treat-

mice and serum was collected after centrifugation. Enzyme-linked immunosorbent assays were used to measure expression of the neuropeptides SP (#ADI-900-018, Enzo Life Sciences, Farmingdale, NJ, USA) and α CGRP (#EK-015-09, CGRP rat/mouse Enzyme Immunoassay (EIA) Kit, Phoenix Pharmaceutical Inc., Burlingame, CA, USA). Murine tartrate-resistant acid phosphatase form 5b (TRAcP5b, MouseTRAP™, SR.TR103, IDS Immunodiagnostic Systems Frankfurt/Main, Germany)

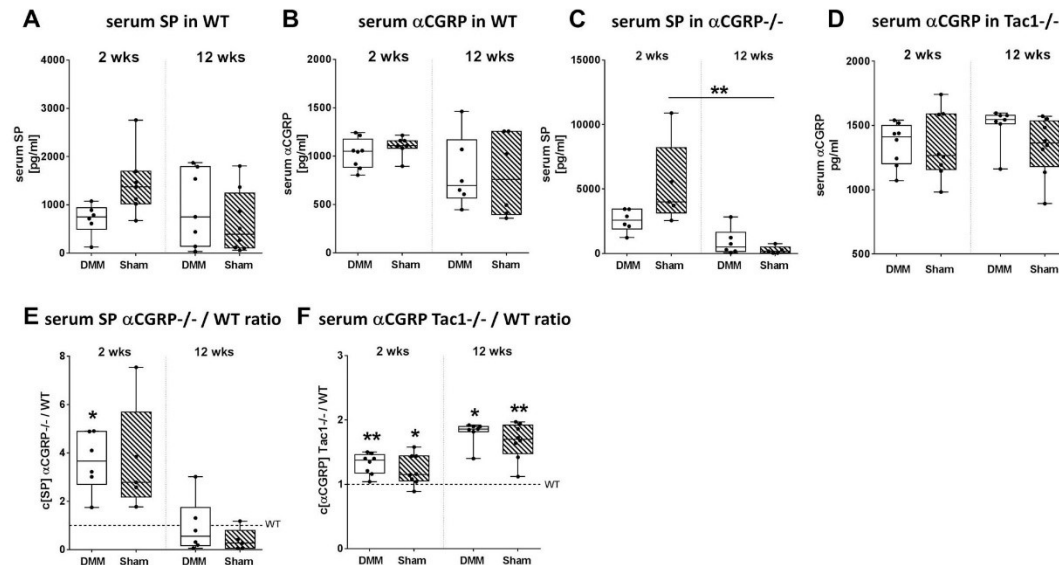


Fig. 1. Impact of murine OA progression on serum concentrations of sensory neuropeptides. A, B) Concentrations of SP (A) and α CGRP (B) in the serum of WT mice at 2 and 12 weeks after DMM or Sham surgery. N = 6–8. C, D) SP concentration in the serum of α CGRP^{-/-} mice (C) and α CGRP concentrations in the serum of Tac1^{-/-} mice (D) at 2 and 12 weeks after DMM and Sham surgery. N = 6–8. E, F) Ratio of serum SP concentrations of α CGRP^{-/-} mice (E) and serum α CGRP concentrations of Tac1^{-/-} mice (F) to respective serum concentrations of WT mice at 2 and 12 weeks after DMM and Sham surgery. Wilcoxon signed rank test compared to 1. *p < 0.05, **p < 0.01. N = 6–8.

(Fig. 1A). α CGRP concentration was by trend reduced over time from 2 to 12 weeks after surgery but was unaffected by OA induction (Fig. 1B). Additionally, we determined SP concentrations in the serum of α CGRP^{-/-} mice 2 and 12 weeks after either DMM or Sham surgery without detecting a DMM effect. Instead, SP concentrations decreased significantly from 2 to 12 weeks after Sham surgery (Fig. 1C). α CGRP concentrations in serum of Tac1^{-/-} mice displayed no DMM or age-related effects (Fig. 1D).

Of note, when we compared serum SP concentrations of α CGRP^{-/-} mice to SP concentrations of WT mice in the corresponding OA and non-OA groups, we observed almost 4 times higher SP concentrations in the α CGRP^{-/-} DMM group compared to WT DMM early after surgery (2 weeks, Fig. 1E). From 2 to 12 weeks, the serum SP concentrations decreased below the average WT serum SP level (Fig. 1E). This effect was not affected by OA induction. Contrarily, serum α CGRP concentrations of Tac1^{-/-} mice were elevated compared to respective WT serum after 2 weeks and continued to increase until 12 weeks after surgery in a non-OA related fashion (Fig. 1F).

3.2. α CGRP deficiency accelerated onset of cartilage matrix degradation after OA induction

Cartilage matrix destruction was evaluated in Safranin-O stained knee joint sections throughout all time-points. Fig. 2A shows representative images of frontal knee joint sections from WT, Tac1^{-/-} and α CGRP^{-/-} mice at 2 weeks after Sham and at 2, 4, 8 and 12 weeks after DMM surgery. As early as 4 weeks after surgery, we observed an increased degradation of articular cartilage matrix in the medial knee joint compartment of α CGRP^{-/-} DMM mice compared to their respective Sham group, but not in the WT and Tac1^{-/-} group (Fig. 2B). OARSI score of WT DMM mice increased significantly compared to WT Sham mice by 8 weeks with no additional increase up to 12 weeks. Cartilage destruction of Tac1^{-/-} DMM mice reached statistical significance in the late OA stage, 12 weeks after DMM surgery (Fig. 2B).

In addition, we evaluated serum levels of IL-1 β known as main driver for cartilage destruction. We did not observe differences in WT mice serum levels nor in serum levels of neuropeptide deficient animals between early (2wks) and late (8 wks) OA or in respective Sham mice (Fig. 2C).

3.3. Neuropeptide deficient mice display inherent cartilage phenotypes leading to altered cartilage biomechanical properties

Biomechanical analysis of the different cartilage matrix zones using IT-AFM (Fig. 3A) highlighted inherent differences in cartilage matrix stiffness for Tac1^{-/-} mice. At 2 and 8 weeks after surgery, superficial zone (SZ) cartilage matrix stiffness of Tac1^{-/-} Sham mice was significantly higher compared to WT and α CGRP^{-/-} Sham mice (Fig. 3B, C). That effect was analyzed in the proteoglycan as well as in the collagen proportion of the cartilage matrix (Fig. 3D, E). Induction of OA decreased SZ proteoglycan and collagen matrix stiffness in Tac1^{-/-} mice after 2 weeks, whereas in contrast, OA induction provoked an increase in SZ cartilage matrix stiffness in WT and α CGRP^{-/-} mice compared to Sham (Fig. 3B, D, E). After 8 weeks, SZ cartilage matrix stiffness of WT and α CGRP^{-/-} DMM mice remained increased compared to Sham, whereas in Tac1^{-/-} mice the stiffness of DMM and Sham SZ cartilage matrix was more or less similar (Fig. 3C) especially in the collagen fraction (Fig. 3E).

Middle zone (MZ) cartilage matrix stiffness increased 2 weeks after DMM induction in all genotypes (Fig. 3D, E, Supplementary Fig. S1A) and remained higher after 8 weeks in the neuropeptide deficient DMM mice (Fig. 3D, E, Supplementary Fig. S1B). Additionally, deep zone (DZ) cartilage matrix stiffness was increased in all genotypes at 2 weeks after OA induction, but the effect was strongest in WT DMM mice (Fig. 3D, E, Supplementary Fig. S2A). From 2 to 8 weeks after OA induction, in Sham WT mice DZ cartilage matrix stiffness increased largely whereas effects were less strong in neuropeptide deficient Sham mice. However, collagen stiffness of α CGRP^{-/-} mice was increased (Fig. 3D, E). Thus, in comparison to Sham, DZ cartilage matrix stiffness appeared reduced

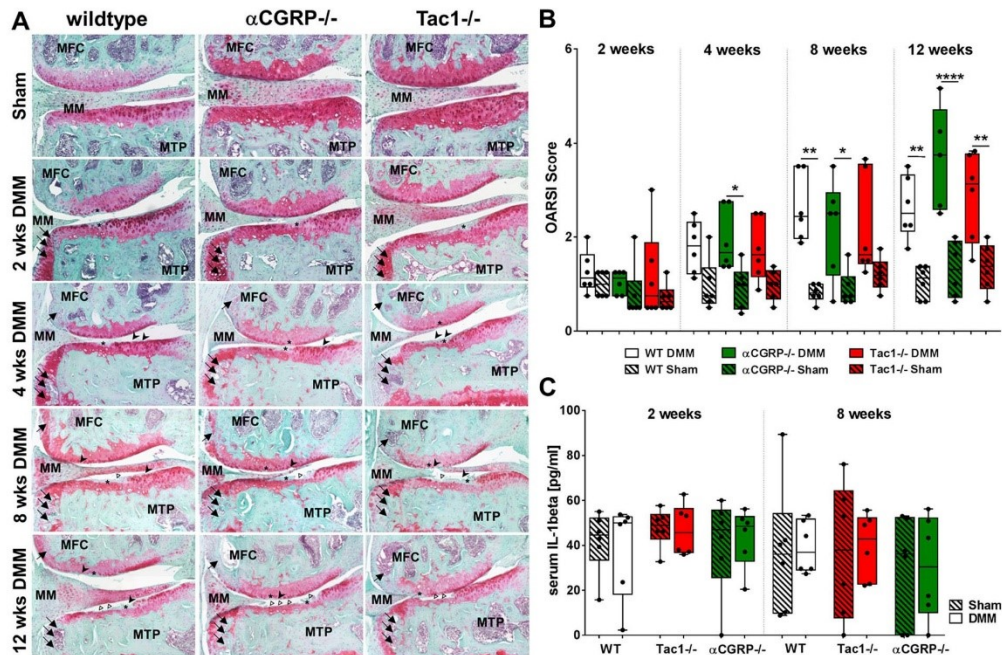


Fig. 2. Impact of sensory neuropeptide deficiency on cartilage degradation after OA induction. A) Representative pictures of Safranin-O stained frontal sections of paraffin embedded knee joints from WT, α CGRP $^{-/-}$ and Tac1 $^{-/-}$ Sham mice after 2 weeks and DMM mice at 2, 4, 8 and 12 weeks after DMM surgery. Cartilage of the medial tibia plateau (MTP) and femoral condyle (MFC) was evaluated for grades of cartilage destruction according to the OARSI guidelines. MM = medial meniscus. Asterix (*) indicates discoloration due to proteoglycan loss, full arrows (\rightarrow) indicate osteophyte formation, arrow heads (\blacktriangleright) indicate irregular cartilage surface and open triangles (Δ) indicate cartilage erosions down to the calcified cartilage zone. B) Comparison of means of the maximal OARSI scores of the medial tibial and femoral cartilage (MFC, MTP) from WT, α CGRP $^{-/-}$ and Tac1 $^{-/-}$ mice, 2, 4, 8 and 12 weeks after either DMM or Sham surgery. One-way ANOVA followed by Bonferroni post-hoc test. * $p < 0.05$, ** $p < 0.01$, **** $p < 0.0001$. N = 6. C) Analysis of serum interleukin (IL)-1 β concentrations in WT, Tac1 $^{-/-}$ and α CGRP $^{-/-}$ mice at 2 and 8 weeks after DMM or Sham surgery. N = 6.

in DMM WT mice at 8 weeks after OA induction whereas in the neuropeptide-deficient DMM mice DZ cartilage matrix stiffness remained elevated (Fig. 3D, E; Supplementary Fig. S2B).

3.4. DMM induced thickening of the calcified cartilage layer

Using nanoCT analysis, the thickness of the calcified cartilage (CC) layer was extracted from the subchondral bone plate by differential grey scale analysis. Resulting heat maps of the medial tibia plateau for DMM and Sham mice from all genotypes are depicted at 8 weeks after surgery in Fig. 4A. Notably at 2 weeks after surgery, the CC thickness of the medial tibia plateau of α CGRP $^{-/-}$ DMM mice was increased compared to WT DMM mice (Supplementary Fig. S3A). The medial CC layer thickened significantly in DMM animals of all genotypes compared to Sham at 8 weeks after surgery whereas the lateral CC thickness remained largely unaffected by OA induction (Fig. 4B). Lateral CC thickness from α CGRP $^{-/-}$ mice appeared increased but the effect can be attributed to an outlier skewing the mean because of the small group size (Fig. 4B).

3.5. DMM surgery induced strong ectopic meniscal bone formation in neuropeptide deficient animals

After induction of OA, DMM mice developed ectopic bone at the impact side increasing the volume of the meniscal ossicles (Fig. 4C). Quantification of the bone volume of the ossicles showed no differences early after surgery (2 wks, Supplementary Fig. S3C). With progression to 8 weeks, BV of ossicles from Tac1 $^{-/-}$ and α CGRP $^{-/-}$ mice

increased significantly compared to WT mice and in all three mouse groups meniscal ossicle formation was stronger in DMM mice compared to Sham mice (Fig. 4D).

To investigate if the stronger ossification might be a direct result of altered reactivity of meniscus cells to SP or α CGRP, we analyzed the expression of their respective receptors in the medial meniscus. Neurokinin receptor 1 (Fig. 5A) was stained as the major SP receptor and CRLR (Fig. 5B) and Ramp1 (Fig. 5C) were stained as the receptor subunits for α CGRP. All menisci stained positive for the receptors although CRLR expression was quite low. The proportion of receptor positive cells in relation to the total meniscal cell number was not affected by OA induction and/or neuropeptide absence.

3.6. Neuropeptide deficiency leads to stronger subchondral bone sclerosis

To analyze bone alterations induced by DMM surgery, μ CT scans were performed and a VOI was placed in the medial subchondral bone compartment of the epiphysis of the right knee joint avoiding bone plate, growth plate and cortical bone (Fig. 6A). Representative examples of μ CT images from WT, Tac1 $^{-/-}$ and α CGRP $^{-/-}$ knee joints at 12 weeks after DMM and Sham surgery are shown in Fig. 6B. Images clearly show an enhanced sclerosis in the medial subchondral bone of WT DMM animals in comparison to Sham mice and a generally higher bone volume of Tac1 $^{-/-}$ and α CGRP $^{-/-}$ mice at 12 weeks after surgery. Quantification of the bone volume to total volume ratio (BV/TV) revealed early sclerotic changes in Tac1 $^{-/-}$ DMM mice compared to their respective Sham group as early as 2 weeks after surgery (Fig. 6C). Furthermore, BV/TV of Tac1 $^{-/-}$ Sham mice was

Fig. 3. Atomic force microscopy-based analysis of cartilage matrix stiffness of the superficial cartilage zone in OA- and non-OA WT, α CGRP $^{-/-}$ and Tac1 $^{-/-}$ mice. A) Overview phase contrast optical microscopy image of a frontal cryosection of native (non-decalcified) mouse cartilage indicating the different cartilage zones included in the analysis: superficial zone (SZ), middle zone (MZ) and deep zone (DZ). B, C) Histograms of Young's modulus (stiffness) distributions of the SZ cartilage matrix of WT, α CGRP $^{-/-}$ and Tac1 $^{-/-}$ mice at 2 (B) and 8 (C) weeks after DMM or Sham surgery are shown here representatively for the other two zones. The black line in each histogram represents a fit to the data using a linear combination of two Gaussian distributions. The dashed black lines show the individual Gaussian distributions representing the proteoglycan (left) and the collagen (right) Young's moduli, respectively, as described in detail in the methods section. Dashed black lines from Sham to DMM histograms indicate peak shifts. N = 3. D, E) Mean Young's modulus (stiffness) of the proteoglycan peak (D) and the collagen peak (E) of SZ, MZ and DZ cartilage of WT, α CGRP $^{-/-}$ and Tac1 $^{-/-}$ mice at 2 and 8 weeks after DMM or Sham surgery. Bars show mean \pm standard error of the mean. 2-Sided *t*-test of independent samples. N = 3.

lower compared to α CGRP $^{-/-}$ Sham mice. In late OA, 12 weeks after surgery, BV/TV of α CGRP $^{-/-}$ DMM and Sham as well as Tac1 $^{-/-}$ Sham mice was significantly increased compared to the respective groups of WT mice (Fig. 6C). Analysis of the bone surface (BS) to bone volume ratio (BS/BV) confirmed similar yet reciprocal effects (Supplementary Fig. S4).

2 weeks after surgery, ultra-high resolution nanoCT analysis detected no differences in the BV/TV of the medial epiphysis

(Supplemental Fig. S4B). With progression of OA until 8 weeks after surgery, nanoCT analysis confirmed that BV/TV of α CGRP $^{-/-}$ DMM and Sham as well as Tac1 $^{-/-}$ DMM mice was significantly increased compared to respective groups of WT mice. BV/TV of the medial epiphysis of Tac1 $^{-/-}$ mice clearly increased after DMM surgery compared to Sham mice (Fig. 6D).

Analysis of the bone mineral density (BMD) of the medial tibial subchondral bone (epiphysis) demonstrated that BMD was not affected

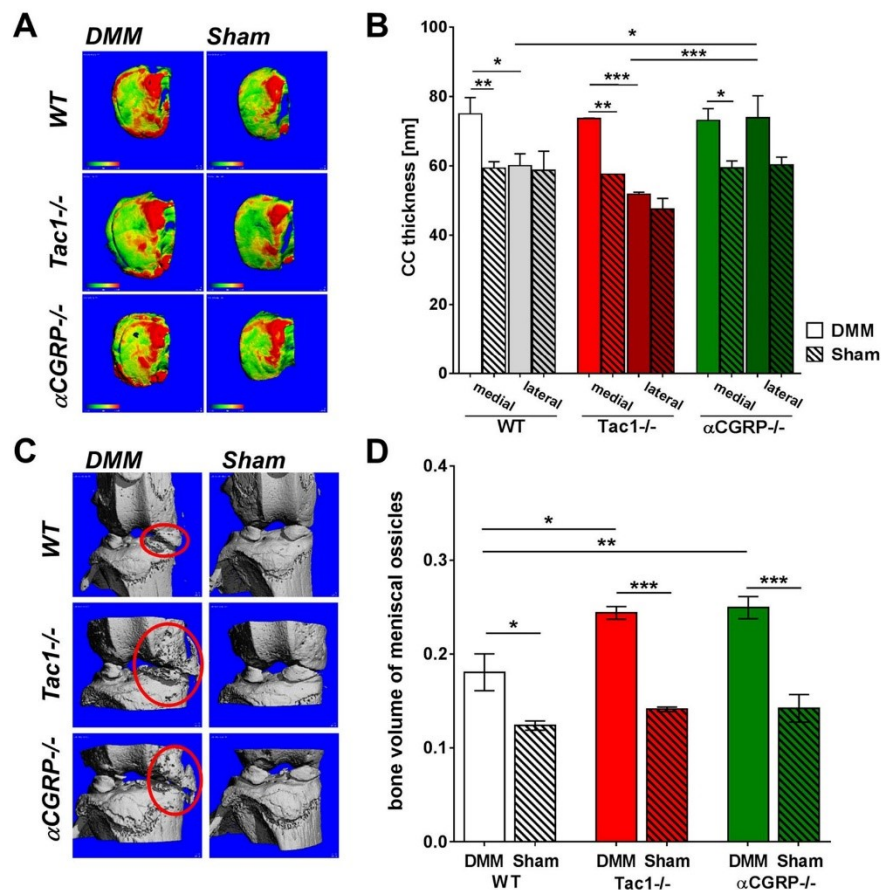


Fig. 4. Influence of DMM on calcified cartilage thickness and meniscal ossification. A) Ultra-high resolution nanoCT images of the calcified cartilage (CC) layer of WT, α CGRP $^{-/-}$ and Tac1 $^{-/-}$ mice at 8 weeks after OA induction. Computational analysis was used to discriminate CC from the subchondral bone plate based on grey scale value differences. Colored heat maps of different grey scales indicate differences in CC thickness (Red \gg green). B) Quantification of the CC thickness in the medial and lateral tibia plateau of WT, α CGRP $^{-/-}$ and Tac1 $^{-/-}$ mice at 8 weeks after DMM or Sham surgery. Two-way ANOVA followed by Tukey post-hoc test. **p* < 0.05, ***p* < 0.01, ****p* < 0.001. N = 3. C) NanoCT analysis highlighted ectopic bone formation (red ellipses) in the medial meniscus of DMM mice at 8 weeks after induction of OA. D) Quantification of the bone volume of meniscal ossicles from WT, α CGRP $^{-/-}$ and Tac1 $^{-/-}$ mice at 8 weeks after DMM or Sham surgery. One-way ANOVA followed by Bonferroni post-hoc test. ***p* < 0.01. N = 3. (For interpretation of the references to color in this figure legend, the reader is referred to the web version of this article.)

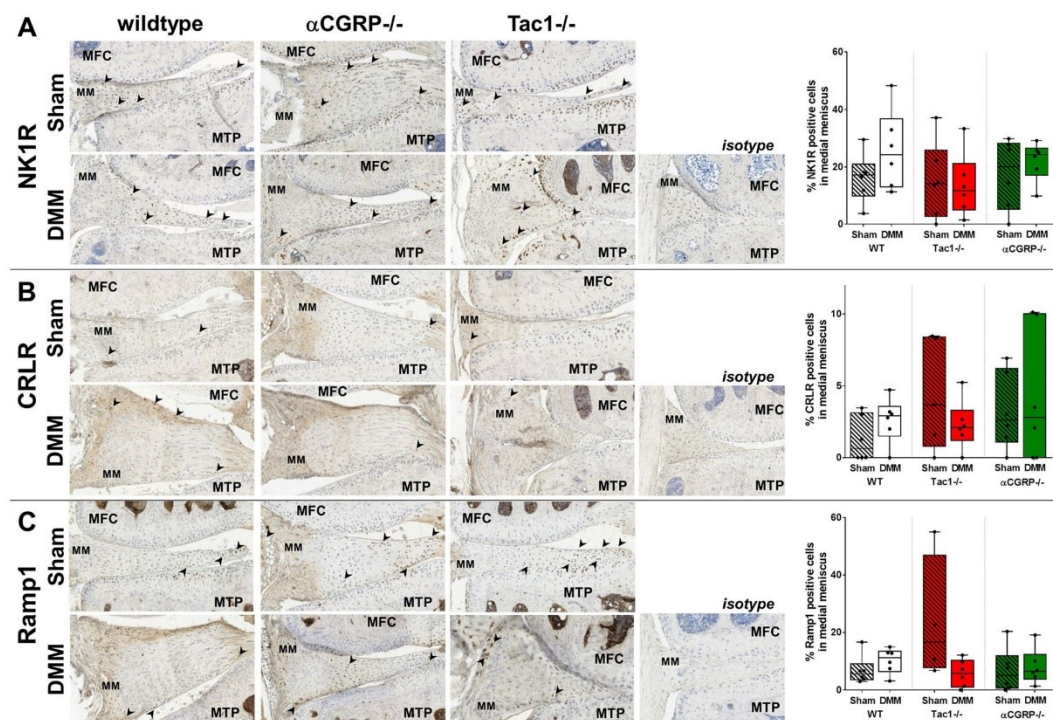


Fig. 5. Expression pattern of sensory neuropeptide receptors in the medial meniscus after DMM and Sham surgery. A–C) Paraffin sections from WT, α CGRP $^{-/-}$ and Tac1 $^{-/-}$ mice at 8 weeks after DMM or Sham surgery were stained with antibodies directed against the SP receptor NK1R (A) and the receptor subunits for α CGRP, CRLR (B) and Ramp1 (C). The number of receptor positive cells (brown staining, arrowheads) was counted in the medial meniscus and set in relation to the total cell number. N = 5–6. NK1R- neurokinin receptor 1, CRLR – calcitonin receptor-like receptor, Ramp1 – receptor activity modifying protein 1. (For interpretation of the references to color in this figure legend, the reader is referred to the web version of this article.)

by DMM surgery or absence of SP or α CGRP (Fig. 6E). Generally, BMD of the epiphysis was higher compared to BMD of meniscal ossicles (Fig. 6E).

3.7. Osteophyte formation in the medial tibia plateau after OA induction

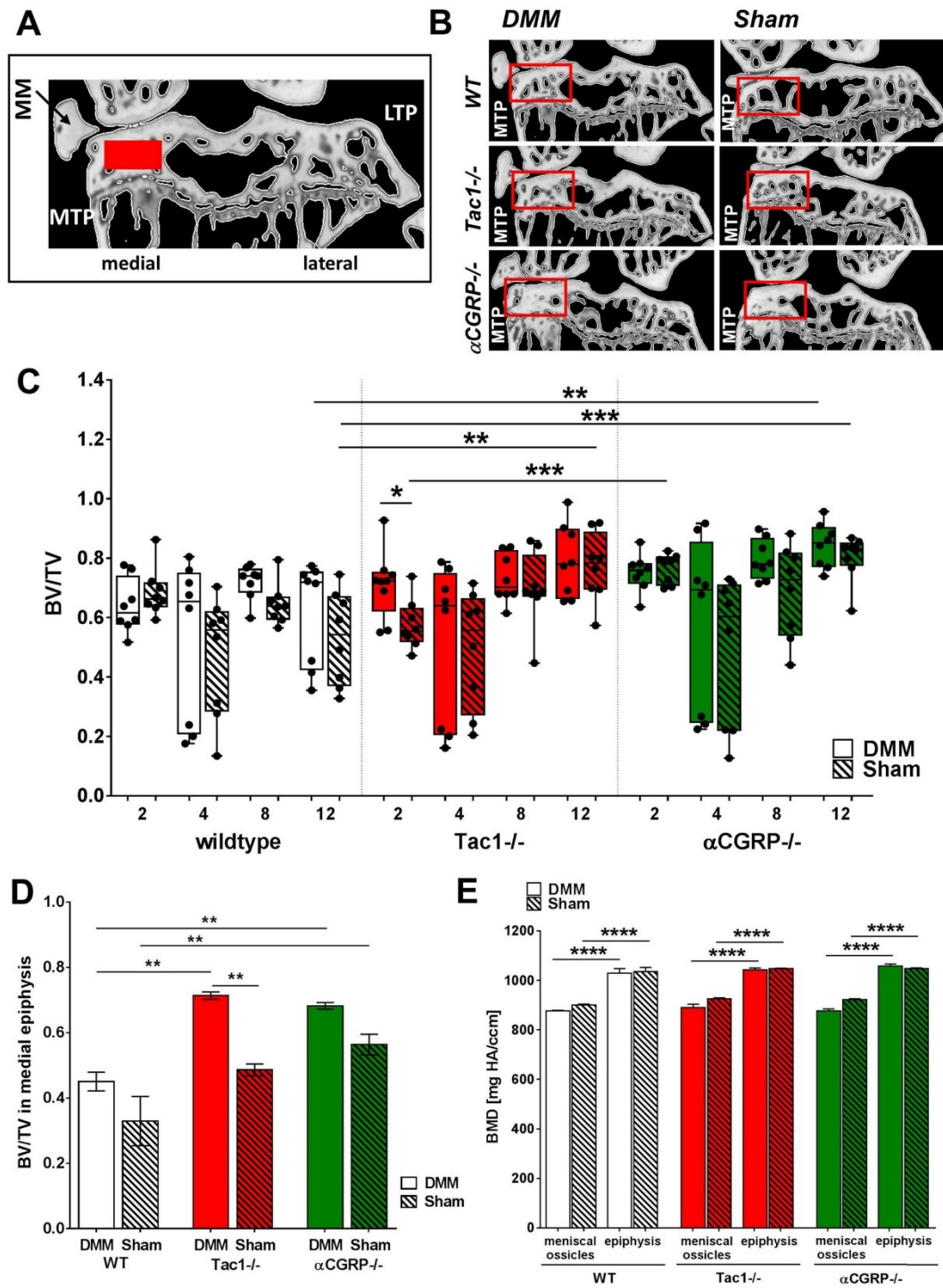
All mice from DMM groups exhibited new bone formation at the medial margins of the knee joint by growing osteophytes over time. The osteophyte formed as an irregular structure at the medial subchondral bone margin, which was accompanied by an increase of the diameter of the medial tibial plateau (Fig. 7A). At 2 weeks after surgery, we observed no DMM-related increase of the tibia plateau diameter. In general, α CGRP $^{-/-}$ DMM and Sham mice had a smaller plateau diameter compared to the respective WT groups (Supplementary Fig. S4D). With progression of OA (8 weeks postoperative), the diameter of the medial tibial plateau increased significantly in the DMM groups of all genotypes compared to their respective Sham groups, but there were no differences between genotypes (Fig. 7B). In comparison, the lateral tibia was generally wider in diameter compared to the medial tibia plateau. The width of the medial condyle in the sham-animals was comparable between genotypes, whereas the width of α CGRP $^{-/-}$ Sham mice lateral condyle width was significantly less than in WT. Condyle diameter of Tac1 $^{-/-}$ mice was in-between WT and α CGRP $^{-/-}$. This suggests a role of sensory signaling for the size of the whole joint. After DMM surgery there was no significant change in the width of the lateral condyle in WT. In contrast, Tac1 $^{-/-}$ mice developed a significantly increased width of the lateral condyle after DMM with a smaller effect yet by trend also observable in the α CGRP $^{-/-}$ mice (Fig. 7B). These

results indicate that osteophyte size was not affected by absence of the sensory neuropeptides but DMM-induced changes in the joint structure of these animals lead to adaptation of the lateral condyle width. Additionally, we used an osteophyte size score to grade Safranin O-stained paraffin sections (Fig. 7C). Osteophytes of α CGRP $^{-/-}$ mice had a larger size score compared to Tac1 $^{-/-}$ DMM mice and were, by trend also larger than WT DMM mice osteophytes (Fig. 7C). To refine the osteophyte analysis, a maturity score was applied categorizing osteophytes with high proteoglycan content (score 1) up to almost complete bony structure (score 3). Osteophytes from α CGRP $^{-/-}$ DMM mice at 8 weeks after surgery were graded more mature than osteophytes from Tac1 $^{-/-}$ DMM mice indicating a higher bone portion (Fig. 7D). The summed score for osteophyte size and maturity confirms this observation (Fig. 7E).

Table 2 presents the number of mice with osteophytes related to the total number of animals in each group.

3.8. Osteoclast numbers and distribution in the subchondral bone after OA induction

Osteoclast numbers were evaluated using histomorphometrical analysis of TRAP-stained sections in the four different compartments of the subchondral bone (medial tibial plateau/femoral condyle; lateral tibial plateau/femoral condyle) and set in relation to the bone surface of the respective compartment. We did not detect differences in osteoclast numbers between the groups in early OA (2 weeks, Fig. 8A and 4 weeks Fig. 8B) or later OA time points (8 and 12 weeks Supplementary Figs. S5A and S5B).



(caption on next page)

Fig. 6. Effect of neuropeptide loss and osteoarthritis induction on bone volume and BMD of the medial subchondral bone. A) Representative image of a micro-computed tomographic section. The red rectangle indicates the approximate location of the region of interest in the subchondral bone of the medial tibia plateau (MTP), also called “medial epiphysis”, that was included in the quantitative analysis. Located opposite to the MTP is the lateral tibia plateau (LTP). The arrow indicates the medial meniscus (MM) that is dislocated from the weight-bearing region of the medial compartment. B) Representative pictures of knee joint micro-computed tomographic scans from WT, α CGRP $^{-/-}$ and Tac1 $^{-/-}$ mice at 12 weeks after DMM or Sham surgery. Red rectangles represent region of interest of the medial tibial subchondral bone. C) Comparison of bone volume (BV) to total volume (TV, BV/TV) of WT, α CGRP $^{-/-}$ and Tac1 $^{-/-}$ mice, 2, 4, 8 and 12 weeks after either DMM or Sham surgery. One-way ANOVA followed by Bonferroni post-hoc test. * $p < 0.05$, ** $p < 0.01$, *** $p < 0.001$. N = 8. D) Ultra-high resolution nanoCt analysis of BV/TV of the subchondral bone of the medial tibia in WT, α CGRP $^{-/-}$ and Tac1 $^{-/-}$ mice at 8 weeks after DMM or Sham surgery. One-way ANOVA followed by Bonferroni post-hoc test. ** $p < 0.01$. N = 3. E) NanoCt analysis of the bone mineral density (BMD) of the medial tibia epiphysis and the meniscal ossicles in WT, α CGRP $^{-/-}$ and Tac1 $^{-/-}$ mice at 8 weeks after DMM or Sham surgery. Two-way ANOVA followed by Tukey post-hoc test. **** $p < 0.0001$. N = 3. (For interpretation of the references to color in this figure legend, the reader is referred to the web version of this article.)

3.9. Serum concentrations of markers related to cartilage and bone matrix degradation

As a marker for bone matrix turnover, carboxy-terminal collagen crosslinks of collagen type I (CTX-I) was analyzed by ELISA in the serum of mice over the course of OA progression. For the early OA time-points (2 and 4 weeks after surgery) we neither observed differences in CTX-I concentrations in the DMM and Sham groups nor between genotypes (Supplementary Figs. S6A and S6B). Also at 8 weeks after surgery, CTX-I serum concentrations were not altered (Fig. 8C). With progression to 12 weeks after surgery, serum CTX-I level of WT Sham mice was significantly increased compared to serum concentrations of Tac1 $^{-/-}$ and α CGRP $^{-/-}$ Sham mice (Fig. 8D).

In order to analyze osteoclast activity, we determined the concentration of TRAcP5b in the serum of mice at 12 weeks after DMM or

Sham surgery. We detected no significant differences between DMM and Sham groups or between the different genotypes (Fig. 8E).

Additionally, we measured the concentration of cartilage matrix degradation marker CTX-II in the urine of mice in relation to the concentration of creatinine. The concentration of CTX-II was low and mostly too close to the detection limit of the respective ELISA to allow reliable conclusions (Supplementary Fig. S6C).

4. Discussion

When studying sensory innervation in the context of osteoarthritis, much effort has been put into elucidation of the role of the sensory neuropeptides SP and α CGRP in pain perception and transmission [17]. Apart from this, other studies evaluated the pleiotropic effects of the sensory neuropeptides on cells of the musculoskeletal system including

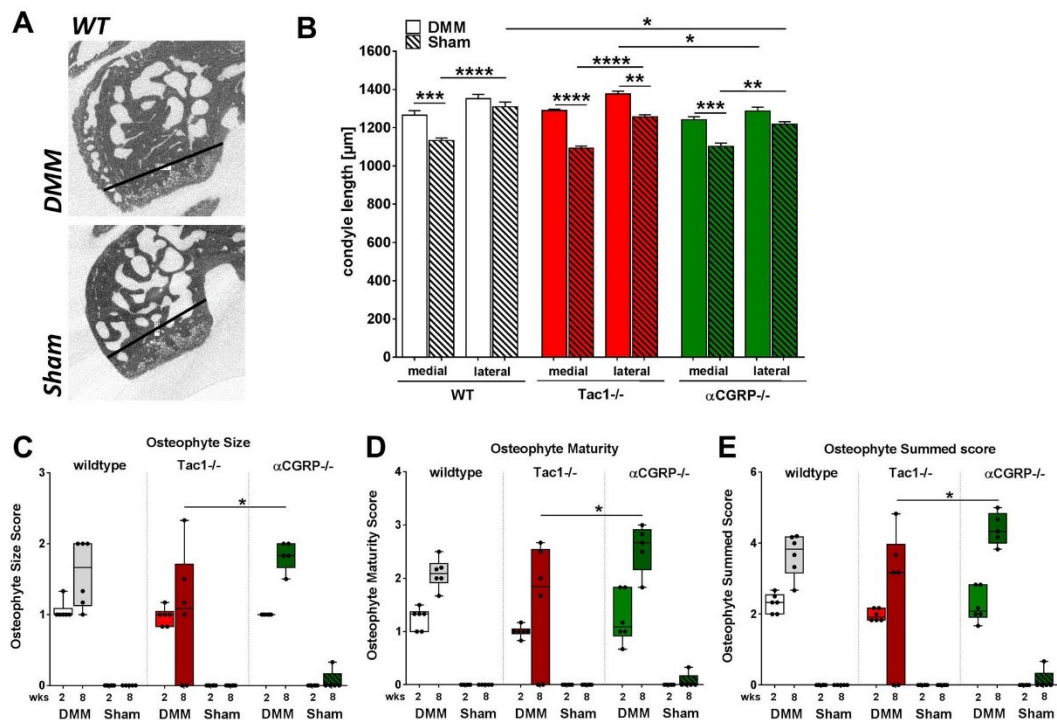


Fig. 7. Characterization of osteophytosis after DMM surgery in WT and neuropeptide deficient mice. A) DMM induced lengthening of the medial tibia plateau as a marker for osteophyte formation. Representative image from WT mice at 8 weeks after DMM and Sham surgery. B) Comparison of the medial tibia plateau diameter of WT, α CGRP $^{-/-}$ and Tac1 $^{-/-}$ mice at 8 weeks after DMM or Sham surgery. Two-way ANOVA followed by Tukey post-hoc test. * $p < 0.05$, ** $p < 0.01$, *** $p < 0.001$, **** $p < 0.0001$. N = 3. C-E) Osteophyte grading of size (C), maturity (D) and the summed score (E) in WT and neuropeptide deficient mice at 8 weeks after DMM and Sham surgery. One-way ANOVA followed by Bonferroni post-hoc test. * $p < 0.05$. N = 6.

D. Muschter, et al.

Bone 133 (2020) 115181

Table 2

Osteophyte development after OA induction.

Osteophytes were identified in TRAP-stained histological sections. Number of animals that developed osteophytes in the medial tibia (A) and the medial femur (B) are presented in relation to the total number of animals analyzed.

	WT		α CGRP $^{-/-}$		Tac1 $^{-/-}$	
	DMM	Sham	DMM	Sham	DMM	Sham
(A) Osteophyte number: tibia						
2 wks	6/6	0/6	6/6	0/6	6/6	0/6
4 wks	6/6	0/6	6/6	1/6	6/6	0/6
8 wks	6/6	1/6	6/6	2/6	6/6	0/6
12 wks	6/6	1/6	6/6	0/6	6/6	0/6
(B) Osteophyte number: femur						
2 wks	4/6	0/6	6/6	0/6	6/6	0/6
4 wks	6/6	0/6	6/6	0/6	5/6	0/6
8 wks	5/5	0/6	5/5	0/6	3/5	0/6
12 wks	6/6	0/6	5/6	0/6	5/6	0/6

OA – osteoarthritis, TRAP – tartrate-resistant acid phosphatase, DMM – destabilized medial meniscus, WT – wildtype, α CGRP – alpha-calcitonin gene-related peptide, Tac1 – Tachykinin 1.

chondrocytes, osteoblasts and osteoclasts but their contribution to OA-related structural changes remained scarcely investigated [6]. Salo and colleagues demonstrated in C57Bl6/Nia mice that sensory innervation is reduced with aging while in parallel these mice developed spontaneous OA [31]. Additional denervation of the joint accelerated the observed OA related structural cartilage matrix damage and disease progression in a rat OA model [32]. The results of this study indicate

that the participation of sensory neuropeptides in OA-induced structural alterations of cartilage and bone deserves more intense investigation.

Apart from their impact on structural changes, we evaluated eligibility of neuropeptide serum concentrations as OA biomarkers but did not find differences between DMM and Sham groups. Of note, in the neuropeptide-deficient mice, we demonstrated instead increased serum concentrations of the respective non-deleted neuropeptide. SP levels were initially higher than respective WT levels, but decreased below WT levels over time, while α CGRP concentrations increased. However, this observation raises the question whether the lack of one neuropeptide or the possibly altered compensatory expression of the other is more responsible for differences in tissue pathophysiology.

Regarding structural alterations, we demonstrate here that SP-deficient mice display an inherent cartilage phenotype with unusually high basal SZ cartilage matrix stiffness that is reduced upon OA induction whereas the deeper cartilage zones stiffness increased with OA progression affecting both the proteoglycan and the collagen proportion of the cartilage matrix. Alterations in the composition and structural orientation of extracellular matrix (ECM) components like proteoglycans and collagens are known to be associated with OA [33]. AFM studies enabled detection of a thickening and stiffening of single collagen fibers associated with OA degenerative changes not only in the superficial cartilage zone but also in the osteochondral unit [34,35]. These structural rearrangements most likely support wear-induced cartilage degradation by an altered biomechanical force transduction [36]. Tac1 $^{-/-}$ mice have a delayed progression of cartilage destruction that might be caused by the increased inherent stiffness of SZ cartilage that is softened after DMM surgery comparably to respective

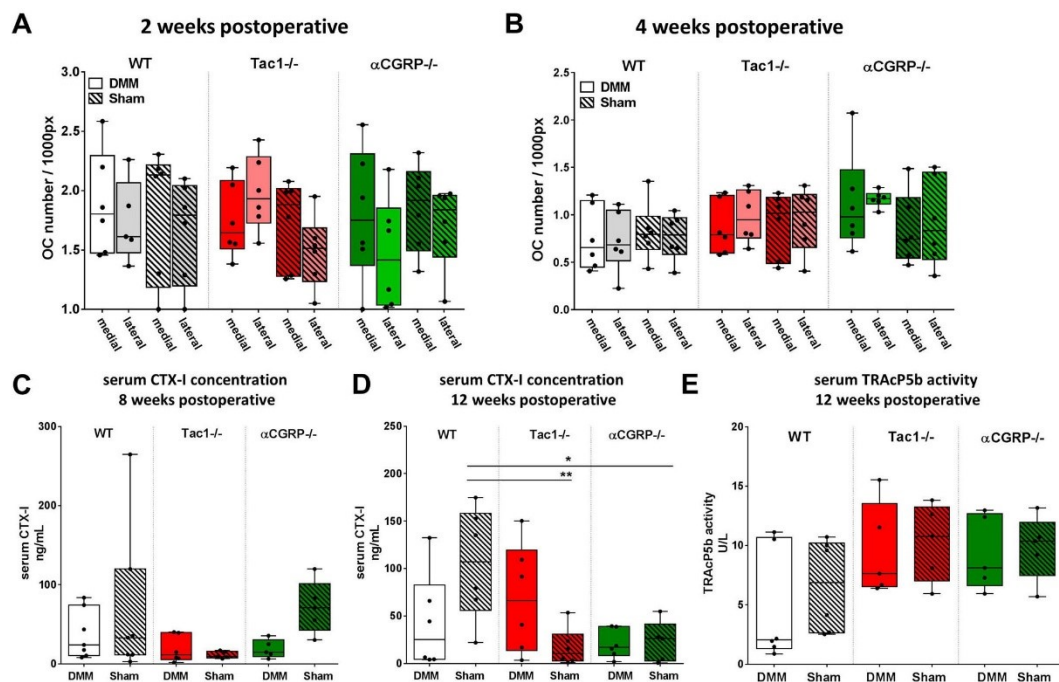


Fig. 8. Influence of OA induction and loss of sensory neuropeptides on osteoclast numbers and serum bone degradation markers. A, B) Mean osteoclast (OC) numbers per bone surface (in pixel, px) were determined from the medial and lateral femoral and tibial subchondral bone. Comparison of OC/px of WT, α CGRP $^{-/-}$ and Tac1 $^{-/-}$ mice at 2 (A) and 4 (B) weeks after DMM and Sham surgery. N = 6. C, D) Serum concentration of C-terminal telopeptide of collagen type I (CTX-I) in WT, α CGRP $^{-/-}$ and Tac1 $^{-/-}$ mice at 8 (C) and 12 (D) weeks after DMM or Sham surgery. One-way ANOVA followed by Bonferroni post-hoc test. *p < 0.05, **p < 0.01. 8 weeks: N = 5–7. 12 weeks: N = 5–6. E) Serum concentration of osteoclast activity marker tartrate-resistant acid phosphatase 5b (TRAcP5b) in WT, α CGRP $^{-/-}$ and Tac1 $^{-/-}$ mice at 12 weeks after DMM or Sham surgery. N = 6.

WT levels. This adjustment in stiffness to WT levels might explain why OARSI scores, indicating severity of structural damage of cartilage matrix, of WT and *Tac1*^{-/-} DMM mice were similar in later OA stages. Doubtlessly, the tachykinin system plays a role in cartilage physiology and pathophysiology. Chondrocytes are equipped with neurokinin receptor 1 (NK1R), the high affinity receptor for SP [37]. Furthermore, chondrocytes produce the neuropeptide SP themselves thereby creating a local neuropeptide micro-milieu independent from the sensory nervous system. NK1R and SP have been linked to chondrocyte mechanoregulation [7] which together with appropriate mechanical stimulation of chondrocytes is crucial to maintain cartilage integrity [38]. Particularly OA chondrocytes upregulated Tachykinin1 mRNA expression (coding gene for SP) after mechanical stimulation [39] and Duarte et al. demonstrated elegantly that experimentally induced lumbar facet-joint OA increased SP expression in the cartilage matrix superficial zone of the ipsilateral neurosegmentally linked knee joint [40]. SP upregulation in cartilage most likely contributes to cartilage deterioration in a pro-catabolic way by stimulating MMP-13 expression. SP could also exert anti-anabolic functions like it was demonstrated by inhibiting BMP-7 induced proteoglycan stimulation and deposition in human adult articular chondrocytes and cartilage matrix [41]. Upregulation of fibronectin (Fn) and Fn fragment formation in OA synovium and cartilage might act protectively and increase SP effects on OA progression by formation of Fn-SP complexes [42–44]. Altogether, these studies would rather suggest a protective effect of a reduced SP expression on cartilage maintenance after OA induction that is in line with our observation that *Tac1*^{-/-} mice have a delayed OA onset. However, our results emphasize an ambivalent role of SP in a strongly context- and tissue-dependent manner. We demonstrate that SP is important in physiological tissue maintenance and most certainly has additional roles in pathophysiological conditions in both tissues, bone and cartilage. Apart from the aforementioned cartilage alterations, loss of SP additionally manifested in increased bone sclerosis compared to Sham *Tac1*^{-/-} mice shortly after OA induction lasting until 8 weeks after surgery. In parallel, *Tac1*^{-/-} Sham mice developed a sclerotic bone phenotype over the observation time. Interestingly, OA induction induced changes in joint morphology of *Tac1*^{-/-} mice (and to a lesser extent also in *αCGRP*^{-/-} mice) by increasing the length of the medial and lateral tibia plateau opposed to WT animals that only developed an increased medial tibia plateau diameter. In a previous study from our group, we provided evidence for the critical role of SP in preservation of physiological bone biomechanical properties and its additional role in pathophysiological conditions as fracture healing [11]. In WT mice, SP staining was increased in the affected tissue region shortly after fracture. In SP-deficient mice, we observed a modified fracture healing process and, additionally, the performance of the non-fractured leg was reduced in biomechanical testing. Thus, induction of SP expression is crucial after acute injury and for physiological tissue maintenance. This observation was also confirmed by studies that observed a correlation of low basic SP-immunoreactivity in the subchondral bone and a strong increase in response after induction of experimental arthritis [4,5]. Other studies revealed an enhanced expression of SP in areas of bone erosion and osteophyte remodeling in OA, as well as in cells of unknown identity located in bone cysts and the subchondral bone plate [15,16].

In contrast to the more complex role of SP, we demonstrated that *αCGRP* is a crucial trophic factor with anabolic functions involved in regulation of predominantly bone and to a lesser extent in cartilage homeostasis. This is supported by a study from Schwab and colleagues that identified frequent and dense innervation of subchondral bone by *αCGRP*-positive nerve fibers but rarely by SP-positive nerves [5]. In general, *αCGRP* effects on bone cells are anabolic with an inhibition of osteoclast numbers after OA induction and positive regulation of osteoblast differentiation and function as summarized in a recent review [6]. We observed that bone cell functions from *αCGRP*^{-/-} mice are impaired in an age-related manner (unpublished data). Here, we

present an increased sclerotic subchondral bone phenotype, independent from OA induction that is subtle in the early observation time point but solidifies in the later observation time points. Again, SP effects on bone cells are more complex compared to *αCGRP* and strictly context-dependent [6,45]. Few studies exist concerning *αCGRP* effects on chondrocytes and cartilage so far. Schwab et al. observed *αCGRP*-positive nerve fiber endings in close contact to chondrocytes of the deeper cartilage layers [5]. One single study described that *αCGRP* stimulation increased cAMP levels in isolated chondrocytes and perichondral cells from rat pups that was not reproducible in whole cartilage explants [46]. In contrast to *Tac1*^{-/-} mice, stiffness of all three cartilage zones from *αCGRP*^{-/-} mice increased during aging and after induction of OA and resembled mostly WT cartilage alterations again supporting the assumption that *αCGRP* effects are more prevalent in bone as we observed a distinct bone phenotype and cartilage defects predominantly in the bone-adjacent deeper layers.

The differential serum concentration of the non-deleted neuropeptide in the k.o. mice complicates interpretation of the results. Clearly, the serum concentration of neuropeptides is not affected by OA induction, therefore early OA effects in the *Tac1*^{-/-} mice involving bone sclerosis and softening of the superficial cartilage layer can, without much doubt, be attributed to the loss of SP in knee joint tissues. This also accounts for alterations of lateral tibia joint morphology. Oppositely, onset of bone sclerosis independent from OA induction in later stages must be regarded with respect to the differential neuropeptide serum concentrations. Bone anabolic effects of an increased *αCGRP* serum concentration in *Tac1*^{-/-} mice and a reduction of SP serum concentrations in *αCGRP*^{-/-} mice will likely add to effects solely attributed to neuropeptide deletion.

Although *Tac1*^{-/-} mice displayed an OA-related sclerotic bone phenotype in the early OA stage, this was not reflected in the serum CTX-I concentrations. That sclerosis might be associated with a reduction in net bone turnover was demonstrated by Klose-Jensen and colleagues in human hip joint OA samples [47]. Bone sclerosis of the neuropeptide deficient mice was accompanied by a reduction in serum CTX-I concentrations after 12 weeks confirming this observation. Detection of altered cartilage or bone degradation biomarker concentration in serum or urine after single joint trauma is questionable and rather unlikely.

Surprisingly, besides differential impact on bone and cartilage alterations, both neuropeptide k.o. mice demonstrated distinct alterations in injury-induced ectopic bone formation. Loss of SP and *αCGRP* induced strong ossification of meniscal tissue, at the side of OA induction. Heterotopic ossification (HO) is a frequent complication after acute inflammation [48]. One might have expected a reduction of ectopic bone formation in mice with a genetic neuropeptide deletion, due to their usual activating effects on osteoblasts and their precursors. In a HO model of the Achilles tendon, Tuzmen et al. observed that SP promoted ectopic bone formation in the Achilles tendon whereas *αCGRP* alone did not provoke a response [49]. Combination of SP and *αCGRP* in their study proved an inhibitory effect of *αCGRP* on SP-induced HO. Intense crosstalk of both neuropeptides, as it occurs most likely in WT mice, might restrain effects observed if only a single sensory neuropeptide is present akin to its effects on BMP-2 induced bone differentiation in C2C12 myoblasts and MC3T3 pre-osteoblasts [50]. Individual treatments of SP or *αCGRP* did not have any direct effects on the cells but the combination of SP and *αCGRP* partially suppressed BMP2-induced ALP activity and mineralization indicating an interaction between both neuropeptides. In that line of thought, the increased heterotopic meniscal ossification in neuropeptide deficient mice might be a consequence of a strong imbalanced expression of the neuropeptides like we found for the serum concentrations of both k.o. mouse models. Furthermore, a tachykinin structurally related to SP, hemokinin-1, mimicked SP-like behavioral effects in mice and gerbils [51]. Due to conserved homology of both neuropeptides, hemokinin-mediated (over)compensatory effects might affect bone and cartilage

homeostasis.

How could the results of our study translate to OA-related clinical research? First, serum concentration of SP and α CGRP seem not to be correlated with OA progression though SP concentrations are by trend reduced in early OA. Hence, both neuropeptides have questionable eligibility as biomarkers. Careful attention should be paid to treatments that specifically target sensory nerves or neuropeptides for reduction of OA pain. Our data clearly state that alterations in neuropeptide availability (especially SP) might induce structural alterations in cartilage and bone that could further contribute to OA progression. In a study performed by Benschop and colleagues, a neutralizing antibody to α CGRP showed promising efficacy in treating OA-related pain in pre-clinical OA models but lacked long-term follow-up of structural changes [52]. Similarly, established therapies addressing sensory neuropeptide blockade as for α CGRP in migraine treatment [53], NK1R blockade with aprepitant in chronic refractory pruritus [54] or as an anti-emetic treatment in patients receiving chemotherapy [55] might require closer monitoring of bone and cartilage structure to avoid structure-related side-effects.

Admittedly, this study contains some limitations that might affect the conclusion of the presented data. First, littermate mice were not used in this study possibly leading to mis- or overinterpretation of how and to which degree neuropeptide deficiency is responsible for the described effects. When backcrossing k.o. mice to a particular background (in our study C57Bl/6J) not only the gene of interest is transferred but also linked chromosomal fragments that were still detectable after backcrossing up to 10 generations (reviewed by Holmdahl and Malissen [56]). Here, C57Bl/6J mice from Charles River were used (which were also used for backcrossing) for comparison with the k.o. strains which might additionally differ from the backcrossed k.o. mice due to epigenetic- and environmental-caused selection [56]. Nonetheless, the use of littermates would provide an extra burden of labor and would be in conflict with the 3R principles (replacement, reduction, refinement). To keep the error minimal, animals were age- and sex-matched and kept strictly under the same housing conditions. Furthermore, background discrepancies so far primarily affected the outcome of immunological studies [56]. For the same 3R principles, we also omitted the use of naïve and heterozygous mice. Heterozygous mice are useful to study deletions that are lethal at an early developmental stage or cause strong phenotypes. Deletion of SP or α CGRP induced a detectable but not overpowering effect in cartilage and bone and induced compensatory expression of the respective other neuropeptide. Therefore, we suppose, that the use of heterozygous mice would be of negligible use and rather complicate interpretation of the results.

In this study, we compared DMM-operated to Sham-operated animals. Both groups experience the inflammatory reactions after opening of the joint capsule and therefore differences observed in bone and cartilage of these animals should solely result from the differences in mechanical impact on these tissues. The use of naïve mice would provide information regarding the impact of inflammation in addition to biomechanics but the two effects would be hardly discernable. We were interested in the purely mechanically induced alterations and therefore and because of the 3R principles, we have chosen only to include Sham-operated animals as the control.

5. Conclusion

Here, we demonstrate that both sensory neuropeptides, SP and α CGRP, are essential modulators of cartilage (predominantly SP) and bone homeostasis. Both neuropeptides protect from age-related bone structural changes.

Challenging mice with DMM-induced OA demonstrates that loss of SP accelerates sclerosis of the subchondral bone being important already in very early OA bone pathology. Furthermore, joint morphology alteration represented by widening of the lateral tibia plateau as a

compensatory reaction to OA induction is more prominent in SP-deficient than in α CGRP-deficient mice emphasizing the role of SP in bone adaptation to acute trauma. Oppositely, α CGRP deficiency leads to general alterations of bone morphology (smaller medial tibia diameter) and age-related bone sclerosis. Absence of both neuropeptides promotes heterotopic ossification of meniscal tissue, whereas osteophyte formation (indicated by lengthening of the medial tibia plateau) is not affected by the neuropeptides at a later OA stage. These observations indicate a crucial preservative role of both neuropeptides in bone homeostasis and formation under pathophysiological conditions.

Cartilage matrix degradation according to OARSI score is not aggravated in the absence of α CGRP, however, occurs earlier than in WT cartilage whereas loss of SP leads to delayed cartilage degradation. Cartilage matrix stiffness, determined by proteoglycan content and collagen network integrity, is altered in SP- and α CGRP-deficient mice, both OA-dependent and endogenously without OA induction.

Of note, we observed an increase of calcified cartilage layer thickness after OA induction in all three groups only in the medial tibia plateau, which constitutes the major load-bearing site of the joint. Calcified cartilage has reduced elastic properties, which will affect cartilage matrix response to mechanical impact and interaction of cartilage with the underlying subchondral bone.

Notably, an important observation of this study is that absence of only one sensory neuropeptide might be counteracted by imbalanced expression of the other neuropeptide.

Due to the bone and cartilage phenotypes, we detected in non-OA neuropeptide deficient animals, therapies targeting α CGRP or SP and their receptors should include monitoring their influence in musculoskeletal tissues carefully.

Funding

This work was funded by the German Research Foundation (DFG) as part of subprojects 1 [CL 409/4-1], 4 [GR 1301/19-1] and 5 [SCHI 857/9-1] of the Research Consortium ExCarBon/FOR2407/1.

Declaration of competing interest

None.

Acknowledgements

We thank Anja Pasoldt and Tanja Späth for their excellent technical assistance in histology and histomorphometry. Dr. Sabine Stöckl kindly agreed to score the Safranin-O stained knee joint sections for the histopathological grading of cartilage destruction.

Contribution

Dominique Muschter: methodology, validation, formal analysis, investigation, provision, data curation, writing – original draft and review and editing, visualization, project administration. Lutz Fleischhauer: methodology, validation, formal analysis, investigation, visualization of IT-AFM measurements, writing – Review & Editing. Shahed Taheri: methodology, validation, formal analysis, investigation, visualization of nanoCT measurements, writing – Review & Editing. Arndt F. Schilling: methodology (nanoCT), resources, writing – Review & Editing, funding acquisition. Hauke Clausen-Schaumann: methodology (IT-AFM), resources, writing – Review & Editing, funding acquisition. Susanne Grässel: conceptualization, writing – Review & Editing, project administration, funding acquisition.

Appendix A. Supplementary data

Supplementary data to this article can be found online at <https://doi.org/10.1016/j.bone.2019.115181>.

References

- [1] M. Cross, E. Smith, D. Hoy, S. Nolte, I. Ackerman, M. Fransen, L. Bridgett, S. Williams, F. Guillemin, C.L. Hill, L.L. Laslett, G. Jones, F. Cicuttini, R. Osborne, T. Vos, R. Buchbinder, A. Woolf, L. March, The global burden of hip and knee osteoarthritis: estimates from the global burden of disease 2010 study, *Ann. Rheum. Dis.* 73 (7) (2014) 1323–1330.
- [2] A. Litwic, M.H. Edwards, E.M. Dennison, C. Cooper, Epidemiology and burden of osteoarthritis, *Br. Med. Bull.* 105 (2013) 185–199.
- [3] R.F. Loeser, S.R. Goldring, C.R. Scanzello, M.B. Goldring, Osteoarthritis: a disease of the joint as an organ, *Arthritis Rheum.* 64 (6) (2012) 1697–1707.
- [4] M. Hukkanen, Y.T. Kontinen, R.G. Rees, S. Santavirta, G. Terenghi, J.M. Polak, Distribution of nerve endings and sensory neuropeptides in rat synovium, meniscus and bone, *International Journal of Tissue Reactions* 14 (1) (1992) 1–10.
- [5] W. Schwab, A. Bilgicyildirim, R.H. Funk, Microtopography of the autonomic nerves in the rat knee: a fluorescence microscopic study, *Anat. Rec.* 247 (1) (1997) 109–118.
- [6] S. Grässel, D. Muschter, Peripheral nerve fibers and their neurotransmitters in osteoarthritis pathology, *Int. J. Mol. Sci.* 18 (5) (2017).
- [7] S.J. Millward-Sadler, A. Mackenzie, M.O. Wright, H.S. Lee, K. Elliot, L. Gerrard, C.E. Fiskerstrand, D.M. Salter, J.P. Quinn, Tachykinin expression in cartilage and function in human articular chondrocyte mechanotransduction, *Arthritis Rheum.* 48 (1) (2003) 146–156.
- [8] I. Pristad, V. Vandevska-Radunovic, K. Fjeld, S.J. Wimalawansa, I. Hals Kvinnsland, NK1, NK2, NK3 and CGRP1 receptors identified in rat oral soft tissues, and in bone and dental hard tissue cells, *Cell Tissue Res.* 311 (3) (2003) 383–391.
- [9] E. Ytteborg, J.S. Torgersen, M.E. Pedersen, S.J. Helland, B. Grisdale-Helland, H. Takle, Exercise induced mechano-sensing and substance P mediated bone modeling in Atlantic salmon, *Bone* 53 (1) (2013) 259–268.
- [10] L.J. Backman, G. Fong, G. Andersson, A. Scott, P. Danielson, Substance P is a mechano-responsive, autocrine regulator of human tenocyte proliferation, *PLoS One* 6 (11) (2011) e27209.
- [11] T. Niedermair, V. Kuhn, F. Doranegard, R. Stange, B. Wieskotter, J. Beckmann, P. Salmen, H.R. Springorum, R.H. Straub, A. Zimmer, J. Grifka, S. Grässel, Absence of substance P and the sympathetic nervous system impact on bone structure and chondrocyte differentiation in an adult model of endochondral ossification, *Matrix Biology: Journal of the International Society for Matrix Biology* 38 (2014) 22–35.
- [12] T. Schinke, S. Liese, M. Priemel, M. Haberland, A.F. Schilling, P. Catala-Lehnen, D. Blicharski, J.M. Rueger, R.F. Gagel, R.B. Emeson, M. Amling, Decreased bone formation and osteopenia in mice lacking alpha-calcitonin gene-related peptide, *J. Bone Miner. Res. Off. J. Am. Soc. Bone Miner. Res.* 19 (12) (2004) 2049–2056.
- [13] S.J. Sample, C.M. Heaton, M. Behan, J.A. Bleedorn, M.A. Racette, Z. Hao, P. Muir, Role of calcitonin gene-related peptide in functional adaptation of the skeleton, *PLoS One* 9 (12) (2014) e113959.
- [14] M.A. Heffner, D.C. Genetos, B.A. Christiansen, Bone adaptation to mechanical loading in a mouse model of reduced peripheral sensory nerve function, *PLoS One* 12 (10) (2017) e0187354.
- [15] S. Suri, S.E. Gill, S. Massena de Camin, D. Wilson, D.F. McWilliams, D.A. Walsh, Neurovascular invasion at the osteochondral junction and in osteophytes in osteoarthritis, *Ann. Rheum. Dis.* 66 (11) (2007) 1423–1428.
- [16] S. Ogino, T. Sasho, K. Nakagawa, M. Suzuki, S. Yamaguchi, M. Higashi, K. Takahashi, H. Moriya, Detection of pain-related molecules in the subchondral bone of osteoarthritic knees, *Clin. Rheumatol.* 28 (12) (2009) 1395–1402.
- [17] K.L. Witt, J.A. Vilesky, The anatomy of osteoarthritic joint pain, *Clinical Anatomy (New York, N.Y.)* 27 (3) (2014) 451–454.
- [18] S.J. Kim, J.E. Kim, S.H. Kim, S.J. Kim, S.J. Jeon, S.H. Kim, Y. Jung, Therapeutic effects of neuropeptide substance P coupled with self-assembled peptide nanofibers on the progression of osteoarthritis in a rat model, *Biomaterials* 74 (2016) 119–130.
- [19] H.L. Ma, T.J. Blanchet, D. Peluso, B. Hopkins, E.A. Morris, S.S. Glasson, Osteoarthritis severity is sex dependent in a surgical mouse model, *Osteoarthr. Cartil.* 15 (6) (2007) 695–700.
- [20] A. Zimmer, A.M. Zimmer, J. Baffi, T. Usdin, K. Reynolds, M. Konig, M. Palkovits, E. Mezey, Hypoalgesia in mice with a targeted deletion of the tachykinin 1 gene, *Proc. Natl. Acad. Sci. U. S. A.* 95 (5) (1998) 2630–2635.
- [21] J.T. Lu, Y.-J. Son, J. Lee, T.L. Jetton, M. Shiota, L. Moscoco, K.D. Niswender, A.D. Loewy, M.A. Magnuson, J.R. Sanes, R.B. Emeson, Mice lacking α -calcitonin gene-related peptide exhibit normal cardiovascular regulation and neuromuscular development, *Mol. Cell. Neurosci.* 14 (2) (1999) 99–120.
- [22] S.S. Glasson, T.J. Blanchet, E.A. Morris, The surgical destabilization of the medial meniscus (DMM) model of osteoarthritis in the 129/SvEv mouse, *Osteoarthr. Cartil.* 15 (9) (2007) 1061–1069.
- [23] H.J. Butt, M. Jaschke, Calculation of thermal noise in atomic force microscopy, *Nanotechnology* 6 (1) (1995) 1–7.
- [24] D. Docheva, D. Padula, C. Popov, W. Mutschler, H. Clausen-Schaumann, M. Schieker, Researching into the cellular shape, volume and elasticity of mesenchymal stem cells, osteoblasts and osteosarcoma cells by atomic force microscopy, *J. Cell. Mol. Med.* 12 (2) (2008) 537–552.
- [25] C. Prein, N. Warmbold, Z. Farkas, M. Schieker, A. Aszodi, H. Clausen-Schaumann, Structural and mechanical properties of the proliferative zone of the developing murine growth plate cartilage assessed by atomic force microscopy, *Matrix biology: Journal of the International Society for Matrix Biology* 50 (2016) 1–15.
- [26] M. Loparic, D. Weir, A.U. Daniels, R. Raiteri, M.R. Vanlandingham, G. Guex, I. Martin, U. Aebi, M. Stolz, Micro- and nanomechanical analysis of articular cartilage by indentation-type atomic force microscopy: validation with a gel-microfibrillar composite, *Biophys. J.* 98 (11) (2010) 2731–2740.
- [27] S.S. Glasson, M.G. Chambers, W.B. Van Den Berg, C.B. Little, The OARSI histopathology initiative - recommendations for histological assessments of osteoarthritis in the mouse, *Osteoarthr. Cartil.* 18 (Suppl. 3) (2010) S17–S23.
- [28] C.B. Little, A. Barai, D. Burkhardt, S.M. Smith, A.J. Fosang, Z. Werb, M. Shah, E.W. Thompson, Matrix metalloproteinase 13-deficient mice are resistant to osteoarthritic cartilage erosion but not chondrocyte hypertrophy or osteophyte development, *Arthritis Rheum.* 60 (12) (2009) 3723–3733.
- [29] N. Fedchenko, J. Reifenrath, Different approaches for interpretation and reporting of immunohistochemistry analysis results in the bone tissue - a review, *Diagn. Pathol.* 9 (1) (2014) 221.
- [30] F. Paul, E. Erdfelder, A.G. Lang, A. Buchner, G*Power 3: a flexible statistical power analysis program for the social, behavioral, and biomedical sciences, *Behav. Res. Methods* 39 (2) (2007) 175–191.
- [31] P.T. Salo, R.A. Seeratten, W.M. Erwin, R.C. Bray, Evidence for a neuropathic contribution to the development of spontaneous knee osteoarthritis in a mouse model, *Acta Orthop. Scand.* 73 (1) (2002) 77–84.
- [32] P.T. Salo, T. Hogervorst, R.A. Seerattan, D. Rucker, R.C. Bray, Selective joint denervation promotes knee osteoarthritis in the aging rat, *Journal of Orthopaedic Research* 20 (6) (2002) 1256–1264.
- [33] S. Saarakkala, P. Julkunen, P. Kiviranta, J. Makitalo, J.S. Jurvelin, R.K. Korhonen, Depth-wise progression of osteoarthritis in human articular cartilage: investigation of composition, structure and biomechanics, *Osteoarthr. Cartil.* 18 (1) (2010) 73–81.
- [34] M. Stolz, R. Gottardi, R. Raiteri, S. Miot, I. Martin, R. Imer, U. Stauer, A. Raducanu, M. Duggelin, W. Baschong, A.U. Daniels, N.F. Friederich, A. Aszodi, U. Aebi, Early detection of aging cartilage and osteoarthritis in mice and patient samples using atomic force microscopy, *Nat. Nanotechnol.* 4 (3) (2009) 186–192.
- [35] C.Y. Wen, C.B. Wu, B. Tang, T. Wang, C.H. Yan, W.W. Lu, H. Pan, Y. Hu, K.Y. Chiu, Collagen fibril stiffening in osteoarthritic cartilage of human beings revealed by atomic force microscopy, *Osteoarthr. Cartil.* 20 (8) (2012) 916–922.
- [36] W. Waldstein, G. Perino, S.L. Gilbert, S.A. Maher, R. Windhager, F. Boettner, OARSI osteoarthritis cartilage histopathology assessment system: a biomechanical evaluation in the human knee, *Journal of Orthopaedic Research* 34 (1) (2016) 135–140.
- [37] A. Opolka, R.H. Straub, A. Pasoldt, J. Grifka, S. Grässel, Substance P and nor-epinephrine modulate murine chondrocyte proliferation and apoptosis, *Arthritis Rheum.* 64 (3) (2012) 729–739.
- [38] D.J. Leong, J.A. Hardin, N.J. Cobelli, H.B. Sun, Mechanotransduction and cartilage integrity, *Annals of the New York Academy of Sciences* 1240 (2011) 32–37.
- [39] M.R. Howard, S.J. Millward-Sadler, A.S. Vasilou, D.M. Salter, J.P. Quinn, Mechanical stimulation induces preproachykinin gene expression in osteoarthritic chondrocytes which is correlated with modulation of the transcription factor neuron restrictive silencing factor, *Neuropeptides* 42 (5–6) (2008) 681–686.
- [40] F.C.K. Duarte, D.P. Zwambag, S.H.M. Brown, A. Clark, M. Hurtig, J.Z. Srebely, Increased substance P immunoreactivity in ipsilateral knee cartilage of rats exposed to lumbar spine injury, *Cartilage* (2018) 1947603518812568.
- [41] H.-J. Im, X. Li, P. Muddasani, G.H. Kim, F. Davis, J. Rangan, C.B. Forsyth, M. Ellman, E.J. Thonar, Basic fibroblast growth factor accelerates matrix degradation via a neuro-endothelial pathway in human adult articular chondrocytes, *J. Cell. Physiol.* 215 (2) (2008) 452–463.
- [42] G. Lust, N. Burton-Wurster, H. Leipold, Fibronectin as a marker for osteoarthritis, *The Journal of Rheumatology* 14 Spec No (1987) 28–29.
- [43] P. Rameshwar, D.D. Joshi, P. Yadav, J. Qian, P. Gascon, V.T. Chang, D. Anjaria, J.S. Harrison, X. Song, Mimicry between neurokinin-1 and fibronectin may explain the transport and stability of increased substance P immunoreactivity in patients with bone marrow fibrosis, *Blood* 97 (10) (2001) 3025–3031.
- [44] R.A. Skidgel, S. Engelbrecht, A.R. Johnson, E.G. Erdos, Hydrolysis of substance p and neurotensin by converting enzyme and neutral endopeptidase, *Peptides* 5 (4) (1984) 769–776.
- [45] T. Niedermair, S. Schirmer, R. Seebrocker, R.H. Straub, S. Grässel, Substance P modulates bone remodeling properties of murine osteoblasts and osteoclasts, *Sci. Rep.* 8 (1) (2018) 9199.
- [46] K. Edoff, C. Hildebrand, Neuropeptide effects on rat chondrocytes and perichondrial cells in vitro, *Neuropeptides* 37 (5) (2003) 316–318.
- [47] R. Kløse-Jensen, L.B. Hartlev, L.W.T. Boel, M.B. Laursen, K. Stengaard-Pedersen, K.K. Keller, E.M. Hauge, Subchondral bone turnover, but not bone volume, is increased in early stage osteoarthritic lesions in the human hip joint, *Osteoarthr. Cartil.* 23 (12) (2015) 2167–2173.
- [48] C.T. Kraft, S. Agarwal, K. Ranganathan, V.W. Wong, S. Loder, J. Li, M.J. Delano, B. Levi, Trauma-induced heterotopic bone formation and the role of the immune system: a review, *The Journal of Trauma and Acute Care Surgery* 80 (1) (2016) 156–165.
- [49] C. Tuzmen, K. Verdels, L. Weiss, P. Campbell, Crosstalk between substance P and calcitonin gene-related peptide during heterotopic ossification in murine Achilles tendon, *Journal of Orthopaedic Research* 36 (5) (2018) 1444–1455.
- [50] C. Tuzmen, P.G. Campbell, Crosstalk between neuropeptides SP and CGRP in regulation of BMP2-induced bone differentiation, *Connect. Tissue Res.* 59 (sup1) (2018) 81–90.
- [51] R.A. Duffy, J.A. Hedrick, G. Randolph, C.A. Morgan, M.E. Cohen-Williams, G. Vassileva, J.E. Lachowicz, M. Laverty, M. Maguire, L.S. Shan, E. Gustafson, G.B. Varty, Centrally administered hemokinin-1 (HK-1), a neurokinin NK1 receptor agonist, produces substance P-like behavioral effects in mice and gerbils, *Neuropharmacology* 45 (2) (2003) 242–250.
- [52] R.J. Benschop, E.C. Collins, R.J. Darling, B.W. Allan, D. Leung, E.M. Conner, J. Nelson, B. Gaynor, J. Xu, X.F. Wang, R.A. Lynch, B. Li, D. McCarty, J.L. Oskins, C. Lin, K.W. Johnson, M.G. Chambers, Development of a novel antibody to

D. Muschter, et al.

Bone 133 (2020) 115181

- calcitonin gene-related peptide for the treatment of osteoarthritis-related pain, *Osteoarthr. Cartil.* 22 (4) (2014) 578–585.
- [53] H. Yuan, C.G. Lauritsen, E.A. Kaiser, S.D. Silberstein, CGRP monoclonal antibodies for migraine: rationale and progress, *BioDrugs: clinical immunotherapeutics, Biopharmaceuticals and Gene Therapy* 31 (6) (2017) 487–501.
- [54] A. He, J.M. Alhariri, R.J. Sweren, M.M. Kwatra, S.G. Kwatra, Aprepitant for the treatment of chronic refractory pruritus, *Biomed. Res. Int.* 2017 (2017) 4790810.
- [55] P. Patel, J.S. Leeder, M. Piquette-Miller, L.L. Dupuis, Aprepitant and fosaprepitant drug interactions: a systematic review, *Br. J. Clin. Pharmacol.* 83 (10) (2017) 2148–2162.
- [56] R. Holmdahl, B. Malissen, The need for littermate controls, *Eur. J. Immunol.* 42 (1) (2012) 45–47.

6. Paper II



International Journal of
Molecular Sciences



Article

Mice Lacking the Matrilin Family of Extracellular Matrix Proteins Develop Mild Skeletal Abnormalities and Are Susceptible to Age-Associated Osteoarthritis

Ping Li ¹, Lutz Fleischhauer ^{1,2,3}, Claudia Nicolae ^{4,†}, Carina Prein ^{1,2,‡}, Zsuzsanna Farkas ¹, Maximilian Michael Saller ¹, Wolf Christian Prall ¹, Raimund Wagener ⁵, Juliane Heilig ^{6,7}, Anja Niehoff ^{6,8}, Hauke Clausen-Schaumann ^{2,3}, Paolo Alberton ¹ and Attila Aszodi ^{1,2,*}

¹ Experimental Surgery and Regenerative Medicine (ExperiMed), Department of General, Trauma and Reconstructive Surgery, Munich University Hospital, Ludwig-Maximilians-University, 80336 Munich, Germany; Ping.Li@med.uni-muenchen.de (P.L.); lutz.fleischhauer@hm.edu (L.F.); carina.prein@uwo.ca (C.P.); Zsuzsanna.Farkas@med.uni-muenchen.de (Z.F.); Maximilian.Saller@med.uni-muenchen.de (M.M.S.); Christian.Prall@med.uni-muenchen.de (W.C.P.); Paolo.Alberton@med.uni-muenchen.de (P.A.)

² Center for Applied Tissue Engineering and Regenerative Medicine, Munich University of Applied Sciences, 80533 Munich, Germany; hauke.clausen-schaumann@hm.edu

³ Center for NanoScience, Ludwig-Maximilians University Munich, 80799 Munich, Germany

⁴ Department of Molecular Medicine, Max Planck Institute for Biochemistry, 82152 Martinsried, Germany; cnicolae@pennstatehealth.psu.edu

⁵ Center for Biochemistry, Medical Faculty, and Center for Molecular Medicine, University of Cologne, 50923 Cologne, Germany; raimund.wagener@uni-koeln.de

⁶ Cologne Center for Musculoskeletal Biomechanics, Faculty of Medicine and University Hospital of Cologne, 50931 Cologne, Germany; juliane.heilig@uni-koeln.de (J.H.); niehoff@dshs-koeln.de (A.N.)

⁷ Center for Biochemistry, Faculty of Medicine, University of Cologne, 50931 Cologne, Germany

⁸ Institute of Biomechanics and Orthopaedics, German Sport University Cologne, 50933 Cologne, Germany

* Correspondence: attila.Aszodi@med.uni-muenchen.de; Tel.: +49-89-4400-55481

† Current address: Department of Biochemistry and Molecular Biology, The Pennsylvania State University College of Medicine, Hershey, PA 17033, USA.

‡ Current address: Department of Physiology and Pharmacology, Schulich School of Medicine and Dentistry, The University of Western Ontario, London, ON N6A 3K7, Canada.

Received: 12 December 2019; Accepted: 15 January 2020; Published: 19 January 2020

Abstract: Matrilins (MATN1, MATN2, MATN3 and MATN4) are adaptor proteins of the cartilage extracellular matrix (ECM), which bridge the collagen II and proteoglycan networks. In humans, dominant-negative mutations in MATN3 lead to various forms of mild chondrodysplasias. However, single or double matrilin knockout mice generated previously in our laboratory do not show an overt skeletal phenotype, suggesting compensation among the matrilin family members. The aim of our study was to establish a mouse line, which lacks all four matrilins and analyze the consequence of matrilin deficiency on endochondral bone formation and cartilage function. *Matn1-4^{-/-}* mice were viable and fertile, and showed a lumbosacral transition phenotype characterized by the sacralization of the sixth lumbar vertebra. The development of the appendicular skeleton, the structure of the growth plate, chondrocyte differentiation, proliferation, and survival were normal in mutant mice. Biochemical analysis of knee cartilage demonstrated moderate alterations in the extractability of the binding partners of matrilins in *Matn1-4^{-/-}* mice. Atomic force microscopy (AFM) revealed comparable compressive stiffness but higher collagen fiber diameters in the growth plate cartilage of quadruple mutant compared to wild-type mice. Importantly, *Matn1-4^{-/-}* mice developed more severe spontaneous osteoarthritis at the age of 18 months, which was accompanied by changes in the biomechanical properties of the articular cartilage. Interestingly, *Matn4^{-/-}* mice also developed age-associated osteoarthritis suggesting a crucial role of MATN4 in maintaining the stability of the articular cartilage. Collectively, our data provide evidence that matrilins are

important to protect articular cartilage from deterioration and are involved in the specification of the vertebral column.

Keywords: matrilin; cartilage; bone development; articular cartilage; osteoarthritis

1. Introduction

Endochondral bone development is a complex process which requires the differentiation of chondrocytes and the production of a tissue-specific extracellular matrix (ECM) by forming cartilaginous templates of the future bones. Cartilage ECM provides physical support for chondrocytes maintaining the integrity and biomechanical properties of the cartilage, such as resistance against tensile strength and compressive forces. The typical transient hyaline cartilage of the developing bones and the permanent articular cartilage are composed of the heterotypic type II/IX/XI collagen fibrils and proteoglycans, mainly aggrecan, and numerous multi-domain adaptor proteins, which interconnect the two macromolecular networks. Among the perifibrillar adaptor proteins, matrilins (MATN) form a subfamily of modular, non-collagenous ECM proteins consisting of four members, namely matrilin-1, -2, -3, and -4 [1]. All matrilin members share similar structures containing one (matrilin-3) or two (matrilin-1, -3 and -4) von Willebrand factor A (VWA) domains, various numbers of epidermal growth factor (EGF) like domains and a coiled-coil (CC) α -helical oligomerization module. In mice, matrilin-1 (MATN1) and matrilin-3 (MATN3) are predominantly expressed in the developing epiphyseal and growth plate cartilages [2,3], while matrilin-2 (MATN2) and matrilin-4 (MATN4), besides cartilage, are also present in various extra-skeletal tissues [4,5]. Matrilins interact with numerous cartilage ECM components including aggrecan (ACAN) [6], collagen II [7], collagen IX [8], cartilage oligomeric matrix protein (COMP) [9] and decorin [10], thereby may interconnect and stabilize the macromolecular networks of collagen fibrils and the aggregating proteoglycan aggrecan [1,10,11].

During skeletal development, MATN1, MATN3, and MATN4 display a largely overlapping expression pattern. These matrilins are abundant in epiphyseal and growth plate cartilage, whereas MATN2 is strongly expressed in the perichondrium/periosteum and moderately in the proliferative zone of the growth plate [12,13]. At the forming articular surface, the outermost superficial cell layers express MATN2 and MATN4, whereas the deeper cell layers of the articular surface express MATN3 and MATN4 but not MATN1 [13]. In more mature articular cartilage, all matrilins are expressed at very low levels [13].

To date, the association of a human connective tissue disorder has been only identified in the genes coding for matrilin-3 and matrilin-1. Multiple epiphyseal dysplasia (MED) is a clinically and genetically heterogeneous skeletal dysplasia characterized by joint pain and stiffness, and early onset of osteoarthritis (OA). Autosomal dominant forms of MED are caused by mutations in the genes encoding matrilin-3 (MATN3), collagen IX chains (COL9A1, COL9A2 and COL9A3) and cartilage oligomeric matrix protein (COMP) [14]. The MED mutations identified in MATN3 are missense and predominantly confined to the β -sheet regions of the VWA domain [15–17]. In vitro experiments suggest that these mutations lead to the retention of the mutant MATN3 in the rough endoplasmic reticulum, where it accumulates as an unfolded intermediate and activates unfolded protein response [18–20]. In addition to MED, mutations in MATN3 have been described in bilateral hereditary micro-epiphyseal dysplasia (BHMED) [21] and spondylo-epi-metaphyseal dysplasia (SEMD) [22] patients. Furthermore, a low occurrence of linkage of *MATN3* to hand OA and spinal disc degeneration has been reported [23–25]. The association of MATN1 with osteoarthritis was described in the Dutch but not in the British population [26,27]. More recently, *MATN1* was suggested as a candidate gene for idiopathic scoliosis [28] and mandibular prognathism [29], and as a genetic modifier of SEMD with joint laxity [30].

Despite the suggested integrative functions of matrilins in the cartilage ECM, ablation of matrilin genes in mice does not lead to an overt phenotype. Single knockout mice lacking matrilin-1 (*Matn1*^{-/-})

or matrilin-3 (*Matn3*^{-/-}) [31,32] were generated in our laboratory and these null mice showed no signs of chondrodysplasia or any other obvious skeletal phenotype. In contrast, subtle defects were identified in other matrilin mutant strains generated by independent laboratories. Abnormal collagen II fibrils and stiffness of the cartilage ECM were reported in the matrilin-1 deficient mice [33,34], while accelerated differentiation of embryonic hypertrophic chondrocytes in the growth plate, increased bone mineral density and higher incidence of knee osteoarthritis were found in matrilin-3 knockout mice [35]. Although, we were unable to detect these skeletal phenotypes in our single knockout lines, we have reported a mild increase of collagen fibrillar thickness in *Matn1*^{-/-}, *Matn3*^{-/-} and matrilin-1/matrilin-3 double deficient mice (*Matn1*^{-/-}/*Matn3*^{-/-}) by electron microscopy [36]. This finding implies that matrilin-1 and matrilin-3 may have only a minor role in the proper ultrastructural organization of collagen network in cartilage. Interestingly, matrilin-2 and matrilin-4 deficient mice, which also develop without obvious skeletal abnormalities [12,37], instead present extra-skeletal phenotypes. *Matn2*^{-/-} mice display impaired functional recovery after femoral nerve lesion, indicating an essential role of matrilin-2 for peripheral nerve regeneration [38], while *Matn4*^{-/-} mice show increased proliferation of hematopoietic stem cells upon myelosuppressive chemotherapy, inflammatory stress and transplantation [37].

The similar structure, function, and expression pattern of matrilins suggest compensation among the family members. Indeed, we previously demonstrated that matrilin-4 is up-regulated in the cartilage of *Matn1*^{-/-} and *Matn1*^{-/-}/*Matn3*^{-/-} mice, providing the first experimental evidence that biochemical compensation could exist between matrilins in vivo [36]. In order to further extend our knowledge about the skeletal function of matrilins, herein we report the analysis of mice lacking all matrilins. Quadruple mutant mice (*Matn1-4*^{-/-}) have a reduced number of lumbar vertebrae due to lumbosacral homeotic transition and osteoarthritic-like degeneration develops in mice older than 18 months. Interestingly, similar articular cartilage degeneration was observed in aged matrilin-4 deficient mice, indicating an unexpected role of matrilin-4 in protecting articular cartilage from age-associated, spontaneous osteoarthritis.

2. Results

2.1. Biochemical Compensation in Cartilage of Mice Lacking Matrilins

Previously we have demonstrated that knockout mice lacking matrilin-1 (*Matn1*^{-/-}), matrilin-3 (*Matn3*^{-/-}) or both matrilin-1 and matrilin-3 (*Matn1*^{-/-}/*Matn3*^{-/-}) exhibit only mild ultrastructural abnormalities of the collagenous fibrillar network of the cartilage without manifestation of any obvious skeletal defects [31,32,36]. We have also found, however, that matrilin-4 (MATN4) is upregulated in *Matn1*^{-/-} and *Matn1*^{-/-}/*Matn3*^{-/-} mice but not in *Matn3*^{-/-} mice in knee cartilage tissues sequentially extracted with high salt containing 10 mM ethylenediaminetetraacetic acid (EDTA) (fraction II) and 4 M guanidine hydrochloride (GuHCl) (fraction III), while matrilin-2 (MATN2) was deposited normally in those mutants compared with controls [36]. In the present study, we have analyzed further compound knockout mice lacking MATN1, MATN2 and MATN3 in various combinations (*Matn2*^{-/-}/*Matn3*^{-/-}; *Matn1-3*^{-/-}), and we could confirm that the homotrimeric form of MATN4 was consistently upregulated in fractions II and III, but not in neutral salt extracts (fraction I) of animals lacking MATN1 and/or MATN2 (Figure 1C). MATN4 compensatory upregulation was especially prominent in mice, which lacked MATN2 in addition to MATN1 and/or MATN3, such as *Matn2*^{-/-}/*Matn3*^{-/-} and *Matn1-3*^{-/-} mice. Importantly, these multiple knockouts including the triple mutant *Matn1-3*^{-/-} mice had normal gross skeleton and displayed normal growth plate and articular cartilage histoarchitectures at birth and at various postnatal stages (Figure 1A,B and not shown). Similarly, mice lacking MATN4 developed a normal skeleton without apparent abnormalities of the zonal and columnar structure of the cartilaginous growth plate of the long bones (Figure 1D). Interestingly, immunohistochemical staining revealed an upregulation of MATN2 deposition in the proliferative and hypertrophic zones of the newborn growth plate cartilage in *Matn4*^{-/-} mice (Figure 1E). Using Western blots, we could confirm stronger signals for MATN2 in fractions II/III of matrilin-4 mutant cartilage extracts compared with wild type, while the levels of MATN1 and MATN3 did

not change significantly (Figure 1F). The expression of *Matn2* at mRNA levels was comparable between control and *Matn4*^{-/-} mice in newborn limb cartilage (data not shown). Collectively, our data demonstrate that MATN2 and MATN4 biochemically compensate for the lack of MATN4 and MATN1, respectively, in the newborn mouse knee cartilage.

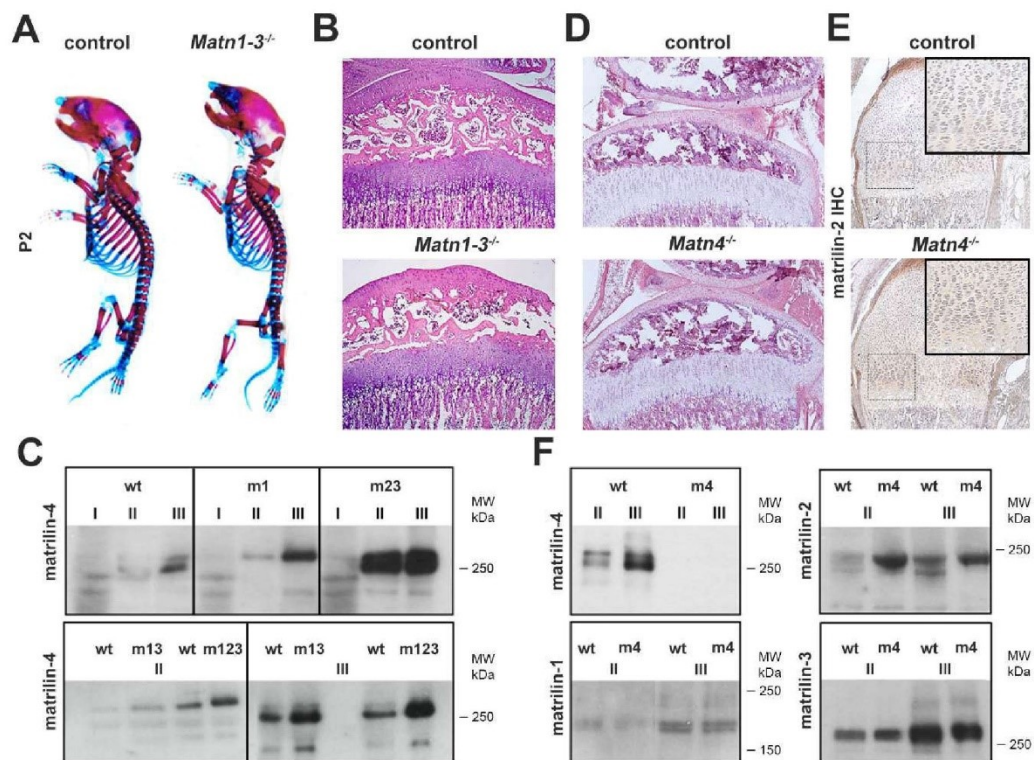


Figure 1. Biochemical compensation among matrilins. (A) Whole-mount skeletal staining at postnatal day 2 (P2) shows no obvious skeletal defects in mice lacking matrilin-1, -2 and -3 (*Matn1-3*^{-/-}) compared to wild type. (B) HE staining of the proximal tibia (original magnification $\times 10$) of the knee joint indicates normal growth plate and articular cartilage structures in *Matn1-3*^{-/-} mice at 4 weeks of age. (C) Western blot analyses of sequential cartilage extracts (I-neutral salt; II-high salt/EDTA; III-GuHCl) from newborn mice indicates upregulation of matrilin-4 in mice lacking matrilin-1 (m1), matrilin-2 and -3 (m23), matrilin-1 and -3 (m13), and matrilin-1, -2, and -3 (m123). (D) HE staining of the proximal tibia (original magnification $\times 10$) of the knee joint at 4 weeks of age demonstrates that mice lacking matrilin-4 (*Matn4*^{-/-}) have a normal structure of long bones. (E) Immunohistochemistry (IHC, original magnification $\times 10$) indicates the increased deposition of matrilin-2 in the growth plate of the humerus (rectangle, original magnification $\times 20$) of *Matn4*^{-/-} mice. (F) Western blot analyses show increased amounts of matrilin-2 in cartilage extracts of *Matn4*^{-/-} mice (m4), while the levels of matrilin-1 and matrilin-3 are unchanged. Abbreviation: MW-molecular weight marker.

2.2. Loss of Matrilins Results in Modulation of Lumbosacral Identity of the Vertebrae

In order to assess the role of matrilins in skeletal development, we have generated quadruple knockout mice lacking all members of the protein family (*Matn1-4*^{-/-}). Homozygous mutant breeding revealed normal litter size with offspring, which had normal life span and developed no apparent gross abnormalities. However, we have noticed by regular inspection of the cages, that *Matn1-4*^{-/-} mice showed reduced fear and anxiety when they were picked up by the tail and, in general, were physically less active and motile in the cage compared with control mice. In this study, we have focused on the skeletal analysis of the mice, therefore, the behavioural abnormalities were not investigated further. Alcian blue and alizarin red double whole-mount skeletal staining of mutant

and wild-type (control) mice at postnatal day 2 (P2) showed normal formation of the elements of the appendicular skeleton (Figure 2A). Closer inspection of the long bones on skeletal preparations or X-ray micrographs demonstrated very moderate but significantly increased lengths of the tibia, femur, and the humerus at P2 in the *Matn1-4^{-/-}* mice compared with control mice ($p < 0.05$). However, the lengths of these skeletal elements were comparable at the ages of four weeks and four months (Figure 2A,C,E). Similarly, the whole body length (the distance between the nose and the tip of the tail) was comparable between wild-type and *Matn1-4^{-/-}* animals at four weeks and four months of age (Figure 2F).

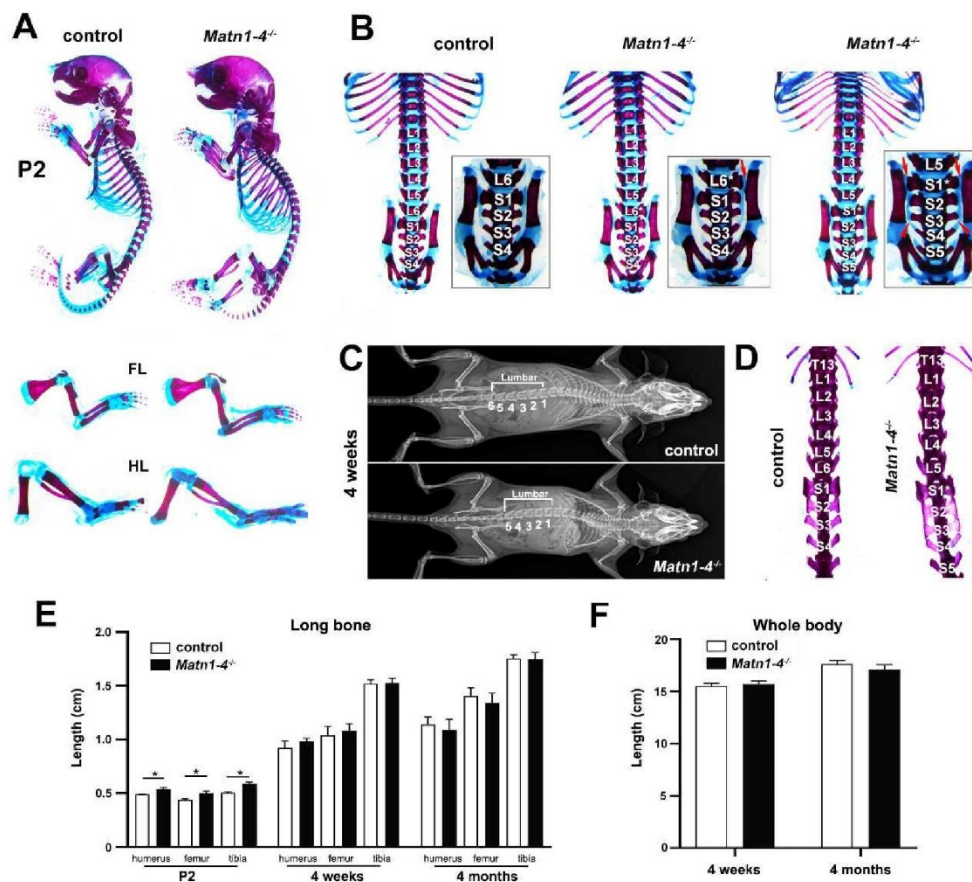


Figure 2. Skeletal phenotype in mice lacking all matrilins. (A) Skeletal staining at P2 showed normal formation of the elements of the appendicular skeleton. (B–D) Skeletal staining and X-ray analyses at P2 and 4 weeks of age revealed a highly penetrant homeotic transformation at the lumbar-sacral border of the axial skeleton. (B) Wild-type (control) mice have 6 lumbar (L1 to L6) and 4 sacral (S1 to S4) vertebrae, S1 articulates to the ilium and S1-S2-S3 are fused. In *Matn1-4^{-/-}* mice, L6 is sacralized (S1*) resulting in 5 lumbar (L1 to L5) and 5 sacral vertebrae (S1 to S5). In the mutants, the sacralized L6 vertebra (S1*) gained the typical S1 wing shape (red arrows on B), S1* and S2 are articulate to the ilium and S1*/S2/S3/S4 are fused. The arrowheads depict the fusion between S3 and S4. The heterozygous offspring exhibit an intermediate pattern with only one side of L6 is sacralized (L6*) by gaining a wing-shaped transverse process and articulating to the ileum (L6*, red arrow), while the other side retained the lumbar identity. (C) Representative X-ray images of wild-type and *Matn1-4^{-/-}* mice at 4 weeks. (D) Skeletal preparations at 4 weeks demonstrate the sacralization of L6 in the quadruple KO mice. (E) Measurements of the lengths of the appendicular skeletal elements indicate a moderate but significantly increased size of mutant long bones at P2. At 4 weeks and 4 months, there is no significant difference between the genotypes. Statistical significance calculated by Mann-

Whitney *U* test where * $p < 0.05$. (F) Comparable body length of wild-type and *Matn1-4^{-/-}* animals at 4 weeks and 4 months of age. Abbreviations: FL-forelimb; HL-hindlimb.

In contrast to the appendicular skeleton, skeletal staining and X-ray analyses revealed a highly penetrant homeotic transformation at the lumbar-sacral border of the axial skeleton (Figure 2B–D). The mouse axial skeleton typically consists of 30 pre-caudal vertebrae including 7 cervical (C), 13 thoracic (T), 6 lumbar (L) and 4 sacral (S) ones giving the formulation of C7/T13/L6/S4 [39,40]. We found that 87.5% of *Matn1-4^{-/-}* mice have five lumbar and five sacral vertebrae (C7/T13/L5/S5), while only 6.7% of wild-type animals presented this vertebral pattern (Figure 2B,C and Table 1). Apparently, the missing L6 vertebrae in the *Matn1-4^{-/-}* mice gained a sacral identity (S1* in Figure 2B,D) resulting a sacral pattern of S1*/S2/S3/S4/S5. In control, S1 articulates to the ilium, S1/S2 acquire wing-shaped transverse processes and S1/S2/S3 are fused. In the mutants, the sacralized L6 vertebra (S1*) and the true S1 (now S2) articulate to the ileum (red arrows on Figure 2B), S1*/S2/S3 have wing-shaped transverse processes and S1*/S2/S3/S4 are fused. Interestingly, when a *Matn1-4^{-/-}* male was crossed with a C57/BL6 female, the heterozygous offspring exhibited either the normal L6/S4 pattern (three out of seven mice), the homeotic transformed L5/S5 pattern (two out of seven) or an intermediate, asymmetric L6*/S4 pattern (two out of seven mice). In the latter case, only one side of L6 is sacralized (L6*) by gaining a wing-shaped transverse process and articulating to the ileum (Figure 2B, *Matn1-4^{-/-}*, L6*, arrows), while the other side retained the lumbar identity.

Table 1. Axial skeletal phenotypes in the respective genotypes.

Lumbosacral Pattern	Control	<i>Matn1-4^{+/-}</i>	<i>Matn1-4^{-/-}</i>
	(n = 45)	(n = 7)	(n = 40)
L6/S4	42 (93.3%)	3 (42.8%)	6 (12.5%)
L6*/S4	0	2 (28.6%)	0
L5/S5	3 (6.7%)	2 (28.6%)	34 (87.5%)

2.3. Lack of Matrilins Has No Adverse Effect on Structural and Functional Properties of the Cartilaginous Growth Plate in Long Bones

Next, we examined long bone development by histological tools at various developmental stages. Hematoxylin and eosin (HE) staining of the hindlimb at embryonic day 15 (E15) demonstrated that the length of the whole tibia and percentage of the hypertrophic zone relative to the entire cartilaginous mass were similar in *Matn1-4^{-/-}* and control animals (Figure 3A,B). At E18, the proximal tibia exhibited comparable columnar organization of the growth plate (Figure 3C) and similar length of the proliferative and hypertrophic zones in control and *Matn1-4^{-/-}* mice (Figure 3D). Similarly, the mineralization of the primary ossification center, judged by Safranin orange-von Kossa staining (Figure 3E), and the resorption at the chondro-osseous junction, visualized by tartrate resistant acid phosphatase (TRAP) activity staining (Figure 3F), were indistinguishable between control and quadruple mutant animals. At postnatal stage two weeks, the columnar organization of the growth plate was normal, and morphometric measurements of the lengths of the resting, proliferative and hypertrophic zones and the total growth plate showed no statistically significant difference between control and *Matn1-4^{-/-}* mice (Figure 3G,H).

Chondrocyte differentiation was investigated in the growth plate of newborn tibia by in situ hybridization. We found no difference in the expression domains of the typical differentiation markers between control and *Matn1-4^{-/-}* mice (Figure 4A). It has been previously suggested that matrilin-3 inhibits chondrocyte hypertrophy by suppressing BMP-2/SMAD-1 signaling [41]. Therefore, we have investigated the activation of SMADs in protein extracts of primary mouse chondrocytes isolated from newborn rib cages using a phospho-specific antibody. Western blotting displayed similar phospho-SMAD-1/5/8 levels between the genotypes (Figure 4B,C), arguing against significantly altered BMP-2 signaling in cartilage lacking matrilins.

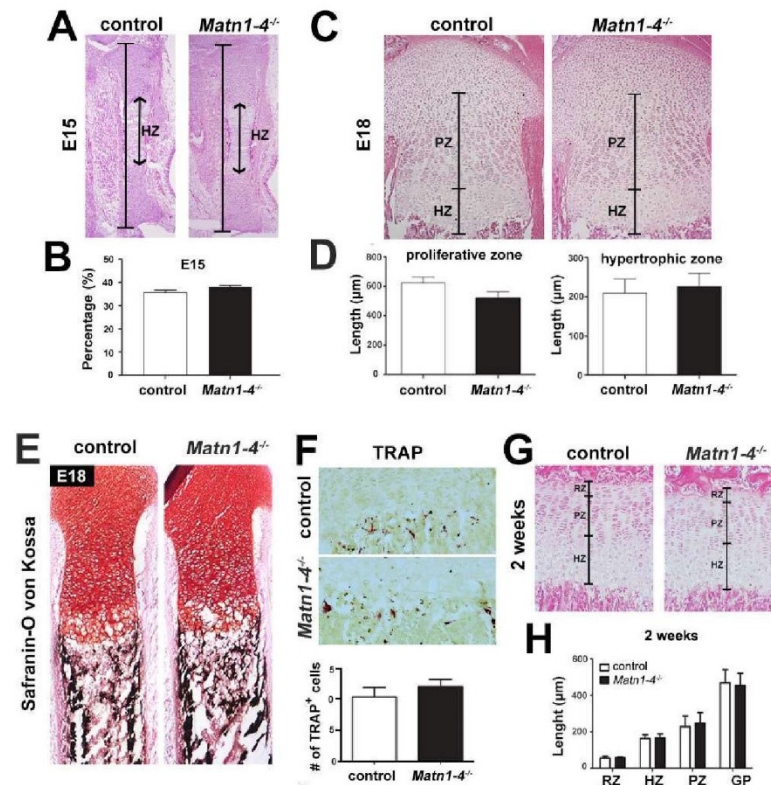


Figure 3. Normal cartilage development and growth plate structure in long bones of *Matn1-4^{-/-}* mice. (A) HE-stained proximal tibiae at E15.5 show normal length, structure and hypertrophic zone (HZ) in *Matn1-4^{-/-}* mice. (B) Percentage of the hypertrophic zone relative to the entire cartilaginous mass of the tibia was similar in *Matn1-4^{-/-}* and in the control animals. (C) HE-stained proximal tibiae at E18 and morphometric measurements of the proliferative (PZ) and hypertrophic (HZ) zones (D) demonstrate normal structure of the growth plate in the *Matn1-4^{-/-}* mice. Safranin O-von Kossa (E) and TRAP staining (F) show comparable mineralization and chondroclast/osteoclast activity at the chondro-osseous junction in control and *Matn1-4^{-/-}* mice. Quantification of the TRAP positive cells in the tibial growth plate of control and *Matn1-4^{-/-}* mice shows no difference at the chondro-osseous junction. (G) HE-staining of the tibial growth plate at 2 weeks and morphometric analysis (H) of the length of the entire growth plate (GP) and the separated growth plate zones (RZ-resting; PL-proliferative; HZ-hypertrophic) indicate normal columnar organization of the chondrocytes and normal GP zonation in *Matn1-4^{-/-}* mice. Original magnifications: $\times 10$ for (A), (C) and (E); $\times 20$ for (F) and (G).

Next, we analyzed the proliferation and survival of the chondrocytes in the tibial growth plate. Proliferation was assessed by bromodeoxyuridine (BrdU) incorporation assays, which revealed a similar proliferation rate in control and *Matn1-4^{-/-}* mice at the newborn stage (Figure 4D,E) or at four and eight weeks of age (data not shown). We further investigated cell death by terminal deoxynucleotidyl transferase dUTP nick end labeling (TUNEL) assay in newborn samples and found comparable numbers of apoptotic chondrocytes at the chondro-osseous junctions in both control and quadruple mutant mice (Figure 4F,G).

Collectively, the data above demonstrate that chondrocyte differentiation, proliferation, and survival occur normally in the growth plate of long bones in mice lacking all matrilins.

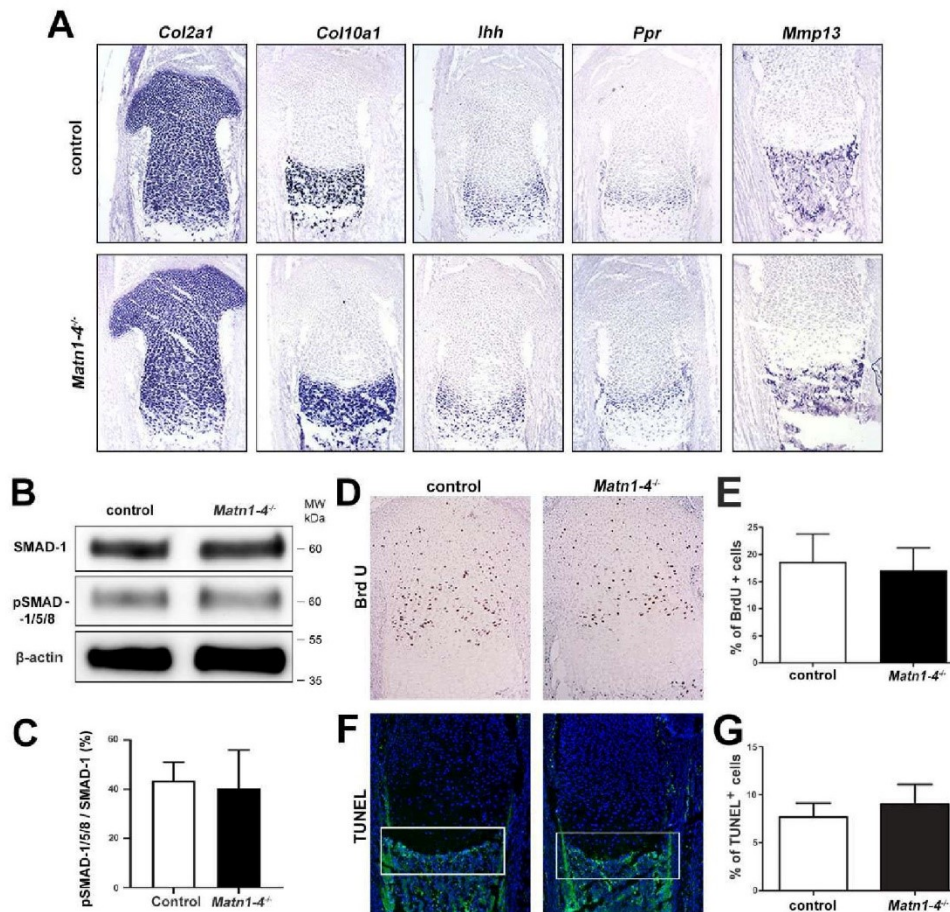


Figure 4. Chondrocyte differentiation, proliferation and apoptosis are not altered in *Matn1-4^{-/-}* mice. (A) Non-radioactive in situ hybridization for collagen II (*Col2a1*), collagen X (*Col10a1*), indian hedgehog (*Ihh*), PTH/PTHrP receptor (*Ppr*) and matrix metalloproteinase-13 (*Mmp13*) show similar expression pattern in newborn control and mutant mice. Western blotting (B) and densitometric quantification (C) indicate normal activation of SMAD-1/5/8 in mutant primary chondrocytes. (D) BrdU incorporation assay and quantification (E) at the newborn stage indicate normal chondrocyte proliferation in the *Matn1-4^{-/-}* growth plate. TUNEL staining (F) and quantification (G) do not reveal any difference in cell death at the chondro-osseous junctions (white boxes) in newborn control and *Matn1-4^{-/-}* mice. Abbreviation: MW-molecular weight marker. Original magnifications: $\times 10$ for (A), (D) and (F).

2.4. Normal Deposition but Altered Extractability of Binding Partners in the Cartilage ECM of Quadruple Knockout Mice

As matrilins are adaptor proteins of the cartilage ECM interacting with aggrecan, COMP, collagen fibrils, and small leucine-rich proteoglycans (e.g., biglycan and decorin) [1], we have investigated the expression and anchorage of some of these binding partners by immunohistochemistry and biochemical analysis. Immunostaining of the proximal tibia in newborn or four-week old limbs indicated no apparent differences in the deposition of collagen II, collagen VI, collagen IX, aggrecan and COMP between control and *Matn1-4^{-/-}* mice (Figure 5A,B). Western blot analysis of sequential extracts of knee cartilage isolated from newborn animals showed slightly increased extractability of collagen II, collagen IX, aggrecan, collagen VI and COMP in fraction I (neutral salt) of *Matn1-4^{-/-}* mice, when compared to wild-type controls. While the amount of matrilin

interacting proteins did not change in fraction II (high salt with 10 mM EDTA), weaker signals for collagen II, collagen IX, and COMP were detected in fraction III (4 M GuHCl) isolated from the cartilage of quadruple knockout mice compared with controls (Figure 5C). At four weeks, the amount of aggrecan increased in all fractions, the amount of collagen IX slightly increased in fraction II, and the amount of COMP moderately decreased in fraction III in *Matn1-4^{-/-}* mice compared to control (Figure 5D).

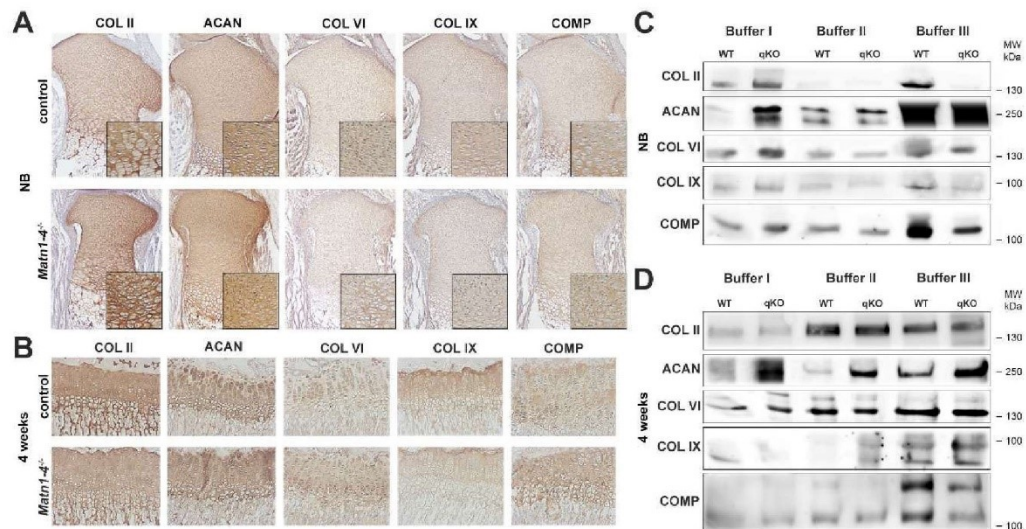


Figure 5. Immunohistochemical and biochemical analysis of the deposition and solubility of the binding partners of matrilins. Immunohistochemistry at newborn (A) and 4 weeks (B) stages indicates no apparent differences in the deposition of collagen II (COL II), collagen VI (COL VI), collagen IX (COL IX), aggrecan (ACAN) and cartilage oligomeric matrix protein (COMP) between control and *Matn1-4^{-/-}* mice. Original magnifications: $\times 10$ for (A) and (B); $\times 20$ for inserts in (A). Western blot analysis of cartilage extracts in newborn (C) and 4 weeks old (D) animals. In newborn, slightly increased extractability of collagen II, collagen IX, aggrecan, collagen VI and COMP in buffer I and significantly weaker signals for collagen II, collagen IX and COMP were detected in fraction III isolated from the cartilage of quadruple knockout mice compared with controls (C). At 4 weeks, the amount of aggrecan is increased in all fractions, the amount of collagen IX is slightly increased in fraction II and the amount of COMP is moderately decreased in fraction III in *Matn1-4^{-/-}* mice compared with the control (D). Abbreviation: MW-molecular weight marker.

To assess the consequence of the lack of matrilins on the ultrastructural and biomechanical properties of the cartilaginous ECM, we applied atomic force microscopy (AFM) (Figure 6). We investigated the proliferative zone of the growth plate at two weeks of age on non-fixed, native sections and recorded high resolution images of the interterritorial matrix (ITM) representing the intercolumnar areas. Topographical images revealed an elaborated network of collagen fibrils in both control and *Matn1-4^{-/-}* mice (Figure 6A). Quantification of the diameter of heterotypic collagen fibrils revealed a significantly increased thickness of the fibers (Figure 6B), similar to the results reported earlier in *Matn1^{-/-}/Matn3^{-/-}* mice [36]. The mean fibril diameter was 45.64 ± 7.29 nm in control and 61.50 ± 12.38 nm in *Matn1-4^{-/-}* mice ($p < 0.001$). Interestingly, nanoindentation measurements indicated comparable compressive stiffness of the ITM. The frequency of the elastic moduli showed a bimodal distribution with a first peak (representing the proteoglycan moiety) at 45.17 ± 0.93 kPa in controls and at 47.91 ± 0.34 kPa in quadruple mutants, and with a second peak (representing the collagen fibrils) at 61.46 ± 7.79 kPa in controls and 59.48 ± 2.14 kPa in *Matn1-4^{-/-}* mice (Figure 6C).

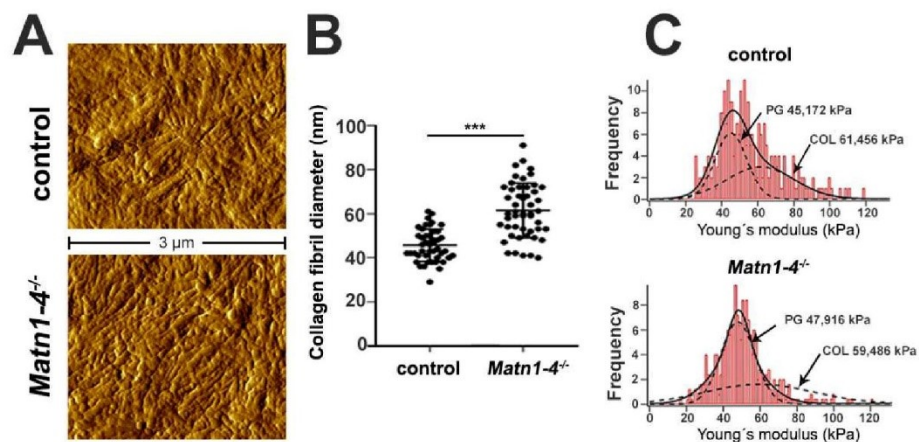


Figure 6. Normal growth plate cartilage stiffness but altered fibril diameter in *Matn1-4^{-/-}* mice. (A) At 2 weeks of age, high-resolution AFM images on tibial sections show comparable organization of the collagenous networks in the interterritorial matrix in control and the mutant animals. (B) Quantification of the fibrillar diameter demonstrates significant thickening of the collagen fibrils in the *Matn1-4^{-/-}* mice (***) ($p < 0.001$). (C) Histograms depicting a comparable, bimodal stiffness distribution between the genotypes determined by nano-scale AFM indentation. On each histogram, the solid line represents the sum of two Gaussian functions, whereas the dashed lines indicate individual fits representing proteoglycans (first peak, PG) and the collagen fibrils (second peak, COL).

Taken together, although the expression and distribution of the analyzed matrilin binding partners were not obviously altered in the growth plate cartilage of *Matn1-4^{-/-}* mice, the solubility of these proteins in the ECM is moderately affected by the loss of all matrilins. Despite this mild biochemical phenotype and the increased diameter of collagen fibrils, the biomechanical behavior of the cartilage ECM, characterized by the compressive stiffness, is apparently not affected in the growth plate of adolescent *Matn1-4^{-/-}* mice.

2.5. Depletion of All Matrilins in the Articular Cartilage Leads to Severe Spontaneous Osteoarthritis in Mice

Next, we analyzed the consequence of the ablation of matrilin genes on age-associated changes of the articular cartilage. All matrilins are expressed in low amounts in peripheral articular cartilage areas of the knee joint in wild-type mice at one year of age (Figure 7A) [13]. We examined articular cartilage degeneration on HE-stained sections of control and *Matn1-4^{-/-}* knee joints at six, 12, and 18 months of age. We found no difference in articular cartilage degradation between the genotypes at six months of age (data not shown), however, histological signs of articular cartilage damage were observed in *Matn1-4^{-/-}* mice at 12 and 18 months of age (Figure 7B). Applying a scoring system for articular cartilage degradation, ranging from normal appearance (score 0) to exposure of the subchondral bone (score 5) [36], the mean histological score was 1.4 for control ($n = 8$) and 2.5 for *Matn1-4^{-/-}* mice ($n = 10$) at 12 months of age. At 18 months of age, the mean histology score was 1.3 for control ($n = 8$) and 2.7 for mutant mice ($n = 11$) ($p < 0.05$) (Figure 7C). These results demonstrate that the lack of the complete matrilin family in cartilage leads to an osteoarthritic-like phenotype in aging mice from one year on, and strongly suggest that matrilins are protective for spontaneous osteoarthritis.

Analyzing the expression of matrilins in healthy and osteoarthritic human knee cartilage by immunohistochemical staining further supported the participation of matrilins in OA progression (Figure 7D). In normal human articular cartilage, matrilins are weakly expressed in the middle and deep zones: MATN1 is localized to the nucleus; MATN2 and MATN4 are associated with the cytoplasm and diffusely with the ECM; while MATN3 displays mainly pericellular/territorial matrix deposition. All matrilins are upregulated in human OA cartilage samples with severe articular

cartilage degeneration (Figure 7D), which may implicate an attempt of repair by enhancing the expression of matrilin family members in the diseased ECM.

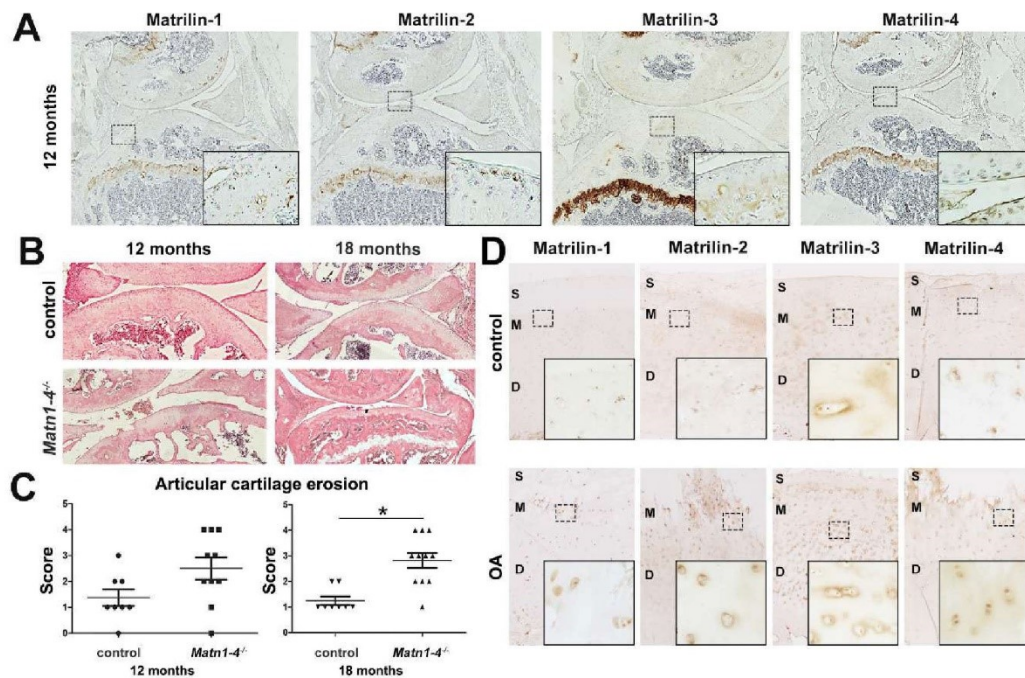


Figure 7. *Matn1-4^{+/-}* mice develop age-associated osteoarthritis. (A) Immunohistochemistry of knee joints demonstrates the moderate expression of matrilins in the articular cartilage of wild-type mice at 12 months of age. All matrilins have strong expression in the growth plate cartilage. Original magnifications: $\times 5$ for overview pictures and $\times 20$ for inserts. (B) HE staining of the knee joint at 12 and 18 months old control and *Matn1-4^{+/-}* mice. Original magnification $\times 10$. (C) Histological grading for cartilage degradation indicates higher incidence and severity of osteoarthritic-like erosion in *Matn1-4^{+/-}* mice compared to age-matched controls (* $p < 0.05$). (D) Analyzing the expression of matrilins in healthy (control) and osteoarthritic human knee articular cartilage derived from the tibia by immunohistochemistry demonstrates upregulation of all matrilins in the OA tissue. The depicted zones: S-superficial; M-middle and D-deep. Original magnifications: $\times 5$ for overview pictures and $\times 20$ for inserts.

The increased severity of spontaneous osteoarthritis in the *Matn1-4^{+/-}* mice might be a consequence of the compromised biomechanical properties of the articular cartilage ECM. Therefore, we have investigated the topography and stiffness of the different articular cartilage zones by AFM on native tissue sections in quadruple mutant and control animals. High-resolution images at four months depicted the well-formed, striated collagen fibrillar network in both genotypes (Figure 8A). Quantification of the collagen fibril diameters revealed fibril thickening in the *Matn1-4^{+/-}* mice (Figure 8B) supporting the findings observed in the growth plate collagen fibrils. In the middle zone, the mean fibrillar diameter was 81.07 ± 17.23 nm in control and 95.31 ± 16.76 nm in *Matn1-4^{+/-}* mice ($p < 0.01$). In the deep zone, the mean fibrillar diameter was 75.52 ± 14.88 nm in control and 93.22 ± 14.71 nm in *Matn1-4^{+/-}* mice ($p < 0.001$). AFM nanoindentation in the superficial, middle and deep zones of the articular cartilage showed bimodal stiffness distribution for proteoglycans and collagen fibrils. At four months of age, we observed a stiffer superficial zone in the mutant compared with wild type, while the elastic moduli in the middle and deep zone were not changed significantly (Figure 8C). At 12 months, in contrast, both peaks of the elastic moduli indicated softer superficial and middle zones

in the quadruple knockout mice compared to control (Figure 8D). Interestingly however, the deep zone was stiffer in the mutant articular cartilage than in the control (Figure 8D).

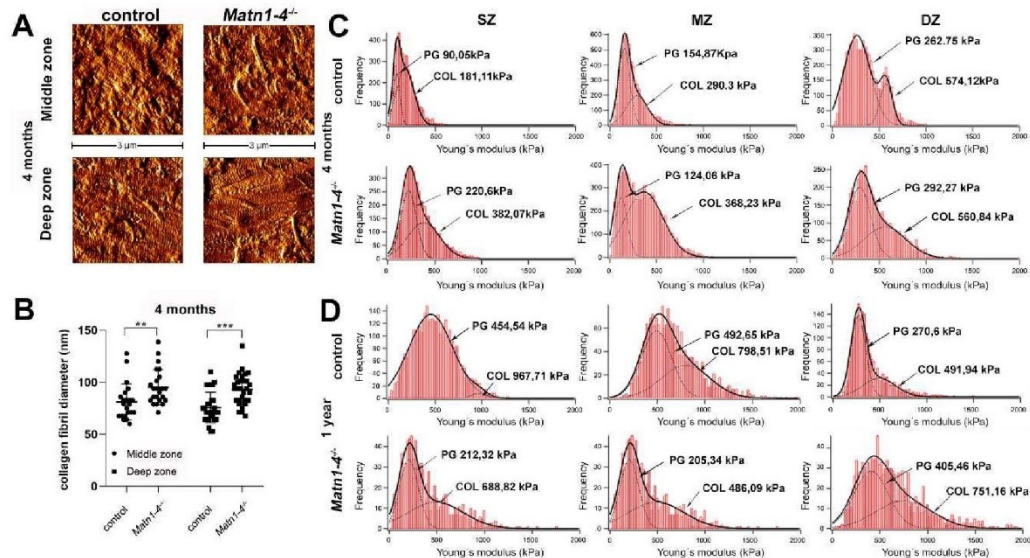


Figure 8. Altered biomechanical properties of articular cartilage in *Matn1-4^{-/-}* mice. High resolution AFM images of articular cartilage at 4 months (A) showed comparable organization of the collagenous networks in control and mutant. (B) Significant thickening of the collagen fibrils was detected in the middle (** $p < 0.01$) and the deep zones (***) $p < 0.001$) of the articular cartilage of *Matn1-4^{-/-}* mice. (C) Nanoindentation AFM demonstrated stiffer mutant matrix in the superficial zone (SZ) at four months. (D) At 1 year, softer ECM was detected in the superficial and middle (MZ) zones, whereas a stiffer matrix was observed in the deep zone (DZ) of the *Matn1-4^{-/-}* mice. On each histogram, the solid line represents the sum of two Gaussian functions, whereas the dashed lines indicate individual fits representing proteoglycans (first peak, PG) and the collagen fibrils (second peak, COL).

To investigate whether matrilins may play a role in inflammation-mediated articular cartilage degradation, we performed an *ex vivo* explant culture experiment in which femoral heads were subjected or not to the influence of the pro-inflammatory cytokine interleukin-1 alpha (IL-1 α). After four days in culture, the explants were investigated for proteoglycan loss by Safranin O staining on histological sections and for sulfated glycosaminoglycan (GAG) release into the medium (Figure 9A,B). Both the histochemical staining and the GAG-release assay indicated no difference in IL-1 α –induced proteoglycan loss between the genotypes.

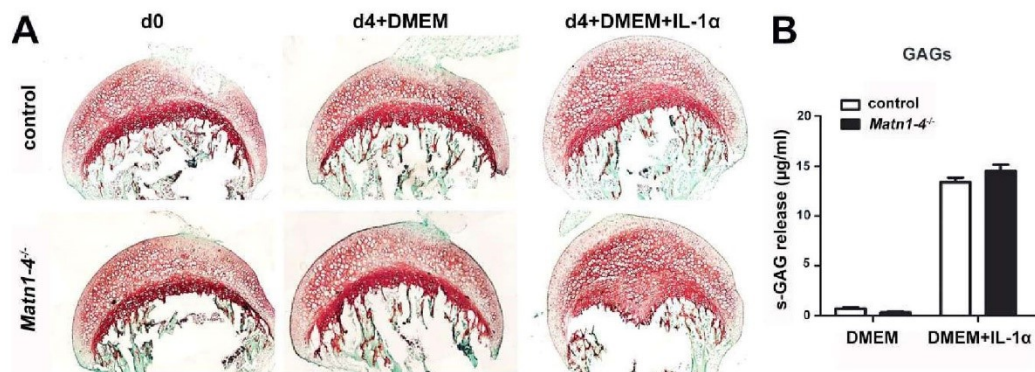


Figure 9. Matrilins are not involved in the interleukin-1-mediated proteoglycan loss of the articular cartilage. (A) Safranin-O and Fast Green staining of hip explants after culturing for 4 days (d4) with

or without 10 ng/mL IL-1 α . Note the similar loss of proteoglycans at the articular cartilage surface after IL-1 α stimulation in control and *Matn1-4^{-/-}* mice. (B) Quantification of the sulfated GAG release into the medium shows no difference after IL-1 α stimulation between the genotypes.

2.6. MATN4 Deficiency Also Enhances Age-Associated Articular Cartilage Degradation

The development of spontaneous osteoarthritis in aged *Matn1-4^{-/-}* mice raised the question about the contribution of the individual matrilins to the phenotype. Previously, we had not observed age-associated osteoarthritis in single MATN1, MATN2, MATN3, or double MATN1/MATN3 deficient mice [12,31,32,36]. However, the MATN4 knockout mice (*Matn4^{-/-}*) have not been yet analyzed for articular cartilage degeneration. Thus, we investigated the pathology of the knee joint in 18–24 month old *Matn4^{-/-}* mice on HE-stained histological sections (Figure 10). *Matn4^{-/-}* animals, similar to the *Matn1-4^{-/-}* mice, exhibited severe osteoarthritis-like phenotype at the age of 24 months often leading to complete erosion of the articular cartilage and exposure of the subchondral bone (Figure 10A). We found that the mean articular cartilage degeneration score was 1.70 in wild-type mice and was 3.67 in the *Matn4^{-/-}* mice ($p < 0.001$) (Figure 10B), implying that MATN4 may protect against osteoarthritis. Interestingly, immunohistochemistry demonstrated that the deposition of MATN2 and MATN3, but not the expression of MATN1, is upregulated in the articular cartilage of the knee joint of aged mice (Figure 10C).

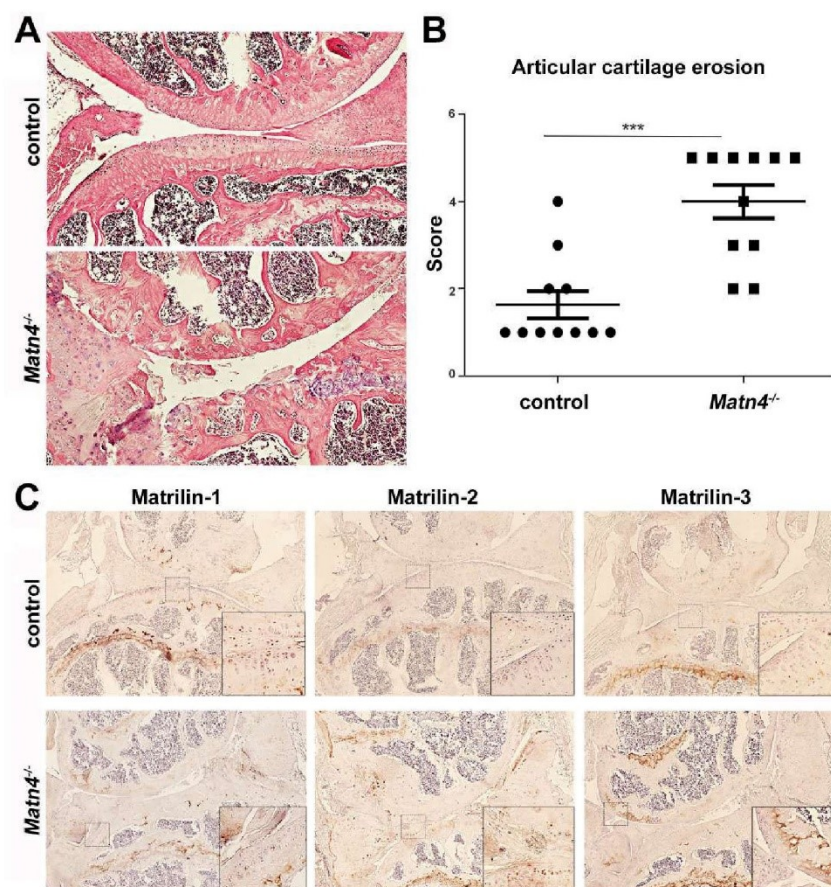


Figure 10. The lack of matrilin-4 leads to age-associated, spontaneous osteoarthritis of the knee joint. (A) HE-stained *Matn4^{-/-}* knee joint (original magnification $\times 10$) at 24 months of age exhibited severe osteoarthritis-like phenotype and (B) a significantly higher articular cartilage degeneration score compared to wild type (** $p < 0.001$). (C) Immunohistochemistry demonstrates upregulated

expression of MATN2 and MATN3 in MATN4-deficient articular cartilage. Original magnifications: × 10 for overview pictures and × 20 for inserts.

3. Discussion

Cartilage extracellular matrix consists of macromolecular suprastructures containing the aggregates of aggrecan and hyaluronan, which are embedded into the network of collagen types II/IX/XI fibrils [42,43]. In order to fulfil biological and biomechanical functions, these macromolecular assemblies are interconnected and stabilized by various adaptor proteins including the FACIT (fibril associated collagen with interrupted triple helices) collagen type IX, family members of thrombospondins (e.g., COMP or thrombospondin-5), small leucine-rich repeat proteoglycans (e.g., decorin and biglycan) and matrilins [8,10,11]. Matrilins are von Willebrand factor A domain containing multi-subunit adaptors with prominent expression in the skeleton, especially in the cartilage [1,13]. All matrilins (MATN1, MATN2, MATN3 and MATN4) are expressed in the growth plate and the articular surface suggesting important roles for both developing, transient and permanent cartilages [1,13]. Despite the anticipated importance of matrilins in the cartilaginous skeleton, no or relatively mild cartilage abnormalities have been reported in knockout mice carrying single or double deletions for matrilin genes, suggesting functional redundancy among the family members [12,32,33,36]. In this study, we have generated and analyzed further single and compound matrilin-deficient mouse lines. We found evidence for biochemical compensation within the matrilin family, which showed that matrilins are important for patterning of the vertebral column and they, especially MATN-4, protect articular cartilage against spontaneous, age-associated osteoarthritis.

Sequential extraction of cartilage tissue is a well-established biochemical tool to assess the protein expression and ECM anchorage of matrilins, and to test their possible compensatory regulations [44]. MATN1 and MATN3 are largely insoluble and require strongly denaturing agent, like 4M GuHCl (buffer III), to be extracted from the tissue, while MATN2 and MATN4 can be partially extracted by milder buffers (e.g., high salt/EDTA, buffer II) [36,44]. We have previously shown by immunoblotting [36] and reproduced in this study (Figure 1C) that MATN4 is upregulated in buffers II and III in mouse strains lacking the matrilin-1 protein (*Matn1^{-/-}* and *Matn1^{-/-}/Matn3^{-/-}*). We found even higher level of MATN4 upregulation when MATN2 was additionally missing in the cartilage of *Matn2^{-/-}/Matn3^{-/-}* and *Matn1-3^{-/-}* mice (Figure 1C). Numerous non-skeletal tissues co-express MATN2 and MATN4, including the brain, the eye, and the lung. Interestingly, in a previous study, we could not observe a similar upregulation of MATN4 protein in extracts of those tissues in *Matn2^{-/-}* mice [12]. However, an increased level of *Matn4* mRNA was reported in damaged sciatic nerves of *Matn2^{-/-}* mice compared with control [38]. As we did not find enhanced *Matn4* mRNA expression in cartilage of *Matn1^{-/-}*, *Matn3^{-/-}*, *Matn1^{-/-}/Matn3^{-/-}* [36] and *Matn1-3^{-/-}* mice (data not shown), our data implicate that MATN4 may exhibit compensatory upregulation for MATN2 only at protein levels, and specifically in cartilage. Importantly, we showed in this study that only MATN2 is upregulated in cartilage of *Matn4^{-/-}* mice, while the protein levels of MATN1 and MATN3 were unchanged in matrilin-4-deficient mice compared with control (Figure 1E,F). Taken together, accumulated evidence from our previous [36] and current studies demonstrate that MATN2 and MATN4 compensate each other mutually at the protein level in mouse cartilage tissue.

The prominent expression of matrilins in the developing long bones and the chondrodysplasia phenotypes associated with dominant-negative mutations of the human *MATN3* gene suggest a role of matrilins for skeletal growth. We showed previously that mice lacking MATN1, MATN2, MATN3 and MATN1/MATN3 have normal skeleton, probably due to functional redundancy of the family members [12,31,32,36]. The lack of obvious cartilage abnormalities in *Matn4^{-/-}* (Figure 1D) and *Matn1-3^{-/-}* mice (Figure 1A,B) further support this hypothesis, which prompted us to analyze skeletal development and cartilage functions in details in mice lacking all matrilins. Surprisingly, *Matn1-4^{-/-}* mice show normal growth indicated by the comparable body weights and the similar length of the skeletal elements of the appendicular skeleton in adolescent (four weeks) and adult (four months) *Matn1-4^{-/-}* mice and control mice (Figure 2A,C,E,F). However, we observed slightly but significantly increased lengths of the femur, tibia, and humerus in *Matn1-4^{-/-}* mice just shortly after birth (P2),

which could possibly be explained by the differences in the genetic background. All matrilin single and multiple mutants were on C57BL/6 × 129/Sv background and *Matn1-4^{-/-}* mice were kept in homozygous breeding. As control, we used wild-type mice on the same, mixed genetic background. However, we could not ensure the same ratio of the C57BL/6 and the 129/Sv genetic material in control and *Matn1-4^{-/-}* mice. Inbred 129/Sv mice have longer gestation length, smaller litter size, and increased body weight at birth compared to inbred C57BL/6 mice [45], which suggest that even a mild shift towards higher 129/Sv contribution in *Matn1-4^{-/-}* mice compared to wild type could result in an enlarged skeleton perinatally. In accordance with our observation that the lengths of skeletal elements were normal from four weeks of age in *Matn1-4^{-/-}* mice, the two inbred strains display a similar body weight at 16 weeks [46].

Importantly, careful histological assessment of the development of the tibia at various embryonic and postnatal stages did not reveal any abnormalities of chondrocyte differentiation, growth plate structure and function in *Matn1-4^{-/-}* mice (Figures 3 and 4). A previous *in vitro* study by Yang et al. showed that MATN3 binds to and inhibits BMP-2, which in turn suppresses SMAD-1/5 promoter activity, reduces SMAD-1 phosphorylation and inhibits the expression of the hypertrophic chondrocyte marker gene collagen X (*Col10a1*) in cultured chondrocytes [41]. It has been also reported that *Matn3^{-/-}* mice, established in the Chen laboratory, display premature hypertrophic differentiation in the embryonic tibial growth plate at E16.5 and E17.5 [35], but not at the newborn stage, which was associated with increased SMAD1 activation in the proliferative zone of the growth plate at E18.5 [41]. Interestingly, in another study, MATN3 induced the chondrogenesis of murine ATDC5 chondroprogenitor cells by elevating the gene expression of aggrecan (*Acan*) and collagen II (*Col2a1*), but did not alter the expression of *Col10a1* [47]. In contrast, MED or SEMD mutant MATN3 constructs abolished *Acan* and/or *Col2a1* mRNAs expression and upregulated *Col10a1* expression by interfering with TGF- β signaling [47]. Although these studies suggest a role of MATN3 for the modulation of hypertrophic differentiation of chondrocytes, *Matn1-4^{-/-}* mice, however, do not show aberrant chondrogenic differentiation. Histomorphometry at different postnatal stages (Figure 3C,D,G,H) and *in situ* hybridization at P2 (Figure 4A) indicated normal lengths of growth plate zones and the normal expression of chondrocyte differentiation markers, respectively. At E15.5, the ratio of the total tibial length and the length of the hypertrophic core was comparable between wild-type and *Matn1-4^{-/-}* animals indicating that the hypertrophic differentiation rate is not affected by the lack of matrilins during embryonic development of long bones (Figure 3A). Furthermore, the normal proliferation rate of growth plate chondrocytes, the proper and timely formation and mineralization of the chondro-osseous junctions, and the normal columnar structure in *Matn1-4^{-/-}* mice clearly indicate that matrilins are dispensable for growth plate morphogenesis.

Matrilins interact through their VWA domains with other matrix constituents, including collagens (collagen types II, IX), proteoglycans (aggrecan, biglycan, decorin) [6], and COMP [9], and they can form both collagen-dependent and collagen-independent networks [3,48,49]. A growing body of evidence suggests that the disturbance of these interacting molecular assemblies could affect the integration of ECM molecules, collagen fibril formation and cartilage mechanical conditions. Ablation of collagen IX in mice results in abnormal perinatal organization of the growth plate architecture [50,51] associated with reduced integrations of COMP, MATN1, MATN3, and MATN4 into the ECM [8,52–54], softer cartilage matrix [54], and increased collagen fibril diameter [8,51]. COMP deficiency mildly impacts growth plate structure [55] and moderately influences the deposition and fibrillar integration of MATN3, but has no apparent effect on collagen fibrillogenesis [8,51]. While collagen fibrils with larger diameters were also reported in *Matn1^{-/-}* and *Matn1^{-/-}/Matn3^{-/-}* knockout mice [33,36], the solubility of the matrilin interacting partners biglycan, decorin, COMP and collagen II were not altered in the cartilage of *Matn1^{-/-}/Matn3^{-/-}* double deficient mice [36]. In the epiphyseal cartilage of *Matn1-4^{-/-}* knockout mice, we did not observe an obvious difference in the deposition of ECM molecules such as aggrecan, COMP and collagen types II, IX, and VI using immunohistochemistry (Figure 5A,B). However, alterations in their extractability were noticed by Western blotting. At the newborn stage, when the cartilage ECM is less mature, all investigated proteins showed increased solubility in neutral salt (buffer I), while collagens II, IX and

COMP were present in a clearly reduced extractable amount in chaotropic buffer containing GuHCl (buffer III) (Figure 5C). At four weeks, when the cartilage matrix is undergoing a maturation process, the amount of extractable aggrecan was increased in all fractions of the cartilage of *Matn1-4^{-/-}* mice compared with that in the control, whereas the solubility of the other ECM proteins did not change significantly (Figure 5D). These results suggest that matrilins may have a matrix-stabilizing role by supporting the firm anchorage of their interaction partners into the ECM when the cartilage undergoes extensive perinatal growth. Using high-resolution AFM imaging, we found collagen fibrils with increased diameters in the growth plate cartilage of two-week old *Matn1-4^{-/-}* mice (Figure 6B), confirming the established role of MATN1 and/or MATN3 in the control of lateral growth of collagen fibrils [33,36]. Nanoscale AFM indentation, however, demonstrated normal stiffness of the growth plate cartilage in *Matn1-4^{-/-}* mice, which implies that matrilins are dispensable for cartilage biomechanics, at least at this stage of postnatal development.

In humans, chondrodysplasia-causing mutations in COMP, collagen IX, or MATN3 are frequently associated with premature osteoarthritis. Matrilin-3 is present at low levels in the joint articular surface and its deposition is upregulated in cartilage and in the synovial fluid of patients with OA as a consequence of cartilage degradation [56–60]. Studies with recombinant MATN3 and human primary chondrocytes have revealed that MATN3 exhibits a context-dependent anabolic or catabolic function by influencing the expression of pro-inflammatory cytokines, ECM degradation enzymes, and ECM synthesis [59,61–63] through the modulation of protein kinase B (AKT) [59], interleukin-6 [62], and interleukin-1 [63,64] signaling pathways. The neoexpression of MATN1 was also observed in the cartilage of OA or rheumatoid arthritis patients [65,66], and MATN2 was recently observed in total knee arthroplasty and suggested as a biomarker for OA [67]. In contrast to other matrilins, down-regulation of *MATN4* gene expression was reported to be associated with knee OA progression [68]. In the present study, we have performed, for the first time, a comprehensive immunohistochemical study to assess the deposition of matrilins in normal and osteoarthritic human knee articular cartilage (Figure 7D). We observed that matrilins are present at various amounts in the healthy articular cartilage, preferentially in the middle and deep zones. MATN1 shows a very weak, cell-associated staining pattern; MATN3 displays predominantly pericellular expression; MATN2 and MATN4 exhibit moderate cellular staining. In severely damaged OA cartilage, all matrilins are upregulated, indicating that each member of the matrilin family participates in the cellular response for the advanced disease as an attempt to protect the tissue from further degradation.

Indeed, the most striking phenotype of the *Matn1-4^{-/-}* mice was the development of severe osteoarthritis in aged mice (Figure 7B,C). In mice, matrilins are differentially expressed in the developing and mature articular cartilage. MATN2 and MATN4 are present, whereas MATN1 and MATN3 are absent at the superficial zone of the growing epiphysis [12,13,31,69,70]. In adult joints, immunohistochemistry demonstrated a very moderate deposition of matrilins in the articular cartilage [13] (Figure 7A). Interestingly, a lineage tracing experiment, in which the matrilin-1-Cre (*Matn1-Cre*) knock-in mice were crossed with the floxed ROSA26-LacZ reporter mouse line (R26R), demonstrated the lack of beta-galactosidase signal at the joint surface, suggesting that matrilin-1 is not expressed in the mature articular cartilage [70]. The OA phenotype in the *Matn1-4^{-/-}* mice was accompanied by increased collagen fibril diameter (Figure 8A,B), confirming our similar results obtained on the growth plate cartilage, and changes in the nanomechanical properties of the knee joint cartilage. Nano-scale indentation-type AFM recorded the typical bimodal stiffness distribution of the articular cartilage (representing proteoglycans and collagens) [71,72] and showed higher stiffness of both macromolecular assemblies at the superficial zone of the articular cartilage in *Matn1-4^{-/-}* mice compared to control already at 4 months of age before any histological sign of cartilage degeneration (Figure 8C). As the stiffness of the middle and deep zones were in the normal range at this age, it seems that matrilin-deficiency primarily affects ECM biomechanics in the outermost zone where the collagen fibrils are oriented parallel to the surface. Of note, a recent study found increased elastic moduli at the articular cartilage surface in *Matn1^{-/-}* mice [34]. Furthermore, stiffening of the articular cartilage before the onset of OA has been also recently observed in hypomorphic aggrecan mutant mice [71]. When OA is histologically visible in one-year old *Matn1-4^{-/-}* mice, the superficial

and middle zones exhibited a reduced Young's modulus for both proteoglycans and collagens (Figure 8D), probably reflecting the advanced deterioration of the ECM [73]. The increased stiffness in the deep zone may be the consequence of a mechanical adaptation mechanism to the weakened upper zones. Importantly, the lack of matrilins did not influence GAG release in IL-1 α stimulated hip explant culture (Figure 9), therefore reasonable to speculate that matrilins protect against OA through biomechanical stabilization of the articular cartilage ECM.

Based on mouse models, the participation of the individual matrilins in OA is controversial. Spontaneous articular cartilage degradation was observed in 1 year old *Matn3*^{-/-} mice generated by Chen and his colleagues [35], while *Matn3*^{-/-} and *Matn1*^{-/-}/*Matn3*^{-/-} mice established in our laboratory showed no obvious signs of accelerated articular cartilage degradation in aged animals [32,36]. Similarly, no OA-related phenotype was reported in mouse strains carrying a human MATN3 MED mutation in wild-type [74] or in *Matn1* null background [75]. Interestingly, a recent study demonstrated that the microRNA miR-483-5p targeted *Matn3* and *Timp2* (tissue inhibitor of metalloproteinase 2), which in turn accelerated articular cartilage degradation in mice with experimental OA [76]. Age-related, spontaneous OA has not been reported in mice lacking MATN1 [31,33] or MATN2 [12]. However, more severe articular cartilage degeneration was observed after surgical destabilization of the medial meniscus in *Matn1*^{-/-} mice compared to wild-type control [34]. Since the role of MATN4 in OA has not been investigated, we have also evaluated spontaneous articular cartilage degradation in aged *Matn4*^{-/-} mice. MATN4 deficiency had a dramatic effect on the joint by exacerbating OA-like erosion of the articular cartilage at a similar level as we observed in the *Matn1-4*^{-/-} mice (Figure 10). Consistent with the observation in the growth plate, we have also found a prominent upregulation of MATN2 expression in the MATN4 deficient articular cartilage (Figure 10C) which, however, was unable to compensate for the lack of MATN4. These findings indicate for the first time that MATN4 is essential to maintain the integrity of the articular cartilage and protect the joints against age-associated osteoarthritis.

The most surprising phenotype what we have observed in the *Matn1-4*^{-/-} mice was the patterning defect of the axial skeleton manifested by the highly penetrant (nearly 90%) transition of the L6 vertebra into a sacral identity (Figure 2B–D and Table 1). Disturbance of the vertebral column specification at the lumbosacral junction was also present in *Matn1-4*^{-/-} mice demonstrated by partial (asymmetric) or complete sacralization of L6 in two-thirds of the investigated animals ($n = 6$). Congenital skeletal anomalies including sacralization of 6th lumbar vertebra (or 26th pre-caudal vertebra) are common in some inbred strains including the strain 129 [77,78]. Depending on environmental factors, the three vertebral types (L6, L6 to S1, asymmetric L6 to S1) occur about the same frequency in this strain [40,77], and the proportion of the normal L6 identity is significantly increased when 129 animals were raised in 129 \times C57BL hybrid females upon ovary transplantation [78]. As we have not observed patterning defects of the vertebral columns in previous single or double knockout matrilin mutant mice [12,31,32,36] maintained on the mixed C57BL/6 \times 129/Sv genetic background, and the *Matn1-4*^{-/-} mice do not display other skeletal abnormalities of the 129 strain (e.g., accessory sternbrae), we are convinced that the phenotype is the consequence of the lack of all matrilins in the axial skeleton. The molecular basis of how matrilins regulate vertebral specification is not clear and warrant further studies. Interestingly, it has been recently shown that mice lacking the nucleus accumbens-associated protein 1 (NAC1) also exhibit the L6 sacralization phenotype accompanied by the reduced mRNA expression of matrilins in *Nacc1*^{-/-} chondrocytes, which is especially significant in case of *Matn3* and *Matn4* [79]. Furthermore, all matrilin family members are expressed in the developing vertebral bodies [12,13], and MATN1 and MATN3 have been implicated in chondrogenic differentiation in vitro [80].

4. Materials and Methods

4.1. Knockout Mice

Outbred mice (C57BL/6 \times 129/Sv) knockout for matrilin-1 (*Matn1*^{-/-}), matrilin-2 (*Matn2*^{-/-}), matrilin-3 (*Matn3*^{-/-}), and matrilin-4 (*Matn4*^{-/-}) were previously generated in our laboratory

[12,31,32,37]. Double knockout mice for matrilin-1 and -3 ($Matn1^{-/-}/Matn3^{-/-}$) [36], matrilin-2 and -3 ($Matn2^{-/-}/Matn3^{-/-}$), triple knockout mice lacking matrilin-1, -2, and -3 ($Matn1-3^{-/-}$), and quadruple knockout mice lacking all matrilins ($Matn1-4^{-/-}$) [37] were generated by intercrossing single and multiple matrilin deficient mice. Wild-type littermates were used as control for single and double knockout mice. Triple and quadruple knockout mice were maintained in homozygous mutant breeding. Age-matched wild-type non-littermates on the same C57BL/6 × 129/Sv background were used as control for the $Matn1-4^{-/-}$ and $Matn1-3^{-/-}$ mice. Mice were kept under 12 h light/dark cycle, constant temperature, in individually ventilated cages in the Central Animal Facility at the Medical Faculty of the Ludwig-Maximilians-University. Mice were housed in groups of 2–5 per cage and received food and water *ad libitum*. The handling and breeding of all mouse strains have been approved by the government of Upper Bavaria (Application number: 55.2-1-54-2532-15-2016).

4.2. Human Samples

Human tibial plateau were obtained from patients undergoing total knee arthroplasty after written consent according to the ethical approval no. 238-15. The whole tissue explant was collected in phosphate buffered saline (PBS) pH 7.4 in the operation room of the Schön Klinik (Munich, Germany) and immediately delivered to our laboratory. Afterwards, cylindrical osteochondral plugs from differently degenerated or non-degenerated areas of the plateau were harvested with the aid of a 7 mm diameter trephine drill, washed once in PBS and fixed in 4% paraformaldehyde (PFA)/PBS overnight at 4 °C. Osteochondral plugs were decalcified in 10% formic acid/dH₂O for 3 days at RT. After that, plugs were thoroughly washed in PBS, immersed in 20% sucrose/PBS for 24 h at 4 °C and embedded in Tissue-Tek cryomedia (Sakura Finetek, Alphen aan den Rijn, The Netherlands) and gradually frozen on a chilled copper plate placed on dry ice. Sagittal sections of 10 µm were cut using a cryotome (HM500 cryostat, Thermo Fischer Scientific, Waltham, MA, USA) and collected on Superfrost Plus glass slides (Thermo Fischer Scientific, Waltham, MA, USA).

4.3. Antibodies

For immunohistochemistry and Western blots, the following primary antibodies were used: Rabbit polyclonal antibodies against matrilin-1, matrilin-2, matrilin-3, matrilin-4, cartilage oligomeric protein (COMP) and collagen VI were described previously [36]. Antibodies against collagen IX were gifts of Susanne Grässel (University of Regensburg, Germany) and Frank Zaucke (Orthopaedic University Hospital Friedrichsheim, Germany). Rabbit polyclonal anti-aggrecan antibody (ab#1031) was obtained from Merck Millipore (Billerica, MA, USA); mouse monoclonal anti-collagen II antibody (CIIC1) was purchased from the Developmental Studies Hybridoma Bank (Iowa, IL, USA); and the rabbit monoclonal antibodies specific for SMAD-1 (D59D7, #6944) and for phospho-SMAD-1/5/8 (D5B10, #13820) were obtained from Cell Signaling Technology (Beverly, MA, USA). Primary antibodies were diluted 1:400 for immunohistochemistry and 1:1000 for immunoblotting.

4.4. Whole-Mount Skeletal Staining and X-ray Analysis

For skeletal staining, 2-day and 4-week old mice were euthanized with carbon dioxide. De-skinned and eviscerated specimens were fixed in 95% ethanol for 3 days and transferred into acetone for additional 2 days. The skeleton was stained with 0.6% Alcian Blue (for cartilage) and 0.02% Alizarin Red (for bone) (both Sigma-Aldrich, St. Louis, MO, USA) in 90% ethanol and 5% acetic acid for 3 days in a 37 °C incubator with continuous shaking. Samples were cleared by incubation in descending potassium hydroxide and ascending glycerol solutions, and were finally preserved in 100% glycerol. To determine the length of the long bones, the humerus, the femur, and the tibia were dissected from five control and five $Matn1-4^{-/-}$ mice, photographed with a Stemi 1000 stereo microscope (Carl Zeiss, Jena, Germany) and measured with the ZEN software (Carl Zeiss, Jena, Germany).

For X-ray analysis, 4-week, 4-month, and 1-year old mice were euthanized, and radiographs were taken using a sealed X-ray cabinet (FAXITRON 43855 A) at 35 kV, 2 mA, and 2 s exposure time.

Total body length (from the snout to the end of the tail) and the length of the skeletal elements (tibia, femur, and humerus) were analyzed with the distance measurement plug-in of the syngo Imaging XS-VA60B software (Siemens, Erlangen, Germany).

4.5. Histology, Immunohistochemistry and In Situ Hybridization

Mouse limbs were dissected from 15.5 and 18 day-old embryos (E15.5 and E18), and from newborn, 2-day (P2), 2-week, 4-week, 2-month, 4-month, 8-month, and 15–24 month old animals. The specimens were routinely fixed in 4% PFA/PBS at 4 °C for 12–24 h. Additionally, forelimbs were fixed in 95% ethanol and 1% acetic acid for immunohistochemical analysis. Samples from 2 weeks of age were decalcified in 15% ethylenediaminetetraacetic acid (EDTA) (Sigma-Aldrich, St. Louis, MO, USA) dissolved in PBS (pH 8.0) for 1–3 weeks. Specimens were processed either for standard paraffin or for cryo embedding. All the embedded tissues were cut into 8- μ m thick sections using a microtome or cryotome. For routine histology, the sections were stained with hematoxylin and eosin (HE), Safranin orange and fast green (SO/FG), and Safranin orange-von Kossa (SO/vK) according to the standard protocols. Morphometric analyses of the growth plate zones were performed as described previously [81]. TRAP (tartrate resistant acid phosphatase) staining to visualize chondroclasts/osteoclasts at the chondro-osseous junction was performed with the leukocyte acid phosphatase kit (Sigma-Aldrich, St. Louis, MO, USA) according to manufacturer instructions. To assess articular cartilage degeneration on HE stained sections, a histological grading score for structural alteration was applied as follow: 0-normal articular cartilage; 1-surface irregularities; 2-cleft to transition zone; 3-cleft to radial zone; 4-cleft extending to calcified zone; 5-exposure of subchondral bone [36].

For immunohistochemistry, paraffin sections were rehydrated in descending ethanol series, rinsed in PBS and treated with bovine testicular hyaluronidase (Sigma-Aldrich, St. Louis, MO, USA) (2 mg/mL in PBS, pH 5.0) for 30 min at 37 °C to facilitate antibody penetration. Primary antibodies were incubated overnight at 4 °C and the subsequent immunohistochemical detection was performed using the corresponding Vectastain ABC Elite kit (Vector Laboratories, Burlingame, CA, USA) and 3,3'-diaminobenzidine (DAB, Sigma-Aldrich, St. Louis, MO, USA) as chromogenic substrate.

For non-radioactive in situ hybridization, deparaffinized sections were rinsed in Tris-buffered saline (TBS) pH 7.5, acetylated with 0.25% acetic anhydride (pH 8.0) for 10 min, rinsed in TBS and dehydrated in ethanol. Sections were hybridized at 70 °C overnight with digoxigenin (DIG)-UTP-labelled antisense riboprobes specific for mouse collagen II (*Col2a1*), collagen X (*Col10a1*), indian hedgehog (*Ihh*), parathyroid hormone/parathyroid hormone-related peptide receptor (*Ppr*) and matrix metalloproteinase-13 (*Mmp-13*) as previously described [32]. After hybridization and subsequent washing in 2 X sodium citrate-chloride buffer (SSC) at 70 °C for 30 min, the sections were blocked with 2% goat serum for 1 h and incubated with a 1:500 diluted alkaline phosphatase-coupled anti-DIG antibody (Roche, Penzberg, Germany) for 2 h. Hybridization signals were detected using the p-nitroblue tetrazolium chloride/5-bromo-4-chloro-3-indolyl phosphate (NBT/BCIP) solution (Roche, Penzberg, Germany) according to the recommendation of the manufacturer. Brightfield microscopy images were acquired with an AxioObserver microscope (Carl Zeiss, Jena, Germany).

4.6. Cell Proliferation and Cell Death Assays

In vivo chondrocyte proliferation was analysed using the 5-bromo-2'-deoxyuridine (BrdU) incorporation assay as described previously [32]. Briefly, mice were injected intraperitoneally (50 μ g/g of body weight) with BrdU solution (10 mg/mL in PBS, pH 7.4). After 2 h, the animals were sacrificed, knee samples were dissected and embedded into paraffin. Deparaffinized sections were treated with 2 M HCl for 30 min, washed in PBS, and incubated with a peroxidase-conjugated antibody against BrdU (Roche, Penzberg, Germany). Detection of proliferative cells in the S phase of the cell cycle was performed with DAB as chromogen substrate. Analysis of apoptotic chondrocytes was carried out using the TUNEL assay according to the manufacturer's instructions (In Situ Cell Death Detection Kit, Roche, Penzberg, Germany).

4.7. Protein Extraction and Western Blotting

Knee joint cartilage was dissected from newborn and 4-week old *Matn1-4^{-/-}* and control mice ($n = 10$). Specimens were weighed, cut into small pieces, and incubated in ten volumes of chilled extraction buffer I (0.15 M NaCl, 50 mM Tris, pH 7.4) overnight at 4 °C with continuous stirring. Next day, the mixture was centrifuged at 14,000 rpm for 1 h and the supernatant was stored at -20 °C, and the obtained pellet was incubated as above in buffer II (1 M NaCl, 10 mM EDTA, 50 mM Tris, pH 7.4) and subsequently in buffer III (4 M guanidine hydrochloride, 10 mM EDTA, 50 mM Tris, pH 7.4). All extraction buffers contained EDTA-free proteinase inhibitor cocktail (Roche, Penzberg, Germany). Aliquots (100 μ L) of all extracts were precipitated with 96% ethanol and the pellets were processed and re-suspended in non-reducing SDS-PAGE (sodium dodecyl sulfate-polyacrylamide gel electrophoresis) sample buffer as described previously [32]. Samples were applied to 4–15% pre-casted SDS-PAGE gels (Bio-Rad, Berkeley, CA, USA) and electrophoresis was performed using a Bio-Rad apparatus. For Western blotting, proteins were transferred to a PVDF membrane (GE Healthcare, Chicago, USA) and incubated with primary antibodies diluted either in 5% skim milk (Sigma-Aldrich, St. Louis, MO, USA) or 5% bovine serum albumin (BSA) (Sigma-Aldrich, St. Louis, MO, USA) in 1X TBST (0.5% Tween 20 in TBS). Bound antibodies were detected by HRP-conjugated secondary antibodies, and the signal was developed using Luminata ECL Forte (Merck Millipore) and acquired on the GE Healthcare imaging system ImageQuant LAS 4000.

Primary chondrocytes were isolated from newborn ribcage as described [71]. Single cell suspensions were lysed in RIPA buffer with phosphatase (PhosSTOP, Roche, Penzberg, Germany) and protease inhibitors. Total protein was normalized using the BCA assay (Thermo Scientific, Waltham, MA, USA) and equal amounts of protein were subjected to 10% SDS-PAGE, transferred to PVDF membrane and imaged as above.

4.8. Explant Culture

Femoral heads were dissected from 4-week-old control and *Matn1-4^{-/-}* mice and cultured in serum-free Dulbecco's modified Eagle's medium (DMEM) supplemented with streptomycin-penicillin for 4 days at 37 °C and 5% CO₂ in the absence or presence of the catabolic cytokine IL-1 α (10 ng/mL) (R&D Systems, Minneapolis, MN, USA). After the culture period, femoral heads were fixed in 4% PFA, cryo-embedded, cut, and stained with SO to examine the loss of proteoglycans. Conditioned culture medium was also collected and analyzed for released sulfated glycosaminoglycan (sGAG) using the Blyscan B1000 GAG assay (Biocolor Ltd., Carrickfergus, UK) according to the instructions of the manufacturers.

4.9. Atomic Force Microscopy (AFM)

Knee joints from 2-week, 4-month, and 1-year-old control and *Matn1-4^{-/-}* animals were dissected and immediately immersed into Tissue-Tek and snap frozen in a liquid nitrogen-cooled bath of isopentane. Sagittal sections (30 μ m) of three animals per genotype were cut using two supportive tapes (one double adhesive and an adhesive) and a cryostat, and placed on Super Frost Plus glass slides as previously described [82]. Sections were stored at -20 °C until the analysis. AFM imaging and indentation measurements were carried out on sections equilibrated at room temperature using the NanoWizard 1 AFM (JPK Instruments, Berlin, Germany) in combination with an inverse optical microscope (Axiovert 200, Carl Zeiss, Göttingen, Germany) as previously described [82]. Briefly, for the growth plate measurements the Young's modulus was determined at each indentation position by fitting a modified Hertz model (pyramidal indenter) to the respective approach curve, using the JPK data processing software (versions 4.2.20 and 5.0.96; JPK Instruments). The contact point was determined manually for each force curve, and the fit range was limited to a maximum indentation depth of 500 nm. For the articular cartilage measurements, the contact point was determined by fitting the modified Hertz model to the entire force range first and then using this fix contact point to fit only the first 500 nm indentation depth. To generate histograms and fitting Gaussian distributions, the data analysis software Origin 8.0 (OriginLab Corporation, Northampton, MA, USA) and Igor Pro

6.37 (Wavematrix, London, UK) were used for growth plate and articular cartilage data, respectively. AFM imaging of the middle and deep zone of the articular cartilage was performed on 20 µm thick, PFA-fixed sections.

4.10. Statistical Analysis

Data are presented as mean ± SD (standard deviation). Statistical significance was assessed using the Mann-Whitney *U* test, *p* values less than 0.05 were considered significant. Histology data are representative of a minimum of six animals for each group.

5. Conclusions

In summary, our data imply that the matrilin family of adaptor proteins is dispensable for the growth of the cartilaginous skeleton, but required for vertebral column specification and articular cartilage stability. Biochemical analyses of cartilages from various matrilin-deficient mouse lines showed compensation among the family members, and indicated that the lack of all four matrilins moderately changes the extractability of binding partners. Atomic force microscopy revealed that matrilins control collagen fibril diameters in the cartilage ECM and modulate the stiffness of the articular cartilage. *Matn1*^{-/-} and *Matn4*^{-/-} mice develop similar age-associated osteoarthritis suggesting a novel function of matrilin-4 for preventing articular cartilage degradation in the murine knee joint.

Author Contributions: All authors have read and agree to the published version of the manuscript. Study conception and design: P.L., P.A., H.C.-S. and A.A.; methodology and investigation, P.L., C.N., L.F., C.P., Z.F. and J.H.; formal analysis, M.M.S.; resources, W.C.P.; writing—original draft preparation, P.L., P.A. and A.A.; writing—review and editing, L.F., C.N., M.M.S., W.C.P., A.N., H.C.-S. and R.W.; supervision, H.C.-S., R.W., A.N., P.A. and A.A.; project administration, H.C.-S., R.W., A.N. and A.A. All authors have read and agreed to the published version of the manuscript.

Funding: This study was supported by the German Research Council to R.W. (FOR 2722-B1) and to A.A. (AS 150/1-1 and AS 150/1-2).

Conflicts of Interest: The authors declare no conflict of interest.

Abbreviations

ACAN	Aggrecan
AFM	Atomic force microscopy
BMP-2	Bone morphogenetic protein-2
BrdU	Bromodeoxyuridine
COL	Collagen
COMP	Cartilage oligomeric matrix protein
ECM	Extracellular matrix
EDTA	Ethylenediaminetetracetic acid
GAG	Glycosaminoglycan
HE	Hematoxylin and eosin
IL-1	Interleukin-1
ITM	Interterritorial matrix
MATN	Matrilin
MED	Multiple epiphyseal dysplasia
OA	Osteoarthritis
PBS	Phosphate buffered saline
PFA	Paraformaldehyde
P2	Postnatal day 2
SDS-PAGE	Sodium dodecyl sulfate-polyacrylamide gel electrophoresis
SEMD	Spondylo-meta-epiphyseal dysplasia
TRAP	Tartrate-resistant acid phosphatase

TUNEL Terminal deoxynucleotidyl transferase dUTP nick end labeling

References

1. Klatt, A.R.; Becker, A.K.; Neacsu, C.D.; Paulsson, M.; Wagener, R. The matrilins: Modulators of extracellular matrix assembly. *Int. J. Biochem. Cell. Biol.* **2011**, *43*, 320–330.
2. Aszodi, A.; Hauser, N.; Studer, D.; Paulsson, M.; Hiripi, L.; Bosze, Z. Cloning, sequencing and expression analysis of mouse cartilage matrix protein cDNA. *Eur. J. Biochem.* **1996**, *236*, 970–977.
3. Klatt, A.R.; Nitsche, D.P.; Kobbe, B.; Morgelin, M.; Paulsson, M.; Wagener, R. Molecular structure and tissue distribution of matrilin-3, a filament-forming extracellular matrix protein expressed during skeletal development. *J. Biol. Chem.* **2000**, *275*, 3999–4006.
4. Piecha, D.; Muratoglu, S.; Morgelin, M.; Hauser, N.; Studer, D.; Kiss, I.; Paulsson, M.; Deak, F. Matrilin-2, a large, oligomeric matrix protein, is expressed by a great variety of cells and forms fibrillar networks. *J. Biol. Chem.* **1999**, *274*, 13353–13361.
5. Klatt, A.R.; Nitsche, D.P.; Kobbe, B.; Macht, M.; Paulsson, M.; Wagener, R. Molecular structure, processing, and tissue distribution of matrilin-4. *J. Biol. Chem.* **2001**, *276*, 17267–17275.
6. Hauser, N.; Paulsson, M.; Heinegård, D.; Morgelin, M. Interaction of Cartilage Matrix Protein with Aggrecan. Increased covalent cross-linking with tissue maturation. *J. Biol. Chem.* **1996**, *271*, 32247–32252.
7. Winterbottom, N.; Tondravi, M.M.; Harrington, T.L.; Klier, F.G.; Vertel, B.M.; Goetinck, P.F. Cartilage matrix protein is a component of the collagen fibril of cartilage. *Dev. Dyn.* **1992**, *193*, 266–276.
8. Budde, B.; Blumbach, K.; Ylostalo, J.; Zaucke, F.; Ehlen, H.W.; Wagener, R.; Ala-Kokko, L.; Paulsson, M.; Bruckner, P.; Grassel, S. Altered integration of matrilin-3 into cartilage extracellular matrix in the absence of collagen IX. *Mol. Cell. Biol.* **2005**, *25*, 10465–10478.
9. Mann, H.H.; Ozbek, S.; Engel, J.; Paulsson, M.; Wagener, R. Interactions between the cartilage oligomeric matrix protein and matrilins. Implications for matrix assembly and the pathogenesis of chondrodysplasias. *J. Biol. Chem.* **2004**, *279*, 25294–25298.
10. Wiberg, C.; Klatt, A.R.; Wagener, R.; Paulsson, M.; Bateman, J.F.; Heinegard, D.; Morgelin, M. Complexes of matrilin-1 and biglycan or decorin connect collagen VI microfibrils to both collagen II and aggrecan. *J. Biol. Chem.* **2003**, *278*, 37698–37704.
11. Wagener, R.; Ehlen, H.W.; Ko, Y.P.; Kobbe, B.; Mann, H.H.; Sengle, G.; Paulsson, M. The matrilins—Adaptor proteins in the extracellular matrix. *FEBS Lett.* **2005**, *579*, 3323–3329.
12. Mates, L.; Nicolae, C.; Morgelin, M.; Deak, F.; Kiss, I.; Aszodi, A. Mice lacking the extracellular matrix adaptor protein matrilin-2 develop without obvious abnormalities. *Matrix Biol.* **2004**, *23*, 195–204.
13. Klatt, A.R.; Paulsson, M.; Wagener, R. Expression of matrilins during maturation of mouse skeletal tissues. *Matrix Biol.* **2002**, *21*, 289–296.
14. Briggs, M.D.; Chapman, K.L. Pseudoachondroplasia and multiple epiphyseal dysplasia: Mutation review, molecular interactions, and genotype to phenotype correlations. *Hum. Mutat.* **2002**, *19*, 465–478.
15. Chapman, K.L.; Mortier, G.R.; Chapman, K.; Loughlin, J.; Grant, M.E.; Briggs, M.D. Mutations in the region encoding the von Willebrand factor A domain of matrilin-3 are associated with multiple epiphyseal dysplasia. *Nat. Genet.* **2001**, *28*, 393–396.
16. Mabuchi, A.; Haga, N.; Maeda, K.; Nakashima, E.; Manabe, N.; Hiraoka, H.; Kitoh, H.; Kosaki, R.; Nishimura, G.; Ohashi, H.; et al. Novel and recurrent mutations clustered in the von Willebrand factor A domain of MATN3 in multiple epiphyseal dysplasia. *Hum. Mutat.* **2004**, *24*, 439–440.
17. Jackson, G.C.; Barker, F.S.; Jakkula, E.; Czarny-Ratajczak, M.; Makitie, O.; Cole, W.G.; Wright, M.J.; Smithson, S.F.; Suri, M.; Rogala, P.; et al. Missense mutations in the beta strands of the single A-domain of matrilin-3 result in multiple epiphyseal dysplasia. *J. Med. Genet.* **2004**, *41*, 52–59.
18. Otten, C.; Wagener, R.; Paulsson, M.; Zaucke, F. Matrilin-3 mutations that cause chondrodysplasias interfere with protein trafficking while a mutation associated with hand osteoarthritis does not. *J. Med. Genet.* **2005**, *42*, 774–779.
19. Cotterill, S.L.; Jackson, G.C.; Leighton, M.P.; Wagener, R.; Makitie, O.; Cole, W.G.; Briggs, M.D. Multiple epiphyseal dysplasia mutations in MATN3 cause misfolding of the A-domain and prevent secretion of mutant matrilin-3. *Hum. Mutat.* **2005**, *26*, 557–565.
20. Nundlall, S.; Rajpar, M.H.; Bell, P.A.; Clowes, C.; Zeeff, L.A.; Gardner, B.; Thornton, D.J.; Boot-Handford, R.P.; Briggs, M.D. An unfolded protein response is the initial cellular response to the expression of mutant matrilin-3 in a mouse model of multiple epiphyseal dysplasia. *Cell Stress Chaperones* **2010**, *15*, 835–849.

21. Mostert, A.K.; Dijkstra, P.F.; Jansen, B.R.; van Horn, J.R.; de Graaf, B.; Heutink, P.; Lindhout, D. Familial multiple epiphyseal dysplasia due to a matrilin-3 mutation: Further delineation of the phenotype including 40 years follow-up. *Am. J. Med. Genet. A* **2003**, *120*, 490–497.
22. Borochoowitz, Z.U.; Scheffer, D.; Adir, V.; Dagonneau, N.; Munnich, A.; Cormier-Daire, V. Spondylo-epimetaphyseal dysplasia (SEMD) matrilin 3 type: Homozygote matrilin 3 mutation in a novel form of SEMD. *J. Med. Genet.* **2004**, *41*, 366–372.
23. Stefansson, S.E.; Jonsson, H.; Ingvarsson, T.; Manolescu, I.; Jonsson, H.H.; Olafsdottir, G.; Palsdottir, E.; Stefansson, G.; Sveinbjornsdottir, G.; Frigge, M.L.; et al. Genomewide scan for hand osteoarthritis: A novel mutation in matrilin-3. *Am. J. Hum. Genet.* **2003**, *72*, 1448–1459.
24. Min, J.L.; Meulenbelt, I.; Riyazi, N.; Kloppenburg, M.; Houwing-Duistermaat, J.J.; Seymour, A.B.; van Duijn, C.M.; Slagboom, P.E. Association of matrilin-3 polymorphisms with spinal disc degeneration and osteoarthritis of the first carpometacarpal joint of the hand. *Ann. Rheum. Dis.* **2006**, *65*, 1060–1066.
25. Pullig, O.; Tagariello, A.; Schweizer, A.; Swoboda, B.; Schaller, P.; Winterpacht, A. MATN3 (matrilin-3) sequence variation (pT303M) is a risk factor for osteoarthritis of the CMCI joint of the hand, but not for knee osteoarthritis. *Ann. Rheum. Dis.* **2007**, *66*, 279–280.
26. Meulenbelt, I.; Bijkerk, C.; Breedveld, F.C.; Slagboom, P.E. Genetic linkage analysis of 14 candidate gene loci in a family with autosomal dominant osteoarthritis without dysplasia. *J. Med. Genet.* **1997**, *34*, 1024–1027.
27. Loughlin, J.; Dowling, B.; Mustafa, Z.; Smith, A.; Sykes, B.; Chapman, K. Analysis of the association of the matrilin-1 gene (CRTM) with osteoarthritis: Comment on the article by Meulenbelt et al. *Arthritis Rheum.* **2000**, *43*, 1423–1425.
28. Montanaro, L.; Parisini, P.; Greggi, T.; Di Silvestre, M.; Campoccia, D.; Rizzi, S.; Arciola, C.R. Evidence of a linkage between matrilin-1 gene (MATN1) and idiopathic scoliosis. *Scoliosis* **2006**, *1*, 21.
29. Jang, J.Y.; Park, E.K.; Ryoo, H.M.; Shin, H.I.; Kim, T.H.; Jang, J.S.; Park, H.S.; Choi, J.Y.; Kwon, T.G. Polymorphisms in the Matrilin-1 gene and risk of mandibular prognathism in Koreans. *J. Dent. Res.* **2010**, *89*, 1203–1207.
30. Chimusa, E.R.; Beighton, P.; Kumuthini, J.; Ramesar, R.S. Detecting genetic modifiers of spondyloepimetaphyseal dysplasia with joint laxity in the Caucasian Afrikaner community. *Hum. Mol. Genet.* **2019**, *28*, 1053–1063.
31. Aszodi, A.; Bateman, J.F.; Hirsch, E.; Baranyi, M.; Hunziker, E.B.; Hauser, N.; Bosze, Z.; Fassler, R. Normal skeletal development of mice lacking matrilin 1: Redundant function of matrilins in cartilage? *Mol. Cell. Biol.* **1999**, *19*, 7841–7845.
32. Ko, Y.; Kobbe, B.; Nicolae, C.; Miosge, N.; Paulsson, M.; Wagener, R.; Aszodi, A. Matrilin-3 is dispensable for mouse skeletal growth and development. *Mol. Cell. Biol.* **2004**, *24*, 1691–1699.
33. Huang, X.; Birk, D.E.; Goetinck, P.F. Mice lacking matrilin-1 (cartilage matrix protein) have alterations in type II collagen fibrillogenesis and fibril organization. *Dev. Dyn.* **1999**, *216*, 434–441.
34. Chen, Y.; Cossman, J.; Jayasuriya, C.T.; Li, X.; Guan, Y.; Fonseca, V.; Yang, K.; Charbonneau, C.; Yu, H.; Kanbe, K.; et al. Deficient mechanical activation of anabolic transcripts and post-traumatic cartilage degeneration in Matrilin-1 knockout mice. *PLoS ONE* **2016**, *11*, e0156676.
35. van der Weyden, L.; Wei, L.; Luo, J.; Yang, X.; Birk, D.E.; Adams, D.J.; Bradley, A.; Chen, Q. Functional knockout of the matrilin-3 gene causes premature chondrocyte maturation to hypertrophy and increases bone mineral density and osteoarthritis. *Am. J. Pathol.* **2006**, *169*, 515–527.
36. Nicolae, C.; Ko, Y.P.; Miosge, N.; Niehoff, A.; Studer, D.; Enggist, L.; Hunziker, E.B.; Paulsson, M.; Wagener, R.; Aszodi, A. Abnormal collagen fibrils in cartilage of matrilin-1/matrilin-3-deficient mice. *J. Biol. Chem.* **2007**, *282*, 22163–22175.
37. Uckelmann, H.; Blaszkiewicz, S.; Nicolae, C.; Haas, S.; Schnell, A.; Wurzer, S.; Wagener, R.; Aszodi, A.; Essers, M.A. Extracellular matrix protein Matrilin-4 regulates stress-induced HSC proliferation via CXCR4. *J. Exp. Med.* **2016**, *213*, 1961–1971.
38. Malin, D.; Sonnenberg-Riethmacher, E.; Guseva, D.; Wagener, R.; Aszodi, A.; Irintchev, A.; Riethmacher, D. The extracellular-matrix protein matrilin 2 participates in peripheral nerve regeneration. *J. Cell. Sci.* **2009**, *122*, 995–1004.
39. Green, E.L. Genetic and non-genetic factors which influence the type of the skeleton in an inbred strain of mice. *Genetics* **1941**, *26*, 192–222.

40. Mc, L.A.; Michie, D. Factors affecting vertebral variation in mice. 4. Experimental proof of the uterine basis of a maternal effect. *Development* **1958**, *6*, 645–659.
41. Yang, X.; Trehan, S.K.; Guan, Y.; Sun, C.; Moore, D.C.; Jayasuriya, C.T.; Chen, Q. Matrilin-3 inhibits chondrocyte hypertrophy as a bone morphogenetic protein-2 antagonist. *J. Biol. Chem.* **2014**, *289*, 34768–34779.
42. Gentili, C.; Cancedda, R. Cartilage and bone extracellular matrix. *Curr. Pharm. Des.* **2009**, *15*, 1334–1348.
43. Hedlund, H.; Hedbom, E.; Heinegard, D.; Mengarelli-Widholm, S.; Reinholt, F.P.; Svensson, O. Association of the aggrecan keratan sulfate-rich region with collagen in bovine articular cartilage. *J. Biol. Chem.* **1999**, *274*, 5777–5781.
44. Paulsson, M.; Wagener, R. Matrilins. *Methods Cell. Biol.* **2018**, *143*, 429–446.
45. Murray, S.A.; Morgan, J.L.; Kane, C.; Sharma, Y.; Heffner, C.S.; Lake, J.; Donahue, L.R. Mouse gestation length is genetically determined. *PLoS ONE* **2010**, *5*, e12418.
46. Reed, D.R.; Bachmanov, A.A.; Tordoff, M.G. Forty mouse strain survey of body composition. *Physiol. Behav.* **2007**, *91*, 593–600.
47. Jayasuriya, C.T.; Zhou, F.H.; Pei, M.; Wang, Z.; Lemme, N.J.; Haines, P.; Chen, Q. Matrilin-3 chondrodysplasia mutations cause attenuated chondrogenesis, premature hypertrophy and aberrant response to TGF-beta in chondroprogenitor cells. *Int. J. Mol. Sci.* **2014**, *15*, 14555–14573.
48. Chen, Q.; Johnson, D.M.; Haudenschild, D.R.; Tondravi, M.; Goetinck, P. Cartilage matrix protein forms a type II collagen-independent filamentous network: Analysis in primary cell cultures with a retrovirus expression system. *Mol. Biol. Cell* **1995**, *6*, 1743–1753.
49. Chen, Q.; Zhang, Y.; Johnson, D.M.; Goetinck, P.F. Assembly of a novel cartilage matrix protein filamentous network: Molecular basis of differential requirement of von Willebrand factor A domains. *Mol. Biol. Cell* **1999**, *10*, 2149–2162.
50. Dreier, R.; Opolka, A.; Grifka, J.; Bruckner, P.; Grassel, S. Collagen IX-deficiency seriously compromises growth cartilage development in mice. *Matrix Biol.* **2008**, *27*, 319–329.
51. Blumbach, K.; Bastiaansen-Jenniskens, Y.; DeGroot, J.; Paulsson, M.; Van Osch, G.; Zaucke, F. Combined role of type IX collagen and cartilage oligomeric matrix protein in cartilage matrix assembly: Cartilage oligomeric matrix protein counteracts type IX collagen-induced limitation of cartilage collagen fibril growth in mouse chondrocyte cultures. *Arthritis Rheum.* **2009**, *60*, 3676–3685.
52. Blumbach, K.; Niehoff, A.; Paulsson, M.; Zaucke, F. Ablation of collagen IX and COMP disrupts epiphyseal cartilage architecture. *Matrix Biol.* **2008**, *27*, 306–318.
53. Brachvogel, B.; Zaucke, F.; Dave, K.; Norris, E.L.; Stermann, J.; Dayakli, M.; Koch, M.; Gorman, J.J.; Bateman, J.F.; Wilson, R. Comparative proteomic analysis of normal and collagen IX null mouse cartilage reveals altered extracellular matrix composition and novel components of the collagen IX interactome. *J. Biol. Chem.* **2013**, *288*, 13481–13492.
54. Kamper, M.; Hamann, N.; Prein, C.; Clausen-Schaumann, H.; Farkas, Z.; Aszodi, A.; Niehoff, A.; Paulsson, M.; Zaucke, F. Early changes in morphology, bone mineral density and matrix composition of vertebrae lead to disc degeneration in aged collagen IX^{-/-} mice. *Matrix Biol.* **2016**, *49*, 132–143.
55. Posey, K.; Hecht, J. The role of cartilage oligomeric matrix protein (COMP) in skeletal disease. *Curr. Drug Targets* **2008**, *9*, 869–877.
56. Pullig, O.; Weseloh, G.; Klatt, A.; Wagener, R.; Swoboda, B. Matrilin-3 in human articular cartilage: Increased expression in osteoarthritis. *Osteoarthr. Cartil.* **2002**, *10*, 253–263.
57. Firner, S.; Zaucke, F.; Michael, J.; Dargel, J.; Schiwy-Bochat, K.-H.; Heilig, J.; Rothschild, M.A.; Eysel, P.; Brüggemann, G.-P.; Niehoff, A. Extracellular Distribution of Collagen II and Perifibrillar Adapter Proteins in Healthy and Osteoarthritic Human Knee Joint Cartilage. *J. Histochem. Cytochem.* **2017**, *65*, 593–606.
58. Hosseininia, S.; Önnertjörð, P.; Dahlberg, L.E. Targeted proteomics of hip articular cartilage in OA and fracture patients. *J. Orthop. Res.* **2019**, *37*, 131–135.
59. Vincourt, J.B.; Etienne, S.; Grossin, L.; Cottet, J.; Bantsimba-Malanda, C.; Netter, P.; Mainard, D.; Libante, V.; Gillet, P.; Magdalou, J. Matrilin-3 switches from anti- to pro-anabolic upon integration to the extracellular matrix. *Matrix Biol.* **2012**, *31*, 290–298, doi:10.1016/j.matbio.2012.03.004.
60. Vincourt, J.B.; Vignaud, J.M.; Lionneton, F.; Sirveaux, F.; Kawaki, H.; Marchal, S.; Lomazzi, S.; Plenat, F.; Guillemain, F.; Netter, P. Increased expression of matrilin-3 not only in osteoarthritic articular cartilage but also in cartilage-forming tumors, and down-regulation of SOX9 via epidermal growth factor domain 1-dependent signaling. *Arthritis Rheum.* **2008**, *58*, 2798–2808.

61. Klatt, A.R.; Klinger, G.; Paul-Klausch, B.; Kuhn, G.; Renno, J.H.; Wagener, R.; Paulsson, M.; Schmidt, J.; Malchau, G.; Wielckens, K. Matriline-3 activates the expression of osteoarthritis-associated genes in primary human chondrocytes. *FEBS Lett.* **2009**, *583*, 3611–3617.
62. Klatt, A.; Paul-Klausch, B.; Klinger, G.; Hillebrand, U.; Kühn, G.; Kobbe, B.; Renno, J.; Johannis, W.; Paulsson, M.; Wagener, R. The matriline-3 VWA1 domain modulates interleukin-6 release from primary human chondrocytes. *Osteoarthr. Cartil.* **2013**, *21*, 869–873.
63. Jayasuriya, C.T.; Goldring, M.B.; Terek, R.; Chen, Q. Matriline-3 induction of IL-1 receptor antagonist is required for up-regulating collagen II and aggrecan and down-regulating ADAMTS-5 gene expression. *Arthritis Res. Ther.* **2012**, *14*, R197.
64. Yang, H.; Wu, D.; Li, H.; Chen, N.; Shang, Y. Downregulation of microRNA-448 inhibits IL-1 β -induced cartilage degradation in human chondrocytes via upregulation of matriline-3. *Cell. Mol. Biol. Lett.* **2018**, *23*, 7.
65. Okimura, A.; Okada, Y.; Makihira, S.; Pan, H.; Yu, L.; Tanne, K.; Imai, K.; Yamada, H.; Kawamoto, T.; Noshiro, M. Enhancement of cartilage matrix protein synthesis in arthritic cartilage. *Arthritis Rheum.* **1997**, *40*, 1029–1036.
66. Ohno, S.; Murakami, K.; Tanimoto, K.; Sugiyama, H.; Makihira, S.; Shibata, T.; Yoneno, K.; Kato, Y.; Tanne, K. Immunohistochemical study of matriline-1 in arthritic articular cartilage of the mandibular condyle. *J. Oral Pathol. Med.* **2003**, *32*, 237–242.
67. Zhang, S.; Peng, J.; Guo, Y.; Javidiparsijani, S.; Wang, G.; Wang, Y.; Liu, H.; Liu, J.; Luo, J. Matriline-2 is a widely distributed extracellular matrix protein and a potential biomarker in the early stage of osteoarthritis in articular cartilage. *BioMed Res. Int.* **2014**, *2014*:986127.
68. Chou, C.-H.; Lee, M.T.M.; Song, I.-W.; Lu, L.-S.; Shen, H.-C.; Lee, C.-H.; Wu, J.-Y.; Chen, Y.-T.; Kraus, V.B.; Wu, C.-C. Insights into osteoarthritis progression revealed by analyses of both knee tibiofemoral compartments. *Osteoarthr. Cartil.* **2015**, *23*, 571–580.
69. Aszódi, A.; Módis, L.; Páldi, A.; Rencendorj, A.; Kiss, I.; Bösze, Z. The zonal expression of chicken cartilage matrix protein in the developing skeleton of transgenic mice. *Matrix Biol.* **1994**, *14*, 181–190.
70. Hyde, G.; Dover, S.; Aszodi, A.; Wallis, G.A.; Boot-Handford, R.P. Lineage tracing using matriline-1 gene expression reveals that articular chondrocytes exist as the joint interzone forms. *Dev. Biol.* **2007**, *304*, 825–833.
71. Alberton, P.; Dugonitsch, H.C.; Hartmann, B.; Li, P.; Farkas, Z.; Saller, M.M.; Clausen-Schaumann, H.; Aszodi, A. Aggrecan hypomorphism compromises articular cartilage biomechanical properties and is associated with increased incidence of spontaneous osteoarthritis. *Int. J. Mol. Sci.* **2019**, *20*, 1008.
72. Gronau, T.; Krüger, K.; Prein, C.; Aszodi, A.; Gronau, I.; Iozzo, R.V.; Mooren, F.C.; Clausen-Schaumann, H.; Bertrand, J.; Pap, T. Forced exercise-induced osteoarthritis is attenuated in mice lacking the small leucine-rich proteoglycan decorin. *Ann. Rheum. Dis.* **2017**, *76*, 442–449.
73. Mieloch, A.A.; Richter, M.; Trzeciak, T.; Giersig, M.; Rybka, J.D. Osteoarthritis Severely Decreases the Elasticity and Hardness of Knee Joint Cartilage: A Nanoindentation Study. *J. Clin. Med.* **2019**, *8*, 1865.
74. Leighton, M.P.; Nundlall, S.; Starborg, T.; Meadows, R.S.; Suleman, F.; Knowles, L.; Wagener, R.; Thornton, D.J.; Kadler, K.E.; Boot-Handford, R.P. Decreased chondrocyte proliferation and dysregulated apoptosis in the cartilage growth plate are key features of a murine model of epiphyseal dysplasia caused by a *matn3* mutation. *Hum. Mol. Genet.* **2007**, *16*, 1728–1741.
75. Bell, P.A.; Pirog, K.A.; Fresquet, M.; Thornton, D.J.; Boot-Handford, R.P.; Briggs, M.D. Loss of matriline 1 does not exacerbate the skeletal phenotype in a mouse model of multiple epiphyseal dysplasia caused by a *Matn3* V194D mutation. *Arthritis Rheum.* **2012**, *64*, 1529–1539.
76. Wang, H.; Zhang, H.; Sun, Q.; Wang, Y.; Yang, J.; Yang, J.; Zhang, T.; Luo, S.; Wang, L.; Jiang, Y. Intra-articular delivery of antago-miR-483-5p inhibits osteoarthritis by modulating matriline 3 and tissue inhibitor of metalloproteinase 2. *Mol. Ther.* **2017**, *25*, 715–727.
77. Runner, M.N. Inheritance of susceptibility to congenital deformity—Embryonic instability. *J. Natl. Cancer Inst.* **1954**, *15*, 637–649.
78. Russell, W.L. Maternal influence on number of lumbar vertebrae in mice raised from transplanted ovaries. *Genetics* **1948**, *33*, 627.
79. Yap, K.L.; Sysa-Shah, P.; Bolon, B.; Wu, R.-C.; Gao, M.; Herlinger, A.L.; Wang, F.; Faiola, F.; Huso, D.; Gabrielson, K. Loss of NAC1 expression is associated with defective bony patterning in the murine vertebral axis. *PLoS ONE* **2013**, *8*, e69099.

Int. J. Mol. Sci. **2020**, *21*, 666

26 of 26

80. Pei, M.; Luo, J.; Chen, Q. Enhancing and maintaining chondrogenesis of synovial fibroblasts by cartilage extracellular matrix protein matrilins. *Osteoarthr. Cartil.* **2008**, *16*, 1110–1117.
81. Aszodi, A.; Hunziker, E.B.; Brakebusch, C.; Fassler, R. Beta1 integrins regulate chondrocyte rotation, G1 progression, and cytokinesis. *Genes Dev.* **2003**, *17*, 2465–2479.
82. Prein, C.; Warmbold, N.; Farkas, Z.; Schieker, M.; Aszodi, A.; Clausen-Schaumann, H. Structural and mechanical properties of the proliferative zone of the developing murine growth plate cartilage assessed by atomic force microscopy. *Matrix Biol.* **2016**, *50*, 1–15.



© 2020 by the authors. Licensee MDPI, Basel, Switzerland. This article is an open access article distributed under the terms and conditions of the Creative Commons Attribution (CC BY) license (<http://creativecommons.org/licenses/by/4.0/>).

7. Paper III

Osteoarthritis and Cartilage 29 (2021) 78–88

Osteoarthritis
and Cartilage

The Matrilin-3 T298M mutation predisposes for post-traumatic osteoarthritis in a knock-in mouse model



P. Seifer †, E. Hay ‡, L. Fleischhauer § ||, J. Heilig † ¶, W. Bloch #, S. Sonntag † †, D. Shmerling † †, H. Clausen-Schaumann §, A. Aszodi § ||, A. Niehoff ¶ §§, M. Cohen-Solal †, M. Paulsson †, R. Wagener †^a, F. Zaucke ||||^{* a}

† Center for Biochemistry, Medical Faculty, University of Cologne, Cologne, Germany

‡ Inserm UMR1132 and Paris Diderot University, Paris, France

§ Center for Applied Tissue Engineering and Regenerative Medicine, Munich University of Applied Sciences, Munich, Germany

|| Experimental Surgery and Regenerative Medicine (Experimed), Department of General, Trauma and Reconstructive Surgery, Munich University Hospital, Ludwig-Maximilians-University, Munich, Germany

¶ Cologne Center for Musculoskeletal Biomechanics (CCMB), Medical Faculty, University of Cologne, Cologne, Germany

Department of Molecular and Cellular Sports Medicine, Institute of Cardiology and Sports Medicine, German Sport University Cologne, Cologne, Germany

†† ETH Phenomics Center (EPIC), Zurich, Switzerland

‡‡ PolyGene AG, Rümlang, Switzerland

§§ Institute of Biomechanics and Orthopaedics, German Sport University Cologne, Cologne, Germany

||| Dr. Rolf M. Schwiete Research Unit for Osteoarthritis, Orthopedic University Hospital Friedrichsheim GmbH, Frankfurt Am Main, Germany

ARTICLE INFO

Article history:

Received 12 May 2020

Accepted 29 September 2020

Keywords:

Matrilin-3

Polymorphism

Extracellular matrix

Osteoarthritis

Animal model

SUMMARY

Objective: The human matrilin-3 T303M (in mouse T298M) mutation has been proposed to predispose for osteoarthritis, but due to the lack of an appropriate animal model this hypothesis could not be tested. This study was carried out to identify pathogenic mechanisms in a transgenic mouse line by which the mutation might contribute to disease development.

Methods: A mouse line carrying the T298M point mutation in the *Matn3* locus was generated and features of skeletal development in ageing animals were characterized by immunohistology, micro computed tomography, transmission electron microscopy and atomic force microscopy. The effect of transgenic matrilin-3 was also studied after surgically induced osteoarthritis.

Results: The matrilin-3 T298M mutation influences endochondral ossification and leads to larger cartilage collagen fibril diameters. This in turn leads to an increased compressive stiffness of the articular cartilage, which, upon challenge, aggravates osteoarthritis development.

Conclusions: The mouse matrilin-3 T298M mutation causes a predisposition for post-traumatic osteoarthritis and the corresponding knock-in mouse line therefore represents a valid model for investigating the pathogenic mechanisms involved in osteoarthritis development.

© 2020 Osteoarthritis Research Society International. Published by Elsevier Ltd. All rights reserved.

Introduction

Matrilin-3 (MATN3) is the smallest member of the matrilin family of extracellular matrix adaptor proteins. It is a tetramer of subunits of 49 kDa and each subunit consists of an N-terminal

positively charged sequence, a von Willebrand factor A (VWA) domain, four epidermal growth factor like (EGF) domains and a C-terminal coiled coil α -helical domain^{1,2}. Most matrilin-3 subunits assemble into homotetramers, but heterooligomers with matrilin-1 subunits do also occur^{3–5}. Matrilin-3 is expressed by most chondrocytes, but while widespread in embryonal cartilage, in adult mice it is found mainly in the deeper layers of the articular cartilage and in the growth plate^{3,6,7}. Here it binds to other extracellular matrix macromolecules, such as collagens II, VI, IX, XI, COMP, aggrecan, decorin and biglycan^{8–11}, thereby regulating collagen fibrillogenesis¹² and, presumably, overall extracellular matrix

* Address correspondence and reprint requests to: F. Zaucke, Dr. Rolf M. Schwiete Research Unit for Osteoarthritis, Orthopedic University Hospital Friedrichsheim GmbH, Marienburgstr. 2, 60528, Frankfurt am Main, Germany. Tel.: 49-69-6705-372

E-mail address: frank.zaucke@friedrichsheim.de (F. Zaucke).

^a These authors contributed equally.

assembly as well as interactions with growth factors and receptors^{13–15}.

The relevance of matrilin-3 for human pathology was first recognized through the identification of mutations in the gene region encoding the VWA domain in patients suffering from multiple epiphyseal dysplasia (MED), a mild to moderately severe form of chondrodysplasia^{16,17}. MED mutations cause a misfolding of the domain and prevent secretion^{18,19}, resulting in an accumulation of matrilin-3 in the endoplasmic reticulum (ER) that may induce ER stress and cell death. Later, also a mutation in the first EGF domain was found to cause spondylo-epi-metaphyseal dysplasia (SEMD)²⁰, a form of chondrodysplasia with some similarity to MED. Chondrodysplasia patients often show early onset osteoarthritis, but this is not the dominating feature of their phenotype. It was therefore novel when a genetic screen of a cohort of Icelandic patients with hand osteoarthritis revealed the matrilin-3 mutation T303M (in mouse T298M) in 2% of the patients²¹. The mutation concerns a threonine residue in the first EGF domain of matrilin-3 that is exchanged to methionine and is caused by a C>T transition in exon 3. In these patients, X-ray analysis showed osteoarthritis that was limited to the carpometacarpal and scaphotrapezotrapezoidal joints²². Independent studies of the T303M mutation in patient cohorts of other ethnicity however only partially confirmed these result and instead demonstrated a linkage to spinal disc degeneration in addition to osteoarthritis in the carpometacarpal joint²³ or to osteoarthritis in the carpometacarpal joint but not in the knee joint²⁴.

Two matrilin-3 deficient mouse lines have been generated. One of these²⁵ did not show any osteoarthritis, but slight increases in cartilage collagen fibril diameter and volume density¹² that became more pronounced in matrilin-1/matrilin-3 double deficient mice. The other line²⁶ was found to be predisposed to osteoarthritis in addition to showing premature hypertrophy and an increased total body bone mineral density. The reason for the phenotypic discrepancy between both knock out lines is not known. Even though one line shows some alterations related to osteoarthritis, the effects of a mutant matrilin-3 variant cannot be studied in knock out models.

The pathogenic mechanisms that link the matrilin-3 T303M mutation to cartilage degeneration are not well understood. So far, only *in vitro* experiments using transfected cells or purified proteins have been performed. Expression of matrilin-3 with the T298M mutation in primary mouse chondrocytes showed normal secretion of the protein, while matrilin-3 with chondrodysplasia mutations was retained in the ER¹⁹. However, purified recombinant matrilin-3 carrying the T298M mutation severely affected *in vitro* collagen fibrillogenesis, giving wider fibrils, without showing changes in its collagen affinity¹⁰.

In the present study, we generated a knock-in mouse model expressing mouse matrilin-3 carrying the T298M mutation that allows us to study events triggered by the mutation in an *in vivo* setting. We characterized this mouse line and demonstrated that the matrilin-3 T298M mutation affects collagen fibril organization and mechanical properties in articular cartilage and indeed predisposes for osteoarthritis in a surgical model where the knee joint is destabilized by meniscectomy.

Methods

Mice

Mice carrying the T298M mutation in the mouse *Matn3* gene were generated by PolyGene AG (Rümlang, Switzerland) using gene targeting in C57BL/6N-derived embryonic stem (ES) cells. Resulting heterozygous mice were further bred to the C57BL/6N background

and housed in a specific pathogen-free facility. The study protocol and all animal procedures were in compliance with the principles of laboratory animal care and the German laws on the protection of animals (§4 Abs.2 TierSchG). Animal protocols were approved by the veterinary agency of North-Rhine Westphalia (Landesamt für Natur, Umwelt und Verbraucherschutz [LANUV], Germany). Genotyping of mice was done by polymerase chain reaction (PCR) on deoxyribonucleic acid (DNA) derived from ear tacking. Mice were housed in individually ventilated cages and subjected to a 12:12-h light/dark cycle at a temperature of 22°C. Water and standard food were available *ad libitum*. At each time point a matrilin-3 T298M group was compared to a wildtype C57BL/6N (Charles River) control group.

Histology, immunohistochemistry and immunofluorescence

Stainings were performed on frontal forepaw and sagittal knee sections of at least three animals per genotype per time point. Paraffin sections (7 µm) were de-waxed in xylene and rehydrated. Visualization of proteoglycans and immunohistochemical staining to detect matrilin-1 (rabbit polyclonal, 1:1000)²⁷, matrilin-3 (rabbit polyclonal, 1:1000)³ and aggrecan (Merck, rabbit polyclonal, 1:100) was performed as described²⁸. The 3-amino-9-ethylcarbazole (AEC) substrate-chromogen kit (DAKO) was used for a more sensitive detection. For detection of collagen II (Calbiochem, mouse monoclonal, 1:500) and collagen X (mouse monoclonal, 1:200)²⁹ additional epitope unmasking with pepsin (1 mg/ml) for 15 min at 37°C was necessary, prior to hyaluronidase digestion (500 U/ml, 37°C for 30 min).

Primary chondrocytes were freshly isolated from newborn mice (postnatal days 0–2) and cultured as described⁸. For immunofluorescence staining chondrocytes were grown on plastic coverslips for up to 6 days, fixed with 4% formaldehyde in phosphate-buffered saline (PBS), permeabilized with 0.2% Triton-X-100 in PBS and blocked with 1% NGS (normal goat serum) in PBS. Antibody incubation and mounting was performed as described⁸. Images were acquired using a Nikon Eclipse TE2000-U fluorescence microscope.

Collagen II and proteoglycans

Articular cartilage from proximal tibiae of 4-week-old mice was isolated and crushed in liquid nitrogen. For collagen extraction, tissue was resuspended in 1.5 ml 0.5 M acetic acid/0.1 mg pepsin and incubated for 24 h at 4°C. To release proteoglycans, tissue was extracted in PBS for 24 h at 4°C and subsequently in 4M guanidine hydrochloride (50 mM Tris-HCl pH 7.5) for 24 h at 4°C. Cell debris was removed by centrifugation and the supernatant used to determine the proteoglycan concentration using the Blyscan Glycosaminoglycan Assay (Bicolor).

SDS-PAGE and immunoblotting

SDS-PAGE was performed under reducing conditions in Tris-glycine with a 5% polyacrylamide stacking gel and a 12% running gel. Proteins were transferred onto nitrocellulose membranes by electrophoresis, the membranes blocked with 5% skim milk, and incubated overnight at 4°C with an affinity-purified rabbit polyclonal antibody against matrilin-3³ (dilution, 1:1000) or a mouse monoclonal antibody against collagen II (Calbiochem). After washing, the membrane was incubated with the appropriate secondary antibody/horseradish peroxidase conjugate. Antibody detection was performed using 1.25 mM luminol, 0.225 mM p-coumaric acid, 0.012% (v/v) H₂O₂ as a luminescent agent followed by exposure on X-ray films.

Micro computed tomography (μ CT)

Bone microstructure of mouse forepaw and proximal tibia was analyzed using a high-resolution μ CT scanner (μ CT 35, Scanco Medical AG). Forepaws were scanned with an isotropic voxel-size of $7 \times 7 \times 7 \mu\text{m}$ using 70 kVp energy, 114 μA current and 400 ms integration time. Tibiae were measured with an isotropic voxel-size of $3.5 \times 3.5 \times 3.5 \mu\text{m}$ using 45 kVp energy, 177 μA current and 400 ms integration time. To remove image noise, gray-scale data of raw images were preprocessed using a 3D Gaussian filter algorithm. The mineralized tissue was separated from soft tissues by a global thresholding procedure (31). The segmentation steps were applied with support = 1.0, sigma = 0.8. The image data were segmented using different thresholds of the maximum gray scale value (depending on the age and tissue) of 24 % (forepaw), 27 % (tibia, 2 weeks), 29 % (tibia, 4 weeks) and 37 % (tibia, 8 weeks).

Electron microscopy (EM)

Forepaws were taken from mice 4 weeks to 12 months of age and proximal tibiae from mice 2–8 weeks of age. All specimens were immersion-fixed for 8 h in 2% paraformaldehyde and 2% glutaraldehyde in 0.1 M cacodylate buffer, pH 7.2, at room temperature, rinsed in 0.1 M cacodylate buffer and stored in PBS. After washing in 0.1 M cacodylate buffer, pH 7.2, at 40°C, samples were fixed with 2% OsO_4 for 2 h and stained in 1% uranyl acetate. Dehydrated biopsies were embedded in araldite resin and ultrathin sections (30–40 nm) placed on copper grids. Transmission electron microscopy was performed using a Zeiss EM109 electron microscope. Collagen fibril diameters were determined by using ImageJ (National Institutes of Health [NIH], USA).

Indentation-type atomic force microscopy (IT-AFM)

Proximal tibiae from 4 weeks old mice were immersed in optimal cutting temperature (OCT) compound, and were snap frozen in liquid nitrogen-cooled isopentane. 20 μm native (non-decalcified) sagittal sections of three animals per genotype were cut using a cryotome (Leica CM1950) and positioned on the adhesive side of transparent adhesive tape (tesafilm Nr.: 57,330–00000) and subsequently immobilized on glass slides (Roth) using transparent double adhesive tape (tesafilm Nr.: 56661–00002). Sections were stored at -20°C and allowed to equilibrate at room temperature before AFM analysis. AFM indentation measurements were carried out using a NanoWizard I AFM (JPK Instruments) mounted on an inverted optical microscope (Axiovert 200, Carl Zeiss Microscopy) as described previously³⁰

Induction of osteoarthritis and analysis

Ten-week-old male matrilin-3 T298M ($n = 10$) and C57/Bl6N mice ($n = 10$) underwent medial meniscectomy of the right knee to induce joint instability³¹. A sham operation was performed on the left knee. Mice were pair-fed in order to control for bodyweight and sacrificed 6 weeks after surgery. The experiments complied with the Guidelines for Animal Experimentation issued by the local Ethics Committee on Animal Care and Experimentation (Ethical committee Lariboisiere-Villemin, Paris, France). The committee specifically approved this study (APAFIS#12530-2017121116307412 v3). The histological osteoarthritis score was assessed on slides stained with Safranin-O as described³¹. Osteoarthritic lesions were assessed using the OARSI grading and staging system with a score ranging from 0 to 24³²

Statistical analysis

Results are expressed as the mean \pm SEM. Statistical analysis was performed using Stat-View version 5 software (SAS Institute, Cary, NC). Parameters were compared by analysis of variance (ANOVA), followed by Fisher's least significant difference test. A p -value less than 0.05 was considered as statistically significant.

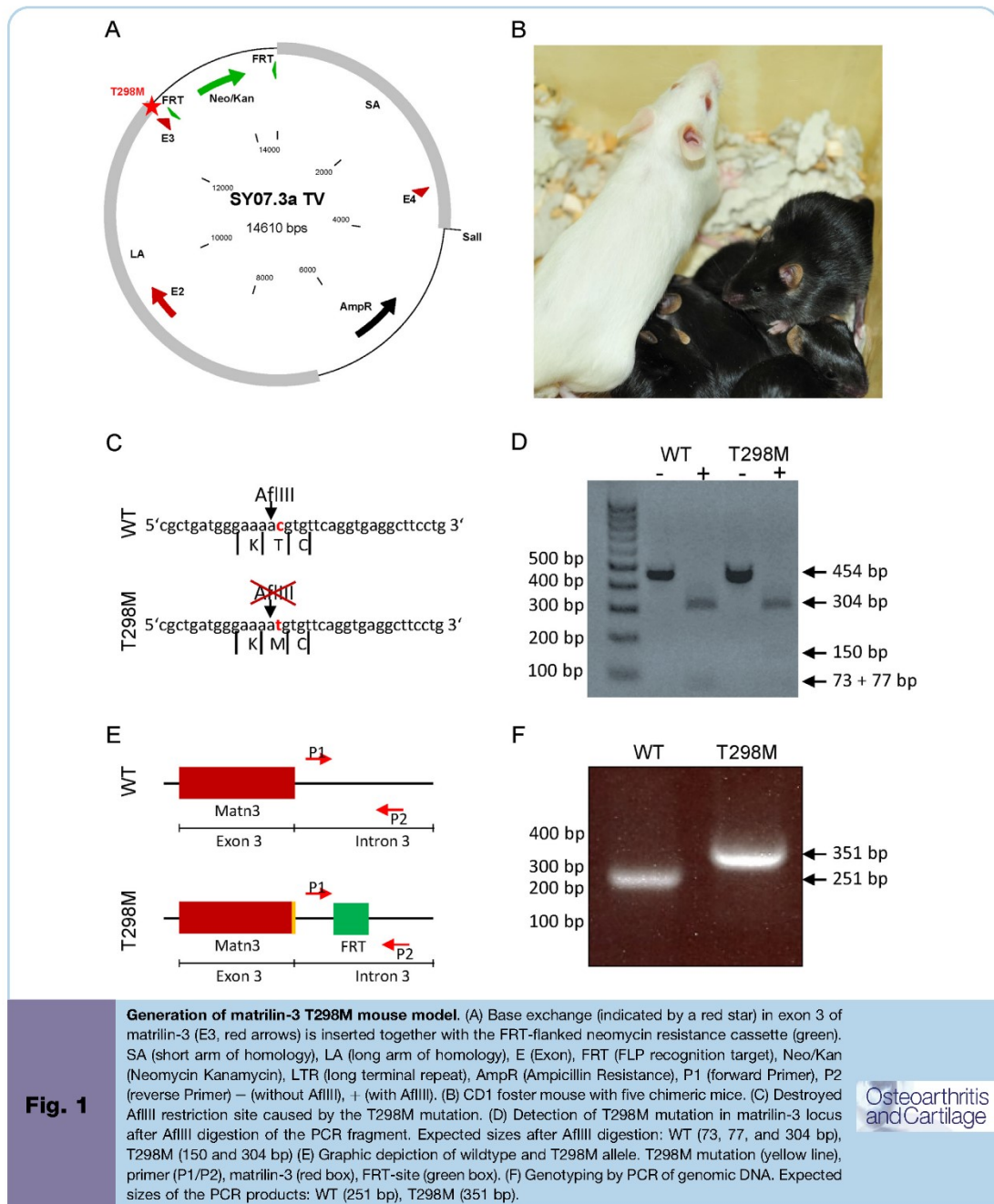
Results

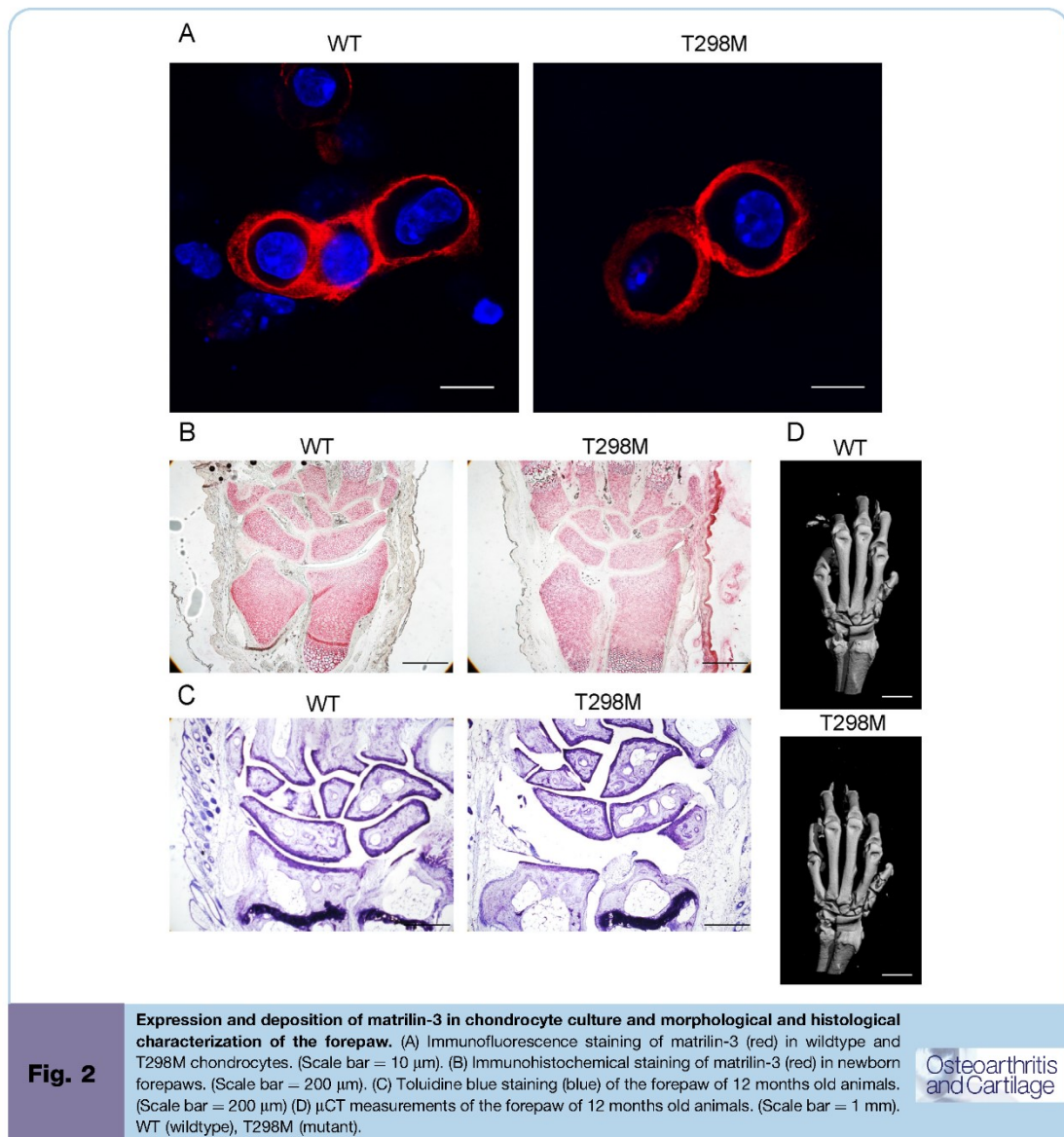
The matrilin-3 T298M mouse line was generated by the company Polygene AG (Rümlang, Switzerland). To introduce the T298M point mutation into the *Matn3* locus, the targeting vector SY07.3a.TV was generated [Fig. 1(A)]. This vector contains, in addition to the mutation, two homologous regions downstream and upstream as well as a Neomycin resistance cassette. The vector was linearized and transfected into C56Bl/6N-derived embryonic stem cells through electroporation. After selection with G418, positive stem cells were identified by PCR analysis. These cells were injected into grey C56Bl/6N mouse blastocysts, which were then transferred into a white CD-1 surrogate mother. To remove the Neomycin cassette, chimeric mice [Fig. 1(B)] were bred to grey FLP-deleter mice. The resulting black offspring were tested by PCR for removal of the Neomycin cassette and the presence of the mutated *Matn3* allele in the germline [Fig. 1(C) and (D)]. Genotyping was performed by PCR of genomic DNA. In mutant mice, the insertion of a flippase recognition target (FRT)-site in intron 3 resulted in a PCR product of 351 bp. In wildtype animals, a band of 251 bp was amplified [Fig. 1(E) and (F)]. Only wildtype and homozygous matrilin-3 T298M mice were compared and used for the experiments. No gender specific differences could be observed.

In initial experiments, primary chondrocytes were isolated from the knee joint of newborn mice and cultured for 6 days. Immunofluorescence microscopy showed that the matrilin-3 T298M protein was integrated into a pericellular matrix in a manner similar to the wildtype protein. Intracellular staining was not observed, even after permeabilization of the cells, indicating the absence of intracellular inclusions that would have been expected if the protein had been retained in the endoplasmic reticulum [Fig. 2(A)]. These findings are in agreement with earlier results showing unhindered secretion of matrilin-3 T298M in transfected chondrocytes¹⁹.

Initial analysis of the tissue expression of matrilin-3 T298M protein focused on the forepaw, as hand osteoarthritis is the prominent feature in patients carrying the corresponding T303M mutation. Immunohistochemical staining of forepaw sections from newborn mice showed a wide expression of both T298M and wildtype matrilin-3 in all cartilages [Fig. 2(B)]. The staining intensity for T298M and wildtype matrilin-3 at this time point was identical. Toluidine blue staining was used to determine integrity of the articular cartilages as well as the aggrecan concentration, as loss of aggrecan is the earliest sign of osteoarthritis. At 12 months of age, neither cartilage degeneration nor loss of aggrecan could be observed [Fig. 2(C)]. Similarly, μ CT imaging of forepaws from 12 months old animals showed neither differences in bone architecture nor signs of osteoarthritis like presence of osteophytes between T298M and wildtype animals [Fig. 2(D)].

As osteoarthritis could not be detected in the forepaw, also joints that may be under a higher mechanical load were investigated. First, the expression of matrilin-3 and matrilin-1 in the proximal tibia of 2 weeks old mice was studied by immunohistochemistry [Fig. 3(A)]. As in the forepaws (not shown), a much weaker signal for both matrilin-3 and matrilin-1 was seen in the cartilage of T298M mutants than in wildtype. Conversely, collagen X, used as a marker for the hypertrophic chondrocytes of the





growth plate, showed an increased staining in the mutant. In addition, the secondary center of ossification appeared larger in the mice expressing matrilin-3 T298M. To confirm the latter finding, μ CT analysis was carried out [Fig. 3(B)]. A significant enlargement of the secondary center of ossification was observed in 2 and 4 weeks old mutant mice when compared to wildtype. Furthermore, cross-sectional analysis indicated changes in bone architecture. The differences were most pronounced in 4 weeks old animals, where the network of thin bone trabeculae seen in the center of the secondary

center of ossification in wildtype mice was in part missing in the matrilin-3 T298M mutant mice. The center also showed a change in shape and some dense, bony areas in the mutants. The differences were, however, transient and could hardly be seen in 8 weeks old mice.

The clearly lower expression of matrilin-3 in the articular cartilage of the proximal tibia in T298M mutant mice led us to investigate the consequences for the extracellular matrix ultra-structure in the articular cartilage of 2 and 4 weeks old mice

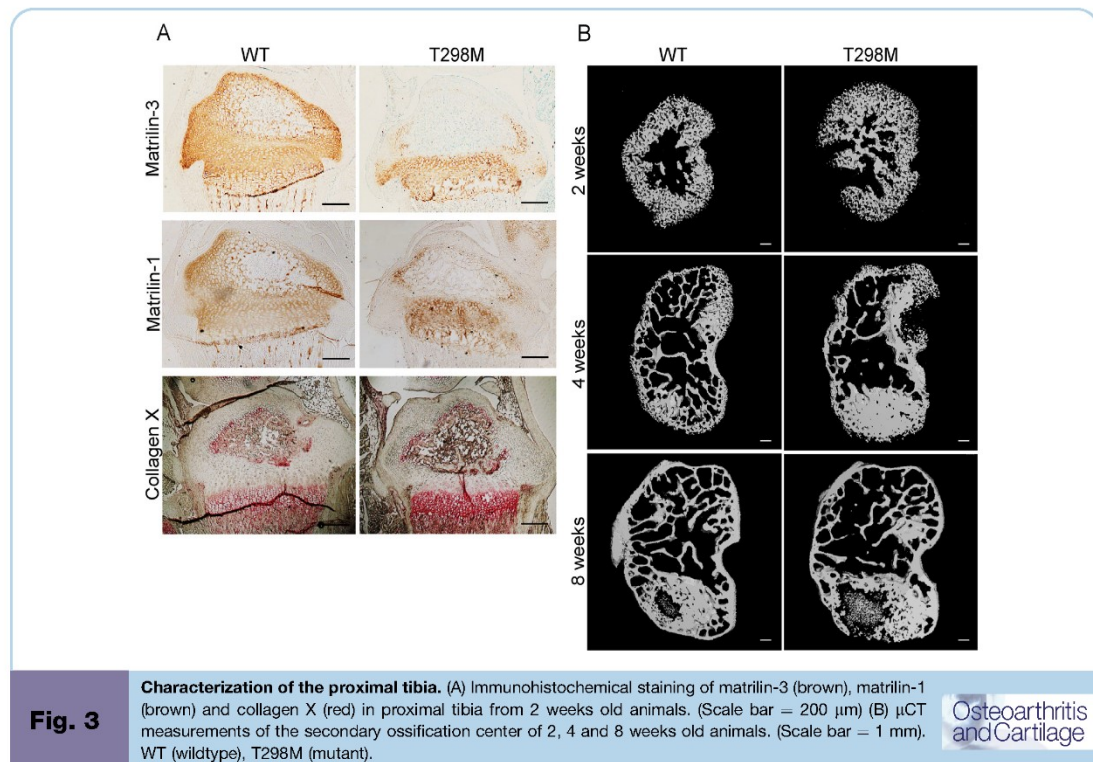


(Fig. 4(A) and not shown). At both time points, collagen fibrils of larger diameter were seen in the matrilin-3 T298M mutant cartilage compared to wildtype and this difference that was particularly pronounced at 4 weeks of age [Fig. 4(A)]. While the wildtype fibrils typically had diameters of 30–60 nm, those in the mutant were in the range of 135–190 nm [Fig. 4(C)]. An immunoblot analysis of pepsin-digested collagen II showed that this difference was not due to changes in collagen II amounts [Fig. 4(B)]. By immunohistochemistry, there was no obvious difference between the genotypes in the amount and distribution of aggrecan, the predominant cartilage proteoglycan [Fig. 4(D)]. However, when the articular cartilage was extracted with physiological saline and glycosaminoglycan content in the supernatant measured, much more glycosaminoglycan was released from the cartilage of the matrilin-3 T298M mutant mice, indicating a decreased anchorage of aggrecan in the collagen fibril network [Fig. 4(E)]. Subsequent extraction with 4 M guanidine hydrochloride showed that the overall amount of aggrecan was not changed in the mutant cartilage [Fig. 4(F)].

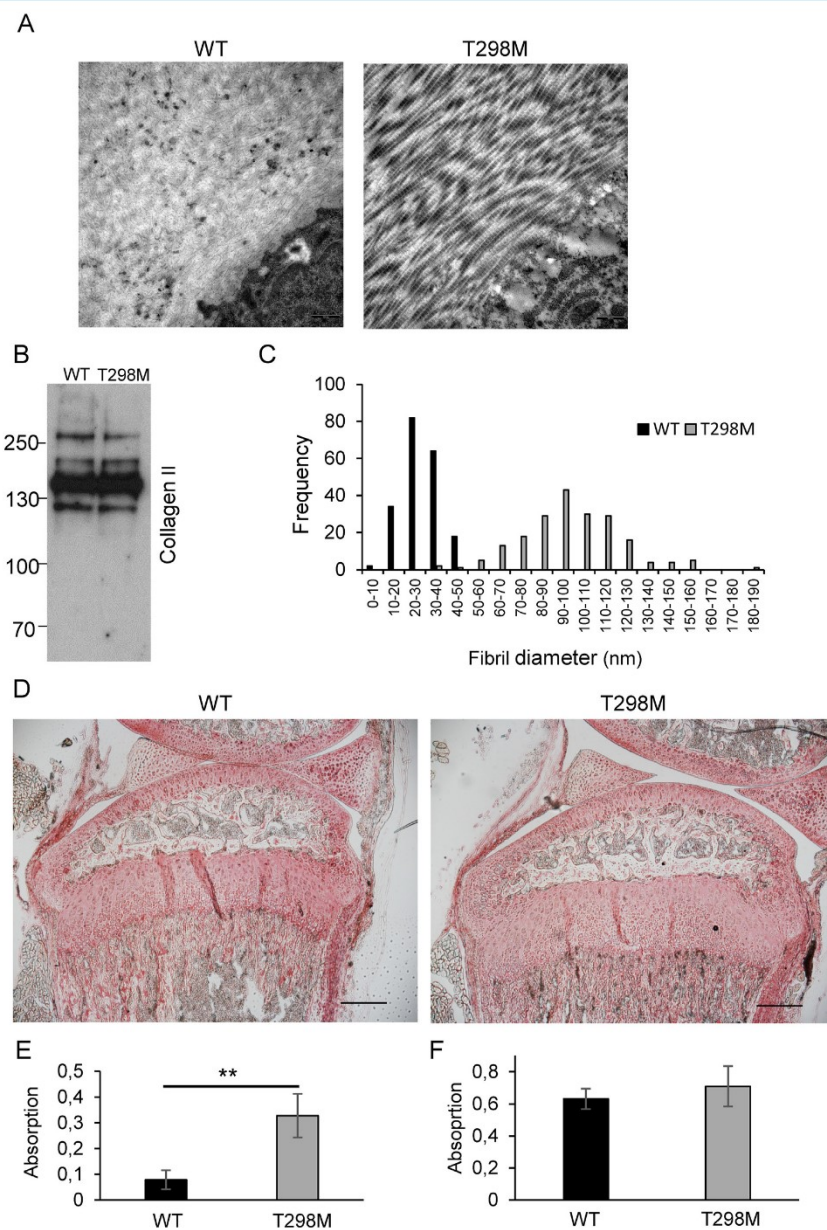
The rather drastic effects of the matrilin-3 T298M mutation on the organization of the articular cartilage extracellular matrix could lead to changes in its biomechanical properties, which may in turn predispose for osteoarthritis. In order to investigate biomechanical properties, nano-scaled indentation-type atomic force microscopy was applied on the superficial, middle and deeper zones of articular cartilage at 4 weeks of age (Fig. 5). The measured compressive stiffness (the Young's modulus) exhibited

unimodal distribution in the superficial zone, while a bimodal distribution was observed in the middle and deep zones, with two peaks representing the softer proteoglycans (E1) and the stiffer collagens (E2) (35). While the stiffness of the superficial layer was similar between the genotypes, clearly stiffer matrix was observed in the middle and deep zones of the matrilin-3 T298M articular cartilage compared to wildtype. Particularly in the deep zone, the stiffness values were E1 = 146.77 kPa and E2 = 269.79 kPa for wildtype compared to E1 = 340.99 kPa and E2 = 616.13 kPa for the T298M mutant (Fig. 5).

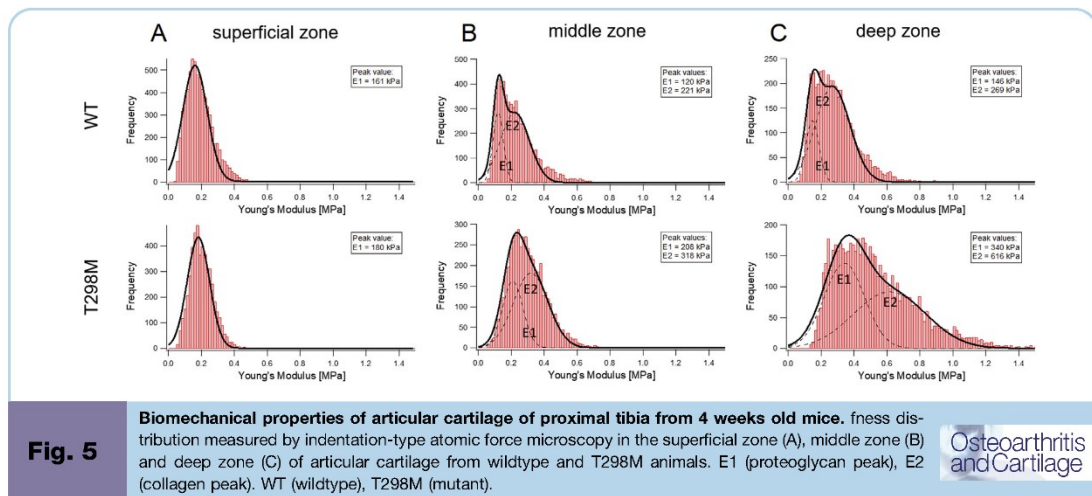
Despite the ultrastructural and biomechanical changes of the articular cartilage, we could not observe increased severity of spontaneously occurring osteoarthritis in matrilin-3 T298M mice compared to wildtype until 12 months of age (data not shown). In order to force pathophysiological loading, we used medial meniscectomy, a murine knee joint instability model for osteoarthritis³³. Matrilin-3 T298M mice challenged by meniscectomy exhibited significantly more severe articular cartilage degeneration than wildtype mice or sham operated mutant mice (Fig. 6). Histological analysis revealed that 6 weeks post-meniscectomy, wildtype mice mainly show loss of proteoglycans from the articular cartilage, whereas T298M matrilin-3 mutant mice display an almost complete delamination of the superficial and middle cartilage layers. These findings were reflected in an increase of the average OARSI score from 3.8 in wildtype to 7.5 in matrilin-3 T298M mice. Thus, the T298M matrilin-3 mutation truly predisposes for osteoarthritis that occurs as the consequence of a mechanical challenge.

84

P. Sejfer et al. / Osteoarthritis and Cartilage 29 (2021) 78–88

**Fig. 4**

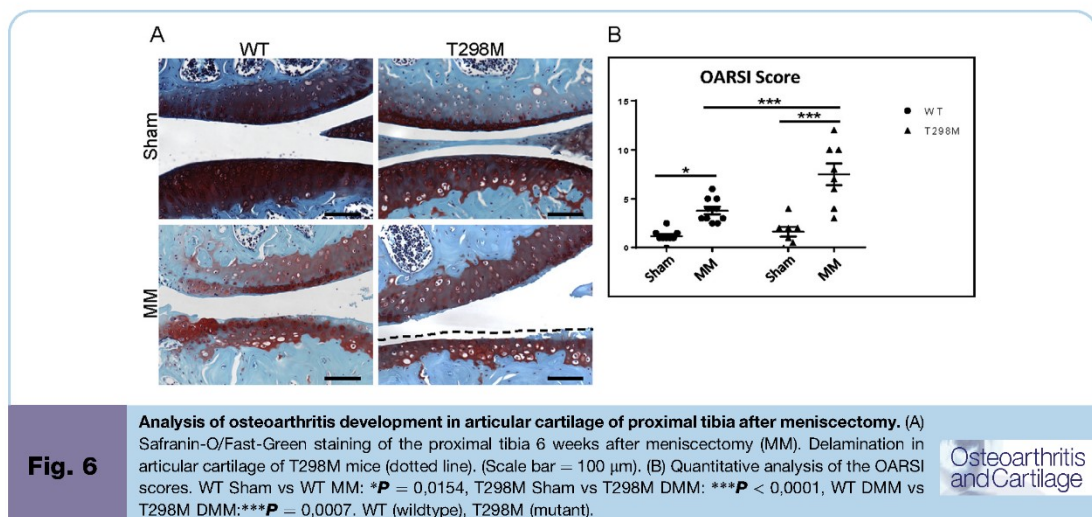
Analysis of the proximal tibia of 4 weeks old mice. (A) Electron microscopy images of the articular cartilage from wildtype and T298M mutant. (B) Immunoblot analysis under non-reducing conditions of extracted collagen II from articular cartilage. (C) Statistical analysis of the fibril diameter. (D) Immunohistochemical staining of aggrecan (red). (Scale bar = 200 μ m). (E) Measurement of the proteoglycan extractability in articular cartilage with PBS. WT vs TM: ****P** < 0.01. (F) Measurement of the proteoglycan extractability in articular cartilage with 4M guanidine hydrochloride (1:10 Dilution). WT (wildtype), T298M (mutant).



Discussion

In order to allow a detailed characterization of effects caused by the osteoarthritis-associated matrilin-3 variant *in vivo*, we first generated an appropriate animal model that copies the human genotype. Matrilin-3 knock out lines were available and provided some insight into the function of matrilin-3. However, the transferability of results from these models to the human situation is questionable, in particular as there is no real human equivalent for the complete absence of matrilin-3. As long as a mutant protein is synthesized, knock out lines can hardly be regarded as suitable models to study effects of disease-causing mutations.

The T303M mutation in human matrilin-3 was first described as predisposing for osteoarthritis in the carpometacarpal and scaphotrapeziotrapezoidal joints^{21,22}. For this reason, the characterization of the mouse line carrying the corresponding T298M matrilin-3 mutation was first focused on the forepaw. However, neither histochemical analysis nor μ CT indicated any osteoarthritic changes. To our knowledge, there are no literature reports on osteoarthritis in the mouse forepaw, while in the human hand osteoarthritis is common. The reason for this difference could lie in how the hands and forepaws are used in the two species and the consequences for mechanical loading. While the mouse mainly uses the forepaw for stabilization of the movement and for holding



food, the main function of the human hand is in grabbing. The forces needed to grab puts the hand joints under a much higher mechanical load. In particular, the thumb is under a heavy load, as it must counterbalance the force of the other four fingers.

The possibility that low mechanical loading of the joints in the mouse forepaw makes them less suited as a model for human osteoarthritis made us turn to larger joints, e.g., the mouse knee joint, to ascertain if the T298M mutation predisposes for osteoarthritis. We demonstrated that the mutation caused a decrease of the amounts of both matrilin-3 and matrilin-1 present in the articular cartilage of the proximal tibia in 2 weeks old mutant mice. The effect of the matrilin-3 mutation also on the matrix deposition of matrilin-1 may be due to the fact that matrilin-3 and matrilin-1 are able to form heterooligomers^{3 5}. Thus, deficiency or defects in matrilin-3 could also affect the assembly and secretion of matrilin-1 containing molecules.

Microscopical images of the proximal tibia at 2 weeks of age also showed an enlargement of the secondary center of ossification in the matrilin-3 T298M mutant mice compared to wildtype. Further, we detected an enlarged collagen X positive area indicating premature hypertrophy. This is in agreement with the observation of van der Weyden *et al.*²⁶ demonstrating accelerated hypertrophic differentiation in the embryonic growth plate of the tibia in matrilin-3 deficient mice. μ CT analysis corroborates the faster ossification of the epiphysis and, in addition, revealed bone architectural abnormalities in the secondary center of ossification in 4 weeks old mutants characterized by disturbances in the trabecular networks and accumulation of excessive bony material. Apparently, the changes in extracellular matrix composition in the matrilin-3 T298M mutant mice affect ossification. This may be mediated by the decreased amount of matrilin-1 in the proximal tibia, as matrilin-1 has been shown to inhibit angiogenesis both *in vitro* and *in vivo*³⁴. A loss of matrilin-1 could cause an earlier vascular invasion into the cartilage of the developing tibial epiphysis head and, thereby, further promote the formation of the secondary center of ossification.

The decreased matrilin amounts in the cartilage of matrilin-3 T298M mutant mice made us perform a more detailed investigation of the extracellular matrix in the articular cartilage of the proximal tibia. First, we performed an ultrastructural analysis using transmission electron microscopy and found that matrilin-3 T298M mutant mice exhibit a strikingly increased collagen fibril diameter compared to wildtype. This observation corroborates our previous result showing that addition of matrilin-3 T298M leads to larger fibrils in an *in vitro* collagen fibrillogenesis assay¹⁰. Similar changes in fibril diameters have been observed in matrilin-3 single knockout and, more pronounced, in matrilin-1/matrilin-3 double knockout mice¹². These matrilin-3 deficient mouse lines did not develop spontaneous osteoarthritis, however, osteoarthritic changes have been described for another matrilin-3 deficient mouse line²⁶. Furthermore, quadruple knockout mice lacking all members of the matrilin family display larger collagen fibril diameters in the articular cartilage and an osteoarthritis-like degeneration that develops in mice older than 18 months³⁵. Accordingly, structural changes in the cartilage collagen network could be an underlying molecular mechanism for osteoarthritis occurring as a consequence of mutations or deficiency in matrilin-3.

The mechanical properties of the articular cartilage extracellular matrix are likely to be influenced by the organization of the collagen network, as the collagen is important for distributing forces applied upon joint loading. To better understand the pathogenic mechanisms that links the matrilin-3 T303M mutation to cartilage degeneration, we carried out an atomic force microscopy analysis of the different zones of the tibial articular cartilage using a nano-tip indentation technique. IT-AFM indeed demonstrated an

increased compressive stiffness of the middle and deeper cartilage layers in T298M mice, similar to findings in decorin deficient mice³⁶. Decorin has been shown to bind to collagen fibrils and regulate their diameter³⁷, but also to interact with matrilins (11). Complexes consisting of matrilins and decorin interconnect collagens and aggrecan¹¹ and we could show that aggrecan was less anchored in matrilin-3 T298M mutant mice. In line with these findings, mice lacking all matrilins³⁵ or carrying a hypomorphic aggrecan mutation³⁸ also exhibit nanomechanical changes in the articular cartilage. This may indicate a link between matrilins, decorin, collagens and aggrecan in regulating cartilage matrix stiffness.

Our results imply that the matrilin-3 T298M mutation causes a molecular phenotype, which may make articular cartilage more susceptible for osteoarthritis. In accordance with previous studies using various matrilin-3 mutant mice^{12,25,26,37}, we could not detect any spontaneously occurring osteoarthritic changes in the T298M mutant mice up to the age of 12 months. Osteoarthritis development depends on multiple factors, which in addition to age and genetic predisposition also include trauma and aberrant joint loading. We therefore mechanically challenged our matrilin-3 T298M mutant mice by applying medial meniscectomy in the knee joint. Indeed, we could demonstrate that the mutation aggravates osteoarthritis, as the matrilin-3 T298M mice developed a much more severe osteoarthritis than wildtype mice 6 months after surgery exposed to the same challenge. This finding indicates that in contrast to age-associated osteoarthritis the development of post-traumatic knee osteoarthritis is evidently affected by the matrilin-3 T298M mutation. Interestingly, matrilin-1 deficient mice also age without significant articular cartilage degeneration but develop more severe post-traumatic osteoarthritis than wildtype after surgical destabilization of the medial meniscus³⁹.

In conclusion, we show that the matrilin-3 T298M mutation in mice increases the severity of post-traumatic osteoarthritis. Thus, this knock-in mouse line represents a valid model for studying the pathogenesis of articular cartilage degeneration upon mechanical challenge. The mutation transiently influences secondary ossification of long bones and, more importantly, it regulates cartilage collagen fibril diameter and aggrecan anchorage in the extracellular matrix. This, in turn, elevates compressive stiffness of the articular cartilage, which may pre-dispose for osteoarthritis after abnormal mechanical stimuli.

Author contributions

Substantial contributions to acquisition of data: P. S., E. H., L. F., J. H., W. B., and S. S. Substantial contributions to analysis and interpretation of data: P. S., E. H., L. F., J. H., W. B., S. S., D. S., H. C–S., A. A., A. N., M. C–S., M. P., R. W., F. Z.

Substantial contributions to study conception and design: M. P., R. W., F. Z.

Drafting the article: M. P.

Revising it critically for important intellectual content: P. S., E. H., L. F., J. H., W. B., S. S., D. S., H. C–S., A. A., A. N., M. C–S., M. P., R. W., F. Z.

Final approval of the version of the article to be published: P. S., E. H., L. F., J. H., W. B., S. S., D. S., H. C–S., A. A., A. N., M. C–S., M. P., R. W., F. Z.

Conflict of interest

None of the authors has competing interests to declare. Except for the abovementioned funding sources, none of the authors discloses any financial and personal relationships with other people or organizations that could potentially and inappropriately influence their work and conclusions.

Role of funding sources

The abovementioned funding sources did neither have any role in the study design, collection, analysis and interpretation of data, in the writing of the manuscript nor in the decision to submit the manuscript for publication.

Acknowledgements

This study was supported by German Research Foundation Grants FOR 2722-B1 (to R. W. and M. P.), FOR 2722-D1, Ni 1083/3–1 (to A. N.) and FOR 2722-D2 (to F. Z.) and by the European Community's Seventh Framework Programme. Grant Number: FP7/2007–2013 602300 (to S. S., M. C.–S., M. P., R. W. and F. Z.).

References

- Belluoccio D, Trueb B. Matrilin-3 from chicken cartilage. *FEBS Lett* 1997;415(2):212–6.
- Wagener R, Kobbe B, Paulsson M. Primary structure of matrilin-3, a new member of a family of extracellular matrix proteins related to cartilage matrix protein (matrilin-1) and von Willebrand factor. *FEBS Lett* 1997;413(1):129–34.
- Klatt AR, Nitsche DP, Kobbe B, Mörgelein M, Paulsson M, Wagener R. Molecular structure and tissue distribution of matrilin-3, a filament-forming extracellular matrix protein expressed during skeletal development. *J Biol Chem* 2000;275(6):3999–4006, <https://doi.org/10.1074/jbc.275.6.3999>.
- Kleemann-Fischer D, Kleemann GR, Engel D, Yates JR, Wu JJ, Eyre DR. Molecular properties of matrilin-3 isolated from human growth cartilage. *Arch Biochem Biophys* 2001;387(2):209–15, <https://doi.org/10.1006/abbi.2000.2256>.
- Wu JJ, Eyre DR. Matrilin-3 forms disulfide-linked oligomers with matrilin-1 in bovine epiphyseal cartilage. *J Biol Chem* 1998;273(28):17433–8, <https://doi.org/10.1074/jbc.273.28.17433>.
- Klatt AR, Paulsson M, Wagener R. Expression of matrilins during maturation of mouse skeletal tissues. *Matrix Biol J Int Soc Matrix Biol* 2002;21(3):289–96.
- Zhang Y, Chen Q. Changes of matrilin forms during endochondral ossification. Molecular basis of oligomeric assembly. *J Biol Chem* 2000;275(42):32628–34, <https://doi.org/10.1074/jbc.M002594200>.
- Budde B, Blumbach K, Ylöstalo J, Zaucke F, Ehlen H, Wagener W, et al. Altered integration of matrilin-3 into cartilage extracellular matrix in the absence of collagen IX. *Mol Cell Biol* 2005;25(23):10465–78, <https://doi.org/10.1128/MCB.25.23.10465-10478.2005>.
- Mann HH, Ozbek S, Engel J, Paulsson M, Wagener R. Interactions between the cartilage oligomeric matrix protein and matrilins. Implications for matrix assembly and the pathogenesis of chondrodysplasias. *J Biol Chem* 2004;279(24):25294–8, <https://doi.org/10.1074/jbc.M403778200>.
- Otten C, Hansen U, Talke A, Wagener R, Paulsson M, Zaucke F. A matrilin-3 mutation associated with osteoarthritis does not affect collagen affinity but promotes the formation of wider cartilage collagen fibrils. *Hum Mutat* 2010;31(3):254–63, <https://doi.org/10.1002/humu.21182>.
- Wiberg C, Klatt AR, Wagener R, Paulsson M, Bateman JF, Heinigard D, et al. Complexes of matrilin-1 and biglycan or decorin connect collagen VI microfibrils to both collagen II and aggrecan. *J Biol Chem* 2003;278(39):37698–704, <https://doi.org/10.1074/jbc.M304638200>.
- Nicolae C, Ko Y-P, Miosge N, Niehoff A, Studer D, Enggist L, et al. Abnormal collagen fibrils in cartilage of matrilin-1/matrilin-3-deficient mice. *J Biol Chem* 2007;282(30):22163–75, <https://doi.org/10.1074/jbc.M610994200>.
- Jayasuriya CT, Zhou FH, Pei M, Wang Z, Lemme NJ, Haines P, et al. Matrilin-3 chondrodysplasia mutations cause attenuated chondrogenesis, premature hypertrophy and aberrant response to TGF- β in chondroprogenitor cells. *Int J Mol Sci* 2014;15(8):14555–73, <https://doi.org/10.3390/ijms150814555>.
- Vincourt J-B, Etienne S, Grosse L, Cottet J, Bantsimba-Malanda C, Netter P, et al. Matrilin-3 switches from anti- to pro-anabolic upon integration to the extracellular matrix. *Matrix Biol J Int Soc Matrix Biol* 2012;31(5):290–8, <https://doi.org/10.1016/j.matbio.2012.03.004>.
- Yang X, Trehan SK, Guan Y, Sun C, Moore DC, Jayasuriya CT, et al. Matrilin-3 inhibits chondrocyte hypertrophy as a bone morphogenetic protein-2 antagonist. *J Biol Chem* 2014;289(50):34768–79, <https://doi.org/10.1074/jbc.M114.583104>.
- Chapman KL, Mortier GR, Chapman K, Loughlin J, Grant ME, Briggs MD. Mutations in the region encoding the von Willebrand factor A domain of matrilin-3 are associated with multiple epiphyseal dysplasia. *Nat Genet* 2001;28(4):393–6, <https://doi.org/10.1038/ng573>.
- Das L, Dhiman V, Van Hul W, Bhansali A, Gogate Y, Steenackers E, et al. Spondylo-epi-metaphyseal dysplasia due to a homozygous missense mutation in the gene encoding Matrilin-3 (T120M). *Bone Rep* 2020;12:100245, <https://doi.org/10.1016/j.bonr.2020.100245>.
- Cotterill SL, Jackson GC, Leighton MP, Wagener R, Mäkitie O, Cole WG, et al. Multiple epiphyseal dysplasia mutations in MATN3 cause misfolding of the A-domain and prevent secretion of mutant matrilin-3. *Hum Mutat* 2005;26(6):557–65, <https://doi.org/10.1002/humu.20263>.
- Otten C, Wagener R, Paulsson M, Zaucke F. Matrilin-3 mutations that cause chondrodysplasias interfere with protein trafficking while a mutation associated with hand osteoarthritis does not. *J Med Genet* 2005;42(10):774–9, <https://doi.org/10.1136/jmg.2004.029462>.
- Borochowitz ZU, Scheffer D, Adir V, Dagoneau N, Munnich A, Cormier-Daire V. Spondylo-epi-metaphyseal dysplasia (SEMD) matrilin 3 type: homozygote matrilin 3 mutation in a novel form of SEMD. *J Med Genet* 2004;41(5):366–72, <https://doi.org/10.1136/jmg.2003.013342>.
- Stefánsson SE, Jónsson H, Ingvarsson T, Manolescu I, Jónsson HH, Olafsdóttir G, et al. Genomewide scan for hand osteoarthritis: a novel mutation in matrilin-3. *Am J Hum Genet* 2003;72(6):1448–59.
- Eliasson GJ, Verbruggen G, Stefánsson SE, Ingvarsson T, Jónsson H. Hand radiology characteristics of patients carrying the T(303)M mutation in the gene for matrilin-3. *Scand J Rheumatol* 2006;35(2):138–42, <https://doi.org/10.1080/03009740500303215>.
- Min JL, Meulenbelt I, Riyazi N, Kloppenburg M, Hauwingu-Duistermaat JJ, Seymour AB, et al. Association of matrilin-3 polymorphisms with spinal disc degeneration and osteoarthritis of the first carpometacarpal joint of the hand. *Ann Rheum Dis* 2006;65(8):1060–6, <https://doi.org/10.1136/ard.2005.045153>.
- Pullig O, Tagariello A, Schweizer A, Swoboda B, Schaller P, Winterpacht A. MATN3 (matrilin-3) sequence variation (pT303M) is a risk factor for osteoarthritis of the CMC1 joint of the hand, but not for knee osteoarthritis. *Ann Rheum Dis* 2007;66(2):279–80, <https://doi.org/10.1136/ard.2006.058263>.
- Ko Y, Kobbe B, Nicolae C, Miosge N, Paulsson M, Wagener R, et al. Matrilin-3 is dispensable for mouse skeletal growth and

- development. *Mol Cell Biol* 2004;24(4):1691–9, <https://doi.org/10.1128/MCB.24.4.1691-1699.2004>.
26. van der Weyden L, Wei L, Luo J, Yang X, Birk DE, Adams DJ, et al. Functional knockout of the matrilin-3 gene causes premature chondrocyte maturation to hypertrophy and increases bone mineral density and osteoarthritis. *Am J Pathol* 2006;169(2):515–27, <https://doi.org/10.2353/ajpath.2006.050981>.
27. Hauser N, Paulsson M. Native cartilage matrix protein (CMP). A compact trimer of subunits assembled via a coiled-coil alpha-helix. *J Biol Chem* 1994;269(41):25747–53.
28. Kamper M, Paulsson M, Zaucke F. Absence of collagen IX accelerates hypertrophic differentiation in the embryonic mouse spine through a disturbance of the Ihh-PTHrP feedback loop. *Cell Tissue Res* 2017;367(2):359–67, <https://doi.org/10.1007/s00441-016-2501-z>.
29. Girkontaite I, Frischholz S, Lammi P, Wagner K, Swoboda B, Aigner T, et al. Immunolocalization of type X collagen in normal fetal and adult osteoarthritic cartilage with monoclonal antibodies. *Matrix Biol J Int Soc Matrix Biol* 1996;15(4):231–8, [https://doi.org/10.1016/s0945-053x\(96\)90114-6](https://doi.org/10.1016/s0945-053x(96)90114-6).
30. Prein C, Warmbold N, Farkas Z, Schieker M, Aszodi A, Clausen-Schaumann H. Structural and mechanical properties of the proliferative zone of the developing murine growth plate cartilage assessed by atomic force microscopy. *Matrix Biol J Int Soc Matrix Biol* 2016;50:1–15, <https://doi.org/10.1016/j.matbio.2015.10.001>.
31. Kadri A, Ea HK, Bazille C, Hannouche D, Lioté F, Cohen-Solal ME. Osteoprotegerin inhibits cartilage degradation through an effect on trabecular bone in murine experimental osteoarthritis. *Arthritis Rheum* 2008;58(8):2379–86, <https://doi.org/10.1002/art.23638>.
32. Pritzker KPH, Gay S, Jimenez SA, Ostergaard MD, Pelletier JP, Revell PA, et al. Osteoarthritis cartilage histopathology: grading and staging. *Osteoarthritis Cartilage* 2006;14(1):13–29, <https://doi.org/10.1016/j.joca.2005.07.014>.
33. Muschter D, Fleischhauer L, Taheri S, Schilling AF, Clausen-Schaumann H, Grässel S. Sensory neuropeptides are required for bone and cartilage homeostasis in a murine destabilization-induced osteoarthritis model. *Bone* 2020;133:115181, <https://doi.org/10.1016/j.bone.2019.115181>.
34. Foradori MJ, Chen Q, Fernandez CA, Harper J, Li X, Tsang PCW, et al. Matrilin-1 is an inhibitor of neovascularization. *J Biol Chem* 2014;289(20):14301–9, <https://doi.org/10.1074/jbc.M113.529982>.
35. Li P, Fleischhauer L, Nicolae C, Prein C, Farkas Z, Saller MM, et al. Mice lacking the matrilin family of extracellular matrix proteins develop mild skeletal abnormalities and are susceptible to age-associated osteoarthritis. *Int J Mol Sci* 2020;21(2), <https://doi.org/10.3390/ijms21020666>.
36. Gronau T, Krüger K, Prein C, Aszodi A, Gronau I, Iozzo RV, et al. Forced exercise-induced osteoarthritis is attenuated in mice lacking the small leucine-rich proteoglycan decorin. *Ann Rheum Dis* 2017;76(2):442–9, <https://doi.org/10.1136/annrheumdis-2016-209319>.
37. Vogel KG, Paulsson M, Heinegård D. Specific inhibition of type I and type II collagen fibrillogenesis by the small proteoglycan of tendon. *Biochem J* 1984;223(3):587–97, <https://doi.org/10.1042/bj2230587>.
38. Alberton P, Dugonitsch HC, Hartmann B, Li P, Farkas Z, Saller MM, et al. Aggrecan hypomorphism compromises articular cartilage biomechanical properties and is associated with increased incidence of spontaneous osteoarthritis. *Int J Mol Sci* 2019;20(5), <https://doi.org/10.3390/ijms20051008>.
39. Chen Y, Cossman J, Jayasuriya CT, Li X, Guan Y, Fonseca V, et al. Deficient mechanical activation of anabolic transcripts and post-traumatic cartilage degeneration in matrilin-1 knockout mice. *PLoS One* 2016;11(6), e0156676, <https://doi.org/10.1371/journal.pone.0156676>.

8. References

- [1] F. Berenbaum, I. J. Wallace, D. E. Lieberman, and D. T. Felson, “Modern-day environmental factors in the pathogenesis of osteoarthritis,” *Nat. Rev. Rheumatol.*, vol. 14, no. 11, pp. 674–681, 2018.
- [2] S. Safiri *et al.*, “Global, regional and national burden of osteoarthritis 1990-2017: A systematic analysis of the Global Burden of Disease Study 2017,” *Ann. Rheum. Dis.*, vol. 79, no. 6, pp. 819–828, 2020.
- [3] J. T. Evans, R. W. Walker, J. P. Evans, A. W. Blom, A. Sayers, and M. R. Whitehouse, “How long does a knee replacement last? A systematic review and meta-analysis of case series and national registry reports with more than 15 years of follow-up,” *Lancet*, vol. 393, no. 10172, pp. 655–663, 2019.
- [4] Y. Zhang and J. M. Jordan, “Epidemiology of osteoarthritis,” *Epidemiol. Osteoarthr.*, vol. 26, no. 3, pp. 355–369, 2010.
- [5] T. D. Spector and A. J. MacGregor, “Risk factors for osteoarthritis: Genetics,” *Osteoarthr. Cartil.*, vol. 12, pp. 39–44, 2004.
- [6] A. E. Peters, R. Akhtar, E. J. Comerford, and K. T. Bates, “The effect of ageing and osteoarthritis on the mechanical properties of cartilage and bone in the human knee joint,” *Sci. Rep.*, vol. 8, no. 5931, pp. 1–13, 2018.
- [7] M. Rahmati, G. Nalesso, A. Mobasheri, and M. Mozafari, “Aging and osteoarthritis: Central role of the extracellular matrix,” *Ageing Res. Rev.*, vol. 40, pp. 20–30, 2017.
- [8] A. D. Woolf and B. Pfleger, “Burden of major musculoskeletal conditions,” *Bull. World Health Organ.*, vol. 81, no. 9, pp. 646–656, 2003.
- [9] S. Glyn-Jones *et al.*, “Osteoarthritis,” *Lancet*, vol. 386, pp. 376–87, 2015.

- [10] Y. He *et al.*, “Pathogenesis of osteoarthritis: Risk factors, regulatory pathways in chondrocytes, and experimental models,” *Biology (Basel)*, vol. 9, no. 8, pp. 1–32, 2020.
- [11] T. L. Vincent and A. K. T. Wann, “Mechanoadaptation : articular cartilage through thick and thin,” vol. 5, pp. 1271–1281, 2019.
- [12] S. Grässel and D. Muschter, “Recent advances in the treatment of osteoarthritis,” *F1000Research*, vol. 9, p. 325, 2020.
- [13] C. B. Carballo, Y. Nakagawa, I. Sekiya, and S. A. Rodeo, “Basic Science of Articular Cartilage,” *Clin. Sports Med.*, vol. 36, no. 3, pp. 413–425, 2017.
- [14] B. He, J. P. Wu, T. B. Kirk, J. A. Carrino, C. Xiang, and J. Xu, “High-resolution measurements of the multilayer ultra-structure of articular cartilage and their translational potential,” *Arthritis Res. Ther.*, vol. 16, no. 2, p. 205, 2014.
- [15] S. Ricard-Blum, “The Collagen Family,” *Cold Spring Harb. Perspect. Biol.*, vol. 3, no. 1, pp. 1–19, 2011.
- [16] S. Li *et al.*, “Transgenic mice with targeted inactivation of the Col2a1 gene for collagen II develop a skeleton with membranous and periosteal bone but no endochondral bone,” *Genes Dev.*, vol. 9, pp. 2821–2830, 1995.
- [17] M. M. Hyttinen *et al.*, “Inactivation of one allele of the type II collagen gene alters the collagen network in murine articular cartilage and makes cartilage softer,” *Ann. Rheum. Dis.*, vol. 60, no. 3, pp. 262–268, 2001.
- [18] D. Eyre, “Collagen of articular cartilage,” *Arthritis Res.*, vol. 4, no. 1, pp. 30–35, 2002.
- [19] R. Fujioka, T. Aoyama, and T. Takakuwa, “The layered structure of the articular surface,” *Osteoarthr. Cartil.*, vol. 21, no. 8, pp. 1092–1098, 2013.

- [20] S. Hosseininia *et al.*, “Evidence for enhanced collagen type III deposition focally in the territorial matrix of osteoarthritic hip articular cartilage,” *Osteoarthr. Cartil.*, vol. 24, no. 6, pp. 1029–1035, 2016.
- [21] C. Wang *et al.*, “Type III collagen is a key regulator of the collagen fibrillar structure and biomechanics of articular cartilage and meniscus,” *Matrix Biol.*, vol. 85–86, pp. 47–67, 2020.
- [22] M. Cescon, F. Gattazzo, P. Chen, and P. Bonaldo, “Collagen VI at a glance,” *J. Cell Sci.*, vol. 128, no. 19, pp. 3525–3531, 2015.
- [23] L. G. Alexopoulos, I. Youn, P. Bonaldo, and F. Guilak, “Developmental and osteoarthritic changes in Col6a1-knockout mice: Biomechanics of type VI collagen in the cartilage pericellular matrix,” *Arthritis Rheum.*, vol. 60, no. 3, pp. 771–779, 2009.
- [24] K. L. Posey, K. Hankenson, A. C. Veerisetty, P. Bornstein, J. Lawler, and J. T. Hecht, “Skeletal abnormalities in mice lacking extracellular matrix proteins, thrombospondin-1, thrombospondin-3, thrombospondin-5, and type IX collagen,” *Am. J. Pathol.*, vol. 172, no. 6, pp. 1664–1674, 2008.
- [25] Y. Y. Luo and M. A. Karsdal, *Chapter 11 - Type XI Collagen*. Elsevier Inc., 2016.
- [26] Y. Luo *et al.*, “The minor collagens in articular cartilage,” *Protein Cell*, vol. 8, no. 8, pp. 560–572, 2017.
- [27] C. Kiani, L. Chen, Y. J. Wu, A. J. Yee, and B. B. Yang, “Structure and function of aggrecan,” *Cell Res.*, vol. 12, no. 1, pp. 19–32, 2002.
- [28] R. C. Gupta, R. Lall, A. Srivastava, and A. Sinha, “Hyaluronic acid: Molecular mechanisms and therapeutic trajectory,” *Front. Vet. Sci.*, vol. 6, p. 192, 2019.
- [29] P. Alberton *et al.*, “Aggrecan Hypomorphism Compromises Articular Cartilage Biomechanical Properties and Is Associated with Increased Incidence of Spontaneous Osteoarthritis,” *Int. J. Mol. Sci.*, vol. 20, no.

- 1008, 2019.
- [30] S. Grässer and A. Aszodi, *Cartilage - Volume I: Physiology and Development*, vol. 1. 2016.
- [31] B. Doyran, W. Tong, Q. Li, H. Jia, X. Zhang, and C. Chen, “Nanoindentation Modulus of Murine Cartilage: A Sensitive Indicator of the Initiation and Progression of Post-Traumatic Osteoarthritis,” *Osteoarthr. Cartil.*, vol. 25, no. 1, pp. 108–117, 2017.
- [32] D. R. Chery *et al.*, “Early Changes in Cartilage Pericellular Matrix Micromechanobiology Portend the Onset of Post-Traumatic Osteoarthritis,” *Acta Biomater.*, vol. 111, pp. 267–278, 2020.
- [33] P. Verma and K. Dalal, “ADAMTS-4 and ADAMTS-5: Key enzymes in osteoarthritis,” *J. Cell. Biochem.*, vol. 112, no. 12, pp. 3507–3514, 2011.
- [34] M. Wang *et al.*, “MMP13 is a critical target gene during the progression of osteoarthritis,” *Arthritis Res. Ther.*, vol. 15, no. 1, pp. 1–11, 2013.
- [35] D. D. D’Lima, B. J. Fregly, S. Patil, N. Steklov, and C. W. Colwell, “Knee joint forces: Prediction, measurement, and significance,” *Proc. Inst. Mech. Eng. Part H J. Eng. Med.*, vol. 226, no. 2, pp. 95–102, 2012.
- [36] W. Lee *et al.*, “Synergy between Piezo1 and Piezo2 channels confers high-strain mechanosensitivity to articular cartilage,” *Proc. Natl. Acad. Sci.*, vol. 111, no. 47, pp. E5114–E5122, 2014.
- [37] C. J. O’Conor, H. A. Leddy, H. C. Benefield, W. B. Liedtke, and F. Guilak, “TRPV4-mediated mechanotransduction regulates the metabolic response of chondrocytes to dynamic loading,” *Proc. Natl. Acad. Sci.*, vol. 111, no. 4, pp. 1316–1321, 2014.
- [38] J. Z. Kechagia, J. Ivaska, and P. Roca-Cusachs, “Integrins as biomechanical sensors of the microenvironment,” *Nat. Rev. Mol. Cell Biol.*, vol. 20, no. 8, pp. 457–473, 2019.

- [39] J. Kim *et al.*, “Matrix cross-linking – mediated mechanotransduction promotes posttraumatic osteoarthritis,” *Proc. Natl. Acad. Sci.*, vol. 112, no. 30, pp. 9424–9429, 2015.
- [40] H. P. Lee, L. Gu, D. J. Mooney, M. E. Levenston, and O. Chaudhuri, “Mechanical confinement regulates cartilage matrix formation by chondrocytes,” *Nat. Mater.*, vol. 16, no. 12, pp. 1243–1251, 2017.
- [41] S. J. Millward-Sadler *et al.*, “Tachykinin expression in cartilage and function in human articular chondrocyte mechanotransduction,” *Arthritis Rheum.*, vol. 48, no. 1, pp. 146–156, 2003.
- [42] K. Edoff and C. Hildebrand, “Neuropeptide effects on rat chondrocytes and perichondrial cells in vitro,” *Neuropeptides*, vol. 37, no. 5, pp. 316–318, 2003.
- [43] S. Suri, S. E. Gill, S. M. De Camin, D. Wilson, D. F. McWilliams, and D. A. Walsh, “Neurovascular invasion at the osteochondral junction and in osteophytes in osteoarthritis,” *Ann. Rheum. Dis.*, vol. 66, no. 11, pp. 1423–1428, 2007.
- [44] M. R. Howard, S. J. Millward-Sadler, A. S. Vasilliou, D. M. Salter, and J. P. Quinn, “Mechanical stimulation induces preprotachykinin gene expression in osteoarthritic chondrocytes which is correlated with modulation of the transcription factor neuron restrictive silence factor,” *Neuropeptides*, vol. 42, no. 5–6, pp. 681–686, 2008.
- [45] C. J. Alves *et al.*, “Nociceptive mechanisms driving pain in a post-traumatic osteoarthritis mouse model,” *Sci. Rep.*, vol. 10, no. 1, p. 15271, 2020.
- [46] J. I. Nagy, L. L. Iversen, M. Goedert, D. Chapman, and S. P. Hunt, “Dose-Dependent Effects of Capsaicin on Primary Sensory Neurons in the Neonatal Rat,” *J. Neurosci.*, vol. 3, no. 2, pp. 399–406, 1983.
- [47] M. A. Heffner, D. C. Genetos, and B. A. Christiansen, “Bone adaptation to mechanical loading in a mouse model of reduced

- peripheral sensory nerve function,” *PLoS One*, vol. 12, no. 10, pp. 1–20, 2017.
- [48] D. Hirt and G. W. Bernard, “CGRP-beta unlike CGRP-alpha has no osteogenic stimulatory effect in vitro,” *Peptides*, vol. 18, no. 9, pp. 1461–1463, 1997.
- [49] S. J. Sample *et al.*, “Role of calcitonin gene-related peptide in functional adaptation of the skeleton,” *PLoS One*, vol. 9, no. 12, pp. 1–18, 2014.
- [50] T. Niedermaier *et al.*, “Absence of substance P and the sympathetic nervous system impact on bone structure and chondrocyte differentiation in an adult model of endochondral ossification,” *Matrix Biol.*, vol. 38, pp. 22–35, 2014.
- [51] A. R. Klatt, A. K. A. Becker, C. D. Neacsu, M. Paulsson, and R. Wagener, “The matrilins: Modulators of extracellular matrix assembly,” *Int. J. Biochem. Cell Biol.*, vol. 43, no. 3, pp. 320–330, 2011.
- [52] X. Yang *et al.*, “Matrilin-3 inhibits chondrocyte hypertrophy as a bone morphogenetic protein-2 antagonist,” *J. Biol. Chem.*, vol. 289, no. 50, pp. 34768–34779, 2014.
- [53] L. Montanaro *et al.*, “Evidence of a linkage between matrilin-1 gene (MATN1) and idiopathic scoliosis,” *Scoliosis*, vol. 1, p. 21, 2006.
- [54] I. Strusberg *et al.*, “Association analysis of genotypic frequencies of matrilin-1 gene in patients with osteoarthritis,” *Clin. Exp. Rheumatol.*, vol. 20, no. 4, pp. 543–545, 2002.
- [55] A. Aszódi *et al.*, “Normal Skeletal Development of Mice Lacking Matrilin 1: Redundant Function of Matrilins in Cartilage?,” *Mol. Cell. Biol.*, vol. 19, no. 11, pp. 7841–7845, 1999.
- [56] X. Huang, D. E. Birk, and P. F. Goetinck, “Mice lacking matrilin-1 (cartilage matrix protein) have alterations in type II collagen

- fibrillogenesis and fibril organization,” *Dev. Dyn.*, vol. 216, no. 4–5, pp. 434–441, 1999.
- [57] K. L. Chapman, G. R. Mortier, K. Chapman, J. Loughlin, M. E. Grant, and M. D. Briggs, “Mutations in the region encoding the von Willebrand factor A domain of matrilin-3 are associated with multiple epiphyseal dysplasia,” *Nat. Genet.*, vol. 28, no. 4, pp. 393–396, 2001.
- [58] S. E. Stefánsson *et al.*, “Genomewide scan for hand osteoarthritis: A novel mutation in matrilin-3,” *Am. J. Hum. Genet.*, vol. 72, no. 6, pp. 1448–1459, 2003.
- [59] Y. Ko *et al.*, “Matrilin-3 Is Dispensable for Mouse Skeletal Growth and Development,” *Mol. Cell. Biol.*, vol. 24, no. 4, pp. 1691–1699, 2004.
- [60] L. Van Der Weyden *et al.*, “Functional knockout of the matrilin-3 gene causes premature chondrocyte maturation to hypertrophy and increases bone mineral density and osteoarthritis,” *Am. J. Pathol.*, vol. 169, no. 2, pp. 515–527, 2006.
- [61] O. Pullig, G. Weseloh, A. R. Klatt, R. Wagener, and B. Swoboda, “Matrilin-3 in human articular cartilage: Increased expression in osteoarthritis,” *Osteoarthr. Cartil.*, vol. 10, no. 4, pp. 253–263, 2002.
- [62] A. R. Klatt *et al.*, “Matrilin-3 activates the expression of osteoarthritis-associated genes in primary human chondrocytes,” *FEBS Lett.*, vol. 583, no. 22, pp. 3611–3617, 2009.
- [63] C. Nicolae *et al.*, “Abnormal collagen fibrils in cartilage of matrilin-1/matrilin-3-deficient mice,” *J. Biol. Chem.*, vol. 282, no. 30, pp. 22163–22175, 2007.
- [64] L. Mátés, C. Nicolae, M. Mörgelin, F. Deák, I. Kiss, and A. Aszódi, “Mice lacking the extracellular matrix adaptor protein matrilin-2 develop without obvious abnormalities,” *Matrix Biol.*, vol. 23, no. 3, pp. 195–204, 2004.

- [65] S. Zhang *et al.*, “Matrilin-2 is a widely distributed extracellular matrix protein and a potential biomarker in the early stage of osteoarthritis in articular cartilage,” *Biomed Res. Int.*, vol. 2014, p. 986127, 2014.
- [66] G. Binnig, C. F. Quate, and C. Gerber, “Atomic Force Microscope,” *Phys. Rev. Lett.*, vol. 56, no. 9, pp. 931–934, 1986.
- [67] M. Radmacher, R. W. Tillmann, M. Fritz, and H. E. Gaub, “From molecules to cells: Imaging soft samples with the atomic force microscope,” *Science (80-.)*, vol. 257, no. 5078, pp. 1900–1905, 1992.
- [68] C. Prein, N. Warmbold, Z. Farkas, M. Schieker, A. Aszodi, and H. Clausen-Schaumann, “Structural and mechanical properties of the proliferative zone of the developing murine growth plate cartilage assessed by atomic force microscopy,” *Matrix Biol.*, vol. 50, pp. 1–15, 2016.
- [69] H. Hertz, “Über die Berührung fester elastischer Körper.,” *J. für die reine und Angew. Math.*, vol. 92, pp. 156–171, 1882.
- [70] I. N. Sneddon, “The relation between load and penetration in the axisymmetric boussinesq problem for a punch of arbitrary profile,” *Int. J. Eng. Sci.*, vol. 3, no. 1, pp. 47–57, 1965.
- [71] G. G. Bilodeau, “Regular pyramid punch problem,” *J. Appl. Mech. Trans. ASME*, vol. 59, no. 3, pp. 519–523, 1992.
- [72] L. Han and A. J. Grodzinsky, *Advances and Applications of Nanomechanical Tools in Cartilage Tissue Engineering*. 2015.
- [73] B. Hartmann *et al.*, “Early detection of cartilage degeneration: A comparison of histology, fiber bragg grating-based micro-indentation, and atomic force microscopy-based nano-indentation,” *Int. J. Mol. Sci.*, vol. 21, no. 19, p. 7384, 2020.
- [74] D. Lin *et al.*, “Loss of tenomodulin expression is a risk factor for age-related intervertebral disc degeneration,” *Aging Cell*, vol. 19, no. 3, p. e13091, 2020.

- [75] S. Dex *et al.*, “Tenomodulin is Required for Tendon Endurance Running and Collagen I Fibril Adaptation to Mechanical Load,” *EBioMedicine*, vol. 20, pp. 240–254, 2017.
- [76] A. A. Mieloch, M. Richter, T. Trzeciak, M. Giersig, and J. D. Rybka, “Osteoarthritis Severely Decreases the Elasticity and Hardness of Knee Joint Cartilage: A Nanoindentation Study,” *J. Clin. Med.*, vol. 8, no. 11, p. 1865, 2019.
- [77] E. Aro *et al.*, “Severe extracellular matrix abnormalities and chondrodysplasia in mice lacking collagen prolyl 4-hydroxylase isoenzyme II in combination with a reduced amount of isoenzyme I,” *J. Biol. Chem.*, vol. 290, no. 27, pp. 16964–16978, 2015.
- [78] M. Stolz *et al.*, “Early detection of aging cartilage and osteoarthritis in mice and patient samples using atomic force microscopy,” *Nat. Nanotechnol.*, vol. 4, no. March, pp. 186–192, 2009.
- [79] C. Y. Wen *et al.*, “Collagen fibril stiffening in osteoarthritic cartilage of human beings revealed by atomic force microscopy,” *Osteoarthr. Cartil.*, vol. 20, no. 8, pp. 916–922, 2012.
- [80] J. A. Wahlquist *et al.*, “Indentation Mapping Reveals Poroelastic, but not Viscoelastic, Properties Spanning Native Zonal Articular Cartilage,” *Acta Biomater.*, vol. 64, pp. 41–49, 2017.
- [81] P. Seifer *et al.*, “The Matrilin-3 T298M mutation predisposes for post-traumatic osteoarthritis in a knock-in mouse model,” *Osteoarthr. Cartil.*, vol. 29, no. 1, pp. 78–88, 2021.
- [82] P. Li *et al.*, “Mice Lacking the Matrilin Family of Extracellular Matrix Proteins Develop Mild Skeletal Abnormalities and Are Susceptible to Age- Associated Osteoarthritis,” *Int. J. Mol. Sci.*, vol. 21, no. 2, p. 666, 2020.
- [83] M. A. McLeod, R. E. Wilusz, and F. Guilak, “Depth-dependent anisotropy of the micromechanical properties of the extracellular and

- pericellular matrices of articular cartilage evaluated via atomic force microscopy,” *J. Biomech.*, vol. 46, no. 3, pp. 586–592, 2013.
- [84] T. Gronau *et al.*, “Forced exercise-induced osteoarthritis is attenuated in mice lacking the small leucine-rich proteoglycan decorin,” *Ann. Rheum. Dis.*, vol. 76, no. 2, pp. 442–449, 2016.
- [85] D. R. Chery *et al.*, “Decorin regulates cartilage pericellular matrix micromechanobiology,” *Matrix Biol.*, vol. 96, pp. 1–17, 2021.
- [86] D. Muschter, L. Fleischhauer, S. Taheri, A. F. Schilling, H. Clausen-Schaumann, and S. Grässel, “Sensory neuropeptides are required for bone and cartilage homeostasis in a murine destabilization-induced osteoarthritis model,” *Bone*, vol. 133, p. 115181, 2020.
- [87] L. Fleischhauer, D. Muschter, P. Alberton, S. Grässel, A. Aszodi, and H. Clausen-Schaumann, “Biomechanical analysis with IT-AFM of the articular cartilage zones in the murine DMM model,” *Manuscript*.
- [88] M. Loparic *et al.*, “Micro- And nanomechanical analysis of articular cartilage by indentation-type atomic force microscopy: Validation with a gel-microfiber composite,” *Biophys. J.*, vol. 98, no. 11, pp. 2731–2740, 2010.
- [89] R. Reuten *et al.*, “Basement membrane stiffness determines metastases formation,” *Nat. Mater.*, vol. 20, no. 6, pp. 892–903, 2021.
- [90] J. Candiello *et al.*, “Biomechanical properties of native basement membranes,” *FEBS J.*, vol. 274, no. 11, pp. 2897–2908, 2007.
- [91] L. Fleischhauer, H. Clausen-schaumann, and R. Reuten, “Assesment of the basement membrane stiffness via IT-AFM,” *Unpublished*.
- [92] L. M. Westermann *et al.*, “Imbalanced cellular metabolism compromises cartilage homeostasis and joint function in a mouse model of mucopolidosis type III gamma,” *Dis. Model. Mech.*, vol. 13, no. 11, p. dmm046425, 2020.
- [93] B. Han *et al.*, “AFM-Nanomechanical Test : An Interdisciplinary Tool

- That Links the Understanding of Cartilage and Meniscus Biomechanics, Osteoarthritis Degeneration, and Tissue Engineering,” *ACS Biomater.*, vol. 3, pp. 2033–2049, 2017.
- [94] S. S. Glasson, T. J. Blanchet, and E. A. Morris, “The surgical destabilization of the medial meniscus (DMM) model of osteoarthritis in the 129/SvEv mouse,” *Osteoarthr. Cartil.*, vol. 15, no. 9, pp. 1061–1069, 2007.
- [95] H. Iijima *et al.*, “Destabilization of the medial meniscus leads to subchondral bone defects and site-specific cartilage degeneration in an experimental rat model,” *Osteoarthr. Cartil.*, vol. 22, no. 7, pp. 1036–1043, 2014.
- [96] H. Fang *et al.*, “Early Changes of Articular Cartilage and Subchondral Bone in The DMM Mouse Model of Osteoarthritis,” *Sci. Rep.*, vol. 8, no. 1, p. 2855, 2018.
- [97] C. L. Blaker, E. C. Clarke, and C. B. Little, “Using Mouse Models to Investigate the Pathophysiology, Treatment, and Prevention of Post-Traumatic Osteoarthritis,” *J. Orthop. Res.*, vol. 35, no. 3, pp. 424–439, 2017.
- [98] L. Li *et al.*, “Biomechanical analysis of the effect of medial meniscus degenerative and traumatic lesions on the knee joint,” *Am. J. Transl. Res.*, vol. 11, no. 2, pp. 542–556, 2019.
- [99] J. J. Wu and D. R. Eyre, “Matrilin-3 forms disulfide-linked oligomers with matrilin-1 in bovine epiphyseal cartilage,” *J. Biol. Chem.*, vol. 273, no. 28, pp. 17433–17438, 1998.

Supplement A: Paper IV

© 2020. Published by The Company of Biologists Ltd | Disease Models & Mechanisms (2020) 13, dmm046425. doi:10.1242/dmm.046425



RESEARCH ARTICLE

Imbalanced cellular metabolism compromises cartilage homeostasis and joint function in a mouse model of mucopolipidosis type III gamma

Lena Marie Westermann¹, Lutz Fleischhauer^{2,3}, Jonas Vogel³, Zsuzsa Jenei-Lanzl⁴, Nataniel Floriano Ludwig⁵, Lynn Schau⁶, Fabio Morellini⁶, Anke Baranowsky¹, Timur A. Yorgan¹, Giorgia Di Lorenzo^{1,*}, Michaela Schweizer⁷, Bruna de Souza Pinheiro⁸, Nicole Ruas Guarany⁹, Fernanda Sperb-Ludwig⁸, Fernanda Visioli¹⁰, Thiago Oliveira Silva¹¹, Jamie Soul¹², Gretl Hendrickx^{1,‡}, J. Simon Wiegert¹³, Ida V. D. Schwartz^{8,11}, Hauke Clausen-Schaumann³, Frank Zaucke⁴, Thorsten Schinke¹, Sandra Pohl^{1,§,¶} and Tatyana Danyukova^{1,§,¶}

ABSTRACT

Mucopolipidosis type III (MLIII) gamma is a rare inherited lysosomal storage disorder caused by mutations in *GNPTG* encoding the γ -subunit of GlcNAc-1-phosphotransferase, the key enzyme ensuring proper intracellular location of multiple lysosomal enzymes. Patients with MLIII gamma typically present with osteoarthritis and joint stiffness, suggesting cartilage involvement. Using *Gnptg* knockout (*Gnptg*^{ko}) mice as a model of the human disease, we showed that missorting of a number of lysosomal enzymes is associated with intracellular accumulation of chondroitin sulfate in *Gnptg*^{ko} chondrocytes and their impaired differentiation, as well as with altered microstructure of the cartilage extracellular matrix (ECM). We also demonstrated distinct functional and structural properties of the Achilles tendons isolated from *Gnptg*^{ko} and *Gnptab* knock-in (*Gnptab*^{ki}) mice, the latter displaying a

more severe phenotype resembling mucopolipidosis type II (MLII) in humans. Together with comparative analyses of joint mobility in MLII and MLIII patients, these findings provide a basis for better understanding of the molecular reasons leading to joint pathology in these patients. Our data suggest that lack of GlcNAc-1-phosphotransferase activity due to defects in the γ -subunit causes structural changes within the ECM of connective and mechanosensitive tissues, such as cartilage and tendon, and eventually results in functional joint abnormalities typically observed in MLIII gamma patients. This idea was supported by a deficit of the limb motor function in *Gnptg*^{ko} mice challenged on a rotarod under fatigue-associated conditions, suggesting that the impaired motor performance of *Gnptg*^{ko} mice was caused by fatigue and/or pain at the joint.

This article has an associated First Person interview with the first author of the paper.

KEY WORDS: MLIII gamma, Lysosomal enzymes, Joints, Extracellular matrix, Cartilage, Tendon

INTRODUCTION

Mucopolipidosis type II and III are rare inherited lysosomal storage disorders that are characterized by an extensive clinical spectrum. Mucopolipidosis type II (MLII; MIM #252500), the most severe form of the disease, is caused by mutations in the *GNPTAB* gene encoding the membrane-bound precursor of α - and β -subunits of GlcNAc-1-phosphotransferase (EC 2.7.8.17) (Tiede et al., 2005). This enzyme catalyzes the formation of mannose 6-phosphate (M6P) residues on lysosomal enzymes for their proper targeting to lysosomes (Tiede et al., 2005; Kollmann et al., 2010). In patients with MLII, a complete loss of the activity of GlcNAc-1-phosphotransferase results in severe skeletal abnormalities with prenatal or neonatal onset, coarse face features, progressive neurodevelopmental delay, and cardiac and respiratory insufficiency, leading to death in early childhood (Velho et al., 2019). Although biochemically related to MLII, mucopolipidosis type III (MLIII) has a later onset of clinical symptoms and a slower disease progression, enabling survival to adulthood. Patients with MLIII can present with mild face coarsening, skin thickening, spinal deformities, tarsal/carpal tunnel syndrome and hip dysplasia, as well as joint stiffness and pain in the shoulders, hips, wrists, knees and/or ankles (Cathey et al., 2010; Oussoren et al., 2018; Tüysüz et al., 2018; Velho et al., 2019). MLIII can be caused by mutations in either *GNPTAB* or *GNPTG*, the latter encoding the γ -subunit of the hexameric ($\alpha_2\beta_2\gamma_2$) GlcNAc-1-phosphotransferase complex (Bao

¹Department of Osteology and Biomechanics, University Medical Center Hamburg-Eppendorf, 20246 Hamburg, Germany. ²Laboratory of Experimental Surgery and Regenerative Medicine, Clinic for General Trauma and Reconstructive Surgery, Ludwig-Maximilians University, 80336 Munich, Germany. ³Center for Applied Tissue Engineering and Regenerative Medicine (Center), University of Applied Sciences, 80533 Munich, Germany. ⁴Dr. Rolf M. Schwiete Research Unit for Osteoarthritis, Orthopedic University Hospital Friedrichsheim gGmbH, 60528 Frankfurt/Main, Germany. ⁵Post-Graduate Program in Genetics and Molecular Biology, Federal University of Rio Grande do Sul, 90040-060 Porto Alegre, Brazil. ⁶RG Behavioral Biology, Center for Molecular Neurobiology Hamburg (ZMNH), University Medical Center Hamburg-Eppendorf, 20251 Hamburg, Germany. ⁷Center for Molecular Neurobiology Hamburg (ZMNH), University Medical Center Hamburg-Eppendorf, 20251 Hamburg, Germany. ⁸Department of Genetics, Federal University of Rio Grande do Sul, 90040-060 Porto Alegre, Brazil. ⁹Occupational Therapy Faculty, Federal University of Pelotas, 96010-610 Pelotas, Brazil. ¹⁰Pathology Department, Federal University of Rio Grande do Sul, 90040-060 Porto Alegre, Brazil. ¹¹Post-Graduate Program in Medicine: Medical Sciences, Federal University of Rio Grande do Sul, 90040-060 Porto Alegre, Brazil. ¹²Skeletal Research Group, Biosciences Institute, Newcastle University, Newcastle upon Tyne NE1 3BZ, UK. ¹³RG Synaptic Wiring and Information Processing, Center for Molecular Neurobiology Hamburg (ZMNH), University Medical Center Hamburg-Eppendorf, 20251 Hamburg, Germany. ^{*}Present address: Telethon Institute of Genetics and Medicine (TIGEM), Pozzuoli, Napoli, Italy. [‡]Present address: Center of Medical Genetics, Antwerp University Hospital and University of Antwerp, Antwerp, Belgium. [§]These authors contributed equally to this work.

[¶]Authors for correspondence (s.pohl@uke.de; t.danyukova@uke.de)

© N.R.G., 0000-0002-7145-2528; F.S.-L., 0000-0002-2460-7064; S.P., 0000-0001-7409-7042; T.D., 0000-0002-6449-3636

This is an Open Access article distributed under the terms of the Creative Commons Attribution License (<https://creativecommons.org/licenses/by/4.0/>), which permits unrestricted use, distribution and reproduction in any medium provided that the original work is properly attributed.

Handling Editor: Monica J. Justice
Received 3 July 2020; Accepted 15 September 2020

et al., 1996; Raas-Rothschild et al., 2000; Tiede et al., 2005). Based on the affected gene, MLIII is accordingly classified into MLIII alpha/beta (MIM #252600) and MLIII gamma (MIM #252605) (Cathey et al., 2008). In contrast to MLII, in which the activity of GlcNAc-1-phosphotransferase is completely abolished, GlcNAc-1-phosphotransferase displays residual activity in individuals with MLIII alpha/beta and MLIII gamma, which might explain variable clinical presentation among these patients (Velho et al., 2019).

Whereas the majority of lysosomal storage disorders are caused by deficiency of a single lysosomal enzyme, lack of GlcNAc-1-phosphotransferase activity in MLII and MLIII leads to mistargeting of multiple enzymes from the lysosome, provokes their hypersecretion, and thus compromises lysosomal catabolic function in various tissues (Kollmann et al., 2010; Velho et al., 2019). This may result in the accumulation of non-degraded material within lysosomes that eventually impairs cellular homeostasis and imbalances cell metabolism. Previously, we have described a *Gnptg* knockout (*Gnptg^{ko}*) mouse model of human MLIII gamma, in which the lysosomal proteome and secretome were remarkably altered due to deficiency of the γ -subunit of GlcNAc-1-phosphotransferase (Di Lorenzo et al., 2018). In particular, we have shown that a subset of lysosomal enzymes involved in the degradation of sulfated glycosaminoglycans (GAGs), including arylsulfatase B (ArSB), β -galactosidase and β -hexosaminidase (HexB), were mistargeted from the lysosome in *Gnptg^{ko}* mouse fibroblasts and secreted into the extracellular space, thus leading to intracellular accumulation of heparan sulfates and chondroitin sulfate (CS)/dermatan sulfate (DS).

Sulfated GAGs represent one of the major components of the extracellular matrix (ECM) and are indispensable for ECM function, especially in the articular cartilage, which provides resistance to compressive and shear forces in the joint. Maintenance of cartilaginous ECM is regulated by a constant turnover of the collagen network and proteoglycans/GAGs by cartilage-resident cells, chondrocytes (Kuettner, 1992; Umlauf et al., 2010; Krishnan and Grodzinsky, 2018). Furthermore, alterations in the GAG sulfation pattern have been linked to aging and degeneration in the articular cartilage (Decker, 2017; Zhang et al., 2019). Because extensive joint pathology, such as limited joint mobility, osteoarthritis and hip joint destruction, is the main clinical complication in patients with MLIII gamma (Velho et al., 2019), it is particularly important to study the role of *Gnptg* in ECM maintenance in the joint.

Using the previously described *Gnptg^{ko}* mouse model, we investigated the impact of *Gnptg* deficiency on cartilage development, homeostasis and metabolism, as well as the involvement of lysosomal enzymes in the composition and structure of cartilaginous ECM in mice. Although we did not detect a severe skeletal phenotype in *Gnptg^{ko}* mice, we found that lack of *Gnptg* causes significant alterations at both cellular and tissue level. More specifically, we showed (1) hypersecretion of a number of GAG-degrading lysosomal enzymes in *Gnptg^{ko}* mouse chondrocytes, (2) altered intracellular morphology of *Gnptg^{ko}* chondrocytes due to accumulation of non-degraded GAGs, (3) impaired differentiation of *Gnptg^{ko}* chondrocytes, and (4) altered structure of the cartilage ECM in *Gnptg^{ko}* mice. Furthermore, as joint stiffness and limited mobility are clinical symptoms observed in both MLII and MLIII patients, we provide comparative data on joint mobility in MLII, MLIII alpha/beta and MLIII gamma patients, which indicate distinct joint pathology in these patients. Finally, by functional and structural analyses of the Achilles tendons isolated from *Gnptab-* and *Gnptg-*deficient mice, we demonstrate that deficiency of either α/β - or γ -subunits of GlcNAc-1-phosphotransferase confers the tendons distinct mechanical properties.

RESULTS

Patients with MLIII alpha/beta, MLIII gamma and MLII show differential joint mobility

Progressive joint stiffness of the hips, shoulders and fingers is a common clinical symptom in patients with MLIII and MLII (Pohl et al., 2010; Tüysüz et al., 2018; Velho et al., 2019). In this study, we performed a comparative analysis of the mobility characteristics of joints in patients with MLIII alpha/beta, MLIII gamma or MLII (Table S1). Using standard goniometric techniques, we assessed the range of motions (ROMs) as a parameter of the movement amplitude at large (shoulders, hips, elbows and knees) and medium (wrists and ankles) joints in four patients with MLII, two patients with MLIII alpha/beta and three patients with MLIII gamma (Fig. 1; Table S2). The analysis revealed differential joint mobility in these patients, with shoulders, hips and ankles being the stiffest joints in MLIII patients. In particular, the MLIII gamma patients presented a significantly decreased ROM during abduction and internal/external rotation of the shoulders, abduction and external rotation of the hips, as well as flexion of the ankles (Fig. 1).

MLII patients presented similar joint mobility defects during shoulder abduction, shoulder internal rotation and hip external rotation, while showing almost normal ankle plantar flexion. In line with the goniometry data on the hip joint mobility in MLIII gamma patients, histological analysis of the femur head articular cartilage from a 43-year-old patient diagnosed with MLIII gamma (Patient 9, Table S1) revealed that the articular surface of the analyzed bone fragment is very irregular and associated with the presence of cracks (or clefts) extending to the deep layer of the cartilaginous tissue (Fig. S1). In addition, pronounced cartilage erosion, chondroblast disorganization and clustering, as well as loss of proteoglycans were observed, whereas the subchondral bone tissue appeared to be preserved. These data suggest that the limited hip joint mobility in MLIII gamma patients could result from pathological alterations in the cartilaginous tissue of the femur head articular surface. Therefore, we next aimed to investigate the role of the γ -subunits of GlcNAc-1-phosphotransferase in cartilage function and homeostasis, using *Gnptg*-deficient mice.

Lysosomal accumulation of CS is associated with impaired differentiation of primary *Gnptg^{ko}* chondrocytes

Recently, we have shown that embryonic fibroblasts from *Gnptg^{ko}* mice are characterized by impaired M6P formation on a subgroup of lysosomal enzymes, resulting in their disturbed delivery to lysosomes and subsequent secretion into the extracellular space (Di Lorenzo et al., 2018). Among them are, in particular, lysosomal enzymes involved in the degradation of CS (Fig. 2A). CSs attached to proteoglycans are a predominant type of sulfated GAGs present in cartilaginous ECM produced by chondrocytes (Thorpe and Dorfman, 1963), and their constant turnover is essential for the maintenance of cartilage function. Similar to *Gnptg^{ko}* fibroblasts, decreased intracellular and increased extracellular activities of ArSB, HexB and β -glucuronidase (Gusb) were observed in *Gnptg^{ko}* chondrocytes, indicating missorting of these lysosomal enzymes in the absence of γ -subunits of GlcNAc-1-phosphotransferase (Fig. 2B). By contrast, lysosomal targeting of GalNAc-6-sulfatase (GalNS) was not affected (Fig. 2B). Consistently, the capability for lysosomal degradation of CS was significantly impaired in cells deficient for γ -subunits, as demonstrated by the 5-fold accumulation of [^{35}S]-CS moieties in *Gnptg^{ko}* chondrocytes versus wild-type control cells upon metabolic ^{35}S labeling (Fig. 2C). Importantly, supplementation with human recombinant ARSB led to a significant reduction of the accumulating CS in cultured *Gnptg^{ko}*

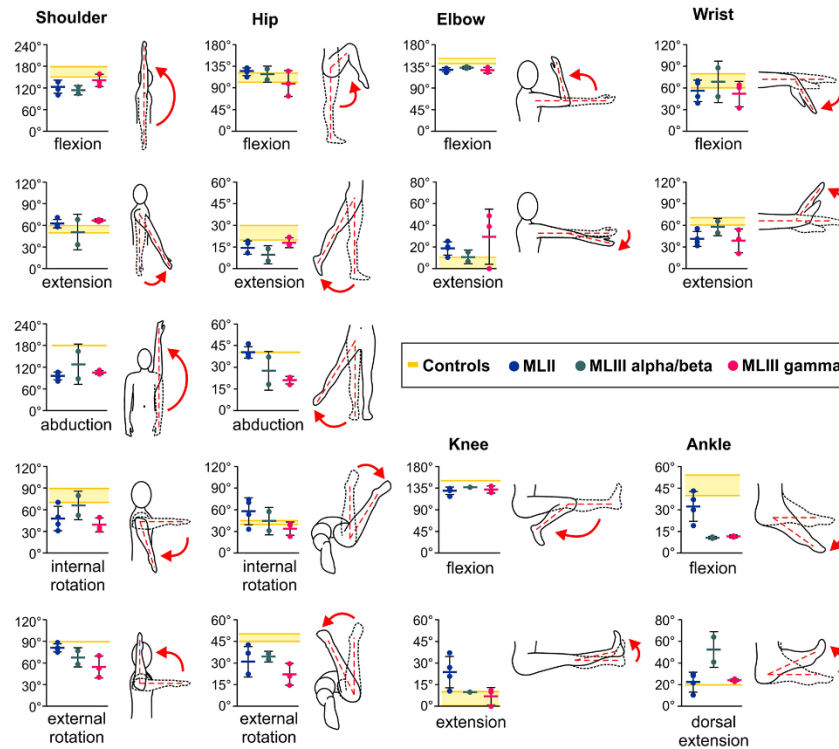


Fig. 1. Mobility characteristics of patients with MLII, MLIII alpha/beta and MLIII gamma. Range of motions (ROMs, in °) of shoulders, hips, elbows, wrists, knees and ankles were assessed in four patients with MLII, two patients with MLIII alpha/beta and three patients with MLIII gamma using standard goniometric techniques. Values represent the maximum angle and are means±s.d. of three measurements made by the same evaluator. Reference ROMs are indicated in yellow.

chondrocytes by ~70% (Fig. 2C). These results show that *Arsb* plays a crucial role in the degradation and turnover of sulfated GAGs in mouse chondrocytes.

To identify other lysosomal enzymes that are essential for chondrocyte function, we performed a comprehensive quantitative PCR (qPCR) expression analysis of 36 selected genes encoding soluble lysosomal enzymes (Fig. 2D). The transcript levels normalized to *Gapdh* expression varied between ~2.6 and 11.2, indicating a differential expression of lysosomal enzymes in chondrocytes (Fig. 2D; Table S3). In particular, we detected high mRNA levels of *Ctsb*, *Ctsl*, *Ctsk* and *Ctss*, encoding lysosomal cathepsins involved in the lysosomal proteolysis of endocytosed proteoglycans and collagenous proteins of cartilaginous ECM (Troeborg and Nagase, 2012). Using western blot analysis, we found that lysosomal targeting of these four cathepsins was not affected in *Gnptg*^{ko} chondrocytes because the mature, lysosomal forms of the enzymes were present in cell extracts of both wild-type and *Gnptg*^{ko} chondrocytes (Fig. 2E). Of note, besides extracellularly secreted matrix metalloproteinases and ADAM/ADAMTS proteases, lysosomal cathepsins can also mediate degradation of ECM proteins (Vizovišek et al., 2019). Accordingly, we observed a pronounced secretion of the precursor forms of cathepsin B, L and K into the cell culture media of wild-type chondrocytes, which was even more elevated in *Gnptg*^{ko} cells (Fig. 2E). We therefore

assume that proteolytic degradation of endocytosed ECM proteins by cysteine proteases in lysosomes is hardly affected in *Gnptg*^{ko} cells; nevertheless, increased secretion of the cathepsins B, L and K by *Gnptg*^{ko} chondrocytes could enhance degradation of the ECM extracellularly.

Aiming to assess the impact of *Gnptg* deficiency on morphology and function of chondrocytes, we first analyzed sections of the ribcage cartilage from 3-week-old *Gnptg*^{ko} mice by light microscopy. We observed intracellular inclusions inside the ribcage chondrocytes, indicating storage material accumulation, as well as clustering of the cells (Fig. 2F), suggesting aberrant ECM metabolism (Karim et al., 2018). Consistently, by performing ultrastructural analysis of the same tissue region, we identified a remarkable number of enlarged electron-lucent lysosomes, both in chondrocytes of the superficial layer and in hypertrophic chondrocytes of the deep layer in *Gnptg*^{ko} ribcage cartilage (Fig. 2G). The observed lysosomal storage material likely represents non-degraded CS, as identified in cultured chondrocytes isolated from *Gnptg*^{ko} mice (Fig. 2C). As impaired degradation of proteoglycans and other proteins of cartilaginous ECM can affect the functionality of chondrocytes, we next assessed the expression of cartilage-specific markers in primary *Gnptg*^{ko} chondrocytes by reverse transcription qPCR (qRT-PCR). We found that mRNA levels of aggrecan (*Acan*), the most abundant

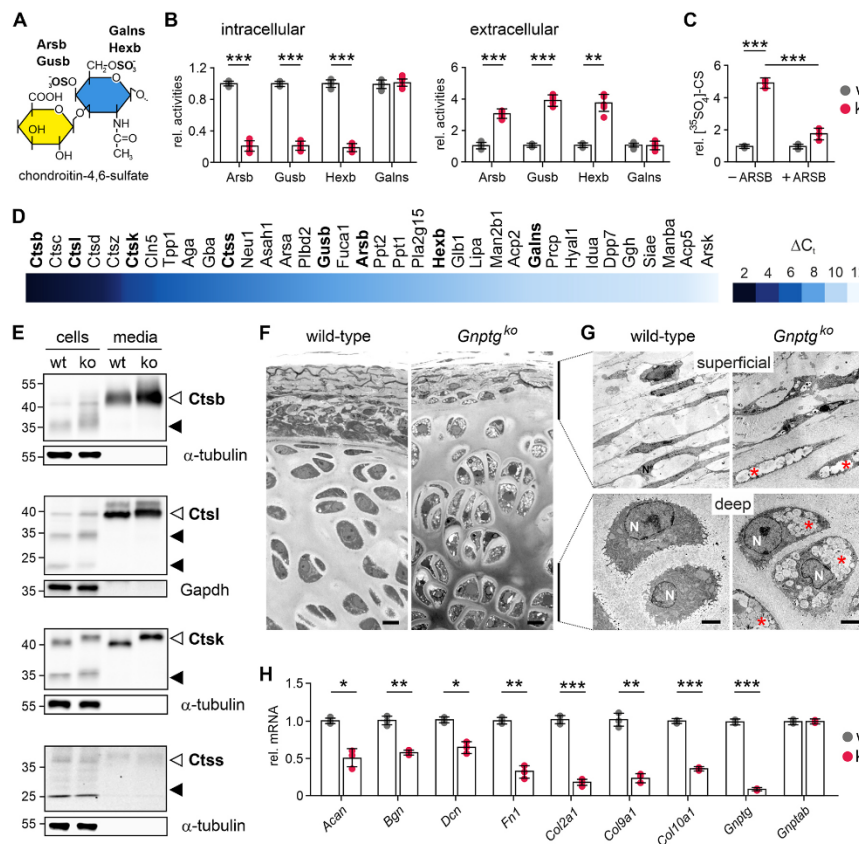


Fig. 2. Hypersecretion of lysosomal enzymes in *Gnptg*^{ko} ribcage chondrocytes is associated with impaired chondroitin sulfate degradation, chondrocyte differentiation and ECM protein expression. (A) Schematic overview of lysosomal enzyme degradation of chondroitin-4,6-sulfate, which consists of glucuronate (yellow) and N-acetylgalactosamine (blue). Of note, monosulfated chondroitin-4-sulfate or chondroitin-6-sulfate are also present. The lysosomal glycosidases β -glucuronidase (Gusb) and β -hexosaminidase (Hexb), as well as the lysosomal arylsulfatase B (Arsb) and GalNAc-6-sulfatase (Galns), cleaving C4- or C6-sulfates, respectively, are indicated. (B) Relative intracellular and extracellular enzyme activities of Arsb, Gusb, Hexb and Galns in cell extracts and corresponding media of wild-type (wt) and *Gnptg*^{ko} (ko) chondrocytes. Data are shown as means \pm s.d. generated in at least three independent experiments. **C** Relative total [³⁵S]-chondroitin sulfate (CS) content in wild-type (wt) and *Gnptg*^{ko} (ko) chondrocytes after 24 h pulse and 24 h chase in the absence (–) or presence (+) of human recombinant ARSB. Data are shown as means \pm s.d. from three independent experiments. **D** Heat map showing the expression (ΔC_t) of 36 selected genes encoding lysosomal enzymes normalized to *Gapdh* expression. Results were obtained by qPCR analysis of wild-type chondrocytes on day 10 of cultivation and represent mean values of three independent experiments (Table S3). Lysosomal enzymes, which were further analyzed here, are marked in bold. (E) Western blot analyses of whole-cell extracts (25 μ g protein) and aliquots (20%) of corresponding media of wild-type (wt) and *Gnptg*^{ko} (ko) chondrocytes using antibodies against cathepsins B (Ctsb), L (Ctsl), K (Ctsk) and S (Ctss). Representative blots of three independent experiments are shown. Endogenous *Gapdh* and α -tubulin in cell extracts were used as loading controls. The positions of precursors (open arrowheads) and mature forms (filled arrowheads) of the cathepsins are indicated. (F) Light microscopy of Methylene Blue-stained semi-thin sections (0.5 μ m) of ribcage cartilage isolated from 3-week-old wild-type and *Gnptg*^{ko} mice. Representative images from two mice per genotype are shown. Scale bars: 10 μ m. (G) Representative electron micrographs of the superficial and deep layers of the ribcage cartilage shown in F. Electron-lucent storage material is indicated (red asterisks). N, nuclei. Scale bars: 2 μ m. (H) Relative mRNA expression levels of *Acan*, *Bgn*, *Dcn*, *Fnl*, *Col2a1*, *Col9a1*, *Col10a1*, *Gnptg* and *Gnptab* in wild-type (wt) and *Gnptg*^{ko} (ko) ribcage chondrocytes. Data are shown as means \pm s.d. from three independent experiments (Table S4). **P* \leq 0.05, ***P* \leq 0.01, ****P* \leq 0.001 (unpaired two-tailed Student's *t*-test).

proteoglycan synthesized by chondrocytes, of the proteoglycans biglycan (*Bgn*) and decorin (*Dcn*) and of the structural glycoprotein fibronectin (*Fnl*) were significantly decreased in *Gnptg*^{ko} chondrocytes compared to wild-type cells, suggesting that the composition of the cartilage ECM is affected by *Gnptg* deficiency (Fig. 2H; Table S4). In addition, the expression of *Col2a1*, encoding

the predominant fibrillar collagen type in proliferating chondrocytes, of *Col10a1*, the marker of differentiated hypertrophic chondrocytes, as well as that of *Col9a1*, encoding fibril-associated collagen type IX, was strongly reduced in *Gnptg*^{ko} cells. Importantly, *Gnptab* expression in *Gnptg*^{ko} chondrocytes was normal, whereas *Gnptg* transcripts were almost absent in the same cells, indicating that the

observed defects were solely associated with deficiency of the γ -subunit of GlcNAc-1-phosphotransferase (Fig. 2H; Table S4).

Taken together, these data demonstrate that the lack of functional γ -subunits of GlcNAc-1-phosphotransferase leads to intracellular accumulation of storage material, owing to decreased intracellular activities of CS-degrading lysosomal enzymes as well as to impaired differentiation of *Gnptg*^{ko} chondrocytes.

***Gnptg*^{ko} mice display altered ECM homeostasis and compromised chondrocyte function in the cartilage**

Chondrocytes in the growth plate play a pivotal role in promoting longitudinal bone growth by endochondral ossification. More specifically, chondrocytes proliferate before differentiating into hypertrophic chondrocytes, which then undergo apoptosis followed by vascularization, resorption of the residual cartilage matrix by osteoclasts, and deposition of new bone by osteoblasts (Karsenty and Wagner, 2002). Based on the above data, showing impaired differentiation of isolated *Gnptg*^{ko} chondrocytes *in vitro*, we studied the consequences of the impaired chondrocyte differentiation *in vivo*. Therefore, we performed Movat pentachrome staining of the growth plate in undecalcified tibia sections from 4-week-old wild-type and *Gnptg*^{ko} mice. The organization of the growth plate between epiphyseal and metaphyseal bone, as well as the characteristic vertical column architecture of the growth plate chondrocytes, was not disturbed in *Gnptg*^{ko} mice (Fig. 3A). Accordingly, by histomorphometric analysis of Toluidine Blue-stained undecalcified tibia sections from 4- and 25-week-old wild-type and *Gnptg*^{ko} mice, we did not observe alterations in the thickness of the proliferating and hypertrophic zones of the growth plates (Fig. 3B,C). Finally, contact radiography revealed a moderate growth impairment in 4-week-old *Gnptg*^{ko} mice, which was accompanied by a reduced weight gain (Fig. S2). Although no alterations were found in the growth plate architecture and organization, ultrastructural analysis of the growth

plate in decalcified tibiae cryosections from 25-week-old *Gnptg*^{ko} mice revealed a remarkable number of enlarged electron-lucent lysosomes in hypertrophic chondrocytes (Fig. 3D), similarly to the appearance of chondrocytes in the ribcage cartilage of 3-week-old *Gnptg*^{ko} mice (Fig. 2G).

Whereas the growth plate cartilage is responsible for longitudinal bone growth, the articular cartilage serves as a load-bearing cushion that minimizes forces bones are subjected to. Similar to an unaltered tissue structure of the growth plate cartilage in 4- and 25-week-old *Gnptg*^{ko} mice (Fig. 3), we found no significant changes in the overall tissue morphology of the tibiae articular cartilage in *Gnptg*^{ko} mice at 40 weeks of age (Fig. 4). In particular, quantitative analysis of Toluidine Blue-stained tibiae sections revealed no difference in the articular cartilage thickness or in the chondrocyte number between wild-type and *Gnptg*^{ko} mice (Fig. 4A). In contrast to the chondrocytes of ribcage or tibia growth plate, we did not detect storage material inside the articular cartilage chondrocytes (Fig. 4B). Nevertheless, the ECM surrounding single chondrocytes appeared to be altered in all zones of the articular cartilage in *Gnptg*^{ko} mice, as evidenced by the presence of electron-dense aggregates outside the cells (Fig. 4B). Noteworthy, most of these aggregates had an elongated shape and were aligned along the ECM network surrounding the cells.

Collagen type II is the most abundant fibrillar protein in cartilage and produces a strong second harmonic generation (SHG) signal; thus, alterations in the SHG intensity reflect changes in the collagen structure and organization (Kim et al., 2000). Therefore, to assess changes in the collagen fibrillar network, we performed SHG microscopy of articular cartilage from 60-week-old wild-type and *Gnptg*^{ko} mice. In contrast to the low and homogenous SHG signal observed in wild-type animals, we found patches of elevated SHG intensity in the cartilage ECM of *Gnptg*^{ko} mice, which occurred in close proximity to the chondrocyte lacunae and indicated collagen

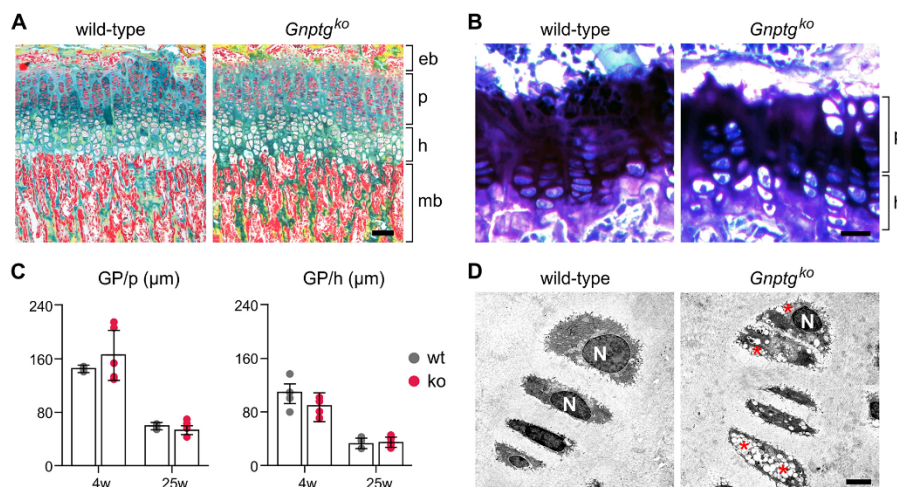


Fig. 3. *Gnptg*^{ko} mice display unaltered architecture of the growth plate. (A) Representative Movat pentachrome staining of the growth plate in undecalcified tibia sections from 25-week-old female wild-type and *Gnptg*^{ko} mice. eb, epiphysal bone; h, hypertrophic zone; mb, metaphysal bone; p, proliferating zone. Scale bar: 50 μm . (B) Representative Toluidine Blue staining of the growth plate in undecalcified tibia sections from 25-week-old female wild-type and *Gnptg*^{ko} mice. h, hypertrophic zone; p, proliferating zone. Scale bar: 20 μm . (C) Quantification of the growth plate (GP) width in proliferating (p) and hypertrophic (h) zones in 4- and 25-week-old wild-type (wt) and *Gnptg*^{ko} (ko) mice ($n=4$). (D) Representative electron micrographs of the growth plate hypertrophic chondrocytes in decalcified tibiae cryosections from 25-week-old female wild-type and *Gnptg*^{ko} mice. Storage material is indicated (red asterisks). N, nuclei. Scale bar: 2.5 μm .

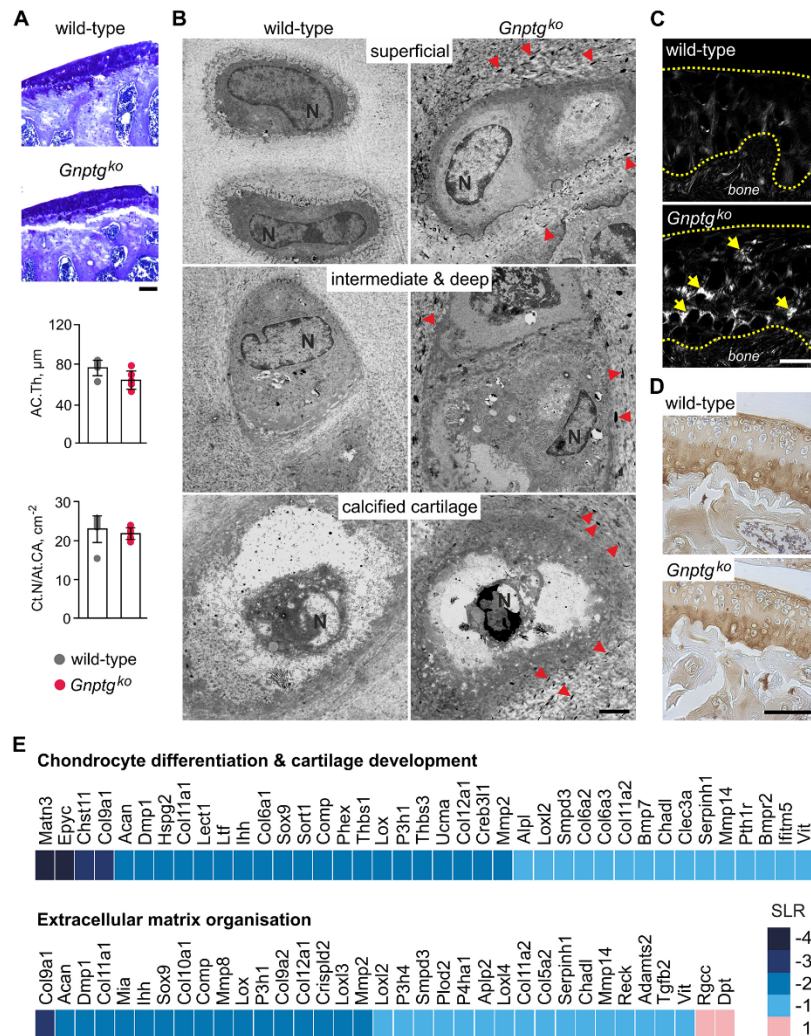


Fig. 4. The articular cartilage in *Gnptg^{ko}* mice has normal tissue morphology but altered ECM. (A) Representative Toluidine Blue staining of articular cartilage of undecalcified tibia sections from 40-week-old female wild-type and *Gnptg^{ko}* mice. Scale bar: 100 μm. Quantifications of articular cartilage thickness (AC.Th) and chondrocyte number per articular cartilage area (Cl.N/At.CA) of the same mice are given below (mean ± s.d., n=5). (B) Ultrastructural analysis of chondrocytes in the articular cartilage from 45-week-old female wild-type and *Gnptg^{ko}* mice. Representative images of different cartilage layers from two mice per genotype are shown. Red arrowheads indicate electron-dense aggregates in the extracellular matrix of *Gnptg^{ko}* mice. Scale bar: 2 μm. (C) Second harmonic generation (SHG) imaging of sagittal sections of the articular cartilage (outlined by dashed yellow lines) from 60-week-old female wild-type and *Gnptg^{ko}* mice. Representative images from three mice per genotype are shown. Yellow arrows point to the sites of collagen fibrillation. Scale bar: 50 μm. (D) Immunostaining of sagittal paraffin-embedded sections of the knee joint articular cartilage from 60-week-old wild-type and *Gnptg^{ko}* mice against collagen type II. Representative images from three mice per genotype are shown. Scale bar: 100 μm. (E) Heat map generated from microarray data (GEO accession number GSE157180) showing gene expression in the hip joint articular cartilage of 12-week-old female *Gnptg^{ko}* mice. The mean values of calculated Signal Log2 Ratio (SLR) relative to wild-type littermate mice are shown for each gene (n=6).

structure reorganization (Fig. 4C) (Chen and Broom, 1998; Kim et al., 2000). It should be noted that, despite the stronger SHG signal, the levels of collagen type II in the cartilage of *Gnptg^{ko}* mice were unaltered relative to those in wild-type animals, as

demonstrated by immunohistochemistry of the knee joint tissues (Fig. 4D). Thus, the elevated SHG signal in the cartilage of *Gnptg^{ko}* mice likely reflects structural changes in the collagen type II fibrillar network rather than its increased abundance.

To gain more information on the molecular mechanisms leading to alterations in the cartilage ECM in *Gnptg*-deficient mice, we performed gene expression profiling of the hip joint articular cartilage from 12-week-old wild-type and *Gnptg*^{ko} mice. Gene ontology enrichment analysis of the obtained microarray data revealed decreased expression of a number of genes involved in chondrocyte differentiation, cartilage development and ECM organization. Among those, matrilin-3 (*Matn3*) and epiphycan (*Epyc*), which are essential components of collagen fibrillar network in cartilage (Klitt et al., 2011; Brachvogel et al., 2013), were the most downregulated in *Gnptg*^{ko} mice, with a Log2 ratio of -4 compared to wild-type animals (Fig. 4E). Genes encoding other collagen fibril-associated proteins, such as collagen type IX (*Col9a1*), cartilage oligomeric matrix protein (*Comp*) and thrombospondin-1 (*Thbs1*), were found to be moderately downregulated (Log2 ratios between -2 and -3). Although we could not detect significant alterations in the protein amounts of collagen type IX, COMP, Matn3 and Thbs1 in the articular cartilage of *Gnptg*^{ko} mice (Fig. S3) at the age of 60 weeks, we suppose that cartilaginous ECM homeostasis can be affected in *Gnptg*^{ko} mice by transcriptional downregulation of these genes at a younger age. In line with the gene expression data in ribcage chondrocytes (Fig. 2H), the hypertrophic chondrocyte markers *Acan* and *Col10a1*, as well as the transcription factor *Sox9*, were strongly downregulated in *Gnptg*^{ko} mice, suggesting impaired chondrocyte differentiation. Based on these data, we conclude that *Gnptg* deficiency compromises both ECM homeostasis and chondrocyte function in mouse cartilage and may thus affect overall stability and movement of the joint.

Structural and functional analysis of the Achilles tendon in *Gnptg*^{ko} mice reveals an age-dependent reduction in the stiffness of collagen fibrils

Movement at the joint occurs owing to contracting muscles that transmit forces onto bones through collagenous connective tissues, called tendons. The Achilles tendon is the strongest and largest tendon in the human body that, acting together with the shin muscles, controls plantar flexion of the ankle joint. Because patients with MLIII, but not MLII, displayed impaired plantar flexion in their ankles (Fig. 1), we performed structural and functional analyses of the Achilles tendons isolated from 30- and 60-week-old *Gnptg*^{ko} and 30-week-old *Gnptab*^{kt} mice. By electron microscopy of the Achilles tendons, we found enlarged lysosomal compartments in tendon cells (tenocytes) of both mutant mouse models, which were filled with electron-lucent storage material (Fig. 5A), indicating compromised cell metabolism and matrix turnover in the tendon.

The ECM of tendons consists of collagen fibrils that align laterally to form fibril bundles and fibers, the structure and composition of which define their mechanical properties (Zhang et al., 2005). Therefore, by means of atomic force microscopy (AFM), we measured the diameter of single collagen fibrils in tendons of 30-week-old *Gnptg*^{ko}, *Gnptab*^{kt} and wild-type mice. The tendon fibril thickness in *Gnptg*^{ko} mice was comparable to that in wild-type controls (~ 170 nm), whereas the tendons from *Gnptab*^{kt} mice were composed of fibrils of a significantly decreased diameter (~ 150 nm; Fig. 5B). Furthermore, using the calculated mean angle between collagen fibrils and the proximodistal axis of the fiber as a measure of fibril alignment, we found that fibrils in the tendons of 30-week-old *Gnptg*^{ko} and *Gnptab*^{kt} mice align normally, whereas 60-week-old *Gnptg*^{ko} mice display a modest but significant fibril misalignment in their tendons compared to age-matched wild-type mice ($-1.4 \pm 0.7^\circ$ in *Gnptg*^{ko} versus $-0.3 \pm 0.8^\circ$ in wild-type mice)

(Fig. 5C,D). Finally, by means of indentation-type (IT) AFM, we analyzed the elastic modulus of collagen fibrils of the Achilles tendons from *Gnptg*^{ko} and *Gnptab*^{kt} mice, which is defined as Young's modulus (Fig. 5E). Significantly increased Young's modulus values were observed in 30-week-old *Gnptab*^{kt} mice compared to age-matched wild-type mice (271.8 ± 1.3 kPa in *Gnptab*^{kt} versus 262.6 ± 1.4 kPa in wild-type mice), indicating elevated tendon stiffness in the mutant mice. By contrast, stiffness of collagen fibrils in *Gnptg*^{ko} mice at 30 weeks of age was decreased, as demonstrated by significantly reduced Young's modulus values (248.6 ± 1.6 kPa in *Gnptg*^{ko} versus 262.6 ± 1.4 kPa in wild-type mice), with the difference from that in wild-type mice being even more pronounced at 60 weeks of age (264.6 ± 1.9 kPa in *Gnptg*^{ko} versus 319.0 ± 2.2 kPa in wild-type mice). Altogether, these data suggest that defects in either *Gnptg* or *Gnptab* define differential mechanical properties of the Achilles tendon in mice, resulting in lower tendon stiffness in *Gnptg*^{ko} mice or increased tendon stiffness in *Gnptab*^{kt} mice.

Age-dependent motor impairment in *Gnptg*^{ko} mice

Previous studies have reported behavioral deficits, in particular in motor function, in mouse models of MLII and MLIII (Idol et al., 2014; Paton et al., 2014). We thus assessed motor function in 4-, 6- and 8-month-old *Gnptg*^{ko} and wild-type mice in the rotarod test using two different protocols. In the accelerated rotarod test, the performance of *Gnptg*^{ko} mice did not differ from that of wild-type mice, suggesting that coordination and motor learning, and thereby cerebellar function, are normal in *Gnptg*^{ko} mice (Fig. 6A). We then used a protocol that challenges motor performance by forcing the mice to run at a high rotation speed in three consecutive trials within a daily session. In this case, the mixed two-way ANOVA detected a significant effect of the interaction between genotype and trial in mice aged 6 ($F_{2,30}=9.665$; $P=0.0006$) and 8 ($F_{2,30}=2.713$; $P=0.0826$) months, but not in those aged 4 months ($F_{2,30}=0.137$; $P=0.8724$). Post hoc comparisons showed that 6- and 8-month-old *Gnptg*^{ko} mice fell faster from the rod than the age-matched wild-type mice, specifically in the third trial of each session, suggesting that their impaired motor performance was caused by fatigue or pain (Fig. 6B). Noteworthy, there were no differences between the genotypes in the grip strength test performed in 5- and 7-month-old mice, suggesting that the impaired performance of *Gnptg*^{ko} mice in the rotarod test was not due to impaired muscular function (Fig. S4A). In contrast to the mild neurological deficits of *Gnptg*^{-/-} male mice reported previously (Idol et al., 2014), we did not detect any abnormal behavior in our *Gnptg*^{ko} male mice at similar ages. Specifically, the open field test did not reveal differences in the performance of 4- and 6-month-old *Gnptg*^{ko} and wild-type mice, indicating that general locomotion and novelty-induced exploration and anxiety are not affected in *Gnptg*^{ko} mice (Fig. S4B,C).

DISCUSSION

Formation of M6P moieties by GlcNAc-1-phosphotransferase confers lysosomal enzymes a targeting signal that ensures their delivery to lysosomes and proper lysosomal function (Tiede et al., 2005; Kollmann et al., 2010). Accordingly, lack of GlcNAc-1-phosphotransferase activity due to defects in the α -, β - or γ -subunits compromises lysosomal catabolic function in the cell and can eventually cause MLII, MLIII alpha/beta or MLIII gamma in humans (Velho et al., 2019). In MLII and MLIII patients, clinical symptoms are generally broad, but skeletal abnormalities are common. Whereas MLII results in severe skeletal defects and is

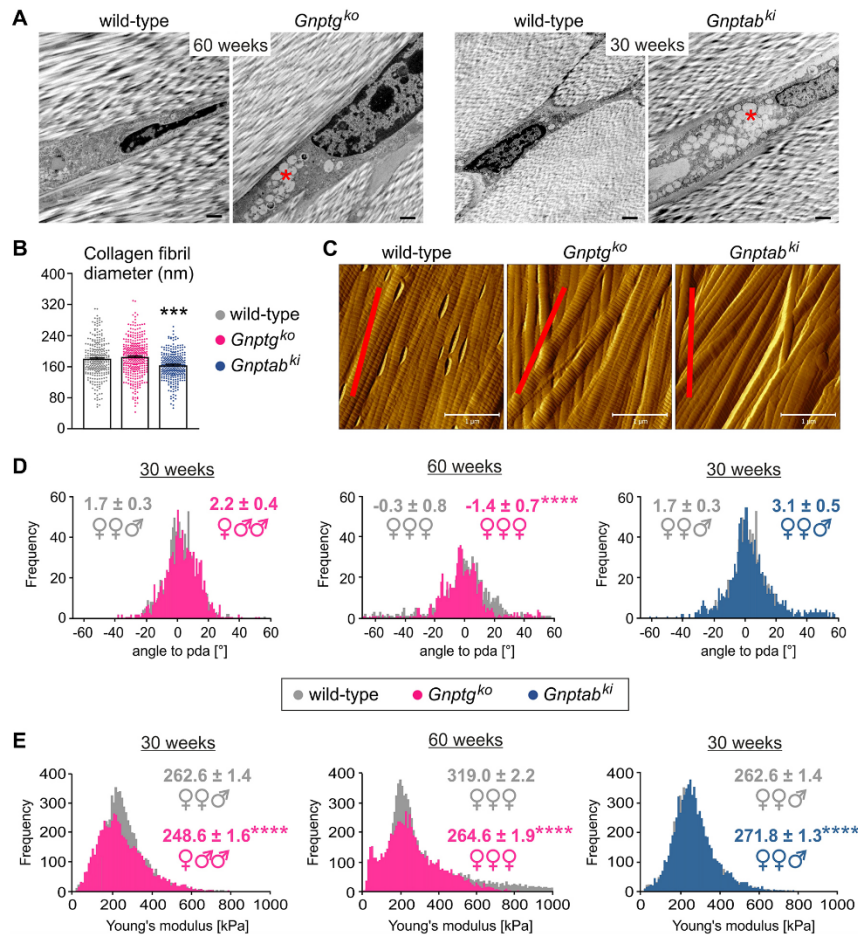


Fig. 5. Structural and functional analysis of the Achilles tendon in *Gnptab^{ki}* and *Gnptg^{ko}* mice. (A) Ultrastructural analysis of the Achilles tendon from *Gnptg^{ko}* (60-week-old), *Gnptab^{ki}* (30-week-old) and age-matched wild-type mice. Representative images from two mice per genotype are shown. Electron-lucent storage material is indicated (red asterisks). Scale bars: 1 μ m. (B-E) Atomic force microscopy (AFM) analysis of collagen type I fibrils in the Achilles tendons of 30- and 60-week-old mice. The results obtained from three mice per genotype per age are shown (sex of each mouse is indicated as σ or ρ). (B) Average collagen fibril diameters in 30-week-old mice (mean \pm s.e.m.). Each dot represents a single fibril measured. *** P < 0.0001 (unpaired two-tailed Student's t -test). (C) Representative AFM topographical images of collagen type I fibrils of 30-week-old mice. The proximodistal axis (pda) is shown as a red line. Scale bars: 1 μ m. (D) Frequency distribution of angles to pda for single collagen fibrils in 30- and 60-week-old mice. Values shown are mean \pm s.e.m. **** P < 0.0001 (two-tailed Mann-Whitney test). (E) Frequency distribution of Young's modulus denoting the elastic properties of collagen fibrils in 30- and 60-week-old mice. Values shown are mean \pm s.e.m. **** P < 0.0001 (two-tailed Mann-Whitney test).

recognizable at birth, MLIII alpha/beta and MLIII gamma patients have much milder forms of skeletal pathology, such as joint stiffness, osteoarthritis and hip joint destruction, and are clinically indistinguishable. Because MLIII gamma is often misdiagnosed and not verified by genetic analyses, there is a lack of correlation between the clinical course of MLIII gamma and mutations in *GNPTG*, encoding the γ -subunit of GlcNAc-1-phosphotransferase (Velho et al., 2019). The present study provides new insights into the role of the γ -subunit in coupling lysosomal homeostasis with skeletal function, including chondrocyte differentiation, cartilage

maintenance, as well as the structure of cartilaginous and tendinous ECM, using a mouse model of MLIII gamma.

In *Gnptg^{ko}* embryonic fibroblasts, impaired M6P formation on a subset of GAG-degrading lysosomal enzymes results in the secretion of these enzymes into the extracellular space, while bypassing lysosomes (Di Lorenzo et al., 2018). CS is the major type of sulfated GAGs synthesized by chondrocytes and its turnover is essential for cartilage maintenance (Thorpe and Dorfman, 1963). Our data suggest that *Gnptg* deficiency not only disturbs lysosomal homeostasis through hypersecretion of the CS-degrading lysosomal

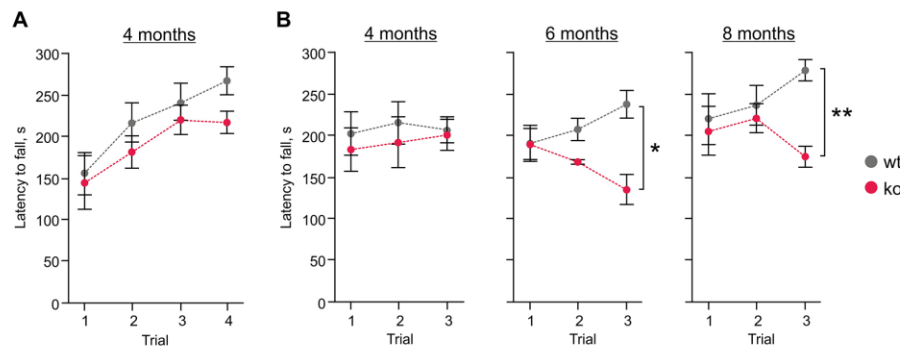


Fig. 6. *Gnptg*^{ko} mice display age-dependent impaired motor performance on a rotating rod. (A,B) *Gnptg*^{ko} (ko) and wild-type (wt) male mice were tested on a rod rotating at an accelerating speed in four consecutive trials (A) or at a constant speed in three consecutive trials (B). Values are shown as means \pm s.e.m. ($n=10$ for wild-type, $n=7$ for *Gnptg*^{ko}). * $P<0.05$, ** $P<0.01$ (Sidak's multiple comparisons following a mixed two-way ANOVA).

enzymes *Arsb*, *Hexb* and *Gusb*, but also affects the chondrocyte program for differentiation and ECM synthesis. Secretion of the lysosomal cysteine proteases cathepsin B, L and K appeared to be more pronounced in *Gnptg*^{ko} chondrocytes. In addition to their intracellular function, these proteases also act extracellularly, by cleaving a number of ECM components including the glycoproteins laminin and fibronectin, as well as collagens (Buck et al., 1992; Mort et al., 2016; Vidak et al., 2019). Therefore, hypersecretion of these proteases by chondrocytes could result in increased degradation of cartilaginous ECM and compromised cartilage homeostasis in *Gnptg*-deficient mice. Cartilage possesses limited self-regenerative capacity, and the efficiency of cartilage repair depends on the composition and structure of ECM, which delivers specific biological signals to the embedded chondrocytes (Emans and Peterson, 2014; Mao et al., 2019). Hence, even minor changes in the cartilage ECM can affect chondrocyte differentiation and provide a positive feedback that aggravates cartilage dysfunction.

Although cultured *Gnptg*^{ko} ribcage chondrocytes exhibited decreased intracellular activity of *Arsb* and elevated accumulation of CS, the addition of recombinant human ARSB (Naglazyme[®]) to the culture medium resulted in significant restoration of CS degradation. These data support our previous findings in *Gnptg*^{ko} fibroblasts (Di Lorenzo et al., 2018) and point to a critical role of *Arsb* in the turnover of CS by chondrocytes. In fact, *Arsb* is a key lysosomal enzyme regulating skeletal remodeling, and its deficiency in mice results in growth retardation and lysosomal storage in both bone cells and chondrocytes (Pohl et al., 2018). Treatment of mouse *Arsb*^{mm} chondrocytes with Naglazyme[®] *in vitro* has been shown to significantly reduce lysosomal defects, despite a relatively low uptake of the recombinant ARSB by chondrocytes (Hendrickx et al., 2020). However, cartilage deficits could not be corrected in *Arsb*^{mm} mice receiving Naglazyme[®], probably due to poor delivery of the systemically administered ARSB into chondrocytes (Hendrickx et al., 2020). Although it is tempting to recognize recombinant ARSB as a potential therapeutic for correcting cartilage defects caused by abnormal GAG accumulation in MLIII gamma, the issue of poor targeted delivery of ARSB to chondrocytes needs to be considered in future *in vivo* studies.

Short stature and abnormal bone development (dysostosis multiplex) are typically recognized in MLIII patients, suggesting growth plate involvement (Cathey et al., 2010; Oussoren et al., 2018; Tüysüz et al., 2018). Although storage material was found to accumulate in the growth plate chondrocytes from *Gnptg*^{ko} mice, the

morphology of the growth plate was normal, while skeletal growth was only moderately retarded in *Gnptg*-deficient mice. Despite the lack of obvious skeletal defects in *Gnptg*^{ko} mice, in contrast to MLIII patients, which can be explained by distinct posture and body weight distribution in mice and humans, *Gnptg*^{ko} mice displayed remarkable alterations in the articular cartilage ECM. The articular cartilage endures continuous mechanical stress during load bearing, thus protecting the bone. This is accomplished by a collagen fibrillar network that confers the ECM tensile properties, while proteoglycans (e.g. the most abundant aggrecan) endow it with compression stiffness (Poole et al., 2001). One of the earliest features of articular cartilage damage, e.g. in osteoarthritis, is softening of the tissue, which is associated with radial alignment of collagen fibrils in the middle and deep layers of the cartilage, even when no macroscopic tissue damage can be observed (Broom, 1982; Chen and Broom, 1998; Hosseini et al., 2013). In striking accordance with this, *Gnptg*^{ko} mice demonstrated no morphological changes in the articular cartilage but displayed significant fibrillation within the tissue, as evidenced by radially aligned SHG-positive structures. The enhanced SHG signal in *Gnptg*^{ko} mice likely arises from structural changes in the collagenous network that is formed by collagen type II, as a dominant fibril-forming collagen in the cartilage, and minor collagen types IX and XI, maintaining integrity of the fibrils and allowing the formation of collagen networks (Eyre and Wu, 1995; Wu and Eyre, 1995; Chen and Broom, 1998). Supporting this idea, we found *Col9a1* and *Col11a1* to be downregulated in the articular cartilage of *Gnptg*^{ko} mice, while collagen type II abundance was not altered. In addition, *Gnptg*^{ko} mice displayed a significantly impaired limb motor function, this defect becoming more obvious with age and suggesting that the deficient motor function in *Gnptg*^{ko} mice is associated with fatigue and/or pain at the joint. Importantly, our findings in *Gnptg*^{ko} mice are consistent with the limited mobility of hips, shoulders and ankles, as well as with severe osteoarthritic destruction of the femoral head cartilage, that we observed in MLIII gamma patients. Based on these data, we postulate that deficiency of the γ -subunit of GlcNAc-1-phosphotransferase causes structural changes in the fibrillar network of articular cartilage ECM, which likely precede the osteoarthritic damage typically observed in patients with MLIII gamma.

In contrast to most of the lysosomal storage diseases, lack of GlcNAc-1-phosphotransferase activity in MLII and MLIII compromises the activities of multiple lysosomal enzymes, resulting in a plethora of molecular and pathological events in various tissues

(Kollmann et al., 2010; Velho et al., 2019). Because physical movement at the joint is accomplished by the coordinated action of muscles, tendons and ligaments, one can expect a complex involvement of these connective tissues into the impaired joint mobility in patients with MLII and MLIII. In this study, we found that deficiency of either the α - or γ -subunits of GlcNAc-1-phosphotransferase confers the Achilles tendons isolated from *Gnptab^{kl}* and *Gnptg^{ko}* mice distinct mechanical properties. Specifically, collagen fibrils of the tendons of *Gnptab^{kl}* mice were significantly decreased in diameter, suggesting that increased tendon stiffness in *Gnptab*-deficient mice results from disorganized tendinous ECM rather than from tendon hypertrophy (Franchi et al., 2013; Wiesinger et al., 2015). In contrast, tendons from *Gnptg^{ko}* mice were more compliant, with no altered thickness of collagen fibrils observed. Akin to other mechanosensitive tissues, mechanical properties and structure of tendons are defined by changes in ECM organization, as well as in gene expression, occurring in tenocytes in response to mechanical stimuli (Nourissat et al., 2015; Wiesinger et al., 2015). Accordingly, accumulation of storage material that we observed in tenocytes of *Gnptab^{kl}* and *Gnptg^{ko}* mice suggests that altered cellular metabolism and ECM turnover might affect tendon remodeling and overall joint function in the mutant mice. This study is the first to propose the contribution of tendons to the MLII and MLIII joint pathology. However, it remains unclear how deficiency of either the α - or γ -subunits causes distinct adaptive responses of tenocytes to a mechanical strain and leads to differential collagen fibril organization in the mouse tendon. Future studies will examine the effects of different mechanical strains on the structural and functional properties of tendons and joints in *Gnptab^{kl}* and *Gnptg^{ko}* mice.

In conclusion, our data suggest that lack of GlcNAc-1-phosphotransferase activity resulting from defects in the γ -subunit is causative of structural changes in the ECM of connective and mechanosensitive tissues, such as cartilage and tendons, resulting in functional abnormalities of the joint. In mice, *Gnptg* deficiency affects cartilage function both intracellularly, through imbalanced lysosomal homeostasis, and extracellularly, via an altered ECM that can disturb chondrocyte differentiation. Although joint cartilage destruction and stiffness have been recognized as hallmarks of MLIII gamma, the exact molecular mechanisms underlying these defects are poorly understood. The activity of GlcNAc-1-phosphotransferase is critical in disease progression and severity, yet additional molecular factors might be involved (Velho et al., 2019). Therefore, it remains to be investigated whether joint abnormalities in MLIII gamma are solely caused by a comprehensive lysosomal dysfunction owing to reduced GlcNAc-1-phosphotransferase activity, and thus can be corrected by respective lysosomal enzyme replacement therapies, or the defects result from a disturbed, yet undefined, function of the γ -subunit as well.

MATERIALS AND METHODS

Antibodies

Western blot analyses were performed using the following antibodies: mouse monoclonal anti-cathepsin K (sc-48353; 1:1000), goat polyclonal anti-cathepsin S (sc-6503; 1:500) and rabbit polyclonal anti-Gapdh (sc-25778; 1:2000) antibodies from Santa Cruz Biotechnology; goat polyclonal anti-cathepsin B antibody (GT15047; 1:1000) from Neuromics; goat polyclonal anti-cathepsin L antibody (AF1515; 1:500) from R&D Systems; mouse monoclonal anti- α -tubulin antibody (T9026; 1:1000) from Sigma-Aldrich. For immunohistochemistry, the following antibodies were used: mouse anti-collagen type II (CP18, Merck; 1:500), rabbit anti-collagen type IX [1:3000; self-made (Budde et al., 2005)], rabbit anti-cartilage oligomeric matrix protein 4-1 (COMP) [1:500; self-made (Mayorca-Guiliani et al., 2019)], rabbit anti-Matn3 [1:500; self-made (Klati et al., 2000)] and mouse anti-Thbs1 (BA24, Calbiochem; 1:200).

Animals

Gnptg^{ko} (C57BU6) and *Gnptab^{kl}* (C57BU6-129/SvJ, 50:50) mice have been described previously (Kollmann et al., 2012, 2013; Di Lorenzo et al., 2018). We generally analyzed female littermate mice from heterozygous matings, unless stated differently. All mice were kept in a pathogen-free environment with a 12-h light/dark cycle, 45% to 65% relative humidity and 20°C to 24°C ambient temperature, in open or individually ventilated cages with wood shavings bedding and nesting material, in groups not surpassing six animals. The mice had access to tap water and standard rodent chow *ad libitum*. All animal experiments were approved by the animal facility of the University Medical Center Hamburg-Eppendorf and by Behörde für Gesundheit und Verbraucherschutz. The care and use of experimental animals complied with all relevant local animal welfare laws, guidelines and policies.

Skeletal analysis

After sacrifice, the dissected skeletons were fixed in 3.7% phosphate buffered saline (PBS)-buffered formaldehyde for 18 h at 4°C and then stored in 80% ethanol. All skeletons were first analyzed by contact radiography using a Faxitron X-ray cabinet (Faxitron Xray) to measure the length of the lumbar spine, femora and tibia. For undecalcified bone histology, tibiae were dehydrated in ascending alcohol concentrations and then embedded in methylmetacrylate as described previously (Schulze et al., 2011). Sections of 4 μ m thickness were cut in the sagittal plane on a Microtec rotation microtome (Techno-Med). Sections were stained following a standard protocol for Toluidine Blue staining, and histomorphometry was performed according to the American Society for Bone and Mineral Research (ASBMR) guidelines (Parfitt et al., 1987) using the OsteoMeasure histomorphometry system (Osteometrics). Movat pentachrome staining (Morphisto) was carried out according to the manufacturer's instructions.

Histological analysis of cartilage

For cartilage ECM protein staining, the hind legs were washed in PBS for 24 h and decalcified in 10% tris-ethylenediaminetetraacetic acid (EDTA) for 10-14 days. Decalcified limbs were further processed and embedded in paraffin in sagittal orientation. Serial sections were taken at a thickness of 8 μ m. Joint sections were stained with antibodies against collagen type II, collagen type IX, COMP, Matn3 and Thbs1. For collagen type II staining, the sections were initially digested using pepsin (0.025% in 0.2 M HCl; Merck) for 15 min at 37°C. An enzymatic digestion with hyaluronidase (500 U/ml in hyaluronidase buffer pH 5.0; Merck) for 30 min at 37°C and proteinase K (10 μ g/ml in proteinase buffer pH 7.4; Merck) for 10 min at 55°C was conducted for all the antibodies to demask the antigens. After quenching the endogenous peroxidase with 3% H₂O₂ for 10 min and blocking with Zytomed blocking solution (Zytomed Systems) for 5 min at room temperature, the sections were incubated with respective primary antibodies overnight at 4°C. ZytoChem Plus HRP-polymer anti-rabbit or anti-mouse secondary antibodies (Zytomed Systems) and 3,3'-diaminobenzidine (0.05% DAB and 0.015% H₂O₂ in 0.01 M PBS pH 7.2; Merck) were used to detect the specific primary antibody bindings. The brownish staining through the oxidation of the DAB was complemented with a nuclear counterstaining with Mayer's Hematoxylin (Merck) for 10 s at room temperature.

Isolation and culture of primary chondrocytes

Chondrocyte progenitor cells were isolated from 10-day-old *Gnptg^{ko}* or wild-type mice. Sterna from four to five mice per genotype were collected, and the cells were separated by digesting the tissue in 0.1% collagenase Ia solution followed by 0.2% collagenase Ia solution. The isolated cells were then cultured in Dulbecco's modified eagle medium/Ham's F-12 (1:1) medium supplemented with 10% fetal calf serum (Biochrom AG). At a total cell confluence of 80%, chondrocyte differentiation was induced by the addition of ascorbic acid (50 μ g/ml) and culture for 10 days.

Transcriptome analysis

To yield enough material for gene array, six wild-type and six *Gnptg^{ko}* mice were sacrificed at 12 weeks of age, hip joints were dissected, and cartilage caps were isolated and placed on dry ice. Using a mortar and pestle, the cartilage samples were then crushed into a fine powder in liquid nitrogen and

RESEARCH ARTICLE

Disease Models & Mechanisms (2020) 13, dmm046425. doi:10.1242/dmm.046425

subjected to RNA isolation. Total RNAs were extracted using PEQ Gold Total RNA Isolation Kit (VWR) according to the manufacturer's instructions. RNA quality was assessed by photospectrometry (NanoDrop 1000, Thermo Fisher Scientific) and integrity analysis (Tapestation 2200, Agilent Technologies). The genome-wide gene expression analysis was performed using the Clariom D mouse system (Thermo Fisher Scientific) according to the manufacturer's GeneChip™ WTPLUS reagent kit manual. Briefly, 100 ng of total RNA samples pooled from six mice per genotype were used for the synthesis of second-cycle single-stranded complementary DNA (cDNA). Subsequently, 5.5 µg of fragmented and labeled cDNA were used for gene chip hybridization. After washing and staining with the Affymetrix Fluidics Station 450, microarrays were scanned with the Affymetrix Gene Chip Scanner 7G, and the signals were analyzed with the Transcriptome Analysis Console software (TAC 4.0, Thermo Fisher Scientific) using default analysis settings (version 2) and Gene+Exon -SST-RMA (Signal Space Transformation-Robust Multi-Chip Analysis) as summarization. For gene ontology enrichment analysis, differentially expressed genes (absolute 1.5 SLR and adjusted P -value ≤ 0.05) were used to find enriched gene ontology biological processes using Goseq (Young et al., 2010). Gene ontology terms with an adjusted P -value ≤ 0.05 were regarded as statistically significant. For quantitative mRNA expression analysis, RNA isolation from cultured cells, cDNA synthesis and quantitative real-time PCR using pre-designed Taqman-Assays (Thermo Fisher Scientific) were performed as previously described (Di Lorenzo et al., 2018). Relative mRNA expression levels of analyzed genes were normalized to the level of *Gapdh* mRNA in the same sample using the comparative CT method ($2^{-\Delta\Delta CT}$).

Protein analysis

Primary chondrocytes were cultured in serum-free Opti-MEM™ medium (Gibco) for 24 h before the cells and conditioned media were collected. Media were concentrated 4-fold using Amicon Ultra-0.5 ml (3 kDa cutoff) centrifugal filters (Merck). Cells were lysed in PBS containing 0.5% Triton X-100 and protease inhibitors for 30 min at 4°C. Lysates were clarified by centrifugation at 16,000 g , and the protein content in supernatants was measured using the Roti® quant Protein Assay (Carl Roth). Cell extracts and concentrated conditioned media were solubilized in reducing Laemmli sample buffer for 5 min at 95°C, separated by sodium dodecyl sulphate-polyacrylamide gel electrophoresis (SDS-PAGE) and transferred to nitrocellulose membranes. Membranes were blocked in Tris-buffered saline (TBS; pH 7.4) containing 0.05% Tween 20 and 5% milk powder or 1% bovine serum albumin for 1 h, and then incubated with the respective primary antibodies in blocking buffer for 1 h or overnight at 4°C. Blots were washed with TBS containing 0.05% Tween 20 and incubated for 1 h at room temperature with appropriate horseradish peroxidase-coupled secondary antibodies (Dianova) diluted in blocking buffer. Membranes were washed, and immunoreactive protein bands were visualized by chemiluminescence. The enzymatic activities of lysosomal enzymes in protein extracts of primary cultured cells and corresponding conditioned media were assayed using appropriate 4-nitrophenol- or 4-methylumbelliferone-based substrates (Kollmann et al., 2012; Di Lorenzo et al., 2018).

GAG analysis

For GAG analysis, primary chondrocytes were incubated for 24 h in serum-free Opti-MEM™ medium containing 100 µCi/ml $\text{Na}_2^{35}\text{SO}_4$ (Hartmann Analytic). Cells were then washed twice with PBS and incubated for 24 h with serum-free Opti-MEM™ medium in the presence or absence of 10 µg/ml human recombinant ARSB (Naglazyme®, BioMarin). GAGs were isolated from cell lysates using DEAE-Sepharose (Sigma-Aldrich) anion exchange chromatography and subjected to digestion with heparinase I, II and III kindly provided by Dr J. Esko, University of California, San Diego, CA, USA (Lawrence et al., 2012). The treatment-resistant CS/DS were purified and radioactivity quantified by liquid scintillation counting (Lamanna et al., 2011).

Electron microscopy

Tibiae were fixed with 4% paraformaldehyde and 1% glutaraldehyde in 0.1 M phosphate buffer (pH 7.4) overnight and decalcified for 3–4 weeks in 10% EDTA. Thereafter, 100 µm thick sections were prepared with a

vibratome and post-fixed in 1% OsO_4 , dehydrated and embedded in Epon. Ultrathin sections (60 nm) were cut and mounted on copper grids. Sections were stained using uranyl acetate and lead citrate.

SHG microscopy

For SHG analysis of articular cartilage, undecalcified knee joint samples from 60-week-old wild-type and *Gnptg^{ko}* mice were dehydrated in ascending alcohol concentrations and embedded into methylmethacrylate. Sections of 4 µm thickness were cut in the sagittal plane on the microtome and then mounted in Poly-Mount™ mounting medium (Polysciences). SHG imaging was carried out using a multiphoton scanning microscope (DF-scope from Sutter Instrument), custom modified by Rapp OptoElectronic and controlled by ScanImage 2017b (Vidrio Technologies). Second harmonics were excited with an ytterbium-doped 1070-nm fiber laser (Fidelity-2, Coherent), which was focused on the sample using a 25× water immersion objective (Leica HC FLUOTAR L 25x/0.95 W VISIR, Leica). The laser power in the focal plane was 110 mW. The forward-propagating green SHG signal was collected through an oil immersion condenser (numerical aperture 1.4, Olympus), separated from excitation light by a filter set (ET700SP-2P short-pass filter, 560 DXCR dichroic mirror, ET525/70m-2P emission filter, Chroma Technology) and detected by a GaAsP photomultiplier tube (H11706-40, Hamamatsu Photonics).

AFM measurements

IT AFM measurements and contact-mode imaging were carried out using an MFP-3D-BIO AFM (Asylum Research/Oxford Instruments) in combination with an inverse optical microscope (IX71S1F-3, Olympus). This guaranteed a precise lateral positioning of the AFM tip. The whole setup was placed on an active vibration isolation table (Halcyonics_i4, Accurion) inside a 1 m³ soundproof box to reduce the influence of external noise. All AFM experiments were performed with silicone-nitride cantilevers (MLCT, Cantilever E from Bruker AFM Probes) with a nominal spring constant of 0.1 N/m, a nominal tip radius of 20 nm and a pyramidal tip shape. For each cantilever the spring constant was determined individually using the thermal noise method (Butt and Jaschke, 1995). Native Achilles tendon tissues were snap frozen and cut with a cryotome (Leica CM 1950, Leica) into 20 µm sections. In order to preserve tissue integrity throughout AFM measurements, transparent adhesive tape was used to obtain the tissue sections, which were then attached to a glass slide via a double adhesive tape. Imaging was carried out in air. All images were recorded with a resolution of 512×512 pixels at a line rate of 1 Hz. Image processing and measurements were performed in Gwyddion 2.53. Outliers were removed and a simple plane fit was applied to every image.

Collagen fibers (10–15 µm) in tendons are laying perfectly in the proximodistal axis; therefore, a Fourier transformation of the 90×90 µm² images was performed, showing the angle of the proximodistal axis (pda). The alignment of the collagen fibrils (~150 nm) was determined by angle measurements with reference to the pda. Then, tissue sections were immersed in Dulbecco's PBS without $\text{Mg}^{2+}/\text{Ca}^{2+}$ (Biochrom AG) during the indentation measurements. Every force map contained 24×25 force-indentation curves equally distributed over an area of 3×3 µm². The vertical tip velocity was constant at 10 µm/s and a setpoint of 3 V was used throughout all measurements. Two different sections per animal were used, and on each slide 3×600 on the central Achilles tendon and 3×600 curves on the lateral part were assessed. No differences were found between the central and the lateral part; therefore, the measurements were merged. In total, 12×600 force curves were assessed for each animal, each genotype and each age group. The Young's modulus was extracted via fitting the Hertz–Sneddon model for a pyramidal shaped tip onto the approach part of the force-indentation curves up to an indentation depth of 500 nm, using a custom software written in MATLAB 2019a (MathWorks). The software automatically corrects the baseline and sets the contact point. Subsequently, stiffness distributions were generated with Igor Pro software (Version 6.3.7.2, WaveMetrics).

Behavioral tests

Because MLIII gamma equally affects male and female subjects, we performed the behavioral analyses on only male mice to reduce the number

RESEARCH ARTICLE

Disease Models & Mechanisms (2020) 13, dmm046425. doi:10.1242/dmm.046425

of tested animals in accordance with the 3Rs principles for animal welfare. Therefore, ten wild-type and seven *Gnptg*^{ko} male mice underwent a longitudinal study to assess different behavioral functions. All tests were performed during the dark cycle of the mice, and the experimental room was illuminated with red light. The strength of the forelimbs was measured in 5- and 7-month-old mice using a GripStrengthMeter system (TSE Systems), as previously described (Morellini and Schachner, 2006). Mice were suspended by the tail and allowed to grasp with the front paws a stainless steel grip attached to a dynamometer. The maximal force applied while pulling the mice until they released the grip was recorded. Mice were tested in three sessions of three trials with an inter-trial interval (ITI) of 10 s and an inter-session interval of 45 min. The mean of three maximal values among the three trials was used for analysis. Locomotor activity and novelty induced behavior were assessed in 4- and 6-month-old mice in the open field test. Briefly, mice were placed in one corner of a white box (50 cm×50 cm and 40 cm high; 20 lux), and their behavior was analyzed for 20 min with EthoVision software (Noldus), as previously described (Brandewiede et al., 2005).

The coordinated motor function of the four limbs was evaluated with the rotarod test (RotaRod, TSE Systems) with mice at the age of 4, 6 and 8 months. Mice were first familiarized with the rotarod by letting them stay for 120 s on the rod rotating at 2 rotations per minute (rpm). Motor learning was assessed by training the mice with an accelerated rotarod protocol of four trials (ITI=45 min), during which the rod accelerated from 4 rpm to 34 rpm within 4.5 min. Possible fatigue- or pain-induced decline in motor performance was tested by leaving the mice on the rod rotating at a constant speed of 32 rpm over three consecutive trials (ITI=45 min). All trials had a maximal duration of 300 s and were interrupted when the mouse fell, or it stopped walking on the rotating rod.

Patients

Clinical and genetic information on the patients who participated in this study is provided in Tables S1 and S2. Written informed consents on the research procedures were obtained from all patients. The study protocol complies with the Declaration of Helsinki.

To measure joint mobility, a standard mechanical goniometer was placed across the hip, shoulder, elbow, knee, ankle or wrist joint as per standard procedure (Gajdosik and Bohannon, 1987), and maximal angular distances of joint motions (ROMs) were recorded. All the evaluations were performed by the same specialist (an occupational therapist), except for one MLIII alpha/beta patient (evaluation of whom was performed by a physical therapist). Each measurement was performed in triplicate by the same evaluator, and a mean value was calculated.

During surgical hip arthroplasty of Patient 9 (at the age of 43 years) at the Pathology Department, a femoral head specimen was collected and preserved in formalin. Following decalcification in 5% nitric acid for 3 days, the specimen was embedded in paraffin and cut in sagittal orientation to prepare 5 µm thick sections. Staining of the femur head sections was carried out according to standard protocols using Alcian Blue solution (Dinâmica) to detect GAGs and Haematoxylin/Eosin (Merck) to visualize general tissue structure. In addition, Toluidine Blue staining was performed to detect GAGs.

Statistical analyses

Data are shown as mean±s.d. or mean±s.e.m. Statistical analysis of the data was performed using an unpaired, two-tailed Student's *t*-test (Microsoft Excel), a two-tailed Mann-Whitney test (GraphPad Prism 8), or a mixed two-way ANOVA with genotype as between factor and time bin (for the open field test) and trial (for the rotarod test) as within groups factors, followed by Sidak's multiple comparisons when appropriate (GraphPad Prism 8). All tests were two-tailed, and differences between the values were considered statistically significant when the *P*-value was ≤0.05.

Acknowledgements

We thank all patients and their families for supporting this study. We are grateful to J. Brand, L. Sandoval Flores, L. Rosenthal, O. Winter and A. Thieke for excellent technical assistance.

Competing interests

The authors declare no competing or financial interests.

Author contributions

Conceptualization: F.Z., T.S., S.P., T.D.; Methodology: L.M.W., L.F., J.V., Z.J.-L., N.F.L., L.S., F.M., A.B., T.A.Y., G.D.L., M.S., B.d.S.P., N.R.G., F.S.-L., F.V., T.O.S., J.S., G.H., J.S.W., T.D.; Investigation: L.M.W., L.F., J.V., Z.J.-L., N.F.L., L.S., F.M., A.B., T.A.Y., G.D.L., M.S., B.d.S.P., N.R.G., F.S.-L., F.V., T.O.S., J.S., G.H., I.V.D.S., H.C.-S., F.Z., T.S., S.P., T.D.; Writing - original draft: S.P., T.D.; Writing - review & editing: I.V.D.S., H.C.-S., F.Z., T.S.; Supervision: F.Z., T.S., S.P., T.D.; Funding acquisition: G.H., J.S.W., F.Z., S.P.

Funding

This study was supported by the Research Animal Facility and the Isotope Lab Facility of the University Medical Center Hamburg-Eppendorf, Deutsche Forschungsgemeinschaft (PO 1539/1-1 to S.P.; SFB877-B3 to L.M.W., S.P. and T.D.; FOR2722/D2 to F.Z.) and the European Research Council (Marie Skłodowska-Curie grant no. 794386 to G.H. and a Starting Grant LIFE-Synapses no. 714762 to J.S.W.).

Data availability

Genome-wide expression data have been deposited in the Gene Expression Omnibus (GEO) database under accession number GSE157180.

Supplementary information

Supplementary information available online at <https://dmm.biologists.org/lookup/doi/10.1242/dmm.046425.supplemental>

References

- Bao, M., Booth, J. L., Elmendorf, B. J. and Canfield, W. M. (1996). Bovine UDP-N-acetylglucosamine: Lysosomal-enzyme N-Acetylglucosamine-1-phosphotransferase. I. Purification and subunit structure. *J. Biol. Chem.* **271**, 31437-31445.
- Brachvogel, B., Zaucke, F., Dave, K., Norris, E. L., Stermann, J., Dayaki, M., Koch, M., Gorman, J. J., Bateman, J. F. and Wilson, R. (2013). Comparative proteomic analysis of normal and collagen IX null mouse cartilage reveals altered extracellular matrix composition and novel components of the collagen IX interactome. *J. Biol. Chem.* **288**, 13481-13492. doi:10.1074/jbc.M112.444810
- Brandewiede, J., Schachner, M. and Morellini, F. (2005). Ethological analysis of the senescence-accelerated P8 mouse. *Behav. Brain Res.* **158**, 109-121. doi:10.1016/j.bbr.2004.08.012
- Broom, N. D. (1982). Abnormal softening in articular cartilage. Its relationship to the collagen framework. *Arthritis. Rheum.* **25**, 1209-1216. doi:10.1002/art.1780251010
- Buck, M. R., Karustis, D. G., Day, N. A., Honn, K. V. and Sloane, B. F. (1992). Degradation of extracellular-matrix proteins by human cathepsin B from normal and tumour tissues. *Biochem. J.* **282**, 273-278. doi:10.1042/bj2820273
- Budde, B., Blumbach, K., Ylästalo, J., Zaucke, F., Ehlen, H. W. A., Wagener, R., Ala-Kokko, L., Paulsson, M., Bruckner, P. and Grässel, S. (2005). Altered integration of matrilin-3 into cartilage extracellular matrix in the absence of collagen IX. *Mol. Cell. Biol.* **25**, 10465-10478. doi:10.1128/MCB.25.23.10465-10478.2005
- Butt, H.-J. and Jaschke, M. (1995). Calculation of thermal noise in atomic force microscopy. *Nanotechnology* **6**, 1-7. doi:10.1088/0957-4484/6/1/001
- Cathey, S. S., Kudo, M., Tiede, S., Raas-Rothschild, A., Brailke, T., Beck, M., Taylor, H. A., Canfield, W. M., Leroy, J. G., Neufeld, E. F. et al. (2008). Molecular order in mucopolidiosis II and III nomenclature. *Am. J. Hum. Genet.* **146A**, 512-513. doi:10.1002/ajmg.a.32193
- Cathey, S. S., Leroy, J. G., Wood, T., Eaves, K., Simensen, R. J., Kudo, M., Stevenson, R. E. and Friez, M. J. (2010). Phenotype and genotype in mucopolidiosis II and III alpha/beta: A study of 61 probands. *J. Med. Genet.* **47**, 38-48. doi:10.1136/jmg.2009.067736
- Chen, M.-H. and Broom, N. (1998). On the ultrastructure of softened cartilage: a possible model for structural transformation. *J. Anat.* **192**, 329-341. doi:10.1046/j.1469-7580.1998.19230329.x
- Decker, R. S. (2017). Articular cartilage and joint development from embryogenesis to adulthood. *Semin. Cell Dev. Biol.* **62**, 50-56. doi:10.1016/j.semcdb.2016.10.005
- Di Lorenzo, G., Velho, R. V., Winter, D., Thelen, M., Ahmadi, S., Schweizer, M., De Pace, R., Cornils, K., Yorgan, T. A., Grüb, S. et al. (2018). Lysosomal proteome and secretome analysis identifies missorted enzymes and their nondegraded substrates in mucopolidiosis III mouse cells. *Mol. Cell. Proteomics* **17**, 1612-1626. doi:10.1074/mcp.RA118.000720
- Eman, P. J. and Peterson, L. (eds.) (2014). *Developing Insights in Cartilage Repair*. London, UK: Springer-Verlag London.
- Eyre, D. R. and Wu, J. J. (1995). Collagen structure and cartilage matrix integrity. *J. Rheumatol. Suppl.* **43**, 82-85.
- Franchi, M., Torricelli, P., Giavaresi, G. and Fini, M. (2013). Role of moderate exercising on Achilles tendon collagen crimping patterns and proteoglycans. *Connect. Tissue Res.* **54**, 267-274. doi:10.3109/03080207.2013.807808

RESEARCH ARTICLE

Disease Models & Mechanisms (2020) 13, dmm046425. doi:10.1242/dmm.046425

- Gajdosik, R. L. and Bohannon, R. W. (1987). Clinical measurement of range of motion: review of goniometry emphasizing reliability and validity. *Phys. Ther.* **67**, 1867-1872. doi:10.1093/ptj/67.12.1867
- Hendrickx, G., Danyukova, T., Baranowsky, A., Rolvien, T., Angermann, A., Schweizer, M., Keller, J., Schröder, J., Meyer-Schwesinger, C., Muschol, N. et al. (2020). Enzyme replacement therapy in mice lacking arylsulfatase B targets bone-remodeling cells, but not chondrocytes. *Hum. Mol. Genet.* **29**, 803-816. doi:10.1093/hmg/ddaa006
- Hosseini, S. M., Veldink, M. B., Ito, K. and van Dongelaar, C. C. (2013). Is collagen fiber damage the cause of early softening in articular cartilage? *Osteoarthr. Cartil.* **21**, 136-143. doi:10.1016/j.joca.2012.09.002
- Idol, R. A., Wozniak, D. F., Fujiwara, H., Yuede, C. M., Ory, D. S., Kornfeld, S. and Vogel, P. (2014). Neurologic abnormalities in mouse models of the lysosomal storage disorders mucopolidiosis II and mucopolidiosis III γ . *PLoS ONE* **9**, e109768. doi:10.1371/journal.pone.0109768
- Karim, A., Amin, A. K. and Hall, A. C. (2018). The clustering and morphology of chondrocytes in normal and mildly degenerate human femoral head cartilage studied by confocal laser scanning microscopy. *J. Anat.* **232**, 686-698. doi:10.1111/joa.12768
- Karsenty, G. and Wagner, E. F. (2002). Reaching a genetic and molecular understanding of skeletal development. *Dev. Cell* **2**, 389-406. doi:10.1016/S1534-5807(02)00157-0
- Kim, B.-M., Eichler, J., Reiser, K. M., Rubenchik, A. M. and Da Silva, L. B. (2000). Collagen structure and nonlinear susceptibility: Effects of heat, glycation, and enzymatic cleavage on second harmonic signal intensity. *Lasers Surg. Med.* **27**, 329-335. doi:10.1002/1096-9101(2000)27:4<329::AID-LSM5>3.0.CO;2-C
- Klatt, A. R., Nitsche, D. P. C., Kobbe, B., Mörgelin, M., Paulsson, M. and Wagener, R. (2000). Molecular structure and tissue distribution of matrilin-3, a filament-forming extracellular matrix protein expressed during skeletal development. *J. Biol. Chem.* **275**, 3999-4006. doi:10.1074/jbc.275.6.3999
- Klatt, A. R., Becker, A.-K. A., Neacsu, C. D., Paulsson, M. and Wagener, R. (2011). The matrilins: Modulators of extracellular matrix assembly. *Int. J. Biochem. Cell Biol.* **43**, 320-330. doi:10.1016/j.biocel.2010.12.010
- Kollmann, K., Pohl, S., Marschner, K., Encarnaçao, M., Sakwa, I., Tiede, S., Poorthuis, B. J., Lübke, T., Müller-Loennies, S., Storch, S. et al. (2010). Mannose phosphorylation in health and disease. *Eur. J. Cell Biol.* **89**, 117-123. doi:10.1016/j.ejcb.2009.10.008
- Kollmann, K., Damme, M., Markmann, S., Morelle, W., Schweizer, M., Hermans-Borgmeyer, I., Röcher, A. K., Pohl, S., Lübke, T., Michalski, J.-C. et al. (2012). Lysosomal dysfunction causes neurodegeneration in mucopolidiosis II 'knock-in' mice. *Brain* **135**, 2661-2675. doi:10.1093/brain/awt209
- Kollmann, K., Peska, J. M., Kühn, S. C., Schweizer, M., Schöne, E., Karkmann, K., Otomo, T., Catala-Lehnen, P., Falla, A. V., Marshall, R. P. et al. (2013). Decreased bone formation and increased osteoclastogenesis cause bone loss in mucopolidiosis II. *EMBO Mol. Med.* **5**, 1871-1886. doi:10.1002/emmm.201302979
- Krishnan, Y. and Grodzinsky, A. J. (2018). Cartilage diseases. *Matrix Biol.* **71-72**, 51-69. doi:10.1016/j.matbio.2018.05.005
- Kuettner, K. E. (1992). Biochemistry of articular cartilage in health and disease. *Clin. Biochem.* **25**, 155-163. doi:10.1016/0009-9120(92)90224-G
- Lamanna, W. C., Lawrence, R., Sarrazin, S. and Esko, J. D. (2011). Secondary storage of dermatan sulfate in Sanfilippo disease. *J. Biol. Chem.* **286**, 6955-6962. doi:10.1074/jbc.M110.192062
- Lawrence, R., Brown, J. R., Al-Mafraji, K., Lamanna, W. C., Beitel, J. R., Boons, G.-J., Esko, J. D. and Crawford, B. E. (2012). Disease-specific non-reducing end carbohydrate biomarkers for mucopolysaccharidoses. *Nat. Chem. Biol.* **8**, 197-204. doi:10.1038/nchembio.766
- Mao, Y., Block, T., Singh-Varma, A., Sheldrake, A., Leeth, R., Griffey, S. and Kohn, J. (2019). Extracellular matrix derived from chondrocytes promotes rapid expansion of human primary chondrocytes in vitro with reduced dedifferentiation. *Acta Biomater.* **85**, 75-83. doi:10.1016/j.actbio.2018.12.006
- Mayorca-Gulliani, A. E., Willacy, O., Madsen, C. D., Rafeeva, M., Elisabeth Heumüller, S., Bock, F., Sengle, G., Koch, M., Imhof, T., Zaucke, F. et al. (2019). Decellularization and antibody staining of mouse tissues to map native extracellular matrix structures in 3D. *Nat. Protoc.* **14**, 3395-3425. doi:10.1038/s41596-019-0225-8
- Morellini, F. and Schachner, M. (2006). Enhanced novelty-induced activity, reduced anxiety, delayed resynchronization to daylight reversal and weaker muscle strength in tenascin-C-deficient mice. *Eur. J. Neurosci.* **23**, 1255-1268. doi:10.1111/j.1460-9568.2006.04657.x
- Mort, J. S., Beaudry, F., Thérault, K., Emmott, A. A., Richard, H., Fisher, W. D., Lee, E. R., Poole, A. R. and Laverty, S. (2016). Early cathepsin K degradation of type II collagen in vitro and in vivo in articular cartilage. *Osteoarthr. Cartil.* **24**, 1461-1469. doi:10.1016/j.joca.2016.03.016
- Nourissat, G., Bärenbaum, F. and Duprez, D. (2015). Tendon injury: from biology to tendon repair. *Nat. Rev. Rheumatol.* **11**, 223-233. doi:10.1038/nrheum.2015.26
- Oussoren, E., van Eerd, D., Murphy, E., Lachmann, R., van der Meijden, J. C., Hoefsloot, L. H., Verdjik, R., Ruijter, G. J. G., Maas, M., Hollak, C. E. M. et al. (2018). Mucopolidiosis type III, a series of adult patients. *J. Inher. Metab. Dis.* **41**, 839-848. doi:10.1007/s10545-018-0186-z
- Parfitt, A. M., Drezner, M. K., Glorieux, F. H., Kanis, J. A., Malluche, H., Meunier, P. J., Ott, S. M. and Recker, R. R. (1987). Bone histomorphometry: standardization of nomenclature, symbols, and units: report of the asbmr histomorphometry nomenclature committee. *J. Bone Miner. Res.* **2**, 595-610. doi:10.1002/jbmr.5650020617
- Paton, L., Bitoun, E., Kenyon, J., Priestman, D. A., Oliver, P. L., Edwards, B., Platt, F. M. and Davies, K. E. (2014). A novel mouse model of a patient with mucopolidiosis II mutation recapitulates disease pathology. *J. Biol. Chem.* **289**, 26709-26721. doi:10.1074/jbc.M114.586156
- Pohl, S., Encarnaçao, M., Castrichini, M., Müller-Loennies, S., Muschol, N. and Braulke, T. (2010). Loss of N-acetylglucosamine-1-phosphotransferase gamma subunit due to intronic mutation in *GNPTG* causes mucopolidiosis type III gamma: implications for molecular and cellular diagnostics. *Am. J. Med. Genet. Part A* **152A**, 124-132. doi:10.1002/ajmg.a.33170
- Pohl, S., Angermann, A., Jeschke, A., Hendrickx, G., Yorgan, T. A., Makrypidi-Fraune, G., Steigert, A., Kuehn, S. C., Rolvien, T., Schweizer, M. et al. (2018). The lysosomal protein arylsulfatase B is a key enzyme involved in skeletal turnover. *J. Bone Miner. Res.* **33**, 2186-2201. doi:10.1002/jbmr.3563
- Poole, A. R., Kojima, T., Yasuda, T., Mwale, F., Kobayashi, M. and Laverty, S. (2001). Composition and structure of articular cartilage: a template for tissue repair. *Clin. Orthop. Relat. Res.* **391**, S26-S33. doi:10.1097/00003086-200110001-00004
- Raas-Rothschild, A., Cormier-Daire, V., Bao, M., Genin, E., Salomon, R., Brewer, K., Zeliger, M., Mandel, H., Toth, S., Roe, B. et al. (2000). Molecular basis of variant pseudo-Hurler polydystrophy (mucopolidiosis IIIC). *J. Clin. Invest.* **105**, 673-681. doi:10.1172/JCI5826
- Schulze, J., Bickert, T., Bell, F. T., Zaiss, M. M., Albers, J., Wintges, K., Streichert, T., Klaetschke, K., Keller, J., Hissnauer, T.-N. et al. (2011). Interleukin-33 is expressed in differentiated osteoblasts and blocks osteoclast formation from bone marrow precursor cells. *J. Bone Miner. Res.* **26**, 704-717. doi:10.1002/jbmr.269
- Thorp, F. K. and Dorfman, A. (1963). The occurrence of intracellular chondroitin sulfate. *J. Cell Biol.* **18**, 13-17. doi:10.1083/jcb.18.1.13
- Tiede, S., Storch, S., Lübke, T., Henrissat, B., Barga, R., Raas-Rothschild, A. and Braulke, T. (2005). Mucopolidiosis II is caused by mutations in *GNPTA* encoding the $\alpha\beta$ GlcNAc-1-phosphotransferase. *Nat. Med.* **11**, 1109-1112. doi:10.1038/nm1305
- Troeborg, L. and Nagase, H. (2012). Proteases involved in cartilage matrix degradation in osteoarthritis. *Biochim. Biophys. Acta Proteins Proteomics* **1824**, 133-145. doi:10.1016/j.bbapap.2011.06.020
- Tüysüz, B., Kasapçopur, Ö., Alkaya, D. U., Zahirin, S., Sözeri, B. and Yeşil, G. (2018). Mucopolidiosis type III gamma: three novel mutation and genotype-phenotype study in eleven patients. *Gene* **642**, 398-407. doi:10.1016/j.gene.2017.11.052
- Umlauf, D., Frank, S., Pap, T. and Bertrand, J. (2010). Cartilage biology, pathology, and repair. *Cell. Mol. Life Sci.* **67**, 4197-4211. doi:10.1007/s00018-010-0498-0
- Velho, R. V., Hams, F. L., Danyukova, T., Ludwig, N. F., Frieze, M. J., Cathey, S. S., Filocamo, M., Tappino, B., Güneş, N., Tüysüz, B. et al. (2019). The lysosomal storage disorders mucopolidiosis type II, type III alpha/beta, and type III gamma: Update on GNPTAB and GNPTG mutations. *Hum. Mutat.* **40**, 842-864. doi:10.1002/humu.23748
- Vidak, E., Javoršek, U., Vizovišek, M. and Turk, B. (2019). Cysteine cathepsins and their extracellular roles: Shaping the microenvironment. *Cells* **8**, 264. doi:10.3390/cells8030264
- Vizovišek, M., Fonović, M. and Turk, B. (2019). Cysteine cathepsins in extracellular matrix remodeling: extracellular matrix degradation and beyond. *Matrix Biol.* **75-76**, 141-159. doi:10.1016/j.matbio.2018.01.024
- Wiesinger, H.-P., Kösters, A., Müller, E. and Seynnes, O. R. (2015). Effects of increased loading on in vivo tendon properties: a systematic review. *Med. Sci. Sports Exerc.* **47**, 1885-1895. doi:10.1249/MSS.0000000000000603
- Wu, J.-J. and Eyre, D. R. (1995). Structural analysis of cross-linking domains in cartilage type XI collagen. Insights on polymeric assembly. *J. Biol. Chem.* **270**, 18865-18870. doi:10.1074/jbc.270.32.18865
- Young, M. D., Wakefield, M. J., Smyth, G. K. and Oshlack, A. (2010). Gene ontology analysis for RNA-seq: accounting for selection bias. *Genome Biol.* **11**, R14. doi:10.1186/gb-2010-11-2-r14
- Zhang, G., Young, B. B., Ezura, Y., Favata, M., Soslowsky, L. J., Chakravarti, S. and Birk, D. E. (2005). Development of tendon structure and function: regulation of collagen fibrillogenesis. *J. Musculoskelet. Neuronal Interact.* **5**, 5-21.
- Zhang, M., Theleman, J. L., Lygrtsse, K. A. and Wang, J. (2019). Epigenetic mechanisms underlying the aging of articular cartilage and osteoarthritis. *Gerontology* **65**, 387-396. doi:10.1159/000496688

Supplement B: Paper V

nature
materials

ARTICLES

<https://doi.org/10.1038/s41563-020-00894-0>

Basement membrane stiffness determines metastases formation

Raphael Reuten¹✉, Sina Zendeheroud^{2,17}, Monica Nicolau^{1,17}, Lutz Fleischhauer^{3,4}, Anu Laitala¹, Stefanie Kiderlen^{3,4}, Denise Nikodemus¹, Lena Wullkopf¹, Sebastian Rune Nielsen¹, Sarah McNeilly⁵, Carina Prein^{3,4,16}, Maria Rafaeva¹, Erwin M. Schoof^{1,6,7,8}, Benjamin Furtwängler^{1,7,8}, Bo T. Porse^{1,7,8}, Hyobin Kim^{1,8}, Kyoung Jae Won^{1,8}, Stefanie Sudhop⁴, Kamilla Westarp Zornhagen¹, Frank Suhr⁹, Eleni Maniati¹⁰, Oliver M. T. Pearce¹⁰, Manuel Koch^{11,12}, Lene Broeng Oddershede¹³, Tom Van Agtmael⁵, Chris D. Madsen¹⁴, Alejandro E. Mayorca-Guiliani¹, Wilhelm Bloch¹⁵, Roland R. Netz¹⁶, Hauke Clausen-Schaumann¹⁶ and Janine T. Erler¹✉

The basement membrane (BM) is a special type of extracellular matrix and presents the major barrier cancer cells have to overcome multiple times to form metastases. Here we show that BM stiffness is a major determinant of metastases formation in several tissues and identify netrin-4 (Net4) as a key regulator of BM stiffness. Mechanistically, our biophysical and functional analyses in combination with mathematical simulations show that Net4 softens the mechanical properties of native BMs by opening laminin node complexes, decreasing cancer cell potential to transmigrate this barrier despite creating bigger pores. Our results therefore reveal that BM stiffness is dominant over pore size, and that the mechanical properties of 'normal' BMs determine metastases formation and patient survival independent of cancer-mediated alterations. Thus, identifying individual Net4 protein levels within native BMs in major metastatic organs may have the potential to define patient survival even before tumour formation. The ratio of Net4 to laminin molecules determines BM stiffness, such that the more Net4, the softer the BM, thereby decreasing cancer cell invasion activity.

Cancer metastasis is responsible for 66–90% of patient deaths^{1,2}. Cancer cells encounter and must breach basement membranes (BMs) several times during the metastatic process—during invasion, intravasation and extravasation^{3,4}.

The BM, a specialized type of extracellular matrix (ECM) in direct contact with cells, is shaped by two major ECM macromolecule proteins, collagen IV and laminin, which self-assemble into two supramolecular polymers⁵. The collagen IV network is deposited on top of the laminin network, which is the key determinant that maintains cell–BM interaction and mechanical stability⁶. Each laminin chain contains a laminin N-terminal globular domain, and interactions between laminin N-terminal domains from distinct laminin heterotrimers generate the laminin network.

The BM is a dense, nanoporous sheet with a pore size between 10 and 112 nm^{7–9}. Currently, there are two paradigms describing the process of BM breaching. According to the first paradigm,

cancer cells can form actin- and protease-rich invadosomes, which can proteolytically degrade BM components to generate an entry site to breach¹⁰. Recent studies have revealed that cells can transmigrate across the BM in a protease-independent manner. Cancer cells can form invadosomes to plastically generate channels to migrate through the BM¹¹. According to the second paradigm, cancer-associated fibroblasts (CAFs) can pull and stretch the BM in a protease-independent manner to generate gaps via which cancer cells can pass through the BM¹². However, these paradigms of BM breaching exclusively focus on forces applied by cells on the BM and the functional role of the BM's mechanical properties has so far not been demonstrated.

Here we provide evidence for a functional role of BM architecture during the invasion–metastasis process in vitro, in animal models and in several patient tumour types. We examine the relationship between BM composition and cancer patient survival, and identify

¹Biotech Research and Innovation Centre, University of Copenhagen, Copenhagen, Denmark. ²Department of Physics, Freie Universität Berlin, Berlin, Germany.

³Center for Applied Tissue Engineering and Regenerative Medicine–CANTER, Munich University of Applied Sciences, Munich, Germany.

⁴Center for Nanoscience–CeNS, Munich, Germany. ⁵Institute of Cardiovascular and Medical Sciences, College of Medical, Veterinary and Life Sciences, University of Glasgow, Glasgow, UK.

⁶Department of Biotechnology and Biomedicine, Technical University of Denmark, Lyngby, Denmark. ⁷The Finsen Laboratory, Rigshospitalet, Faculty of Health Sciences, University of Copenhagen, Copenhagen, Denmark.

⁸Novo Nordisk Foundation Center for Stem Cell Biology, DanStem, Faculty of Health Sciences, University of Copenhagen, Copenhagen, Denmark. ⁹Exercise Physiology Research Group, Department of Movement Sciences, Biomedical Sciences Group, KU Leuven, Leuven, Belgium.

¹⁰Centre for Tumour Microenvironment, Barts Cancer Institute, Queen Mary University of London, London, UK. ¹¹Center for Biochemistry, Center for Molecular Medicine Cologne (CMMC), Faculty of Medicine and University Hospital Cologne, University of Cologne, Cologne, Germany.

¹²Institute for Dental Research and Oral Musculoskeletal Biology, Faculty of Medicine and University Hospital Cologne, University of Cologne, Cologne, Germany. ¹³Niels Bohr Institute, University of Copenhagen, Copenhagen, Denmark.

¹⁴Department of Laboratory Medicine, Division of Translational Cancer Research, Lund University, Lund, Sweden. ¹⁵Institute of Cardiovascular Research and Sport Medicine, Department of Molecular and Cellular Sport Medicine, German Sport University Cologne, Cologne, Germany.

¹⁶Present address: Department of Physiology and Pharmacology, Schulich School of Medicine & Dentistry, University of Western Ontario, London, Ontario, Canada. ¹⁷These authors contributed equally: S. Zendeheroud, M. Nicolau.

✉e-mail: raphael.reuten@bric.ku.dk; janine.erler@bric.ku.dk

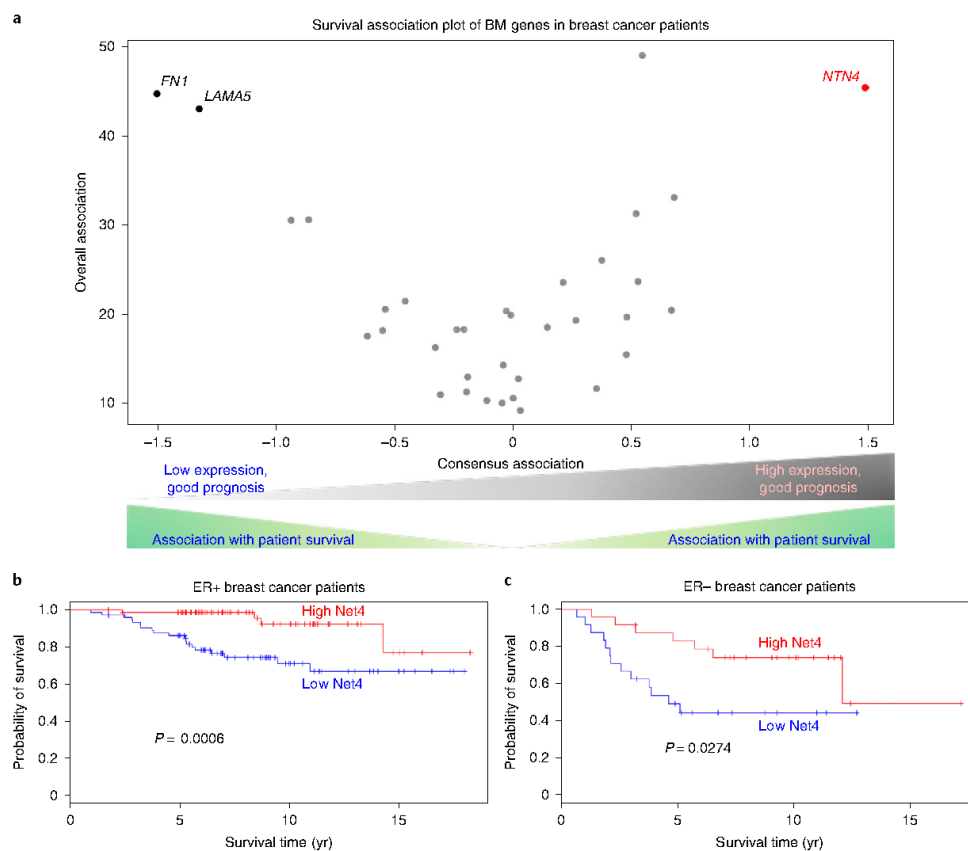


Fig. 1 | Association of the expression of genes encoding for BM proteins with breast cancer patient survival. **a**, For each of 35 BM genes present in the NKI dataset, Cox proportional hazard models were used to compute 28 statistics for association with survival: death and metastasis, in the Normal component and the Disease component, in seven breast cancer subgroups: ER positive; ER negative; HER2 overexpressing; HER2 overexpressing, ER positive (luminal B); HER2 overexpressing, ER negative; HER2 normal, ER negative (basal-like); and HER2 normal, ER positive (luminal A). For the 28 groups we computed an overall association (the sum of the \log_{10} -transformed P values) and a consensus association (the average of the \log_{10} -transformed P values multiplied by +1 (association of high levels with good prognosis), -1 (association of low levels with good prognosis) or 0 (no association)). A plot of consensus association versus overall association shows low levels of fibronectin (*FN1*) and laminin $\alpha 5$ (*LAMA5*) as well as high levels of Net4 (*NTN4*) to be most consistently associated with good prognosis across most tumour groups (highest consensus association). *FN1*, *LAMA5* and *NTN4* reveal the best P values overall (very high overall significance). Grey dots indicate BM genes with a low consensus association between -1.0 and 1.0. **b, c**, Kaplan-Meier survival (death) analysis: tumour group 1, low levels of *NTN4* in the Normal component (33th percentile *NTN4* levels) versus tumour group 2, high levels of *NTN4* in the Normal component (67th percentile *NTN4* levels). Oestrogen-receptor-positive tumours show a strong association ($P=0.0006$) between high levels of *NTN4* in the Normal component and good survival (**b**). Oestrogen-receptor-negative tumours show an association ($P=0.0274$) between high levels of *NTN4* in the Normal component and good survival (**c**).

high levels of the BM protein netrin-4 (Net4) as strongly associated with good prognoses. The more Net4 protein present within the BM, the softer this barrier, resulting in reduced cancer cell invasion which is associated with increased patient survival. Mechanistically, Net4 binds to laminin, thereby opening the laminin ternary node complex, which in turn reduces the overall BM stiffness. We show that the global distribution of Net4 results in bigger pores within the BM and reduced BM stiffness. This article provides direct evidence that the BM mechanics are dominant over BM pore size in regulating cancer progression, and expands our understanding of BM transmigration. This detailed knowledge of the complex BM material additionally may form the basis of future therapeutic interventions to alter metastases formation.

Results

Association of BM gene expression with cancer patient survival.

The BM presents a polymer barrier for cancer cells to breach and is therefore involved in many steps during the invasion-metastasis process^{3,4}. Although the paradigm of BM transmigration is based on cell forces applied to this polymeric material¹⁰⁻¹², we investigated the distinct concept that the architecture of the intact BM might apply physical forces on cancer cells directly, thereby altering their behaviour. The architecture of a material is crucially influenced by its composition. We generated a list of 49 genes encoding for BM components, which we determined from the literature and from our recent report^{5,13-20} (Supplementary Table 1).

We first examined the extent to which BM components might be associated with survival in a public breast cancer dataset from the Netherlands Cancer Institute (NKI) consisting of 295 patients²¹, and a dataset from 13 normal breast samples (three from reduction mammoplasties and ten from pathologically normal breast tissue from breast cancer patients)²². Here we investigated association with survival within multiple patient groupings, along several data components, and then computed a measure of association with survival for each BM gene across all these groupings. Of the 49 BM genes, 35 were present in the breast cancer dataset. The genomic data were first decomposed into Disease and Normal components using the Disease-Specific Genomic Analysis (DSGA) method²². Essentially, the Normal component of a tumour identifies the 'normal'-like profile of the tumour sample from a comparison with normal tissue data. By contrast, the Disease component of a tumour identifies the extent to which the actual tumour data deviate from all possible 'normal'-like signatures.

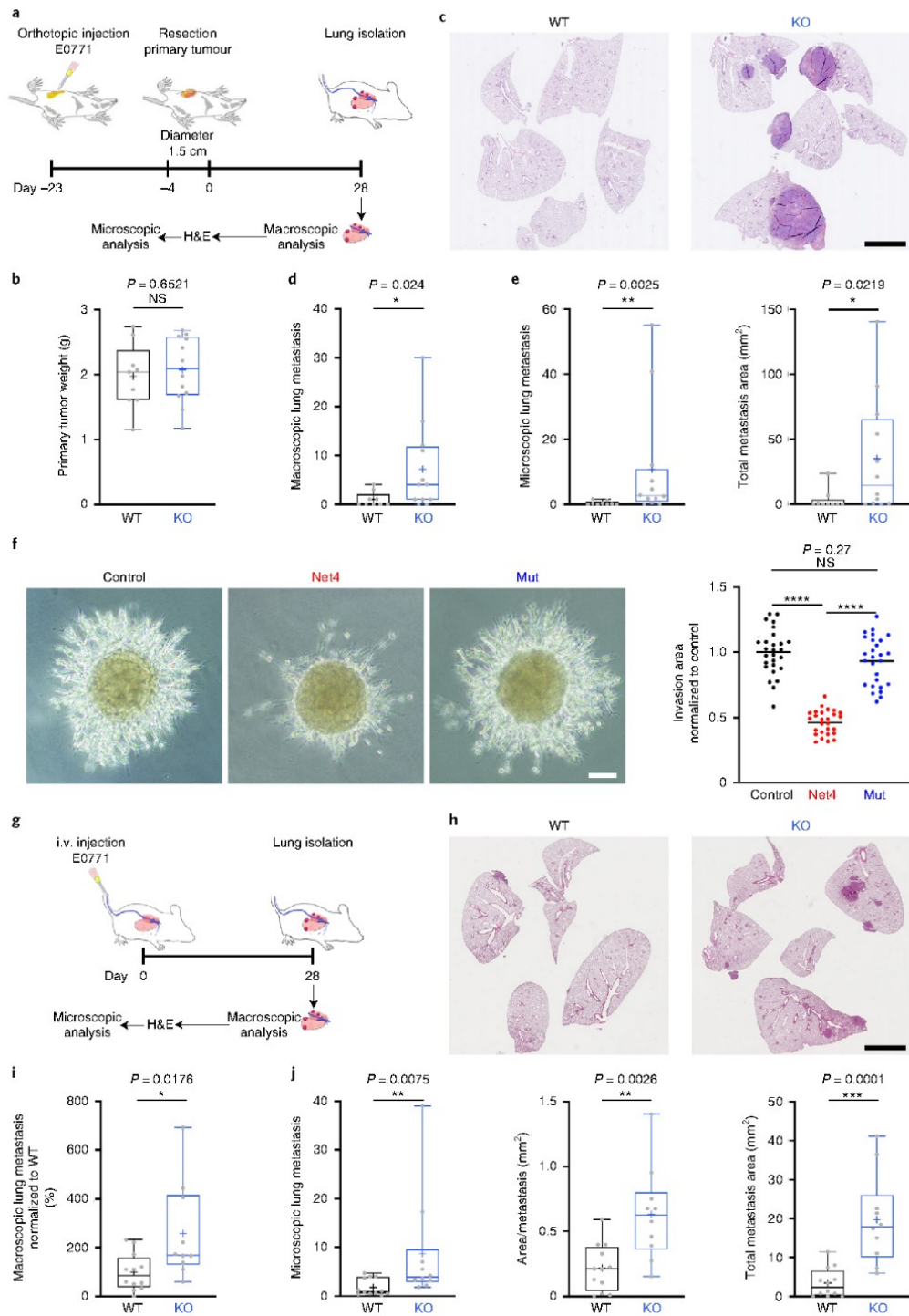
Figure 1a shows the plot of consensus versus overall associations for all BM genes present in the NKI dataset. Net4 (*NTN4*) exhibits both strong overall association and strong positive consensus association with survival. Laminin $\alpha 5$ (*LAMA5*) and fibronectin (*FN1*) likewise show strong overall association and strong negative association with survival (Fig. 1a). We wanted to further explore whether the association was most visible as a type of 'normal' BM present around the tumours (evidenced by the Normal component) or in the possible 'abnormal' modification of the BM in the tumour (evidenced by the Disease component). The Normal component's statistics show a much stronger association with survival than the Disease component or nonDSGA data (not decomposed by DSGA) (Extended Data Fig. 1a). We therefore focused primarily on the association with survival in the Normal component of the data. We concentrated our attention on Net4 because of the availability of a viable knockout mouse²³ to study the impact of 'normal' BM independent of tumour-derived or tumour-induced Net4 levels within BMs on cancer progression, as fibronectin and laminin $\alpha 5$ knockout mice are embryonic lethal^{24,25}. We investigated the association between Net4 and survival in breast cancer patients with ER positive (ER+) or ER negative (ER-) tumours. High levels of Net4 (*NTN4*) were significantly associated with good prognosis in both subtypes (Fig. 1b,c). We further explored the association of *NTN4* expression in the Normal component with survival in renal cell carcinoma^{26,27} using a cohort of 166 renal cell carcinomas together with 35 normal tissue samples. This analysis showed again that high levels of Net4 (*NTN4*) were significantly associated with good prognosis (Extended Data

Fig. 1b,c). Our analysis indicated that 'normal' BMs containing high amounts of Net4 are associated with good prognosis in breast and kidney cancer patients.

BMs deficient for Net4 promote metastases formation. To analyse whether tumour progression is altered in mice lacking Net4 within BMs, we orthotopically injected mouse breast cancer E0771 cells into the mammary fat pad of Net4 wildtype and knockout mice. After primary tumours had reached their maximum size, we resected them in all mice on the same day, and allowed metastases to develop. We analysed lung tissues 28 d postresection (Fig. 2a). The primary tumour weight was similar in both genotypes on the day of resection, indicating that loss of Net4 does not influence primary tumour growth (Fig. 2b). Quantification of lung metastases revealed that loss of Net4 significantly increased the number of metastases (Fig. 2c–e). We investigated the impact of Net4 on stromal cell infiltration, cancer cell proliferation and fibroblast activity to exclude that Net4 directly affects cell behaviour, as Net4 is reported to possess protumorigenic^{28–33} and antitumorigenic^{34–37} activity. Our data demonstrated that loss of Net4 in the host does not alter the abundance of CAFs and immune cells (macrophages and T cells) in E0771 primary tumours (Extended Data Fig. 2a). Additionally, recombinant Net4 slightly promoted the proliferation of mouse breast cancer cells, but not human breast cancer cells or mouse melanoma cells (Extended Data Fig. 2b). However, primary tumour growth was not altered in Net4 wildtype and knockout mice, and formation of lung metastases was significantly increased in mice deficient in Net4. Therefore, these data indicate an additional direct activity of Net4 on cells. Furthermore, low and high doses of Net4 did not influence the contractile ability of CAFs (Extended Data Fig. 2c). These results suggest that the increase in lung metastases in the Net4 knockout mouse cannot be attributed to the loss of direct effects of Net4 on cells.

Therefore, we next investigated whether BMs with or without Net4 alter cancer cell invasion. To this end, we performed a three-dimensional (3D) spheroid invasion assay in a reconstituted BM matrix³⁸ (rBM, Matrigel). To mimic the BM from Net4 knockout and wildtype animals, we embedded breast cancer spheroids into rBM and into rBM supplemented with recombinant Net4 as well as a Net4 mutant protein, substantially decreasing its laminin-binding capacity (Mut), which we recently generated and validated³⁹. Cells invaded rBM and rBM supplemented with the Mut significantly more than into their counterparts supplemented with wildtype Net4 (Fig. 2f and Extended Data Fig. 3a), indicating a laminin binding-related mechanism. Interestingly, addition of the same

Fig. 2 | Net4-deficient alveolar BM favours metastases formation. **a**, Experimental design of orthotopic injection of E0771 mouse breast cancer cells into the mammary fat pad of Net4 wildtype (WT) and knockout (KO) mice followed by primary tumour resection and subsequent analysis. **b**, Box-and-whisker plot of the primary tumour weight on the day of resection (two-tailed unpaired t test, minimum to maximum, median is shown as line, mean is displayed as cross, data points appear as grey dots; $n=9$ (WT), $n=12$ (KO); $t=0.4581$, degrees of freedom (d.f.)=19). NS, not significant. **c**, Representative H&E images of lungs from Net4 WT and Net4 KO mice 28 d postresection of the primary E0771 tumour. Scale bar, 3 mm. **d**, Box-and-whisker plot of macroscopic lung metastasis number in mice injected with E0771 cells into the mammary fat pad of Net4 WT and Net4 KO (two-tailed Mann-Whitney test for all analyses, minimum to maximum, median is shown as line, mean is displayed as cross, data points appear as grey dots; $n=9$ (WT), $n=12$ (KO); $*P<0.05$). **e**, Box-and-whisker plots of microscopic lung metastases (left) and total metastasis area (right) of mice injected with E0771 cells into the mammary fat pad of Net4 WT and Net4 KO (two-tailed Mann-Whitney test for all analyses, minimum to maximum, median is shown as line, mean is displayed as cross, data points appear as grey dots; $n=9$ (WT), $n=12$ (KO); $*P<0.05$, $**P<0.01$). **f**, Representative images of MDA-MB-231 sphere invasion in Matrigel (control) and Matrigel containing 50% Net4 (Net4) or 50% Net4 laminin-binding mutant (Mut) molecules relative to laminin 111 within the Matrigel matrix. Scale bar, 100 μ m. Right: scatter plot of sphere invasion (ordinary one-way ANOVA test, mean is displayed as black line; $n=27$; $F=94.2$, d.f. = 78; $****P<0.0001$). **g**, Time schedule of intravenous injection of E0771 cells into Net4 WT and Net4KO mice and subsequent analysis 28 d postinjection. **h**, Representative H&E images of lungs from Net4 WT and Net4 KO mice 28 d postinjection of E0771 cells. Scale bar, 3 mm. **i**, Box-and-whisker plot of macroscopic lung metastasis (two-tailed Mann-Whitney test, minimum to maximum, median is shown as line, mean is displayed as cross, data points appear as grey dots; $n=12$ (WT), $n=10$ (KO); $*P<0.05$). **j**, Box-and-whisker plots of microscopic lung metastasis (left), area/metastasis (centre) and total metastasis area (right) of intravenous injection of E0771 cells into Net4 WT and Net4 KO mice after 28 d (two-tailed Mann-Whitney test, minimum to maximum, median is shown as line, mean is displayed as cross, data points appear as grey dots; $n=12$ (WT), $n=10$ (KO); $**P<0.01$, $***P<0.001$).



number of Net4 molecules to breast cancer spheroids in a collagen I matrix promoted cell invasion in a manner independent of laminin binding (Extended Data Fig. 3b). These data indicate that BMs containing Net4 restrict the ability of breast cancer cells to move through the BM and additionally uncover a context-dependent pro-invasive activity of Net4, in line with previous studies^{28–32}.

To understand the impact of 'normal' Net4 expression on cancer progression, we determined Net4 localization in the alveolar BM, as this BM is the major barrier for cancer cells to breach in the experimental metastasis model. We decellularized lung tissues from Net4 wildtype and knockout²³ mice using the in situ decellularization of tissues approach^{19,40}, which preserves ECM architecture¹⁹. Net4 was localized inside the alveolar BM (Extended Data Fig. 4a). Collagen IV and laminin had a similar distribution, arrangement and amount in Net4 knockout mice (Extended Data Fig. 4a). To determine whether there are developmental alterations in protein abundance between lung tissues from Net4 knockout and wildtype mice, we performed tandem mass tag (TMT) mass spectrometry analysis of lung tissues. Strikingly, no BM proteins apart from Net4 were altered between Net4 knockout and wildtype mice (Extended Data Fig. 4b and Supplementary Table 2). Thus, these data suggest that the Net4 knockout mouse is ideal for studying the functional role of Net4 within native BMs during metastases formation. Intravenous injection of the E0771 cells (Fig. 2g) into Net4 wildtype and knockout animals resulted in a significant increase in lung tumour burden for all metastasis parameters (foci size, number and area) in animals with an alveolar BM lacking Net4 (Fig. 2h–j).

Together, these data revealed that lung colonization is altered by Net4-containing BMs and further suggest that Net4-containing BMs impact the steps of the invasion–metastasis process³⁴ where the BM plays a role (invasion, intravasation and extravasation).

We confirmed our findings in a second cancer model using HcMcl12 mouse melanoma cells. Net4-containing BMs significantly decreased HcMcl12 cancer cell invasion in spheroid invasion assays (Fig. 3a and Extended Data Fig. 5a). We intravenously injected HcMcl12 cells into Net4 knockout and wildtype mice, isolated lung tissues and further inspected the abdomen for metastases in the peritoneum and mesentery⁴¹ (Fig. 3b). We observed a significant increase in metastases in the lung and the abdominal space in Net4 knockout mice (Fig. 3c,d).

To exclude that endogenous Net4 levels within cancer cells contribute to the alteration in lung metastatic colonization, we next performed quantitative real-time polymerase chain reaction

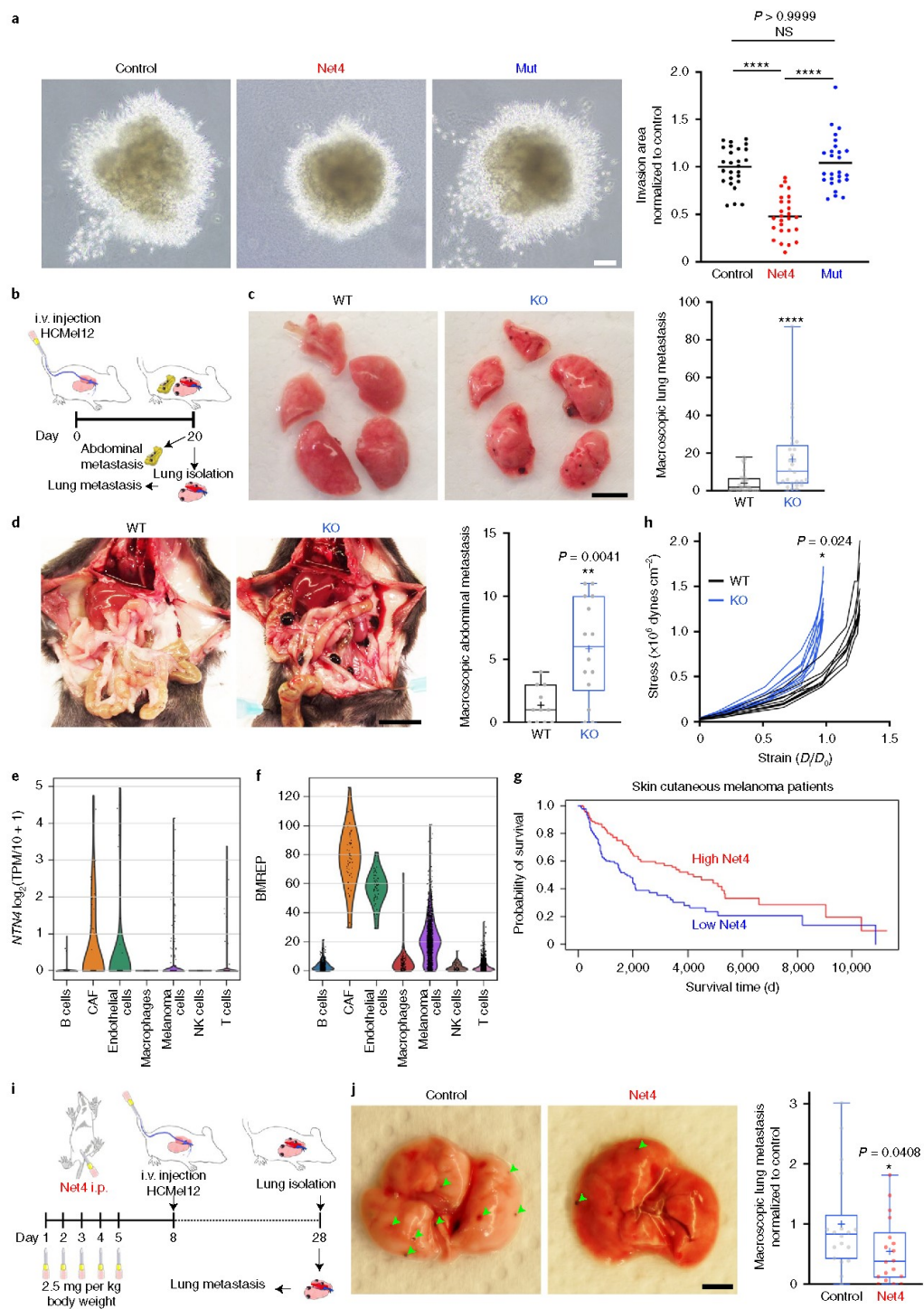
(rtPCR) to determine Net4 (*Ntn4*) expression levels in different cell lines. *Ntn4* expression was higher in E0771 cells than in HcMcl12 cells (Extended Data Fig. 5b). We generated E0771 cells deficient for Net4 using CRISPR/Cas9 technology and repeated the metastasis studies in Net4 knockout and wildtype mice. The generated cells showed a significant increase in lung metastases (number, area and total metastases area) in Net4 knockout mice (Extended Data Fig. 5c–e), demonstrating these effects are independent of tumour-derived Net4.

Our results thus far suggest that BMs containing Net4 affect the formation of metastases. To investigate which cell types produce Net4 in human cancer patients, we analysed a published single-cell RNA sequencing (scRNA-seq) dataset from 19 melanoma patients⁴². We assigned clusters to seven cell types based on cell-type-specific markers (Extended Data Fig. 6a), and found Net4 (*NTN4*) to be mainly produced by CAFs and endothelial cells (Fig. 3e and Extended Data Fig. 6b). To determine whether CAFs and endothelial cells are the major source of BM components, we analysed the expression of 48 BM components within all cell types (Supplementary Table 1). Indeed, CAF and endothelial cells express the major proportion of all BM components (Fig. 3f, Extended Data Fig. 6c and Extended Data Fig. 7). Based on these findings that Net4 is produced by cell types shaping the BM, we determined the association of Net4 expression levels with prognosis in an available dataset with 424 melanoma patients⁴³. High levels of *NTN4* were indeed significantly associated with good prognosis of melanoma patients (Fig. 3g).

Net4 softens BMs. As most of the abdominal metastases in the HcMcl12 model were attached to the mesenteric vessels, we focused on visualizing Net4 within these vessels and confirmed the absence of Net4 in the vascular BM (vBM) of Net4 knockout mice (Extended Data Fig. 8a), indicating a link between increased metastasis and absence of Net4. Mesenteric arteries are a good model to assess the BM stiffness *ex vivo* as they contain only a thin layer of vascular smooth muscle cells separated from the endothelial cell layer by the BM and internal elastic lamina⁴⁴.

To determine the effect of Net4 on the biomechanical properties of the vBM, we performed pressure myography on mesenteric vessels from Net4 wildtype and knockout mice. This revealed that lack of Net4 does not alter the overall structure of the mesenteric vessels (Extended Data Fig. 8b,c). We also employed pressure myography to obtain wall stress and strain parameters to determine the vessel

Fig. 3 | Net4-deficient alveolar and mesenteric vessel BM favours metastases formation. **a**, Representative images of HcMcl12 cell sphere invasion assay in Matrigel (control) and Matrigel containing 50% Net4 or 50% Net4 laminin-binding mutant (Mut) molecules relative to laminin 111 within the Matrigel matrix. Scale bar, 100 μ m. Right: scatter plot of sphere invasion (Kruskal–Wallis test, mean is displayed as black line; $n = 26$; **** $P < 0.0001$). **b**, Experimental design of intravenous injection of HcMcl12 mouse melanoma cells into Net4 WT and Net4 KO mice and subsequent analysis of lungs and abdomen 20 d postinjection. **c**, Representative images of lung lobes from Net4 WT and Net4 KO mice. Black spots on the lung surface are macroscopic metastases. Scale bar, 5 mm. Right: box-and-whisker plot of macroscopic lung metastases in Net4 WT and Net4 KO mice (two-tailed Mann–Whitney test, minimum to maximum, median is shown as line, mean is displayed as cross, data points appear as grey dots; $n = 32$ (WT), $n = 28$ (KO); **** $P < 0.0001$). **d**, Representative images of the peritoneal space from Net4 WT and Net4 KO mice. Black spheroids are abdominal metastases. Scale bar, 10 mm. Right: box-and-whisker plot of macroscopic abdominal metastases in Net4 WT and Net4 KO mice (two-tailed Mann–Whitney test, minimum to maximum, median is shown as line, mean is displayed as cross, data points appear as grey dots; $n = 11$ (WT), $n = 14$ (KO); ** $P < 0.01$). **e**, Violin plots of *NTN4* expression for each cell type using scRNA-seq from 19 melanoma tumour patients⁴². The expression levels of *NTN4* were quantified as $\log_2(\text{TPM}/10 + 1)$, where TPM refers to transcript per million for *NTN4*. **f**, Violin plots of the expression of the 49 BM genes for each cell type. The summed z scores of the 49 BM genes (BMREP) were used as representative expression values for each cell. **g**, Kaplan–Meier plot showing the difference of overall survival between melanoma patients with high (67th percentile *NTN4* levels) and low (33th percentile *NTN4* levels) *NTN4* expression calculated by a log rank test ($P = 0.0008$). **h**, Stress–strain graph of pressure myography analysis of mesenteric vessels from Net4 WT and Net4 KO mice (linear regression test, single line for each dataset; $n = 8$; * $P < 0.05$). **i**, Experimental design of rescue approach, in which Net4 KO mice were treated without (control) and with 2.5 mg per kg body weight recombinant Net4 (Net4) intraperitoneally injected for five consecutive days. Three days after treatment was stopped (day 8), HcMcl12 cells were intravenously injected. Macroscopic lung metastases were analysed 20 d postinjection. **j**, Representative images of lung tissue from control and Net4-treated (Net4) Net4 KO mice. Black spots on the lung surface marked with arrowheads are macroscopic metastases. Scale bar, 5 mm. Right: box-and-whisker plot of macroscopic HcMcl12 lung metastases in control and Net4-treated (Net4) Net4 KO mice (two-tailed Mann–Whitney test, minimum to maximum, median is shown as line, mean is displayed as cross, all data points appear as grey dots (ctrl) and red dots (Net4); $n = 18$; * $P < 0.05$).



stiffness. This analysis revealed a leftward shift of the stress–strain curve in Net4 knockout compared with wildtype mice, indicating increased stiffness in mesenteric vessels (Fig. 3h).

Next, we sought to investigate the impact of reapplying Net4 to Net4 knockout mice on the formation of metastases. Here, we treated Net4 knockout mice for five consecutive days intraperitoneally with 2.5 mg per kg body weight recombinant Net4 before intravenous injection of HcMel12 cells, 3 d after the treatment was stopped (Fig. 3i). Strikingly, the systemic injection of Net4 significantly reduced the formation of lung metastases (Fig. 3j).

As the knockout mice harboured more lung metastases, we next investigated the biomechanical properties of the alveolar BM. There is a growing literature of BM mechanics^{8,12,45–49} yet no measurements of alveolar BM. To keep the native tissue properties preserved we used rehydrated, cryoembedded lung tissues for the atomic force microscopy (AFM) analysis (Fig. 4a), because BM biomechanics are substantially altered in a dehydrated state⁴⁵.

The alveolar BM is localized between an epithelial and endothelial cell layer. To identify the alveolar BM stiffness, we developed a tailored experimental approach where the AFM tip is moved across the alveolar space from the epithelial side to the endothelial side, crossing the alveolar wall and the BM (Fig. 4b). Data acquisition over this distance resulted in a Young's modulus pattern that enabled identification of the BM in between the softer cell layers (Fig. 4b). Using this method, we analysed Net4 knockout and wildtype mice alveolar BM stiffness and found BM to be significantly softer in the presence of Net4 (25 kPa for wildtype versus 50 kPa for knockout mice). These data, together with the pressure myography analysis of mesenteric vessel stiffness, indicated that Net4-containing BMs are generally softer than BMs lacking Net4 (Fig. 4b) and that BM mechanics determined the stiffness of the entire vessel.

Next, we set out to confirm the altered BM stiffness in Net4 knockout animals at a cellular level *in vivo*. Discher and colleagues recently postulated that caveolae structures are formed on soft matrix and are less prominent on stiff matrix^{50,51} (Fig. 4c). Therefore, we employed transmission electron microscopy to assess caveolae structures in the capillary endothelium of alveoli in Net4 knockout and wildtype mice. We observed clear omega-shaped caveolae structures in wildtype mice after fusion with the plasma membrane. However, caveolae-forming structures in the Net4 knockout mice were mainly intracellularly localized, and the number of omega-shaped alveolar BM-fused caveolae was significantly decreased (Fig. 4d). Therefore, we analysed the ratio of alveolar BM-fused to non-fused caveolae. This analysis revealed a significant decrease in the fused to non-fused caveolae ratio in Net4 knockout mice (Fig. 4d). These data support our AFM analysis and pressure myography analysis that found a strong correlation between Net4 presence and BM stiffness (Fig. 3h and Fig. 4b). Moreover, our data suggest that caveolae structures might be useful markers to indicate BM stiffness alterations *in vivo*.

To evaluate whether Net4 expression is associated with tissue stiffness in cancer patients, we analysed a previously published dataset from human high-grade serous ovarian cancer metastasis⁵². *NTN4* was the gene most strongly associated with omental metastasis tissue softness across 31 patient samples (Fig. 4e) and therefore strongly correlates negatively with tumour tissue stiffness (Fig. 4f and Supplementary Table 3). These data suggest that BM organization, and likely its stiffness, may be clinically important in different types of cancer. We further noted that *NTN4* is negatively correlated with the expression of malignant cell markers (*PAX8* and *EPCAM*), and positively correlated with BM-encoding genes (Extended Data Fig. 9a–c and Supplementary Table 4). This suggests that the impact of Net4 is based on its localization within the BM. Moreover, the BM seems to have a similar impact on breast and ovarian cancer patients (Extended Data Fig. 9d).

Laminin ternary node complexes determine BM stiffness. To explore whether Net4 protein levels directly affect BM stiffness, we investigated the stiffness of rBM supplemented with Net4. We performed AFM analysis following two different approaches: premixing of Net4 with rBM before polymerization; and titration of Net4 to the already polymerized rBM (Fig. 5a and Extended Data Fig. 10a). Titration of only 0.6% of Net4 proteins in relation to laminin molecules within the rBM caused a 20% decrease of the rBM Young's modulus compared with a lack of Net4 (Fig. 5b). Addition of 25% Net4 protein to the rBM resulted in a decrease of 50% in rBM Young's modulus. These experiments revealed a strong initial reduction in BM stiffness until approximately 25% of Net4, then the stiffness starts to saturate, reaching 35% of the original Young's modulus at 50% of Net4 (Fig. 5b and Extended Data Fig. 10b,c). Thus, Net4 is indeed able to precisely decrease the stiffness of a BM in a concentration-dependent manner. Moreover, the alteration of the ternary node complex within the laminin network influences the overall stiffness of the BM. As the BM is built of two linked supramolecular networks comprised of collagen IV and laminin^{5,38}, the observed saturation of the stiffness of the rBM at around 50% addition of Net4 might be due to the stiffness of the unaffected collagen IV network.

We recently showed that cancer cells respond to ECM stiffness through adaptation of their intracellular viscoelasticity⁵³. We analysed the intracellular viscoelasticity of cancer cells in rBM and rBM supplemented with Net4 as well as Mut protein using optical tweezers. Cancer cells significantly adapted their intracellular viscoelasticity to the softer matrix in rBM plus Net4 but not in rBM plus Mut protein (Extended Data Fig. 10d,e). These data strongly support that Net4 is altering ECM stiffness.

In order to rationalize our experimental findings, we introduced a coarse-grained model for the BM elastic properties that approximates the laminin network as an ordered two-dimensional honeycomb lattice. The dilution fraction ϕ quantifies the fraction of occupied to the total number of available Net4 binding sites; each

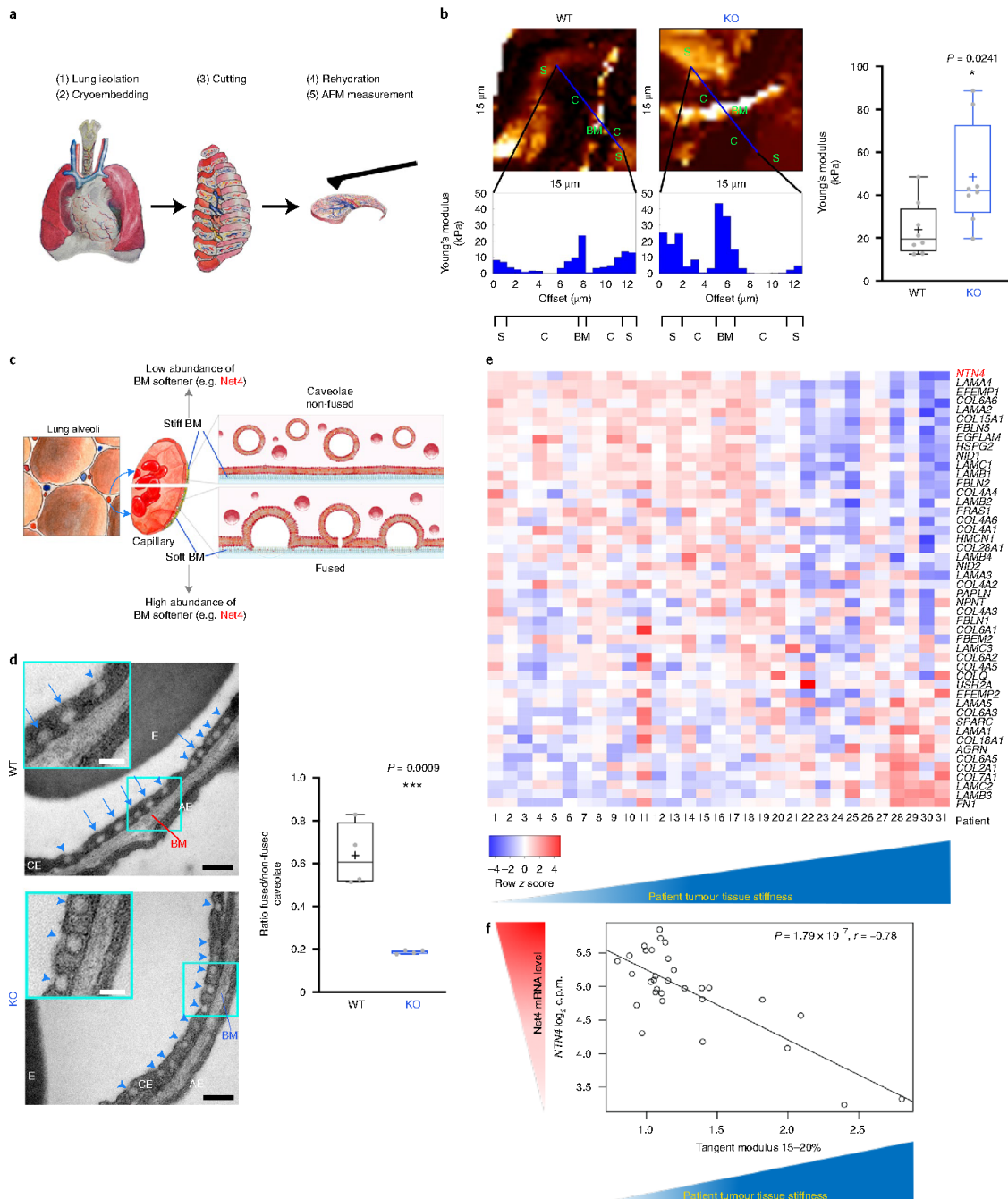
Fig. 4 | Influence of Net4 on the mechanical properties of the BM. **a**, Experimental design of AFM analysis of the alveolar BM from Net4 WT and Net4 KO mice. **b**, Representative AFM measurements to determine the stiffness (Young's modulus) of the alveolar BM in Net4 WT and KO mice. The AFM starts in one alveolus and goes to another, detecting different stiffness patterns corresponding to the alveolar space (S), followed by cell layer (C), followed by the BM (BM), followed by cell layer (C), ending in the opposite alveolar space (S). Right: box-and-whisker plot of the Young's modulus of the pulmonary BM from Net4 WT and Net4 KO mice (two-tailed unpaired *t* test, minimum to maximum, median is shown as line, mean is displayed as cross, data points appear as grey dots; *n* = 8; *t* = 2.529, d.f. = 14; **P* < 0.05). **c**, Scheme of caveolae structures inside capillary endothelial cells underlying a soft (fused) or stiff (non-fused) BM in the lung aveoli. **d**, Representative electron microscopy images of the alveolar BM from Net4 WT and Net4 KO mice. Blue arrows indicate caveolae structures within the capillary endothelium (CE) fused with the plasma membrane directed to the BM. Blue arrowheads indicate non-fused caveolae structures. AE, alveolar epithelium; E, erythrocyte. Scale bars, 250 nm and 100 nm (insets). Right: box-and-whisker plot of the ratio of fused to non-fused caveolae structures in Net4 WT and KO mice (two-tailed unpaired *t* test, minimum to maximum, median is shown as line, mean is displayed as cross, data points appear as grey dots; *n* = 4 (mice); ****P* < 0.001). **e**, Heatmap illustrates row *z* scores of the log₂ c.p.m. (counts per million) gene expression of indicated genes. Samples (columns) ordered by increasing tissue stiffness (CANBUILD dataset-GSE71340 (ref. 52)). Genes (rows) arranged by increasing Pearson's correlation coefficient (*r*) (Supplementary Table 3). **f**, Correlation between the Net4 (*NTN4*) gene expression and patient's tumour tissue stiffness (Pearson's *P* = 1.79 × 10⁻⁷, *r* = -0.78, *n* = 31).

ARTICLES

NATURE MATERIALS

bound Net4 removes a node in the laminin lattice. We modelled the elastic bonds as harmonic springs and determined equilibrium network structures for varying ϕ by energy minimization. Snapshots of networks without strain (Fig. 5c) and under a uniaxial strain of 40% (Fig. 5d) are shown. Diluted strained networks deform to minimize

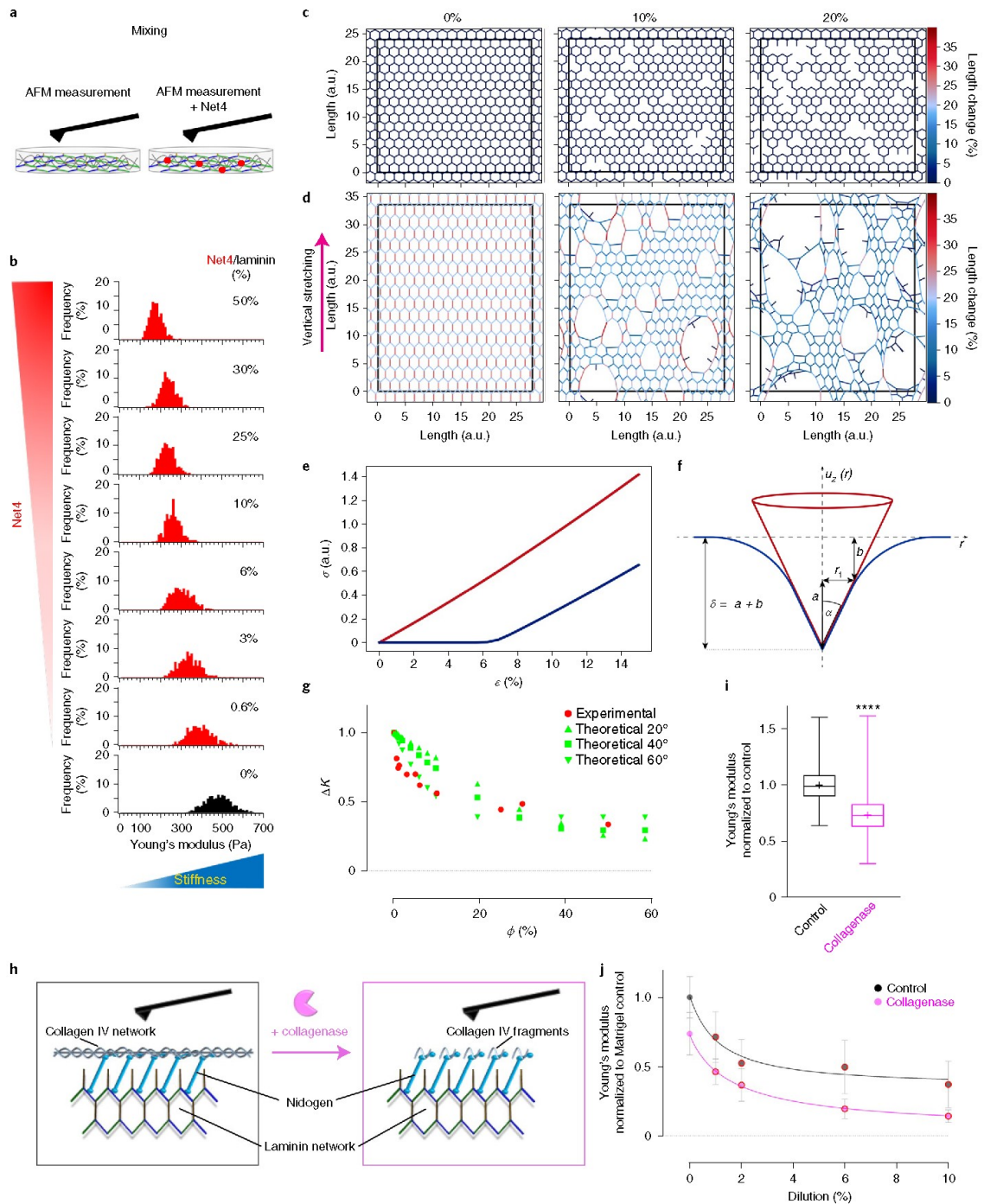
the number of highly stretched bonds (shown in red), giving rise to large pores with deformed bonds concentrated around the pore edges (Fig. 5d). Figure 5e shows calculated stress–strain profiles for two different dilutions. The curve for $\phi = 10\%$ revealed a soft floppy mode⁵⁴, where up to a threshold strain of $\epsilon = 7\%$ no stress arises,



in contrast to the undiluted case $\phi=0$, which exhibited a linear stress-strain relation. The floppy behaviour of the diluted lattice is caused by the node rearrangement around the pores, which allows the system to accommodate large strains at minimal energetic cost

(Fig. 5c,d). The threshold strain increases roughly linearly with dilution (Extended Data Fig. 10f).

To account for the three-dimensional network deformation, as realized in the AFM experiments, we estimated the maximal



ARTICLES

NATURE MATERIALS

Fig. 5 | Decrease of BM stiffness via disrupting ternary laminin node complexes. **a**, Scheme of Young's modulus measurement by AFM of Matrigel and Matrigel mixed with Net4 (red dots). **b**, Histograms reveal the Young's modulus of measurements of pure Matrigel (black) and different Net4 percentages mixed into Matrigel (red). The amount as a percentage of Net4 molecules mixed into Matrigel indicates the ratio between Net4 and laminin 111 molecules. **c,d**, Simulation snapshots for no dilution, 10% dilution and 20% dilution: unstrained diluted system (**c**); diluted system under 40% strain (**d**). **e**, Stress (σ) versus strain (ϵ) relations for the model laminin network at dilutions $\phi=0\%$ (red) and $\phi=10\%$ (blue). **f**, Sketch of the surface of an isotropic elastic medium (blue) deformed by a cone (red). Definitions of indentation depth δ , half-opening angle α and contact radius r_c are shown. **g**, Relative stiffness change (ΔK) of Matrigel plotted against dilution (ϕ) obtained by AFM measurements of Net4 mixed into Matrigel (experimental) and data of the computational simulation (theoretical) for different values of the half-opening angle α of the conical indenter. One Net4 molecule was estimated to open one laminin ternary node complex and the ratio between laminin and Net4 molecules or number of openings in relation to total nodes reveals the dilution. **h**, Scheme of the AFM experiment to determine the Young's modulus of Matrigel and Matrigel mixed with collagenase (indicated as a three-quarter circle shape) followed by titration of recombinant Net4. **i**, Box-and-whisker plot of Young's modulus of untreated (control) and collagenase-treated Matrigel (two-tailed Mann-Whitney test, minimum to maximum, median is shown as line, mean is displayed as cross; $n=569$ (control), $n=494$ (collagenase); **** $P < 0.0001$). **j**, Young's modulus of untreated (control) and collagenase-treated Matrigel with different concentrations of Net4 presenting the dilution of the laminin network as a percentage. All values are normalized to Matrigel control at 0% Net4 and include the standard deviation.

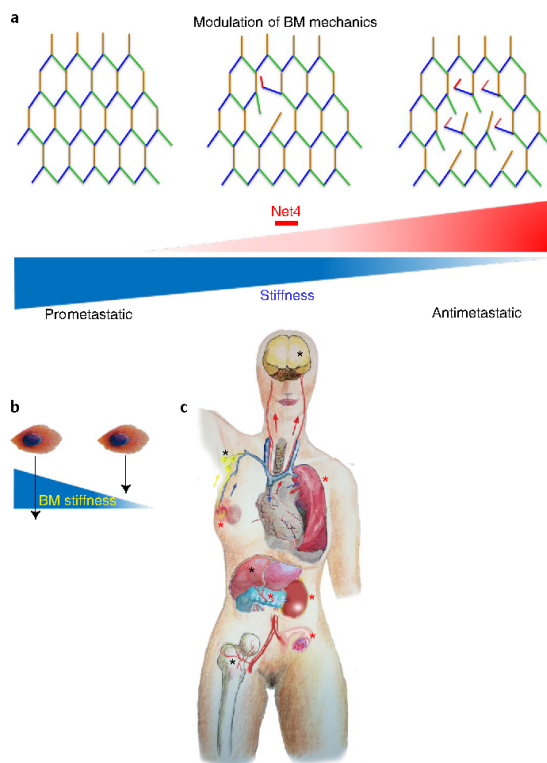


Fig. 6 | Impact of BM mechanics on metastasis. Our study reveals the impact of BM mechanics modulation on metastases formation and patient survival. **a**, The scheme depicts the modulation of the BM through the ECM protein Net4 (red sticks) and how increasing amounts of Net4 reduce the stiffness of a laminin network (ternary node complex through the interaction of laminin $\alpha 1, 2, 3\beta$ and 5 (yellow), $\beta 1, 2$ and 3 (green), and $\gamma 1$ and 3 (blue)) and thereby of the entire BM. We show that stiff BMs favour metastases formation, and the softer a BM gets, the more antimetastatic it becomes. **b**, Our model shows that increasing BM stiffness is associated with increasing cancer cell invasion. **c**, Vessels present the major route for cancer cells to spread throughout the body to colonize secondary sites and establish metastases. Our data highlight that the BM stiffness defines cancer cell intravasation from breast, kidney and ovarian tissues and extravasation into lungs and mesentery (red asterisks). Although Net4 is not the defining factor for BM stiffness in all tissues, we hypothesize that BM stiffness is a key determinant also in these tissues including common metastatic sites such as lymph nodes, brain, liver and bone (black asterisks).

extensional strain of an isotropic elastic medium that is deformed by a cone (Methods), as sketched in Fig. 5f. We included the constant elastic response from the collagen IV background, which added a single fit parameter to our model (Methods). Figure 5g compares the theoretical rescaled deformation modulus $\Delta\kappa(\phi) = \kappa(\phi)/\kappa(0)$ for three different half-opening angles α of a conical indenter as a function of dilution to the experimental AFM data. Although a value of $\alpha = 20^\circ$ best describes the shape of the pyramidal tip used in the AFM experiments, presumably higher values of α are closer to reality, and reflect structural imperfections of the AFM tip and the sample surface as well as torsional and radial strain effects. The background collagen elastic response accounts for the finite value of $\Delta\kappa(\phi)$ for large ϕ . The quite abrupt BM stiffness decrease at low dilutions was well reproduced by the model, especially for $\alpha = 60^\circ$ (Fig. 5f and Methods), and can be explained by the non-linear floppy elastic response of diluted laminin networks. This suggests that the mechanism by which Net4 softens BM consists of a systematic dismantling of the laminin network. Treatment of the Matrigel with collagenase (Fig. 5h) revealed a significant decrease of Matrigel stiffness of approximately 27% (Fig. 5i) and an almost total loss of stiffness at around 10% of laminin node dilution (Fig. 5j). These data reveal that the background stiffness we measured is mainly based on the collagen IV network.

Discussion

ECM stiffness has long been known to be a major influencer of cancer metastasis; however, previous studies have focused on interstitial matrix—the BM, and its contribution to matrix stiffness, has not been explored. Moreover, the functional role of the BM architecture during cancer progression has also not previously been investigated. Here we show that Net4 softens the BM in a laminin-binding-dependent manner by diluting laminin ternary node complexes. The more Net4 molecules are present, the softer the laminin network and the more resistant it is to metastases formation (Fig. 6a). We demonstrate that stiffness is a stronger influencing factor than pore size in the regulation of cancer cell movement through the BM. Thus, we propose a model where BM mechanics determine the ability of cancer cells to breach the BM: the softer a BM, the less breaching by cancer cells (Fig. 6b), extending patient survival.

Our experimental and theoretical data show that the stiffness of the laminin network can be precisely modulated by Net4, resulting in an altered stiffness of the entire BM and vessels. Our study reveals a critical role of BM mechanics at the primary and secondary tumour site independent of tumour-mediated alterations. Therefore, we hypothesize that the 'normal' BM composition may also play a pivotal role in the colonization of other common metastatic sites such as the liver, brain and bone (Fig. 6c) for all metastasizing solid tumours. Excitingly, our data suggest that baseline BM stiffness may predetermine survival even before having cancer throughout one's lifetime. Therefore, the development of tools

to soften BMs at the primary and secondary site could represent a promising approach to decrease or even prevent metastasis.

A vast number of studies report pro- and antitumorigenic activity of Net4. However, all these studies have exclusively focused on a direct impact of Net4 on cells^{28–37}. Our study consistently revealed an indirect antimetastatic activity of Net4 when localized within native BMs, thereby modifying the mechanical properties of this specialized ECM material in many different cancer types. Thus, our data demonstrate the two context-dependent faces of Net4, such that Net4 can be proinvasive via an unknown mechanism and antimetastatic via its laminin interaction which is strongly dependent on the ratio between Net4 and laminin molecules.

The ECM is shaped by a huge number of extracellular proteins defined as the matrisome⁵⁵. Previous reports have focused on the direct impact of single matrisome proteins on cells. However, our data open the possibility that some of these proteins might be reversible regulators of the biochemical and mechanical properties of the overall ECM structure simply through binding to ECM macromolecules. Consequently, our study might open a research area focusing on reversible extracellular matrix regulators (RevMatriRegs) of mechanical properties of the major network-forming proteins.

Online content

Any methods, additional references, Nature Research reporting summaries, source data, extended data, supplementary information, acknowledgements, peer review information; details of author contributions and competing interests; and statements of data and code availability are available at <https://doi.org/10.1038/s41563-020-00894-0>.

Received: 17 January 2020; Accepted: 27 November 2020;

Published online: 25 January 2021

References

- Dillekas, H., Rogers, M. S. & Straume, O. Are 90% of deaths from cancer caused by metastases? *Cancer Med.* **8**, 5574–5576 (2019).
- Chaffer, C. L. & Weinberg, R. A. A perspective on cancer cell metastasis. *Science* **331**, 1559–1564 (2011).
- Fidler, I. J. The pathogenesis of cancer metastasis: the 'seed and soil' hypothesis revisited. *Nat. Rev. Cancer* **3**, 453–458 (2003).
- Valastyan, S. & Weinberg, R. A. Tumor metastasis: molecular insights and evolving paradigms. *Cell* **147**, 275–292 (2011).
- Yurchenco, P. D. Basement membranes: cell scaffoldings and signaling platforms. *Cold Spring Harb. Perspect. Biol.* <https://doi.org/10.1101/cshperspect.a004911> (2011).
- McKee, K. K., Harrison, D., Capizzi, S. & Yurchenco, P. D. Role of laminin terminal globular domains in basement membrane assembly. *J. Biol. Chem.* **282**, 21437–21447 (2007).
- Abrams, G. A., Goodman, S. L., Nealey, P. F., Franco, M. & Murphy, C. J. Nanoscale topography of the basement membrane underlying the corneal epithelium of the rhesus macaque. *Cell Tissue Res.* **299**, 39–46 (2000).
- Gaiko-Shcherbak, A. et al. The acinar cage: basement membranes determine molecule exchange and mechanical stability of human breast cell acini. *PLoS ONE* **10**, e0145174 (2015).
- Yurchenco, P. D. & Ruben, G. C. Basement membrane structure in situ: evidence for lateral associations in the type IV collagen network. *J. Cell Biol.* **105**, 2559–2568 (1987).
- Linder, S. Invadosomes at a glance. *J. Cell Sci.* **122**, 3009–3013 (2009).
- Wisdom, K. M. et al. Matrix mechanical plasticity regulates cancer cell migration through confining microenvironments. *Nat. Commun.* **9**, 4144 (2018).
- Glentis, A. et al. Cancer-associated fibroblasts induce metalloprotease-independent cancer cell invasion of the basement membrane. *Nat. Commun.* **8**, 924 (2017).
- Couchman, J. R. & Gibson, W. T. Expression of basement membrane components through morphological changes in the hair growth cycle. *Dev. Biol.* **108**, 290–298 (1985).
- Nelson, T. R., Charonis, A. S., McIvor, R. S. & Butkowski, R. J. Identification of a cDNA encoding tubulointerstitial nephritis antigen. *J. Biol. Chem.* **270**, 16265–16270 (1995).
- Sasaki, T., Gohring, W., Pan, T. C., Chu, M. L. & Timpl, R. Binding of mouse and human fibulin-2 to extracellular matrix ligands. *J. Mol. Biol.* **254**, 892–899 (1995).
- Sato, S. et al. Pikachurin, a dystroglycan ligand, is essential for photoreceptor ribbon synapse formation. *Nat. Neurosci.* **11**, 923–931 (2008).
- Veit, G. et al. Collagen XXVIII, a novel von Willebrand factor A domain-containing protein with many imperfections in the collagenous domain. *J. Biol. Chem.* **281**, 3494–3504 (2006).
- Timpl, R. & Brown, J. C. Supramolecular assembly of basement membranes. *Bioessays* **18**, 123–132 (1996).
- Mayorca-Guiliani, A. E. et al. Decellularization and antibody staining of mouse tissues to map native extracellular matrix structures in 3D. *Nat. Protoc.* <https://doi.org/10.1038/s41596-019-0225-8> (2019).
- Koch, M. et al. A novel member of the netrin family, beta-netrin, shares homology with the beta chain of laminin: identification, expression, and functional characterization. *J. Cell Biol.* **151**, 221–234 (2000).
- van de Vijver, M. J. et al. A gene-expression signature as a predictor of survival in breast cancer. *N. Engl. J. Med.* **347**, 1999–2009 (2002).
- Nicolau, M., Tibshirani, R., Borresen-Dale, A. L. & Jeffrey, S. S. Disease-specific genomic analysis: identifying the signature of pathologic biology. *Bioinformatics* **23**, 957–965 (2007).
- Li, Y. N. et al. The expression and function of netrin-4 in murine ocular tissues. *Exp. Eye Res.* **96**, 24–35 (2012).
- George, E. L., Georges-Labouesse, E. N., Patel-King, R. S., Rayburn, H. & Hynes, R. O. Defects in mesoderm, neural tube and vascular development in mouse embryos lacking fibronectin. *Development* **119**, 1079–1091 (1993).
- Miner, J. H., Cunningham, J. & Sanes, J. R. Roles for laminin in embryogenesis: exencephaly, syndactyly, and placentopathy in mice lacking the laminin alpha5 chain. *J. Cell Biol.* **143**, 1713–1723 (1998).
- Higgins, J. P. et al. Gene expression in the normal adult human kidney assessed by complementary DNA microarray. *Mol. Biol. Cell* **15**, 649–656 (2004).
- Zhao, H. et al. Gene expression profiling predicts survival in conventional renal cell carcinoma. *PLoS Med.* **3**, e13 (2006).
- Hu, Y. et al. Netrin-4 promotes glioblastoma cell proliferation through integrin beta4 signaling. *Neoplasia* **14**, 219–227 (2012).
- Jayachandran, A. et al. Identifying and targeting determinants of melanoma cellular invasion. *Oncotarget* **7**, 41186–41202 (2016).
- Larrieu-Lahargue, E., Welm, A. L., Thomas, K. R. & Li, D. Y. Netrin-4 induces lymphangiogenesis in vivo. *Blood* **115**, 5418–5426 (2010).
- Lv, B. et al. Netrin-4 as a biomarker promotes cell proliferation and invasion in gastric cancer. *Oncotarget* **6**, 9794–9806 (2015).
- Villanueva, A. A. et al. The netrin-4/neogenin-1 axis promotes neuroblastoma cell survival and migration. *Oncotarget* **8**, 9767–9782 (2017).
- Li, L. et al. Netrin-4 protects glioblastoma cells from temozolomide induced senescence. *PLoS ONE* **8**, e80363 (2013).
- Essegir, S. et al. Identification of NTN4, TRA1, and STC2 as prognostic markers in breast cancer in a screen for signal sequence encoding proteins. *Clin. Cancer Res.* **13**, 3164–3173 (2007).
- Evano, C. et al. Netrin-4 delays colorectal cancer carcinomatosis by inhibiting tumor angiogenesis. *Am. J. Pathol.* **178**, 1861–1869 (2011).
- Fujikane, T. et al. Genomic screening for genes upregulated by demethylation revealed novel targets of epigenetic silencing in breast cancer. *Breast Cancer Res. Treat.* **122**, 699–710 (2010).
- Nacht, M. et al. Netrin-4 regulates angiogenic responses and tumor cell growth. *Exp. Cell Res.* **315**, 784–794 (2009).
- Kleinman, H. K. et al. Basement membrane complexes with biological activity. *Biochemistry* **25**, 312–318 (1986).
- Reuten, R. et al. Structural decoding of netrin-4 reveals a regulatory function towards mature basement membranes. *Nat. Commun.* **7**, 13515 (2016).
- Mayorca-Guiliani, A. E. et al. ISDoT: in situ decellularization of tissues for high-resolution imaging and proteomic analysis of native extracellular matrix. *Nat. Med.* **23**, 890–898 (2017).
- Trout, A. T., Rabinowitz, R. S., Platt, J. F. & Elsayes, K. M. Melanoma metastases in the abdomen and pelvis: frequency and patterns of spread. *World J. Radiol.* **5**, 25–32 (2013).
- Tirosh, I. et al. Dissecting the multicellular ecosystem of metastatic melanoma by single-cell RNA-seq. *Science* **352**, 189–196 (2016).
- Cancer Genome Atlas, N. Genomic classification of cutaneous melanoma. *Cell* **161**, 1681–1696 (2015).
- Tucker, W. D., Arora, Y. & Mahajan, K. *Anatomy, Blood Vessels* (StatPearls, 2020).
- Candiello, J. et al. Biomechanical properties of native basement membranes. *FEBS J.* **274**, 2897–2908 (2007).
- Halfter, W. et al. Protein composition and biomechanical properties of in vivo-derived basement membranes. *Cell Adh. Migr.* **7**, 64–71 (2013).
- Last, J. A., Liliensiek, S. J., Nealey, P. F. & Murphy, C. J. Determining the mechanical properties of human corneal basement membranes with atomic force microscopy. *J. Struct. Biol.* **167**, 19–24 (2009).

ARTICLES

NATURE MATERIALS

48. Bhave, G., Colon, S. & Ferrell, N. The sulfilimine cross-link of collagen IV contributes to kidney tubular basement membrane stiffness. *Am. J. Physiol. Ren. Physiol.* **313**, F596–F602 (2017).
49. Chlasta, J. et al. Variations in basement membrane mechanics are linked to epithelial morphogenesis. *Development* **144**, 4350–4362 (2017).
50. Swift, J. et al. Nuclear lamin-A scales with tissue stiffness and enhances matrix-directed differentiation. *Science* **341**, 1240104 (2013).
51. Irianto, I., Pfeifer, C. R., Xia, Y. & Discher, D. E. SnapShot: mechanosensing matrix. *Cell* **165**, 1820–1820 e1821 (2016).
52. Pearce, O. M. T. et al. Deconstruction of a metastatic tumor microenvironment reveals a common matrix response in human cancers. *Cancer Discov.* **8**, 304–319 (2018).
53. Wullkopf, L. et al. Cancer cells' ability to mechanically adjust to extracellular matrix stiffness correlates with their invasive potential. *Mol. Biol. Cell* **29**, 2378–2385 (2018).
54. Lubensky, T. C., Kane, C. L., Mao, X., Souslov, A. & Sun, K. Phonons and elasticity in critically coordinated lattices. *Rep. Prog. Phys.* **78**, 073901 (2015).
55. Naba, A. et al. The matrisome: in silico definition and in vivo characterization by proteomics of normal and tumor extracellular matrices. *Mol. Cell. Proteomics* **11**, M111 014647 (2012).

Publisher's note Springer Nature remains neutral with regard to jurisdictional claims in published maps and institutional affiliations.

© The Author(s), under exclusive licence to Springer Nature Limited 2021

Methods

Gene expression analysis. We used the NKI²⁰ dataset of 295 breast cancers (<https://ccb.nki.nl/data/>) and a dataset with 13 normal breast tissue samples²¹, three from reduction mammoplasties and ten from pathologically normal breast tissue from breast cancer patients, to explore association with survival of all BM genes. We found 35 out of 49 BM genes present in the NKI dataset. DSGA²² was used to decompose the data into Disease and Normal components. Roughly, the normal tissue breast samples are used to construct a mathematical model for the healthy state. This healthy-state model (HSM) incorporates a multitude of normal breast tissue signatures, including single-cell-type signatures as well as combinations of cell types in a range of states. Mathematically it is obtained from a linear model of the normal tissue data, followed by several steps of dimensionality reduction. The dimensionality reduction steps avoid overfitting the normal tissue data. Each tumour tissue gene expression sample is then mathematically decomposed into a Normal and a Disease component. The Normal component of the tumour is the signature of the cell types present in the tumour sample in their normal/healthy state. It is the profile of the mix of cells present in the tumour tissue sample, but with their healthy/normal gene expression signature. Mathematically it is the best fit of the tumour data to the HSM. The Disease component captures the modifications in the tumour sample from the normal signature; thus in essence the Disease component measures how the sample of cells, tumour and microenvironment have deviated from their normal/healthy phenotype. Mathematically, the Disease component is the vector of residuals from the HSM fit. It is important to point out that the DSGA decomposition of each tumour is done independently of the rest of the tumours in the cohort. In the next step, we first identified the status of each tumour based on the Disease component expression levels of ESR1 and ERBB2 (HER2). The distributions of both ESR1 and ERBB2 in the Disease component was clearly bimodal, and the cutoff was assigned between positive (over) and negative (under) expression status. We then explored the association with survival for each of the 35 BM genes separately, in each of the following breast cancer subset of tumours: ER-negative tumours; ER-positive tumours; HER2 (ERBB2)-overexpressing tumours; basal-like tumours (ER-negative, HER2-normal); luminal A tumours (ER-positive, HER2-normal); luminal B tumours (ER-positive, HER2-overexpressing); and HER2-overexpressing, ER-negative tumours. In the NKI dataset ER-negative, HER2-normal tumours are also PR-negative, thus basal-like. These subsets of tumours clearly overlap. The goal was to explore the association with survival in groups of tumours that were, to some degree, homogeneous with respect to the effects of the particular BM genes studied. For each of the 35 BM genes, inside each of the seven subsets of breast cancer patients, we explored the association of the gene with survival, death and metastasis. We used Cox proportional-hazard models to compute the *P* value of the separation in survival between the tumours with low levels of the gene (33rd percentile) and those with high levels of the gene (67th percentile). We also assigned a value of +1, -1 or 0 if the gene was associated with a good or bad prognosis, or neither. This was done for seven patient groups, 35 genes, Disease components and Normal components of data. Thus, for each BM gene we obtained a vector of 28 *P* values, and a vector of 28 prognosis signs: +1, -1, 0. For each gene, we computed the log base 10 of the *P* values vector. Our criteria are: (1) consistent association with survival across many tumour groups, and (2) highly significant association with survival. Thus, a consensus association is the mean of the signed prognosis vector $\pm \log_{10}(P) : \frac{1}{28} \sum \pm \log_{10}(P)$, and an overall association is the sum of all the log-transformed *P* values $\sum \log_{10}(P)$. Thus, a large overall association value indicates strong association with survival, either in a few groups or across many groups. Large positive or small negative consensus association indicates association with survival across many different tumour groups. In case of the kidney analysis, gene expression from 166 renal cell carcinoma tumours (GSE3538)²³ and 34 normal tissue samples (GSE3931)²⁴ was analysed. DSGA analysis generated the decomposition into the Disease and Normal components of tumour data.

Mouse studies. All animal experiments followed the regulatory standards of, and were approved by, the Animal Experimentation Council of the Ministry of Environment and Food of Denmark. All experiments are controlled by the Danish Inspectorate for Animal Experimentation (permission number 2017-15-0201-01265) according to the Danish Law of Animal Welfare. All mice were housed in individually ventilated cages with a humidity of 55% ± 10%, a temperature of 22°C ± 2°C, and a dark/light cycle of 12 h/12 h with light from 6:00 to 18:00.

Cell culture. HEK293 (M. Koch, University Hospital Cologne, EBNA), mouse melanoma HcMel12 (T. Tüting, University Hospital Magdeburg, C57BL/6-compatible cell line)²⁵, mouse breast cancer E0771 (R. Anderson, University of Melbourne, C57BL/6-compatible cell line)²⁶, mouse breast cancer 4T1 (Karmanos Cancer Institute)²⁷, mouse pancreatic cancer KPC (J. Morton, Beatson Institute)²⁸ and human breast cancer MDA-MB-231 (J. Massagué, Memorial Sloan Kettering Cancer Center)²⁹ cells were cultured in Dulbecco's modified Eagle medium (DMEM)/F-12, GlutaMAX supplement (DMEM/F-12, GlutaMAX supplement, Gibco) supplemented with 10% fetal bovine serum (FBS) and 20% FBS in case of HcMel12 and E0771. Immortalized murine cancer-associated fibroblast cell lines (mCAF1 and mCAF2, E. Sahai, Francis

Crick Institute)³⁰ were cultured in DMEM/10% FBS supplemented with insulin–transferrin–selenium.

Orthotopic mouse breast cancer model. Female mice at the age of 8 weeks from Net4 knockout and the corresponding wildtype litters were used. Cohorts of wildtype and Net4-deficient mice were orthotopically injected with 5×10^5 E0771 cells into the mammary fat pad. Tumour growth was monitored on a regular basis and primary tumours were resected when they reached 1.5 cm in diameter. Mice were killed 28 d after primary tumour resection. The number of macroscopically visible metastases on lung surfaces were counted in a blind fashion. Lungs were further immunohistochemically (haematoxylin & eosin (H&E)) processed to determine and analyse microscopic lung metastases using NanoZoomer Digital Pathology (NDP) scan (NDP.scan version 2.5.90) and view 2 (NDP.view version 2.7.52) software.

Expression and purification of recombinant Net4 proteins. Full-length Net4 from *Mus musculus* (Net4, NP_067295.2; amino acids, 20–628) and its respective laminin-binding mutant E195A,R199A (Mut) were cloned into a modified Sleeping-beauty vector³¹ with a double N-terminal Strep II tag. A pool of HEK293 cells was stably transfected followed by screening for high-level expression. Net4 and its laminin-binding mutant version were purified by Strep-Tactin Sepharose (IBA). The purified proteins were dialysed against 1× PBS. These proteins were further sterile filtered through a 0.22 μm filter for all in vitro experiments.

Proliferation assay. Cancer cells were plated at 2,000 cells per 96 wells and treated without or with different concentrations (0.1, 3.6 and 5.2 μg well⁻¹) of recombinant Net4 for 96 h. Afterwards cells were washed twice with 100 μl of 1× PBS and 100 μl DMEM/F-12, GlutaMAX supplement was added to the cells and the plate was incubated at 37°C for 1 h. After 1 h, 20 μl of MTS solution (Promega) was added to each well including blank wells. Absorbance was measured at 492 nm using a SpectraMax Paradigm plate reader (Molecular Devices; SoftMax Pro version 6.5.1 software) after 1 h. Blank values were subtracted from each value and values were normalized to the respective control wells.

Contraction assay. Cancer-associated fibroblasts (mCAF1 and mCAF2) were mixed with 2 mg ml⁻¹ collagen I matrix, and 100 μl of cell/collagen I mix was plated per well in a 96 well plate to give 80,000 cells well⁻¹. Afterwards, 200 μl of media containing 2% FBS supplemented without (control) and with different amounts of recombinant Net4 and its respective laminin-binding mutant Net4 E195A,R199A. Cells were allowed to contract the collagen I matrix for 72 h. Afterwards, the contracted area was analysed and normalized to the control of the respective repeat.

Immunohistochemistry and immunofluorescence staining of E0771 primary tumours. Mouse tumours were resected, fixed in 10% neutral buffered formalin at 4°C overnight, and paraffin embedded according to a standard protocol. For immunohistochemistry staining, tissue sections were deparaffinized in xylene and rehydrated in graded ethanol (100%, 95%, 70%). Antigen retrieval was performed for 15 min at 95–98°C in 10 mM sodium citrate buffer, pH 6.0. Then, endogenous peroxidase activity was quenched by incubation in 3% H₂O₂ for 10 min. Sections were blocked in PBS + 0.1% Tween-20 and 5% goat or donkey serum. Incubations with primary antibodies (CD8a; Cell Signalling, 98941, clone D4W2Z; 1:200) were performed overnight at 4°C in a humidified chamber, followed by appropriate horseradish peroxidase-conjugated secondary antibodies (Dako, K4001 or K4003) at room temperature. ImmPACT DAB Kit (Vector Laboratories, SK-4105) was used to develop signals according to the manufacturer's instructions. Sections were counterstained with haematoxylin and mounted using DPX mounting medium (CellPath, SEA-1304-00A).

For immunofluorescence staining of tumour slides, antigen retrieval was performed similarly to immunohistochemistry staining, except slides were not incubated with 3% H₂O₂. Primary antibodies (αSMA; Abcam, ab5694; 1:200 and P4/80; eBioscience, 14-4801-85, Clone BM8; 1:100) were incubated at 4°C overnight in a humidified chamber followed by incubation with Alexa Fluor-conjugated secondary antibodies including DAPI (1 μg ml⁻¹) at room temperature for 1 h and mounted using Dako Fluorescent Mounting Medium. Stained sections were imaged using an SP8 confocal microscope (Leica) with Leica Application Suite X software (version 3.5.5.19976).

Preparation of Net4-containing Matrigel matrix. All experiments in which Matrigel has been supplemented with full-length Net4 have been performed at a laminin 111 to Net4 molecular ratio of 2:1. Matrigel containing 50% Net4 molecules compared with laminin 111 molecules was prepared by taking the protein concentration of Matrigel, which was between 8 and 11 mg ml⁻¹ depending on the batch. Afterwards, the estimated laminin 111 content of Matrigel is 60%. Moreover, the molecular weight of laminin 111 is around 10-fold higher than the molecular weight of Net4. As an example, 1 ml of a 10 mg ml⁻¹ Matrigel matrix mix was supplemented with 300 μg full-length Net4 to generate a Matrigel matrix containing approximately 50% Net4 molecules compared with laminin 111 molecules. The amount of recombinant Net4 within one 20 μl matrix

ARTICLES

NATURE MATERIALS

sphere was approximately 5.2 and 2.6 μg for 50% and 25% Net4, respectively, in proportion to laminin.

Sphere invasion assay. MDA-MB-231 and HCmel12 cells were adjusted to 100,000 cells ml^{-1} in DMEM/F-12, GlutaMAX supplement with 10% FBS, 0.24% methylcellulose and 32 μg collagen I. Liquid drops of 20 μl of this mix were placed on the lid of a 10 cm cell culture dish. The lid was placed on top of a dish containing 6 ml of 1 \times PBS and cells were allowed to form spheres in the hanging drops for 120 h. Afterwards, formed spheres were embedded in 20 μl Matrigel and in 20 μl Net4-binding or laminin-binding mutant-containing Matrigel, each supplemented with 0.5 mg ml^{-1} collagen I. In case of the collagen I sphere invasion experiments, formed spheres were embedded in 20 μl 1.5 mg ml^{-1} collagen I matrix and in 20 μl Net4- or laminin-binding mutant-containing collagen I matrix. Plates containing the plugs with spheres were placed upside down at 37 °C for 1 h to allow Matrigel polymerization. Afterwards, plates were filled with DMEM/F-12, GlutaMAX. Sphere invasion was imaged using a bright-field microscope (Olympus CKX53 with Olympus DP22 camera and Olympus cellSens Entry software version 1.1.6) after 18 and 24 h for HCmel12 and MDA-MB-231 cells, respectively. Invasive cell area was quantified using ImageJ version 2.1.0/1.53c.

Decellularization and staining of mouse lung and mesentery tissues. Net4 wildtype and knockout mice were killed and operated on as described previously¹⁹ to perfuse through the aorta and the superior mesenteric artery for lungs and mesentery, respectively. Catheterized organs are perfused by a system in which a peristaltic pump (Ole Dich) connects a reagent reservoir to the catheter connector with sterile silicone tubes (Ole Dich). The tubing has a lumen diameter of 2 mm and an external diameter of 4 mm. The waste-collection tubing has a lumen of 2.5 mm and an external diameter of 4.5 mm. The peristaltic pump is set to a flow output of 0.2 ml min^{-1} . Perfusion begins with 15 min of deionized water. This is followed by a detergent regimen of 0.5% sodium deoxycholate in deionized water for 24 h. Decellularized lung and mesentery tissues were stored in deionized water at 4 °C until staining was initiated. After decellularization, lung and mesentery tissues were blocked with 6% donkey serum and 3% bovine serum albumin in 1 \times PBS overnight. On the next day, the block solution was discarded and primary antibodies for Net4 (polyclonal rabbit anti-Net4; 1:100), laminin γ 1 (monoclonal rat anti-laminin γ 1, Millipore MAB1914P; 1:100) and collagen IV (polyclonal goat anti-collagen IV, Millipore AB769; 1:100) in 3% donkey serum in 1 \times PBS were added to the lungs and incubated overnight. Afterwards, the primary antibody solution was discarded and lung as well as mesentery tissues were washed with 0.05% Tween-20 in 1 \times PBS at least six times for 1 h. Then the secondary antibodies anti-rabbit Alexa488, anti-rat Alexa555 and anti-goat Alexa647 (1:1,000) in 3% donkey serum in 1 \times PBS were added overnight. On the next day, the tissue was washed with 0.05% Tween-20 in 1 \times PBS three times for 1 h and subsequently imaged with an inverted Leica SP5-X MP 2-photon confocal microscope connected to a Ti-sapphire laser (Spectra Physics MaiTai HP DeepSee Laser, Spectral Physics; tunable wavelength 690–1,040 nm) and a Supercontinuum white light laser with the Leica Application Suite X software version 2.7.4.10100.

Sample preparation for mass spectrometry. Lysate preparation and digestion was done according to Kulak et al.²⁰ with some modifications. Briefly, five lung tissue samples from both Net4 wildtype and knockout mice were lysed using 30 μl of lysis buffer (consisting of 6 M guanidinium hydrochloride, 10 mM tris(2-carboxyethyl)phosphine, 40 mM chloroacetamide, 50 mM HEPES pH 8.5) in a Barocycler 2320EXT (Pressure BioSciences) set to 30 cycles of 45,000 p.s.i., 50 s on, 10 s off. Samples were boiled at 95 °C for 5 min, after which they were sonicated on the 'high' setting for 5 \times 30 s in a Bioruptor sonication water bath (Diagenode) at 4 °C. After determining protein concentration with a Pierce Gold BCA kit (Thermo Fisher Scientific), 20 μg was taken forward for digestion. Samples were diluted 1:3 with 10% acetonitrile, 50 mM HEPES, pH 8.5, LysC (mass spectrometry grade, Wako) was added in a 1:50 (enzyme to protein) ratio, and samples were incubated at 37 °C for 4 h. Samples were further diluted to 1:10 with 10% acetonitrile, 50 mM HEPES pH 8.5, trypsin (mass spectrometry grade, Promega) was added in a 1:100 (enzyme to protein) ratio, and samples were incubated overnight at 37 °C. Enzyme activity was quenched by adding 2% trifluoroacetic acid (TFA) to a final concentration of 1%. Prior to TMT labelling, the peptides were desalted on a SOLARi C18 plate (Thermo Fisher Scientific). For each sample, the C18 material was activated with 200 μl of 100% methanol (HPLC grade, Sigma), and 200 μl of buffer B (80% acetonitrile, 0.1% formic acid). The C18 bedding was subsequently equilibrated twice with 200 μl of buffer A (0.1% formic acid), after which 20 μg of sample was loaded using centrifugation at 1,000 r.p.m. After washing the C18 bedding twice with 200 μl of buffer A, the peptides were eluted into clean 1.5 ml Eppendorf tubes using 40% acetonitrile and 0.1% formic acid. The eluted peptides were concentrated in an Eppendorf Speedvac and reconstituted in 100 mM tetraethylammonium bromide (pH 8.5) for TMT labelling. Labelling was done according to the manufacturer's instructions, and labelled peptides were subsequently mixed 1:1:1:1:1:1:1:1:1:1:1:1 (16-plex), acidified to 1% TFA and the acetonitrile concentration brought down to <5% using 2% TFA. Prior to mass spectrometry analysis, the peptides were fractionated using an offline Thermo Fisher Ultimate3000 liquid chromatography system using

high pH fractionation (5 mM ammonium bicarbonate, pH 10) at a flowrate of 5 $\mu\text{l min}^{-1}$. Peptides (20 μg) were separated over a 120 min gradient (from 5% to 35% acetonitrile), while collecting fractions every 120 s. The resulting 60 fractions were pooled into 30 final fractions (fractions 1 + 31, 2 + 32, 3 + 33, and so on), acidified to pH <2 with 1% TEA and loaded onto EvoSep StageTips according to the manufacturer's protocol.

Global TMT-labelled liquid chromatography–mass spectrometry data acquisition. For each fraction, peptides were analysed using the preset '30 samples per day' method on the EvoSep One instrument. Peptides were eluted over a 44 min gradient and analysed on an Exploris 480 instrument (Thermo Fisher Scientific) running in a data-dependent tandem mass spectrometry top-speed mode (3 s cycle time). Full mass spectrometry spectra were collected at a resolution of 60,000, with a normalized automatic gain control target of 300% and automatic maximum injection time, with a scan range of 375–1,500 m/z . The tandem mass spectrometry spectra were obtained at a resolution of 30,000 with the 'turboTMT' functionality enabled, with a normalized automatic gain control target of 100% and automatic maximum injection time, a normalized collision energy of 33 and an intensity threshold of 8 e^6 . First mass was set to 120 m/z to ensure capture of the TMT reporter ions, and precursors were isolated with a 0.7 m/z isolation window and Precursor Fit enabled to 70% at a window of 0.7 m/z . Dynamic exclusion was set to 60 s, and ions with a charge state <2, >7 and unknown were excluded. Mass spectrometry performance was verified for consistency by running complex cell lysate quality-control standards, and chromatography was monitored to check for reproducibility.

TMT quantitative proteomics analysis. The raw files were deposited in the PRIDE database of ProteomeXchange (PXD022145) and analysed using Proteome Discoverer 2.4. TMTPro reporter ion quantitation was enabled in the processing and consensus steps, and spectra were matched against the *Mus musculus* protein database obtained from Uniprot. Dynamic modifications were set as oxidation (M), deamidation (N,Q) and acetyl on protein N termini. Cysteine carbamidomethyl (on C residues) and TMTPro (on peptide N termini and K residues) were set as static modifications. All results were filtered to a 1% false discovery rate, and TMT reporter ion quantitation done using the built-in 'reporter ions quantifier' node, with statistical significance testing done with the built-in analysis of variance (ANOVA) test. Proteins were filtered for those with at least two peptides and visualized in R using the GGplot2 package or with GraphPad Prism.

Metastases formation. All animal experiments were conducted with 8-week-old mice, male as well as female animals from Net4 knockout and the corresponding wildtype littermates were used. Cohorts of wildtype and Net4-deficient mice were intravenously injected with 5 \times 10⁵ HCmel12 melanoma or 2 \times 10⁵ E0771 breast cancer cells. Mice were killed 20 and 28 days after injection of HCmel12 and E0771, respectively. The number of macroscopic metastases on lung surfaces and inside the abdomen (HCmel12) were counted in a blind fashion. In terms of the mouse breast cancer cell injection, lungs were further immunohistochemically (H&E) processed to determine and analyse microscopic lung metastases using NDP software (NDPscan version 2.5.90 and NDPview version 2.7.52). The experimental setup for the rescue experiment was slightly modified. Here Net4 knockout mice were treated with 1 \times PBS (control) or 2.5 mg per kg body weight recombinant Net4 for five consecutive days (days 1–5) prior to intravenous cell injection. After 5 d of treatment, animals were kept without any further treatment for an additional 2 d (days 6–7). On the following day (day 8), 5 \times 10⁵ HCmel12 melanoma cells were injected intravenously into Net4 knockout mice treated with PBS or Net4. Mice were killed on day 28 (20 d after HCmel12 intravenous injection). The number of macroscopic metastases on lung surfaces were counted in a blind fashion.

Pressure myography. All animal work was performed in accordance with UK Home Office Regulations, covered by UK Animal Project license 70/8604 and approved by the University of Glasgow animal ethics committee. Myography was performed on 5-month-old Net4 knockout mice with wildtype littermates as controls. Animals were killed by cervical dislocation and third-order mesenteric arteries were collected by dissection from the mesentery within 1 h of killing using a dissecting microscope (Leica) in cooled calcium-free physiological salt solution (cf-PSS: 0.25 M NaCl, 0.001 M KCl, 2 mM MgSO₄, 50 mM NaHCO₃, 2 mM KH₂PO₄, 1 mM glucose, 0.5 ml of 23 mM EDTA). Perivascular adipose tissue was removed, and mesenteric arteries were transferred into separate 1.5 ml microcentrifuge tubes containing cf-PSS. Samples were kept on ice for pressure myography and used on the day of collection. Mesenteric artery rings were mounted on two glass cannulas on a pressure myograph (Danish Myo Technology) in cf-PSS and maintained at 37 °C under 95% O₂/5% CO₂. The vessels were unbuckled and pressurized at 70 mmHg for 30 min for equilibration. Vessels were then subjected to a pressure curve (10, 20, 40, 60, 80, 100, 110 and 120 mmHg under passive conditions) using cf-PSS and measurements of internal (D_i) and external diameter (D_e) were collected at the end of 5 min at each pressure. Wall thickness, WT, was calculated as $(D_e - D_i)/2$. Circumferential wall stress σ was calculated as $(P \times D_i)/(2 \times WT)$ where P is the pressure. Circumferential wall strain ϵ was calculated as $(D_i - D_{i(10\text{mmHg})})/D_{i(10\text{mmHg})}$

NATURE MATERIALS

ARTICLES

($D_{@10\text{ mmHg}}$). Arterial stiffness independent of geometry is determined by Young's elastic modulus, E (stress/strain)⁶⁴. Statistical analysis was performed with GraphPad Prism version 8.1.1 software calculating the linear regression of stress-strain curves for both Net4 wildtype and knockout.

Quantitative rtPCR. HEK293, MDA-MB-231, E0771, 4T1 and HcMel12 cells were cultured in their respective media until a cell density of approximately 90% was reached. Cells were then trypsinized and centrifuged (1,000 r.p.m.; 5 min). Cell pellets were frozen on liquid nitrogen and stored on -80°C until further processing started. RNA was extracted using the RNeasy Mini Kit (Qiagen) following the manufacturer's instructions. After RNA extraction, RNA concentration was measured using a NanoDrop. Reverse transcription of 1 μg of RNA per cell line and replicate was performed using Transcriptor Universal cDNA Master kit (Roche) following the manufacturer's instructions. Real-time primers corresponding to mouse Net4 (forward: TGAGAATGCTGACCTCACTTGC, reverse: GGCAGCGTTGCATTATCACAC), mouse ribosomal protein lateral stalk subunit P0 (RPLP0) (forward: CATCATCAATGGGTACAAGCGC, reverse: CAGTAAGTGGGAAGGTACTC), human Net4 (forward: CCTGAACGAAGAGCCTCAACAT, reverse: GGTCTGAAGCCATGAACAGGTA) and human RPLP0 (forward: CTGCTGCCTCATATCCGGG, reverse: TGATCTCAGTGAGGTCCTCCTT) were validated for further analysis. Quantitative rtPCR was performed on a LightCycler 480 II (Roche; Light Cycler 480 SW version 1.5.1) by generating standard curves for mouse Net4 using HEK293 cells overexpressing mouse Net4, for human Net4 using HEK293 cells overexpressing human Net4, for the housekeeping gene mouse RPLP0 using E0771 cDNA and for the housekeeping gene human RPLP0 using HEK293 cDNA. Afterwards analysis of the standard curves using the Light Cycler 480 SW version 1.5.1 software was performed for each primer pair, resulting in the concentration of the transcript for each gene. Finally, the expression levels of mouse and human Net4 transcripts were calculated relative to the concentration of the respective RPLP0 expression.

CRISPR/Cas9-mediated *Ntn4* knockout in E0771 mouse breast cancer cells. The guide RNA (sgRNA) against the mouse Net4 gene (*Ntn4*) was generated using the sgRNA design platform of the Broad Institute (<https://portals.broadinstitute.org/gpp/public/analysis-tools/sgRNA-design>). The sgRNA oligos were annealed and cloned into the PX458 CRISPR/Cas9 vector. After sequencing, the vector was transfected into E0771 mouse breast cancer cells. Transfected cells were single-cell sorted into 96 well plates via detection of green fluorescent protein using a fluorescence-activated cell sorter after 24 h. Afterwards, cells were validated for *Ntn4* knockout via isolation of the gDNA followed by the amplification of the genomic region corresponding to the sgRNA binding region and cloned into a TOPO vector. Here, at least 10 clones were sequenced to identify specific *Ntn4* knockout on all alleles. E0771 *Ntn4*-knockout cells were used for intravenous injection into Net4 knockout and the corresponding wildtype litter animals.

scRNA-seq analysis. Using scRNA-seq data in melanoma (GSE72056)⁶², which contains data of 4,645 cells from 19 melanoma patients, including tumours from ten lymphoid metastases, eight distant sites and primary melanoma, we scrutinized which cell types express *NTN4* and additional BM-encoding genes (Supplementary Table 1). Based on cell-type-specific marker genes, we obtained cell clusters composed of seven cell types (Extended Data Fig. 6a): B cells, CAFs, endothelial cells, macrophages, melanoma cells, natural killer (NK) cells and T cells. We also investigated the expression of the additional 48 BM genes for each cell type (Extended Data Fig. 7). To find out the overall expression levels of the whole 49 BM genes in the seven cell types, we calculated an aggregate expression of the 49 BM genes using z scores.

Atomic force microscopy. AFM indentation experiments on Matrigel and lung tissue sections were performed with a NanoWizard 1 (JPK Instruments with JPK Control software 5.0.130) equipped with a $100\ \mu\text{m} \times 100\ \mu\text{m} \times 15\ \mu\text{m}$ piezo scanner. The AFM was mounted on an inverted optical microscope (Axiovert 200, Carl Zeiss) placed on an active isolation table (Micro 60, Halcyonics). The whole setup was placed inside a custom-built 1 m³ soundproof box to reduce the influence of ambient noise. All AFM experiments were carried out in PBS at room temperature, using silicon nitride MLCT cantilevers (Bruker) with a nominal spring constant of $\sim 0.1\ \text{N m}^{-1}$ for lung tissue sections and $\sim 0.03\ \text{N m}^{-1}$ for Matrigel experiments. The cantilever force constant was determined for each cantilever individually, using the thermal noise method⁶⁵. For all experiments, the Young's modulus was derived from the first 500 nm of the indentation part of the curves using a modified Hertz model^{66,7}. For data analysis, the JPK software (version 6.0.69) was used. The indentation experiments on the BM were performed on $15\ \mu\text{m}$ cryosections (Leica CM1950) of fresh, snap frozen, non-fixed lung tissue embedded in Tissue Tek OCT. The tissue slides were thawed and immersed in PBS for AFM measurements. First, overview force maps of $25\ \mu\text{m} \times 25\ \mu\text{m}$ were recorded on the alveolar wall showing the two cell layers and the BM. Then, three $1.5\ \mu\text{m} \times 1.5\ \mu\text{m}$ force maps, comprising the BM and the adjacent tissue were recorded. Each map consisted of 2,500 (50×50) indentation-retract cycles, rendering a lateral resolution of 30 nm for the subsequent Young's modulus analysis. Here, the z-piezo velocity

was $10\ \mu\text{m s}^{-1}$. Two alveolar walls were assessed for each animal. Because of time constraints, in these experiments, the cantilever force constant was assessed after recording the indentation maps. The cantilever deflection signal was limited to 1 V.

In the mixing approach $100\ \mu\text{l}$ of Matrigel matrix (Corning, lot 9091003, reference 354234) was gently mixed with 0.6%, 1%, 1.2%, 3%, 6%, 10%, 25%, 30% and 50% Net4 in PBS (Biochrom Dulbecco's PBS without $\text{Mg}^{2+}/\text{Ca}^{2+}$, pH 7.4) on ice and pipetted into a silicon ring with an inner diameter of 1 cm on top of a precooled microscope slide with a precooled pipette and incubated for 30 min at 37°C . The Matrigel sample was then transferred to the AFM stage, where a droplet of PBS was pipetted on top of the gel prior to AFM experiments. Maps of 10×10 force-distance curves were recorded with a $100\ \mu\text{m} \times 100\ \mu\text{m}$ scan area, at a z-piezo velocity of $5\ \mu\text{m s}^{-1}$. The indentation force was limited to 2 nN. At least five force maps on at least two different gels with a total number of 373–939 force curves per map were analysed.

In the titration experiment 2 ml of Matrigel matrix was plated on a precooled Petri dish (-20°C) followed by an incubation time of 30 min at 37°C . For AFM experiments 9 ml of PBS was added and force curves were recorded on the pure Matrigel. Then 0.1%, 0.5%, 1%, 2.5%, 5%, 10%, 25% and 50% Net4 were added in a titration procedure. Arrays of 10×10 force-distance curves were recorded in a $10\ \mu\text{m} \times 10\ \mu\text{m}$ scan area, at a z-piezo velocity of $5\ \mu\text{m s}^{-1}$. In the titration experiments, the indentation force was limited to 3 nN. In case of the collagenase treatment, Matrigel without collagenase and Matrigel with 200 U of collagenase (Worthington Biochemical) were allowed to polymerize at 37°C for 3 h before Net4 titration (1%, 2%, 6% and 10%) and constant AFM measurement.

Electron microscopy. Ketanest anaesthetized mice were perfusion fixed with 4% paraformaldehyde, 0.1 M PBS at pH 7.4 by cannulation of the left ventricle for 15 min. Following removal, the isolated lung tissue from perfusion-fixed mice was postfixed in 2% paraformaldehyde, 2% glutaraldehyde, 0.1 M cacodylate buffer at pH 7.35 for 6 h. The lung tissue was rinsed in cacodylate buffer three times and then treated with 1% uranyl acetate in 70% ethanol for 8 h to enhance the contrast. The lung tissue was subsequently dehydrated in a graded series of ethanol and then embedded in Araldite (Serva). Semithin sections ($0.5\ \mu\text{m}$) were cut with a glass knife on an ultramicrotome (Reichert) and stained with methylene blue. Ultrathin sections (70 nm) for electron microscopic observation were processed on the same microtome with a diamond knife and placed on copper grids. Transmission electron microscopy was performed using an EM109 electron microscope (Zeiss) with ImageSP version 1.2.6.11 software.

Theoretical modelling. In the simulations, the laminin 111 network in the BM is modelled as an elastic honeycomb network representing the laminin molecules and an additional constant elastic background contribution representing the underlying collagen IV network. In a 2D simulation box with periodic boundary conditions, 512 nodes are arranged on a honeycomb lattice and connected by harmonic bonds with a finite equilibrium length, representing the α , β and γ chains of the laminin heterotrimer. Dilution by Net4 is realized by identifying binding sites in between neighbouring laminin heterotrimers and randomly removing a fraction of these sites according to the Net4 concentration. This procedure is mathematically equivalent to site percolation on half of the sites of a honeycomb lattice. To obtain the elastic modulus, a longitudinal strain is applied by uniformly stretching the network stepwise in all fundamental lattice directions. After each stretching step, the energy of the elastic network is minimized with respect to the node positions using the conjugated gradient algorithm to obtain equilibrium positions and stretching energies. To these energy-strain curves, a purely quadratic energy function is added to account for the underlying collagen IV network. We averaged over 200 different dilution patterns per dilution fraction $\phi = \frac{\text{no. of removed sites}}{\text{no. of total sites}}$ to take care of effects arising from the random nature of dilution. We define the strain inflicted on the simulation box of area A as $\epsilon = \frac{A'}{A}$, where A' denotes the area of the stretched box. We obtain from the simulation the dilution-dependent energy density $w_g(\epsilon)$ as a function of the strain ϵ . The non-linear relationship between the energy density $w_g(\epsilon)$ and the uniaxial strain ϵ of a diluted 2D honeycomb network has the functional form

$$w_g(\epsilon) = \frac{1}{2} E_{\text{coll}} \epsilon^2 + \frac{1}{2} E_{\text{lam}}(\phi) (\epsilon - \epsilon^*(\phi))^2 \theta(\epsilon - \epsilon^*(\phi)), \quad (1)$$

where $\theta(x)$ is the step function and $\epsilon^*(\phi)$ is the dilution-dependent threshold strain (Extended Data Fig. 10f). The modulus $E_{\text{lam}}(\phi)$ is extracted from 2D network simulations (Extended Data Fig. 10g) as the slope of the linear part of the stress-strain curve (Fig. 5c).

In our AFM experiments, the effective BM elastic modulus $\kappa(\phi)$ was determined by measuring force-indentation curves $F(\delta)$, where δ denotes the indentation depth. The stress and strain fields caused by a conical indenter in a 3D material are concentrated in a region near the surface of the material and in the immediate vicinity of the indenter^{68,9}. We therefore approximate the extensional strain as the increase in surface area relative to the undeformed surface and calculate numerically the total energy of the deformed surface.

We estimate the extensional strain of an isotropic elastic medium at the surface indented by a cone by calculating the increased area of the deformed surface with respect to the undeformed state.

ARTICLES

NATURE MATERIALS

In the case of an isotropic elastic medium indented by a cone at the surface, the shape of the deformed surface reads⁶⁸

$$u_z(r, \delta) = \begin{cases} \frac{2\delta}{\pi} \left(\frac{r}{r_1} - \frac{\pi}{2} \right), & r \leq r_1 \\ \frac{2\delta}{\pi} \left(\frac{r}{r_1} - \sqrt{\left(\frac{r}{r_1} \right)^2 - 1} - \sin^{-1} \left(\frac{r}{r_1} \right) \right), & r > r_1 \end{cases} \quad (2)$$

for an indentation depth of δ and an indentation-dependent contact radius $r_1(\delta) = \frac{2\delta}{\pi} \tan(\alpha)$, where α denotes the half-opening angle of the cone. For our estimates, we choose half-opening angles of $\alpha = 20^\circ$, 40° and 60° . Although a value of $\alpha = 20^\circ$ corresponds best to the shape of the pyramidal tip used in the AFM experiments (Atomic force microscopy), presumably higher values of α are closer to reality with respect to phenomena neglected in our simple model, for example, imperfections of the AFM tip and the samples, torsional and radial strains as well as strains inflicted on the 3D material below the surface. The definitions of δ , r_1 and α are sketched in Fig. 5f. Since the total area of the deformed surface is given by

$S = 2\pi \int_0^{r_1} r \sqrt{1 + \left(\frac{du_z}{dr} \right)^2} dr$, we can define the local strain at the surface as

$$\epsilon_{loc}(r, \delta) = \sqrt{1 + \left(\frac{du_z}{dr} \right)^2} - 1 \quad (3)$$

and calculate the total energy of the deformed surface by an integral over the energy densities $w_\phi(\epsilon)$

$$U_\phi(\delta) = 2\pi \int_0^{r_1} dr r w_\phi(\epsilon_{loc}). \quad (4)$$

The dilution-dependent elastic modulus $\kappa(\phi)$ is then extracted from a quadratic fit of the energy function

$$U_\phi(\delta) = \frac{1}{2} \kappa(\phi) \delta^2. \quad (5)$$

to the total deformation energy $U_\phi(\delta)$ given by equation (4) and we thus obtain the rescaled effective modulus $\Delta\kappa(\phi) = \kappa(\phi)/\kappa(0)$ (Fig. 5g). The single parameter of this model is the collagen modulus E_{coll} in equation (1), which we obtain by a global fit of $\Delta\kappa(\phi)$ over all dilutions ϕ to the experimental data. The custom code generated for the theoretical modelling is available at <https://doi.org/10.17169/refubium-28413>.

Intracellular optical tweezers-based microrheology. 4T1 and KPC-mT4 were suspended in Matrigel and Net4 or Mut containing Matrigel (Corning) mixtures at a concentration of 4×10^5 cells mL^{-1} . Microrheology of highly refractive endogenous lipid granules was performed using an optical trap implemented in an inverted Leica DMIRBE microscope as described previously⁶³. The laser (Nd:YVO₄, 5 W Spectra Physics BL106C, $\lambda = 1.064$ nm, TEM₀₀) was highly focused by a water immersion objective (Leica, HCX PL APO 63 \times /1.2), collected by a condenser (Leica, P1 1.40 oil S1) and focused onto a quadrant photodiode (S5981, Hamamatsu) detection system. Data were recorded by an acquisition card (NI PCI-6040E) at a sampling frequency of 22 kHz and processed by LabVIEW software (LabVIEW 2010, National Instruments). For the small thermal fluctuations of lipid granules the voltage output of the photodiode is linearly related to particle displacement with respect to the laser focus⁷⁰. The positional time series were Fourier transformed and the power spectrum was analysed in Matlab R2016a (MathWorks) as described previously⁷¹. The movement of an optically trapped particle inside a viscoelastic environment is well described by a modified Langevin equation (6) where, at frequencies above the corner frequency, the positional power spectrum, $P_x(f)$, scales with an exponent, α :

$$\langle |\tilde{x}(f)|^2 \rangle \propto \frac{1}{f^{(1+\alpha)}} \quad (6)$$

where f denotes frequency. To extract the scaling exponent α , the above equation was fitted to the data in the frequency interval 500–9,900 Hz which is well above the corner frequency. The scaling exponent α carries information about the local viscoelastic landscape^{72,73} within living cells, where subdiffusion (characterized by $\alpha < 1$) is the dominating mode of diffusion. In the subdiffusive regime, a close to 1 indicates a more viscous environment, whereas α closer to 0 describes a more elastic environment.

Statistical analysis. Normality test was performed to determine normal distribution of the acquired data. Based on passing/not passing a normality test, a parametric (two-tailed unpaired *t* test or ordinary one-way ANOVA) or non-parametric test (two-tailed Mann–Whitney or Kruskal–Wallis) was chosen. In the case of pressure myography experiments, the analysis was performed using a linear regression test. The statistical tests used are indicated in the figure legends. Statistical analysis was performed using Prism version 8.4.3 (GraphPad) unless otherwise stated. Pearson's correlations in the ovarian dataset have been calculated

in R version 3.5.1 using the function `cor.test`. The effect size r of Pearson's correlation is indicated in the figures and legends.

Reporting Summary. Further information on research design is available in the Nature Research Reporting Summary linked to this article.

Data availability

All data used to generate graphs are available in the respective source data. The generated liquid chromatography–mass spectrometry data are available via the PRIDE database of ProteomeXchange (PXD022145). Data used in this study were taken from previously published datasets including the NKI breast cancer dataset (<https://ccb.nki.nl/data/>), normal breast data (<https://github.com/monkgroupie/Disease-Specific-Genomic-Analysis>), kidney dataset (GSE3538 and GSE3931), CANBUILD dataset (GEO: GSE71340), human melanoma scRNA-seq dataset (GEO: GSE72056), bulk melanoma RNA-seq data via TCGA (Human Skin Cutaneous Melanoma (SKCM)). Source data are provided with this paper.

Code availability

Custom codes of DSGA analysis of breast and kidney cancer datasets are available at GitHub (https://github.com/monkgroupie/publication_code). The custom code of the mathematical simulation of the impact of node dilution on the laminin network and overall BM stiffness is available via <https://doi.org/10.17169/refubium-28413>.

References

- Bald, T. et al. Ultraviolet-radiation-induced inflammation promotes angiogenesis and metastasis in melanoma. *Nature* **507**, 109–113 (2014).
- Johnstone, C. N. et al. Functional and molecular characterisation of EO771. LMB tumours, a new C57BL/6-mouse-derived model of spontaneously metastatic mammary cancer. *Dis. Model Mech.* **8**, 237–251 (2015).
- Aslakson, C. J. & Miller, F. R. Selective events in the metastatic process defined by analysis of the sequential dissemination of subpopulations of a mouse mammary tumor. *Cancer Res.* **52**, 1399–1405 (1992).
- Morton, J. P. et al. Dasatinib inhibits the development of metastases in a mouse model of pancreatic ductal adenocarcinoma. *Gastroenterology* **139**, 292–303 (2010).
- Minn, A. J. et al. Genes that mediate breast cancer metastasis to lung. *Nature* **436**, 518–524 (2005).
- Calvo, F. et al. Mechanotransduction and YAP-dependent matrix remodelling is required for the generation and maintenance of cancer-associated fibroblasts. *Nat. Cell Biol.* **15**, 637–646 (2013).
- Kowarz, E., Loscher, D. & Marschalek, R. Optimized sleeping beauty transposons rapidly generate stable transgenic cell lines. *Biotechnol. J.* **10**, 647–653 (2015).
- Kulak, N. A., Pichler, G., Paron, I., Nagaraj, N. & Mann, M. Minimal, encapsulated proteomic-sample processing applied to copy-number estimation in eukaryotic cells. *Nat. Methods* **11**, 319–324 (2014).
- Schjorring, O. L., Carlsson, R. & Simonsen, U. Pressure myography to study the function and structure of isolated small arteries. *Methods Mol. Biol.* **1339**, 277–295 (2015).
- Butt, H. J. & Jaschke, M. Calculation of thermal noise in atomic force microscopy. *Nanotechnology* **6**, 1–7 (1995).
- Docheva, D. et al. Researching into the cellular shape, volume and elasticity of mesenchymal stem cells, osteoblasts and osteosarcoma cells by atomic force microscopy. *J. Cell. Mol. Med.* **12**, 537–552 (2008).
- Prein, C. et al. Structural and mechanical properties of the proliferative zone of the developing murine growth plate cartilage assessed by atomic force microscopy. *Matrix Biol.* **50**, 1–15 (2016).
- Sneddon, I. N. Boussinesq's problem for a rigid cone. *Math. Proc. Camb. Philos. Soc.* **44**, 492–507 (1948).
- Sneddon, I. N. The relation between load and penetration in the axisymmetric Boussinesq problem for a punch of arbitrary profile. *Int. J. Eng. Sci.* **3**, 47–57 (1965).
- Ott, D., Reihani, S. N. & Oddershede, L. B. Crosstalk elimination in the detection of dual-beam optical tweezers by spatial filtering. *Rev. Sci. Instrum.* **85**, 053108 (2014).
- Selhuber-Unkel, C., Yde, P., Berg-Sorensen, K. & Oddershede, L. B. Variety in intracellular diffusion during the cell cycle. *Phys. Biol.* **6**, 025015 (2009).
- Tolic-Norrelykke, I. M., Munteanu, E. L., Thon, G., Oddershede, L. & Berg-Sorensen, K. Anomalous diffusion in living yeast cells. *Phys. Rev. Lett.* **93**, 078102 (2004).

Acknowledgements

We thank N.M. Christensen at the Center for Advanced Bioimaging (CAB), University of Copenhagen for providing microscope access, M. Ghilav and C. Hoffman for valuable experimental help on mouse perfusion and electron microscopy preparation, M.K.G. Hög and Britt Kongstoft for preparation of tissue samples, and L. Amandus and B.L. Kristensen for their support with all aspects of mouse handling. The melanoma

patient RNA-seq dataset analysed here is in part based upon data generated by the TCGA Research Network; <https://www.cancer.gov/tcga>. This work was supported by the European Research Council (ERC-2015-CoG-682881-MATRICAN (R.R., M.N., A.E.M.-G. and J.T.E.)); the Danish Cancer Society (R204-A12454 (R.R.), R146-A9250 (A.L.) and R167-A10618 (S.R.N.)); German Cancer Aid (R.R.); a Hallas Møller Stipend from the Novo Nordisk Foundation (J.T.E.); the German Research Foundation (DFG) (NI 1895/1-1 (D.N.), CRC1114/C02 (S.Z. and R.R.N.), FOR2722/B2 (M.K.) and CRC829 (W.B.)); a PhD fellowship from the Lundbeck Foundation (R286-2018-621 (M.R.)); a postdoctoral fellowship from the Lundbeck Foundation (R250-2017-389 (E.M.S.)); a grant from the Novo Nordisk Foundation (Novo Nordisk Foundation Center for Stem Cell Biology, DanStem, NNF17CC0027852 (E.M.S., B.T.P., H.K. and K.J.W.) and NNF19SA0035442 (B.F.)); the Danish Research Council (DFF-4002-00099 (L.W. and L.B.O.)); grants from the UK Medical Research Council (MR/R005567-1 (T.V.A.) and BHF (PG/15/92/31813 (T.V.A.)); a BHF studentship (FS/15/64/32035 (S.M.)); CANTER Research Focus of the Bavarian State Ministry for Science and Education (L.E., S.K., C.P., S.S. and H.C.S.); a CRUK Centre of Excellence Award to Barts Cancer Centre (C16420/A18066 (E.M.)); a CRUK fellowship (A27947 (O.M.T.P.)); the Ragnar Söderberg Foundation Sweden (N91/15 (C.D.M.)); the Swedish Research Council (2017-03389 (C.D.M.)); Cancerfonden Sweden (CAN 2016/783, 19 0632 Pj and 190007 (C.D.M.)); the Åke Wiberg Foundation (M17-0235 (C.D.M.)); and the Crafoord Foundation (20171049 (C.D.M.)).

Author contributions

R.R. hypothesized the mechanism and developed the project idea. R.R. and J.T.E. conceived and designed the study. R.R. defined the BM gene list. R.R., A.L., K.W.Z. and S.R.N. performed animal experiments. M.N. performed the genomic association analysis of BM genes with assistance from R.R. S.R.N. performed staining, imaging and analysis of stromal cells within E0771 primary tumours. R.R. performed proliferation experiments. A.L. performed contraction assays. S.Z., R.R.N. and R.R. developed the laminin network stiffness model. S.Z. and R.R.N. performed elastic module simulation

of the laminin network. L.F. and H.S.C. performed AFM analysis of the alveolar BM. S.K., C.P. and S.S. performed the AFM analysis of Matrigel. D.N. established the cancer cell invasion assay. D.N. and R.R. produced the recombinant proteins and performed invasion assays. M.R., E.M.S., B.F., B.T.P. and R.R. prepared and performed mass spectrometry experiments. H.K. and K.J.W. performed the scRNA-seq analysis. L.W. and L.B.O. performed optical tweezer experiments. S.M. and T.V.A. performed pressure myography measurements. R.R. and F.S. performed the immunofluorescence staining. E.M. and O.M.T.P. performed the analysis of BM gene association with ovarian patient tissue stiffness. M.K. provided the Net4 knockout mouse model and Net4-specific antibody. A.E.M.-G. performed the decellularization of lung and mesentery. C.D.M. and R.R. performed the imaging of the immunofluorescence staining. W.B. performed transmission electron microscopy analysis. R.R., J.T.E., M.N. and S.Z. wrote the paper. A.E.M.-G. drew the illustrations in Figs. 2a,g, 3b,i, 4a,c and 6b,c. R.R. generated the graphics in Figs. 5a,g and 6a and Extended Data Fig. 10a. R.R. and J.T.E. supervised the project. All authors discussed the results and commented on the manuscript text.

Competing interests

The authors declare no competing interests.

Additional information

Extended data are available for this paper at <https://doi.org/10.1038/s41563-020-00894-0>.

Supplementary information is available for this paper at <https://doi.org/10.1038/s41563-020-00894-0>.

Correspondence and requests for materials should be addressed to R.R. or J.T.E.

Peer review information *Nature Materials* thanks P. Mehlen, P. Yurchenco and the other, anonymous, reviewer(s) for their contribution to the peer review of this work.

Reprints and permissions information is available at www.nature.com/reprints.

Acknowledgement

This whole thesis would not have been possible without my two supervisors Attila Aszodi and Hauke Clausen-Schaumann. Thank you for years of encouragement, fruitful discussions and your passion for science.

I also would love to thank all my colleagues for wonderful years of good companionship and a lot of fun in the office. By people like Bastian Hartmann, Stefanie Kiderlen, Tanja Becke, Sascha Schwarz, Benedikt Kaufmann, Amelie Erben, Jakob Schmid and Jun Zhang, just to name a few, working in this laboratory was so enjoyable.

Special thanks also to Conny Hasselberg-Christoph for her perfect organizational skills and her pleasant nature.

I also want to say thank you to all my collaborators in ExCarBon and Copenhagen for being so enthusiastic for science.

Lastly, I want to express my deep gratitude for god who created this world so marvelous and we are still at the beginning to explore it.

Curriculum Vitae

Personal Data

Name: Lutz Fleischhauer

Date of birth: 09.09.1991 in Bad Soden am Taunus

Education:

Since 2017 Ludwig-Maximilians-Universität, München

University of Applied Sciences, München

PhD student

2014 – 2017 Westfälische Wilhelms-University, Münster

Molecular Biomedicine

Master of Science (1.3)

2011 – 2014 Johann Wolfgang Goethe-University, Frankfurt am Main

Biosciences

Bachelor of Science (1.6)

2007 – 2010 Martin-Niemöller Gymnasium, Wiesbaden

Abitur (2.0)

1997 – 2007 Theißtalschule, Niedernhausen